The statistical dynamics of geophysical flows:

An investigation of two-dimensional turbulent flow over topography

Terence J. O'Kane

BSc(Hons) LaTrobe University

MSc The University of Melbourne

School of Mathematical Sciences

Faculty of Science

Monash University

Submitted in fulfilment of the requirements of the degree of Doctor of Philosophy

September 15, 2002

Contents

abstract

The statistics of fluid turbulence is described by an infinite hierarchy of cumulant equations. A major aim of turbulence theory is the development of accurate, tractable closure models that can replace this hierarchy. In this thesis, numerical and computational techniques are presented to solve systems of integro-differential closure equations for inhomogeneous two-dimensional turbulent flow over topography. The closure equations, representing the first tractable closure theory for inhomogeneous flow over mean (single realization) topography, are based on a quasi-diagonal direct interaction approximation (QDIA) derived via renormalization techniques. The equations are computationally challenging due to the potentially long time history integrals. In order to reduce the computational cost a formal restart procedure has been implemented for the two- and three-point cumulant terms. The resulting closure equations with cumulant updates (CUQDIA) are shown to be in good agreement with the closure without restarts. The primary focus of the thesis comprises a comparison of the QDIA and CUQDIA closure equations with direct numerical simulation (DNS) of the primitive equation for barotropic flow over topography on an f-plane. This study involved the development of a numerical model to enable a comprehensive investigation of the relative merits of the DNS, QDIA and CUQDIA. A wide range of topographies have been considered as have inviscid unforced, viscous decay and viscous forced flows. Initially, the dynamics of the system are studied for severely truncated flow models at the level of a single wave triad and for C3 resolution (circularly truncated $k = 3$ wavenumber space), during which an inherent DNS sampling problem is identified. Subsequent higher resolution spectral studies at C16, C48 and C64 are found to demonstrate close agreement between the closure equations and DNS for low Reynolds

number. However, spurious convection effects in the transient fields of the QDIA are shown to produce an under-estimation of the small-scale amplitudes of the energy and enstrophy at moderate Reynolds numbers, as is the case with the direct interaction approximation for homogeneous turbulence. The mean enstrophies on the other hand are found to be in close agreement with DNS. The closure has been further extended to inhomogeneous flow on a generalized β-plane. The generalized β-plane employs a dispersion relation that incorporates terms for both planetary vorticity and the vorticity associated with the large-scale flow thereby allowing a one to one correspondence with the spherical geometry. The β-plane closure model is also compared to DNS at C3 and C16 resolutions for flow over an isolated Gaussian mountain demonstrating comparable agreement to the earlier f-plane study. Although previous closure studies have produced important insights into how random topography determines the spectra of transient vorticity variance this work comprises the first study of two-dimensional turbulent flow over single realization topography. As such the numerical and computational methods developed allow the examination of the effect of the mean topography on the structures of the mean flows with implications for the problem of resolving the interaction of the subgrid scale eddies with the mean topography.

declaration

The work embodied in this thesis was carried out in the School of Mathematical Sciences, Monash University, and at CSIRO Atmospheric Research from April, 1999 to September, 2002. Except where acknowledged in the customary manner, the material presented is, to the best of my knowledge, original and has not been submitted in whole or part for a degree in any University.

Signature.....

dedication

This thesis is dedicated to my wife, Marta and my mother, Mary.

acknowledgements

Throughout the candidature of my PhD thesis I have had the good fortune of having the supervision, support and friendship of two very eminent scientists, namely Dr Jorgen Frederiksen and Prof. David Karoly. I am indebted to my principal supervisor, Jorgen Frederiksen, for his encouragement and generosity in sharing with me some of his deep knowledge of statistical closure theory. Any insight I have gained into the statistical dynamics of geophysical flows has in no small measure been enhanced through many illuminating discussions with Jorgen. As well, I owe a debt of gratitude to my associate supervisor David Karoly, firstly for suggesting that I might work with Jorgen, secondly for always taking an active interest in my work and thirdly for providing an encouraging research environment both at the Co-operative Research Center for Southern Hemisphere Meteorology (CRC-SHM) and at the School of Mathematics, Monash University. I am grateful to CSIRO Atmospheric Research for providing me with a room and access to facilities including computing. I have also been fortunate to receive scholarships from the CRC-SHM, CSIRO Atmospheric Research, the School of Mathematics at Monash University, as well as a Monash University Travelling Scholarship. A PhD is a very stressful undertaking; however the friendship of my fellow postgraduate "comrades" Karl Braganza, Tim Wilkin and my brother Michael has often saved my sanity. I am also grateful for the support of my family who have endured difficult times recently. Finally, as always, without the love and support of my wife Marta this and indeed any endeavor would be as for nought.

preface

The original contributions in this thesis are contained in chapter 3, sections 3.4.2 and 3.5, chapters 4, 5, 6 and appendix III. This work can be largely separated into two categories, theoretical and numerical. The theoretical work contained in sections 3.4.2, 3.5, 6.1 to 6.4.2 and appendix III was developed in close collaboration with Dr Jorgen Frederiksen (CSIRO Atmospheric Research). The numerical work (chapters 4 and 5 as well as sections 6.4.2, 6.5 and 6.6) is solely that of the author with Jorgen Frederiksen providing suggestions regarding the formulation and some of the numerical experiments. The DNS code for flow over topography, QDIA and CUQDIA closure code detailed in chapter 4 used as the starting point DNS code for flow in the absence of topography and DIA closure code for non-topographic homogeneous turbulence developed by Jorgen Frederiksen, Anthony Davies, and Robert Bell at CSIRO Atmospheric Research. Sole responsibility for any error in the body of work contained in this thesis remains with the author.

Chapter 1

Introduction

Before the oarsmen of Odysseus
were able to exhaust the wine-dark sea
I can divine the indefinable forms
of that old god whose name was Proteus.
Shepherd of wave-flocks of the waters
and wielder of the gift of prophecy,
he liked to make a secret of his knowledge
and weave a pattern of ambiguous answers.

"Proteus" from The Book of Sand

Jorge Luis Borges

The study of turbulence holds a central place in modern physics, constantly challenging physicists and fluid dynamicists in a variety of theoretical specialities from scaling theory, statistical dynamics, renormalized group theory, multifractals etc., through to numerical fluid dynamics and large scale computing. The study of turbulence is problematic due to the fact that a continuous range of length scales in the system are excited simultaneously. Thus no small parameter exists and expansions must therefore be made in terms of the complexity of the interactions. The added combination of the coexistence of fluctuations and macroscopic space-time structures place turbulent phenomena squarely in the

domain of the statistical dynamicist. The complexity of geophysical flows has made understanding the processes of the oceans and the atmosphere difficult. This complexity arises precisely because of the nonlinear coupling across many scales of motion and because of inhomogeneities such as introduced by topography and land-sea contrasts in heating. Two dimensional turbulence, despite being non-existent in the natural world in the pure sense, is nevertheless a paradigm for our understanding of geophysical phenomena as it displays many of the features observed in both the oceans and the atmosphere. In addition, the relative thickness of the earth's troposphere compared with the earth's diameter, combined with the quasi-geostrophic large-scale motions of the atmosphere, provide further impetus for our interest in two-dimensional turbulence. The further goal of reliable long term weather and climate prediction may also require our gaining a deep understanding of the roles of coherent structures in the ocean and the atmosphere. Before giving an overview of the work contained in this thesis a brief discussion of some of the features of two-dimensional turbulent flows is presented.

1.1 Fluid turbulence in 2-Dimensions

Turbulence in two- and three-dimensions are very different phenomena. For example, an important difference that is of particular relevance to atmospheric flows is the propensity for coherent structures to form in two-dimensional turbulent flows [1]. In order to develop a background for the ensuing discussion of geophysical fluid turbulence a brief comparison of the fundamentals of turbulence in two- and three-dimensions is in order. Firstly, in fully developed three-dimensional homogeneous turbulence three distinct wavenumber regions may be identified 1) an energy injection region at the largest scales 2) an inertial range at the intermediate scales and 3) a dissipative range at the smallest scales. Three dimensional turbulence consists of a sea of eddies, varying in sizes, whose total kinetic energy is conserved in the absence of viscosity and forcing. It happens that the large, less numerous, eddies may distort the more numerous smaller eddies, whereas the effect of the many random interactions of the small eddies on the large eddies averages out any reciprocal distortions. A crucial point is that all eddy-eddy interactions are local, that

is large eddies interact with small eddies only via eddies of intermediate size. For forced dissipative flows this process leads to an energy cascade by which energy is transferred to smaller and smaller scales until eddies of such small size are produced that they are subject to the effects of viscosity and dissipated away. Kolmogorov [2] showed that a dimensional analysis of the inertial range gives an energy scaling law proportional to $k^{-5/3}$.

Turbulence in two-dimensions is somewhat more complicated due to the presence of an additional quadratic invariant, namely the enstrophy [1]. Enstrophy considerations forced an abandonment of Kolmogorov's picture of an energy cascade (as this would lead to energy creation in 2-D) prompting a search for a new interpretation of how energy and enstrophy are simultaneously distributed among the wavenumbers for forced dissipative 2-D flows. Fjørtoft [3] first demonstrated that the energy cascade hypothesis did not carry over to two dimensions and that if an intermediate scale is forced then rather than an energy cascade an enstrophy cascade results. Conversely the energy undergoes an inverse cascade to the larger scales. The 2-D enstrophy inertial range was later found to have an inertial range law of k^{-3} [4, 5, 6]. As discussed in chapter 2 the realization of a fully self-consistent closure theory that agrees with either the 3-D energy or the 2-D enstrophy scaling law represents a formidable endeavor.

1.2 The closure problem

The rapid spatial and temporal variation in the solutions of the primitive dynamical equations of turbulence is one of the principle reasons[2] that Navier-Stokes flows are resistant to direct numerical simulation at high Reynolds number and high resolution. In contrast statistical closure theory provides descriptions of the average behavior of an ensemble of turbulent realizations. An ensemble average is an average taken over an ensemble of turbulent flows with nearly identical external conditions. These flows differ due to the presence of large fluctuations that typify turbulence as well as uncertainty in the initial conditions thus forcing a statistical treatment. Each ensemble member is referred to as a realization. The dynamics of the ensemble averages are considerably smoother than that

[1] When topography is present the potential enstrophy is conserved.

[2] The large number of interaction coefficients required is another.

of the individual realizations of the primitive equations. In order to describe the statistical behavior of a turbulent flow the underlying nonlinear dynamical equations must be averaged producing an infinite hierarchy of moment equations.

The closure problem can be stated simply: consider a generic equation of motion with quadratic nonlinearity in the random variable $\mathbf{X}(t)$ in Fourier space with components X_i:

$$\frac{\partial}{\partial t} X_i = B_{\mathbf{ijk}} X_{-j} X_{-k}. \tag{1.1}$$

Here $B_{\mathbf{ijk}}$ are the interaction or mode coupling coefficients. Now the correlation between the eddies can be represented by an equation for the second moment which is found to depend on the third order moment

$$\frac{\partial}{\partial t} \langle X_i(t) X_{-i}(\acute{t}) \rangle = B_{\mathbf{ijk}} \langle X_{-k}(t) X_{-j}(t) X_{-i}(\acute{t}) \rangle \tag{1.2}$$

and similarly the third order moment depends on the fourth etc. Statistical turbulence theory is principally concerned with the methods by which this hierarchy is closed and the subsequent dynamics of the closure equations. The majority of closure schemes are derived using perturbation expansions of the nonlinear terms [3] in the primitive dynamical equations, with the most successful theories utilizing formal renormalization techniques for strongly nonlinear flows.

1.3 Geophysical flow over topography

In the case of geostrophic turbulence above topography, with random initial conditions, we find the emergence of a large-scale flow. For barotropic flow over topography it is the interaction of the eddies with the topography that generates this non-zero mean flow. Early numerical simulations, as well as studies based on canonical equilibrium theory [7, 8, 9, 10, 11, 12] led to the development of the dual principles of maximum entropy and minimum enstrophy. The minimum enstrophy principle argues that the enstrophy, which must decay faster than the energy due to preferential dissipation at the largest wavenumbers, is minimized in the system with the resulting streamfunction found to be parallel to the contours of the topography. It was later demonstrated that the maximum

[3] In 2-D turbulence theory we are primarily dealing with quadratic nonlinearities

entropy (canonical equilibrium) and the minimum enstrophy states are the same in the limit of infinite resolution [13].

The interaction of the eddies with the topography generates topographic stresses which play a very important role in determining the circulations of the ocean and the atmosphere. For example, these stresses are responsible for the anticyclonic motion of mean flows over topographic features [14, 15]. The problem of how to develop subgrid-scale parameterizations of the topographic stress in general circulation models is a difficult one [16, 17]. The basis for any parametrization of these effects would ideally have a solid physical and mathematical foundation. One of the fundamental goals of statistical closure theory is the development of a tractable closure scheme that can investigate the effect of the mean topography of the ocean or the atmosphere on the structures of the mean flow. This thesis examines the dynamics and spectra of a just such a closure theory, developing numerical techniques to render the theory computationally tractable, and examining rotating flows both with and without large-scale zonal flow and differential rotation.

1.4 Thesis overview

An overview of the thesis, in which the various chapters and sections are briefly described, will now be presented. The thesis begins with a formal review of the methods and important papers that underpin statistical turbulence theory. The first approach reviewed is the heuristic Eulerian and Lagrangian formulations of the direct interaction approximation (DIA) for stationary, isotropic and homogeneous turbulence in two and three-dimensions. Next an equivalent diagrammatic method similar to the Feynman diagram approach to quantum electrodynamics is presented. This is followed by the more general functional operator and functional path integral methods in which no assumptions of isotropy or homogeneity are made. The next section in the literature review discusses the large body of work where the Markovian approximation is applied to the closure problem. In closing this review a heuristic vertex renormalization, proposed by Kraichnan and only very recently implemented by Frederiksen and Davies, known as the "regularized" DIA is discussed. A more detailed review of the mathematical aspects of the Eulerian DIA is given in appendix

I sections I.1 to I.4. This rather detailed appendix is included for completeness and in order to provide the interested reader with a more mathematically detailed explanation of the assumptions that comprise the DIA. The DIA is fundamental to the discussions contained in this thesis. It should be noted however, that this appendix comprises review material only.

The core of the thesis is contained in the next three chapters. Initially, in chapter 3 a brief discussion of the development of inhomogeneous closure theories for flows with and without topographic terms incorporated is undertaken before presenting in detail the quasi-diagonal DIA (QDIA). The QDIA forms the basic tool for our investigation of geophysical flow over topography; however it unfortunately contains potentially long time-history integrals that render it computationally intractable for anything but short time periods even at low spectral resolution. In order to tackle this problem a formal restart or cumulant update procedure (CUQDIA) has been developed, a discussion of which comprises the remainder of chapter 3. Appendix II contains a derivation of the required interaction coefficients for the Fourier transform of the barotropic vorticity equation while appendix III contains an alternative derivation of the two-point restart terms derived in section 3.4.2.

Chapter 4 presents the development of the computational and numerical methods necessary to implement both the CUQDIA and direct numerical simulation (DNS) of the barotropic vorticity equation for flow over topography. The structure of the code, discretization of wavenumber space, time-stepping scheme, integral methods as well as the implementation of the restart procedure are all dealt with in turn. As well a number of diagnostic tests enabling rigorous testing of the code are developed.

After a brief review of two important previous works dealing with closure theories for turbulent flow over random topographies with zero mean, the main results of the thesis are discussed in chapter 5. The first section deals with an inherent problem with DNS calculations; that is, the sampling error that arises due to an inability to specify the initial fields exactly. The causes of this error are identified and the dynamics of a single triad calculation are investigated. The triad calculation represents a case where an ensemble of initial DNS fields can be constructed such that there is no sampling error

as far as generating homogeneous statistics is concerned. Alternate methods to minimize sampling error are discussed for higher resolution studies. A further investigation is next presented of the dynamics of the modes at circularly truncated $k = 3$ wavenumber space (C3) resolution for inviscid unforced, viscous decay and forced dissipative cases where the topography is chosen such that the magnitudes of the mean and transient enstrophies are equal at equilibrium. This particular choice of topography ensures a strong mean field and topography amplitude at the small-scales and therefore a rigorous test of the theory.

The remainder of this chapter compares the discrete closure theory with DNS at resolutions from C16 to C64 for a variety of topographies commonly employed in idealized studies, as well as including that used for the C3 case. Sections 5.5.2 and 5.5.3 primarily investigate viscous decay from canonical equilibrium finding close agreement between DNS and CUQDIA. However, in section 5.6 it is shown that for moderate Reynolds numbers, and when the small-scale topography is very weak, the CUQDIA underestimates the transient enstrophy due to spurious convection effects arising from the absence of vertex renormalization terms. This behavior is similar to that of the isotropic direct interaction approximation in the absence of topographic interaction.

Finally, in chapter 6 both the closure theory and the numerical model are extended from the f-plane to a β-plane. The "standard" β-plane approximation is problematic in that it neglects the effects of solid body rotation vorticity in the dispersion relation, unlike the spherical geometry formulation. As well the QDIA closure is non-symmetric when formulated on the standard β-plane and therefore is significantly more difficult to implement than the f-plane QDIA. By incorporating a representation of the solid body rotation vorticity term into the dispersion relation we are able to show that the resulting "generalized" β-plane is a better approximation to the spherical geometry. Furthermore, it allows a symmetric formulation of the QDIA equations whereby the additional terms due to the β-plane effect may be incorporated into the model through the interaction coefficients. Sections 6.1-6.4.2 contain the mathematical details of the generalized β-plane closure. Simulation results (at C3 and C16 resolution) comparing the β-plane closure and DNS experiments are presented in sections 6.4.2, 6.5 and 6.6.

Chapter 2

The statistical theory of turbulence

Enmity be between you! Too soon is it for alliance.
Search along separate paths, for that is how truth comes to light.

Freidrich von Schiller

The statistical theories discussed in this chapter are based on the application of the renormalization techniques of quantum field theory to the complex study of classical dynamical fields and in particular to turbulence. Such calculations are difficult due to the fact that turbulence has no small parameter and we must base our expansion in terms of the complexity of the system. It can easily be demonstrated that a naive perturbative expansion in powers of the Reynolds number diverges badly for large values while an expansion in terms of the time of evolution diverges for long evolution times [18].

The direct interaction approximation (DIA) of Kraichnan [19, 20] proved a seminal breakthrough in the theory of statistical closures for equations with quadratic nonlinearities. The DIA was initially formulated in a heuristic manner but has subsequently been derived more systematically via techniques based on renormalization methods developed by Schwinger [21, 22], Dyson [23], and Feynman [24, 25] for quantum electrodynamics. It remains the most successful of the statistical closure theories for turbulence, being in good

agreement with both experimental wind tunnel measurements [26] at moderate Reynolds number and yielding a realistic value of the Kolomogorov constant in Lagrangian form [27]. The Eulerian DIA does however fail to yield the Kolmogorov spectrum in the inertial range due to spurious convection effects which arise from closing the system at second order. It is noted that this failure can be overcome via the implementation of a heuristic vertex renormalization or regularization [28]. This aspect of DIA theory will be discussed in more detail later in this chapter.

A more systematic application of renormalized perturbation theory to the problem of hydrodynamic turbulence was undertaken by Wyld [29]. This approach necessitated analysis of the higher order terms in the series by using a "Feynman" diagram approach. Wyld was able to correctly consider up to fourth order in the interaction coefficients. However, it was the subsequent work of Lee [30] which correctly applied vertex renormalization to extend the method to sixth order for the hydromagnetic case. The DIA is readily obtained from both the Wyld and Lee formalism by the retention of only the simplest terms at second order, that is, the DIA only takes into account directly interacting modes. Indeed, the reduction to the DIA is the standard test for any higher order renormalized theory.

Navier-Stokes based theories attempt to study the universality of the small scale structure of turbulence on scales belonging to the inertial range by analytic and numerical solutions to the equations of fluid mechanics. In order to describe a turbulent fluid flow, we need to provide a statistical description which is achieved using long time averages of the fluctuations of the velocity field $\mathbf{u}(\mathbf{r}, t)$. The physical quantities of interest are the mean field, the two-point covariance or fluctuation function and the function describing the response to infinitesimal disturbances.

It is the purpose of this chapter to present a description of the development of DIA-based statistical theories of turbulence, placing emphasis on the successes, failures and approximations of each theory. The three formalisms that underpin the DIA are the Eulerian closure of Kraichnan [19], the functional operator approach of Martin, Siggia and Rose (MSR) [31], and the path integral method [32, 33]. Firstly we review the Eulerian and Lagrangian formulations of the DIA. Appendix I contains a more detailed mathematical review of the seminal aspects of the Eulerian DIA. This appendix presents a

straight forward heuristic derivation of the DIA (following Kraichnan) from the Navier-Stokes equation. The MSR approach recasts the problem in terms of closed self consistent equations in which only the two-point covariance and exact response to infinitesimal disturbances appear. A Heisenberg operator formalism is developed through the ad hoc introduction of an adjoint field thus allowing "charge" renormalization and providing the correct vertex terms missing from the Wyld formalism. The origin of the adjoint field was demonstrated through the derivation of the Schwinger-Dyson equations from path integrals. This approach was elegantly developed by Jensen [32] who extended the method to consider multiplicative random forces, nonlocal causal interactions and non-Gaussian initial conditions. It is noted that the MSR results can also be derived using path integrals and the equivalence of both methods demonstrated. Throughout this thesis the DIA has been applied both to the 2-D Navier-Stokes equation in velocity $\mathbf{u}$ and vorticity ζ forms.

2.1 Eulerian and Lagrangian formulations

The DIA, as developed by Kraichnan [19, 34], was the first fully self consistent analytical theory of turbulence in fluids, which is remarkable given previous attempts by Heisenberg [35, 36] and Chandrasekar [37]. Despite the failure of the DIA to agree with the experimental results in the inertial range at high Reynolds number, the DIA has led to great insight into the nature of the cascade of energy from small to large wavenumbers in 3-D turbulence as well as the associated enstrophy cascade to larger wavenumbers in 2-D turbulence. Kraichnan noted that the failure of the DIA in the inertial range arises from spurious convection effects in the DIA that is a direct consequence of closure (but not renormalization) at second order. While renormalization restores some higher order effects there remain some spurious interactions between the large and smaller scales and as a consequence the DIA under-represents the kinetic energy in the inertial range [28, 38].

In an attempt to overcome the inertial range problem Kraichnan subsequently developed the Lagrangian-histories DIA (LHDIA) [39, 40, 41], and the abridged-LHDIA (ALHDIA) [40, 42]. The LHDIA was initially derived as heuristic modifications of the Eulerian DIA [27]. However, the LHDIA can also be derived from the DIA via the substitution

of generalized Lagrangian history co-ordinates for Eulerian co-ordinates, coupled with the alteration of the time arguments, in order to create a purely Lagrangian formulation. The ALHDIA represents a further modification of the LHDIA in which the time arguments of the convolution integrals are modified for a subset of the LHDIA equations which is purely Lagrangian. This procedure is described in some detail in section 7.2.4 of McComb [43]. It was also demonstrated that the LHDIA and ALHDIA lowest order expansion term for the passive scalar reproduces Taylors [44] exact result for the dispersion of fluid elements, while the higher order terms govern the deviations of the particle-displacement distribution from Gaussian form.

The problem of generalizing quasi-Lagrangian closures such as the LHDIA and ALHDIA to inhomogeneous flows represents an exceedingly difficult task. Significantly, Frederiksen and Davies [28] have very recently shown that a regularized form of the DIA (RDIA) and the cumulant update RDIA (RCUDIA) are generally superior to the ALHDIA continuous closure results for spectra considered by Herring and Kraichnan (Fig. 8b [42]). However, the RDIA contains a specified "cut-off" parameter α. In particular, the ALHDIA was found to over-estimate the enstrophy inertial transfer rate to high wavenumbers in 2-D turbulence, which is the direct opposite to that of the DIA. Kraichnan [41] was subsequently able to develop systematic renormalized perturbation expansions which were invariant at each order under random Galilean transformations (unlike the DIA) of which the LHDIA represents a lowest order approximation. A further approach is the strain-based LHDIA (SBLHDIA) and strain-based ALHDIA (SBALHDIA) whereby the velocity field is replaced by the rate-of-strain tensor in the primitive perturbation series. This approach was developed by Kraichnan and Herring [45, 46].

The formal renormalization procedure that forms the basis of the DIA is predicated on the idea that the nonlinear couplings can, prior to renormalization, be treated as though they are weak, such as is the case for the quantum electrodynamics problem. However, renormalized perturbation theory has been shown to enjoy enormous success for highly nonlinear systems, partially due to the fact that renormalization acts to remove secular terms, therefore avoiding the so-called infrared and ultraviolet catastrophes associated with naive perturbative approaches. As stated previously, the DIA is physically realizable

thus ensuring positive spectra unlike closures based on the quasi-normal hypothesis [47] [1]. Kraichnan [18] also explored a novel approach to the question of the validity of the DIA for strongly nonlinear systems by first considering a model equation for which the DIA is an exact solution. The solutions to the model equation thus represent exact descriptions of possible dynamic systems thereby displaying consistency properties. The model equations are then modified via the introduction of random couplings into an equation for which the DIA gives the exact statistical average. The important point is that this modification is not predicated on the basis that the nonlinear terms are small. Shivamoggi et al [50] discuss the mathematical aspects of this approach and demonstrate that the application of the DIA to Kraichnan's model equation leads to a functional equation. Kraichnan demonstrated that the model solutions have a representation in the sums of infinite classes in terms of the formal perturbation expansions to the solutions to the true problem. Further, it was shown that the corresponding stochastic model can be used as a guide to the validity of the partial summation of the perturbation series. This approach has obvious relevance to the quantum mechanical many-body problem [51].

2.2 Diagrammatic methods

Perhaps the most illuminating approach to the problem of approximating the higher order moments is the use of Feynman diagrams [23, 52, 24, 29, 30]. The first systematic attempt to deduce a theory of turbulence in an incompressible fluid from first principles using diagrammatic methods similar to those employed in quantum field theory is due to Wyld [29] and was subsequently generalized to stationary isotropic hydromagnetic turbulence by Lee [30] [2]. The approach is to find solutions to the velocity field in the form of a perturbation series and represent the terms in the series by a one-to-one correspondence with diagrams similar to Feynman diagrams. Wyld showed that these diagrams may be rearranged and then partially summed, reducing to integral equations governing the second order correlation functions for the velocity. The equations have the form of infinite

[1] Exceptions are the eddy damped quasi-normal Markovian closure for isotropic turbulence [48] and the realizable Markovian closure of Bowman et al [49]

[2] Hasselmann [53] also developed a set of diagrammatic rules for wave-wave scattering processes.

power series integral equations from which Wyld was able to derive terms to fourth order from an analysis of the diagrams. Approximation at lowest order yields Chandrasekars' equations (Eqs. 36 and 40 [29]), which are essentially the same as the quasi-normal theory applied to two-time correlations [43], while second order gives Kraichnan's DIA.

Reviews of the Eulerian diagrammatic method can be found in McComb [43], Phythian [54] and, L'Vov and Procaccia [33]. We refer the reader to these publications. The diagrammatic form of the DIA is shown in Fig. 2.1. Note that the heavy lines represent the integral equations for the generalized propagator and cumulant functions. The Wyld resummation is only correct to fourth order in the interaction coefficients due to an incorrect vertex renormalization, while Lee [30] derives the correct expansion to sixth order for the hydromagnetic case. L'vov and Proccacia [33] and Phythian [55], among others, have confirmed that Wyld's resummation is indeed correct to fourth order but it was Martin, Siggia and Rose (MSR) [31] who correctly derived the missing higher order vertex terms using a functional operator formalism. The MSR operator formalism is discussed in the following section.

2.3 Functional operator methods

The functional operator formalism of Martin, Siggia and Rose (MSR) [31] employs a Schwinger [22]-Dyson [23] type functional formalism allowing the calculation of the correct renormalized expansions to all orders. This approach is completely general, making no assumptions of isotropy or homogeneity[3]. The MSR approach recasts the statistical dynamics of a classical random variable, that satisfies a nonlinear equation of motion, in terms of a set of closed, self-consistent equations in which only the observable covariances at pairs of points and the exact response to infinitesimal disturbances appear. Consider an equation of motion for the operator $\psi(1)$

$$\frac{\partial \psi\,(1)}{\partial t_1} = U_1\,(1) + U_2(12)\psi(2) + U_3(123)\psi(2)\psi(3) \tag{2.1}$$

where $1 \equiv (t_1, x_1 \ldots x_d, n_1 \ldots n_m) = (t_1, \mathbf{1})$ represents the arguments of the field, namely time (t), space ($\mathbf{x}$), and any additional variables and internal indicies ($\mathbf{n}$) and where the

[3]We note that the DIA also makes no assumptions of isotropy or homogeneity

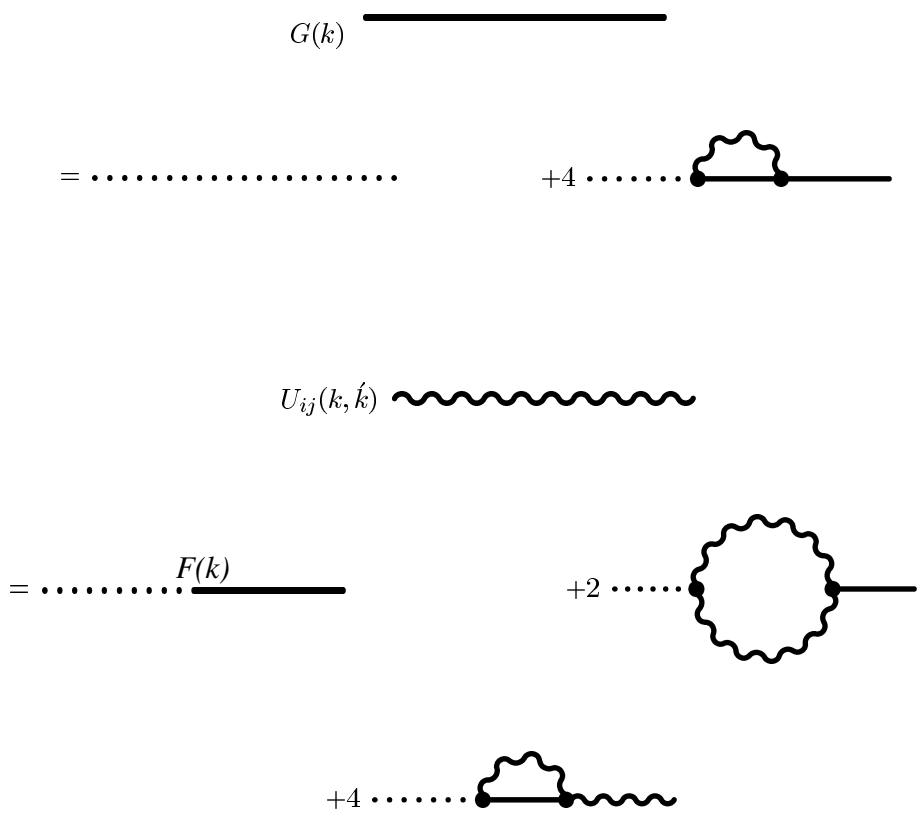

Figure 2.1: The DIA in diagrammatic form. Kraichnan's equations for the velocity correlation U containing correction terms in the generalized propagator G but excluding vertex renormalization. Note that dotted lines are used to denote the 0^{th} order propagator, thick lines represent the generalized propagator and $\bullet$'s are the bare vertices. Finally the forcing $F_{im}(k) = \langle f_i(k) f_m(\acute{k}) \rangle$.

forces and interactions $U_i(1 \dots i)$ obey

$$U_1(12) \propto \delta(t_1 - t_2) \tag{2.2}$$

$$U_3(123) \propto \delta(t_1 - t_2)\delta(t_1 - t_3) \tag{2.3}$$

$$U_3(123) = U_3(132). \tag{2.4}$$

Systems which may be described by such an equation of motion are exemplified by the damped anharmonic oscillator or alternately by a system of particles interacting via 2-body forces in a magnetic field [56] and of course the Navier-Stokes equation. A more generalized path integral approach allows the consideration of Vlasov turbulence [32]. As with the Heisenberg operator formalism of Quantum Mechanics (QM), a probability distribution for the initial values of ψ must first be specified. In the QM case, the expectation values of the field operator ψ and its Hermitian conjugate $\psi^\dagger$ describe both the covariances in the system and its response to external perturbations. However in the classical case, there is no obvious adjoint field, thus in order to determine the response functions Martin et al introduced an operator $\hat{\psi}$ in an ad hoc fashion to be interpreted as an excitation operator causing small perturbations to ψ.

We further note that the MSR formalism, although resembling the Schwinger [21, 22], Dyson [23] method of Quantum Field Theory (QFT), is formally more complicated to implement. Although both QFT and the classical statistical dynamical case require the simultaneous calculation of both the response and two-point covariance functions, the QFT case simplifies due to the linear relation between these two functions via the fluctuation-dissipation theorem (FDT). In the classical case, we unfortunately do not in general have such a relation although Kraichnan [57], Leith [58], Bell [59], Deker and Haake [60], Carnevale et al [61], Herring [62] and McComb et al [63] have considered cases where the FDT holds. That is, in QM systems, the operators are Hermitian whereas, in the classical macroscopic case, they are generally not.

The difficulty with turbulence for perturbative approaches is that, in the limit of large Reynolds number, there is no external expansion parameter which can be used as a basis for an expansion technique. At large Reynolds number, using the language of quantum field theory, it is a problem of an infinitely strong coupling constant requiring that the

expansion must necessarily be in terms of the internal properties of the system, that is, in terms of the complexity of the interactions [4]. The fact that the system is substantially random suggests that the generalized phase space equation, or Liouville equation should be a good approach. However Edwards [64] showed that at best only a DIA like approximation can be reached via this method. Carnevale and Frederiksen [65] further demonstrated that the three different formalisms of Kraichnan [66], Leslie [20] and Edwards [64] theory arise due to differing definitions of the renormalized viscosity with Edwards resulting from an inconsistent identification of the non-stationary energy-spectrum relaxation rate with the viscosity.

As with the Wyld resummation approach, the MSR method reduces to the DIA at second order. Martin et al [31] make the further point that Kraichnan's DIA equations would be rigorous but for vertex renormalization effects and further noted that the failure of Wyld's resummation was the omission of all 3 vertex terms identified by Martin et al [31] using the operator formalism [5]. The salient point here is that the strong turbulence problem is mathematically identical to the problem of vertex renormalization. We do not include the associated diagrammatic operator approach but refer the interested reader to the original paper of Martin et al [31].

2.4 Functional path integral methods

The path integral formalism of Schwinger [21, 22], with the path integral method of Feynman [24, 25, 67], as elucidated by Dyson [23], were first applied to the Navier-Stokes equation by Janssen [68], DeDominicis [69], and, DeDominicis and Peliti [70]. This approach was extended by Phythian [55] to consider the case of multiplicative random forces. However, the approach that is most readily understood, and the one we will follow, is that of Jensen [32]. This functional approach, closely related to that of Jouvet and Phythian [71], generalizes the MSR formalism for deterministic forces and local interactions to the

[4] The case of inviscid unforced dynamics has no flux through the system and is therefore not the same as large Reynolds number turbulence where we take the $lim \;\; \nu \rightarrow 0$

[5] Wyld's resummation only incorporates the $\Gamma_3^{(1)}$ vertex (see section III [31]).

whole class of first order stochastic differential equations described by

$$\frac{\partial}{\partial_{t_1}}\psi(1) = U_1(1) + U_2(12)\psi(2) + U_3(123)\psi(2)\psi(3) + \ldots + U_n(1\ldots n)\psi(2)\ldots\psi(n) + \delta(t_1 - t_0)\psi(\mathbf{1}) \tag{2.5}$$

where $1 \equiv (t_1, x_1 \ldots x_d, n_1 \ldots n_m) = (t_1, \mathbf{1})$ is defined as for Eq. 2.1. Jensen was able to unify the method of mixed averages employed by Deker and Haake [60] with that of Phythian's based on the Novikov Theorem [72] as well as extending these approaches to consider nonlocal random interactions with arbitrary statistics. Incidentally, Jensen fails to take into account the correct time ordering of the connected Green's functions and thus his results fail to incorporate some dissipative terms.

Jensen extended the results of Krommes and Kleva [73] beyond instantaneous local interactions to consider nonlocal interactions. Specifically Jensen considered electromagnetic plasma oscillations using the Vlasov theory. Because of its generality, the functional integral approach is equally applicable to nonlocal causal interactions as it is to local interactions. The functional equations corresponding to Vlasov turbulence can be written in the same form as expressions for hydrodynamic turbulence. The strength of the functional integral formalism is that the problem can be treated in generality where the adjoint field that was introduced in an ad hoc manner in the MSR theory now arises in a natural way [33].

2.5 Markovian closures

By far the majority of the statistical closure computations in the literature are based on a Markovian approximation and thus can only predict equal-time covariance data and approximate time-history effects. In this section we briefly review the development of the important Markovian closures and the approximations that underpin them, beginning with the quasi-normal approximation.

The quasi-normal approximation (QN) is attributed to Millionshtchikov [74] and was independently formulated by Chou [75]. The QN arose out of the observation that approximation of the turbulence velocity field by a Gaussian random function was problematic

as this would eliminate energy transfer between wavenumbers which is proportional to third-order moments in Fourier space. Instead the following approach was taken. The QN approximation, stated simply, is to assume that the fourth-order cumulants are identically zero without any assumption made on the third-order moments. This allows the system to be closed by replacing the fourth-order moment by the Gaussian value taken from its representation in terms of second-order moments. The resulting spectral equations for isotropic turbulence are due to Proudman and Reid [76] and Tatsumi [77].

Unfortunately, nonrealizability, the appearance of negative energies in the energy containing eddies range, was subsequently discovered by Ogura [47]. Orszag [78, 48] showed that this anomalous behavior resulted from a build up of the strength of the third-order moments. The nonrealizability of the quasi-normal closure arises due to the appearance of only linear viscous effects in the memory cut-off integral. It is a direct consequence of the neglect of fourth-order cumulants in the evolution equation for the three-point cumulant Eq. 2.6, which appears in the evolution equation of the triplet correlation function:

$$(\frac{\partial}{\partial t} + 2\nu_k)C_k(t) = \int_0^t ds \exp[-(\nu_k + \nu_p + \nu_q)(t-s)]$$
$$\times \sum_{\mathbf{k}+\mathbf{p}+\mathbf{q}=0} [B^2_{\mathbf{kpq}} C_p(s)C_q(s) + 2B_{\mathbf{kpq}}B_{\mathbf{pqk}}C_q(s)C_k(s)] \tag{2.6}$$

for real $\nu_k = \nu k^2$, $B_{\mathbf{kpq}}$, $\mathbf{k} = (k_x, k_y)$, $k = \sqrt{k_x^2 + k_y^2}$, and where ν_k is the linear damping and $B_{\mathbf{kpq}}$ the mode coupling coefficient. Here $C_k(t)$ is the single time cumulant. Lesieur [79] points out that it was shown experimentally that these moments saturate and that the role of the missing fourth-order cumulants is to provide a damping action required to facilitate saturation.

Orszag proposed that the damping effect of the neglected fourth-order cumulants could be compensated for in the QN theory by the addition of a linear damping term μ_{kpq} defined to be the characteristic eddy damping rate of the third order moment associated with the triad $(\mathbf{k}, \mathbf{p}, \mathbf{q})$. For isotropic turbulence this eddy damping rate can be approximated as

$$\mu_{kpq} = \mu_k + \mu_p + \mu_q \tag{2.7}$$

and thus the exponential term in Eq. 2.6 is replaced by

$$\exp\left(-[\mu_{kpq} + \nu_k + \nu_p + \nu_q](t-s)\right). \tag{2.8}$$

Orszag first introduced eddy-damping [78] as a mechanism to remedy nonrealizability by replacing the viscous damping ν_k by the total eddy viscosity via the eddy-damping parameter μ_k.

Unfortunately this so-called eddy damped quasi-normal (EDQN) theory still does not guarantee realizability and led to Orszag [78] subsequently developing the eddy-damped quasi-normal Markovian closure (EDQNM) via a "best Markovian fit" to the DIA that is consistent with an underlying Langevin representation [49, 80]. The EDQNM is dependent on a choice of an eddy-damping parameter μ_k which can be "tuned" to match the phenomenology of the inertial range. This Markovian approximation assumes that the rate at which the memory integral decays is significantly faster than the time-scale on which the covariances evolve[6]. Thus the characteristic triad interaction time is defined as

$$\Theta_{kpq} = \int_0^t e^{-[\mu_{kpq}+\nu_k+\nu_p+\nu_q](t-s)} ds \tag{2.9}$$

which, if we neglect the time variation of μ_{kpq} [81], takes the form

$$\Theta_{kpq} = \frac{1 - e^{-[\mu_{kpq}+\nu_k+\nu_p+\nu_q]t}}{\mu_{kpq} + \nu_k + \nu_p + \nu_q}. \tag{2.10}$$

That the EDQNM is realizable for the case of homogeneous isotropic turbulence is easily established via the properties of the interaction coefficients [48]. However, Bowman et al [49] pointed out that the EDQNM may not be realizable in cases where linear wave phenomena such as Rossby waves or gravity waves are present.

Bowman et al. [49] noted that realizability is first violated in the EDQNM at the point where the FDT is applied ie $C_k(t,t') = R_k(t,t')C_k(t)$. Instead, an alternate nonstationary FDT ansatz (Eqs. 2.11 and 2.12) was proposed that allowed the DIA covariance equation to be Markovianized. Their FDT is

$$C_k(t,t') = C_k^{1/2}(t) r_k(t,t') C_k^*(t') \tag{2.11}$$

where

$$r_k(t,t') = R_k(t,t') + R_k^*(t,t'). \tag{2.12}$$

[6]This assumption is valid in the inertial range but is questionable in the energy containing range of wavenumbers where the respective rates are of the same order.

Here R_k is determined by the standard EDQNM equation for the response function

$$\frac{\partial}{\partial t}R_k(t,t') = \sum_{\mathbf{k+p+q}=0} B_{\mathbf{kpq}}B^*_{\mathbf{pqk}}\theta^*_{kpq}(t)C_q(t)R_k(t,t') + \delta(t-t') \tag{2.13}$$

with θ_{kpq} the triad interaction time ie the lifetime of the interaction. Using this modified FDT Bowman et al. derived the realizable Markovian closure (RMC).

The EDQNM may also be regarded as a simplification of the more general test-field model (TFM) of Kraichnan [82, 83, 84, 85]. Kraichnan's TFM arose from an investigation of stochastic model representations that paralleled his pursuit of a Lagrangian-history DIA [40]. The TFM derives from an observation that for Navier-Stokes flows, the strength of the interaction of an eddy with the advecting field can be viewed in terms of the rate at which the solenoidal and compressive components of a "test" velocity field are coupled to advection (in the absence of pressure). More simply put, the triad interaction time Θ_{kpq} is evaluated by studying the triple correlation of an auxiliary velocity field transported by the turbulence itself. As incompressibility is lost the test field has to be decomposed into solenoidal and compressible components to be tractable. Kraichnan then removed the nonlinear cross terms coupling the solenoidal and compressive parts of the test field, applied the FDT and Markovianized the statistical equations for the solenoidal and compressive components. The resulting nonlinear eddy-turnover rate modifies the triad interaction time, restoring Galilean invariance, but requiring coupled equations for the evolution of Θ_{kpq}. Herring et al [86] found that this modified triad interaction time reduces to the EDQNM characteristic time, Eq. 2.10, in the inertial range. More recently Bowman and Krommes [87] applied their modified FDT ansatz to develop the realizable test-field model (RTFM) applying it to anisotropic drift-wave dynamics.

2.6 Regularized DIA

Kraichnan [38] noted that the failure of the DIA to be consistent with the Kolmogorov hypothesis arose due to spurious convection effects of small eddies by large eddies. He suggested that these effects could be removed by zeroing the interaction coefficient (vertex function) in the two-time cumulant and response function equations if the triad of inter-

acting wave vectors satisfy the regularizing [7] approximation $p < \frac{k}{\alpha}$ or $q < \frac{k}{\alpha}$, where α is a specified cut-off ratio. Thus, in the regularized DIA, the vertex function is given by

$$\Theta(p - \frac{k}{\alpha})\Theta(q - \frac{k}{\alpha})B_{\mathbf{kpq}} \tag{2.14}$$

where Θ is the Heavyside step function which vanishes for negative argument and is otherwise unity. Only the two-time cumulants and response function are modified as a result of applying Eq. 2.14 while the single-time cumulants are unmodified from the DIA. This approach was called regularization by Frederiksen and Davies [28] as it removes the infrared or low wavenumber divergence of the DIA response function for continuous closures [43, 20]. This approach corresponds to a rather simple heuristic vertex renormalization depending on the parameter α, and is a one parameter theory like the TFM. Frederiksen and Davies [28] compared the RDIA with ensemble-averaged direct numerical simulations (DNS) for decaying two-dimensional turbulence at large-scale Reynolds numbers (up to 4000). They considered discrete wavenumber representations relevant to flows on the doubly periodic plane, focusing on the evolved kinetic energy, enstrophy, palinstrophy, and enstrophy flux spectra as well as skewness evolution. All diagnostics were shown to compare well with DNS for $\alpha = 6$ with no apparent under-estimation of the closure kinetic energy in the small-scales. The RDIA discrete closure was also compared to ALHDIA and SBALHDIA continuous closures [46] with the RDIA comparing more closely to DNS.

2.7 Summary

We have now reviewed the literature and underlying mathematics for the statistical theories of isotropic, homogeneous turbulence via Eulerian and Lagrangian formulations as well as Markovian theories and more general functional methods. However, these methods do not take into account topographic effects such as eddy-topography interactions. In the next chapter we turn our attention to two-dimensional turbulent flow over topography. Table 2.1 contains an overview of some of the statistical theories discussed.

[7] This terminology was coined by Frederiksen and Davies [28]

Table 2.1: Statistical closure theories

Closure theory	Comments
DIA	• R.H. Kraichnan 1958 [19, 34]
	• reduces correctly to perturbation theory
	• self-consistent
	• contains no arbitrary parameter
	• produces two-time cumulants
	• exact stochastic model representation and therefore realizable
	• non-Markovian
	• In 3-D predicts $k^{-3/2}$ energy inertial range
	• In 2-D predicts $k^{-5/2}$ enstrophy inertial range
	• mistreats higher order coherences
TFM	• R.H.Kraichnan 1971 [82, 83]
	• employs characteristic triad interaction time $\theta_{\mathbf{kpq}}$
	• depends on an arbitrary parameter
	• In 3-D predicts $k^{-5/3}$ energy inertial range law
	• computationally significantly faster than the DIA
	• only predicts equal time cumulants
	• does not accurately incorporate time-history effects
	• assumes fluctuation dissipation theorem (FDT)
	• realizable for homogeneous turbulence
	• can predict negative energies if waves are present
	ie not realizable
EDQNM	• S. Orszag 1977 [78, 48]
	• realizable for homogeneous isotropic turbulence
	• may violate realizability in the presence of linear

continued on next page

continued from previous page

Closure theory	Comments
	wave phenomena
	• not readily generalized ie there exists no general multiple field formulation
	• depends on the choice of an eddy-damping parameter $\mu_{\mathbf{k}}$
	• assumes that the rate at which the memory integral decays is much faster than the time-scale on which the covariances evolve ie Markovian
RMC	• J.C. Bowman, J.A. Krommes and M. Ottaviani 1993 [49]
	• based on the EDQNM closure
	• one parameter theory
	• nonstationary FDT ansatz is applied to the DIA
RTFM	• J.C. Bowman and J.A. Krommes 1997 [87]
	• employs a nonstationary form of the FDT ie amplitude decorrelation to approximate the decay of infinitesimal disturbances
	• predicts non-negative energies
	• has an underlying Langevin equation
	• Markovian
	• one parameter theory
	• both the frequency and damping rates are renormalized
RDIA	• Kraichnan 1964 [38] and, Frederiksen and Davies 2002 [28]
	• heuristic vertex renormalization
	• one parameter theory
	• yields correct inertial range energy spectra
	• has all the advantageous properties of the DIA

Chapter 3

Flow over topography

"Nobody who has gone deeply into the matter will deny that in practice
the world of phenomena uniquely determines the theoretical system ..."
"I am convinced that we can discover by means of purely mathematical constructions
the concepts and the laws connecting them with each other,
which furnish the key to the understanding of natural phenomena."

Albert Einstein

The interaction of eddies with topography can have an enormous influence on oceanic or atmospheric circulations. Holloway (1992) [17] proposed that for ocean circulations, the topographic force may be separated into two components, namely the gravity wave drag and a vortex drag. He further argues that gravity wave drag may not be as significant as vortex drag in the abyssal ocean. This is due to the relatively small size of the free-stream velocity (characterizing a mean flow above some boundary layer) resulting in only a narrow band of topographic variance at a relatively high wavenumber contributing to the gravity wave drag. Thus the vortex drag or eddy-topographic force may be one of the stronger driving forces for ocean circulations.

Merryfield and Holloway [16] subsequently examined the physical basis for parameterizing topographic stress due to unresolved eddies in a quasi-geostrophic barotropic model, arguing that the effects of the subgrid-scale eddies are to drag the barotropic component of

the flow toward a local statistical equilibrium state with topographically-correlated mean currents. A second effect examined was the concentration of potential enstrophy dissipation at small scales, relative to dissipation of energy for viscous flows. Although Holloway's [17] subgrid-scale parameterization seemed to ameliorate the problem of the under representation of topographic stress in ocean circulation models [16, 88, 89, 90] arising due to inadequate resolution of the eddies, it nevertheless lacked a rigorous underlying basis. Holloway recognized that the principle problem with his theory was that the quantities describing the local barotropic canonical equilibrium state are free parameters, as is the viscosity, which must be chosen so that the results are reasonable for ocean circulations. Frederiksen [91] noted that, as the flow is simply relaxing to a local equilibrium state that has been "tuned" to the observations, perhaps this is the only reason satisfactory results are obtained.

Frederiksen [91] was subsequently able to put Holloway's heuristic argument on a solid theoretical foundation via his quasi-diagonal DIA (QDIA) which generalizes Kraichnan's [92] diagonalising approximation for Boussinesq turbulence. In this chapter, we will consider a detailed presentation of the QDIA and introduce a method for approximating the time-history integrals which result in what we will call the cumulant update QDIA (CUQDIA). However, we will first briefly review the development of statistical dynamical closure theory and canonical equilibrium theory with regard to flow over topography on an $f-$plane.

3.1 Nonlinear barotropic flow over irregular topography

Prior to the Frederiksen's quasi-diagonal DIA (QDIA), the only tractable closure theories for flow over topography were for the case of ensembles of random topography with zero mean value, with comparable complexity to homogeneous turbulence closures. The first such closure is due to Herring [93] and was motivated by the observations of Holloway and Hendershott [7] and Bretherton and Haidvogel [9] that for two-dimensional rotating turbulence above a random topography (with negligible Rossby number) the vorticity tended rapidly to be strongly anti-correlated to the topography. This occurred in a time signifi-

cantly less than the eddy circulation time. Bretherton and Haidvogel further showed that the system was tending to minimize enstrophy for a fixed total energy. This interpretation has become known as the "minimum enstrophy principle". Carnevale and Frederiksen [13] discuss the nonlinear stability and statistics of minimum enstrophy states, and their correspondence to maximum entropy states, for inviscid barotropic flows. This work built on previous studies [11, 94] of the relationship between canonical equilibrium solutions (with zero transients) and nonlinearly stable steady-state solutions for barotropic flows over topography. In the absence of forcing and viscosity (or where forcing and viscosity are in balance) it is also possible to examine the effects of mean topography on the climate of barotropic flows using semianalytic methods from statistical mechanics thus enabling the derivation of canonical equilibrium solutions for both planar [8] and spherical [95] geometries. Studies of these maximum entropy states have led to greater understanding of the behavior of forced dissipative flows [15, 96, 97, 98, 99, 100].

Herring [93] compared both DIA and TFM methods to the problem of 2-D rotating turbulent flow above a random topography. A Gaussianly and homogeneously distributed topographic height field was considered where the ensemble averaging extended to include the topographic field (whose mean is zero). The TFM was extended so as to avoid the assumption that correlation times are equal to response times in anticipation of the strong locking of large scales to the topography. In removing the Markovian restriction of the TFM, Herring found that the Green's function, resulting from equating the triple moment dephasing rate to the rate of conversion of solenoidal to compressive components of a test field with pressure terms removed, was insensitive to random large-scale convection. The only problem was that the new Green's functions were not Galilean invariant precisely because the basic topographic interaction is not invariant. Herring also noted that the extended TFM exhibited a spurious dependence of the decorrelation time Θ_k on the large-scale topography. The DIA and extended TFM were found to qualitatively agree with some significant quantitative disagreement. Random topographies with topographic amplitudes squared of the form $\frac{H_0}{1+k^4}$ and $\frac{H_0 k}{1+k^3}$ where $H_0 = 2, 4, 8, 16, 64$ were considered. The primary finding was that the topography induces in stationary turbulence a static component in the energy spectrum whose magnitude increases with topography. This was demonstrated

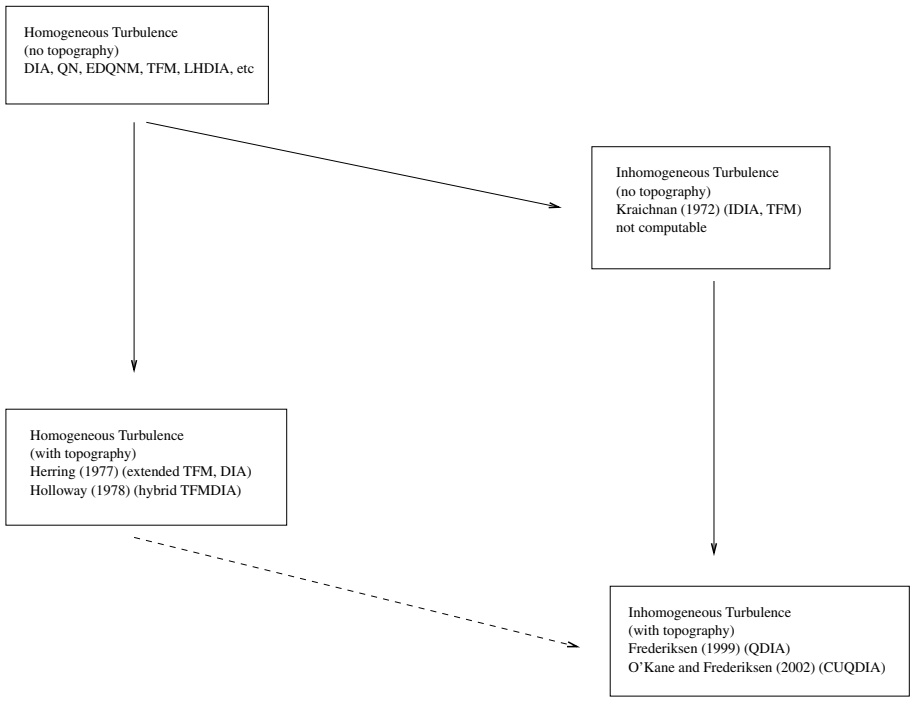

Figure 3.1: An overview of the development of the inhomogeneous closure theory.

for inviscid, thermal equilibrium, by application of the FDT.

Holloway [101] proposed a hybrid theory by taking the turbulence timescale of the TFM and the topographic timescale of the DIA. Holloway's TFM-based theory considers the time evolution of the energy or vorticity variance spectrum and of the vorticity-topography correlation spectrum described by a pair of coupled integral equations in terms of the single-time second moments $\langle \zeta_{\mathbf{k}}(t)\zeta_{-\mathbf{k}}(t)\rangle$ and $\Re(\langle \zeta_{\mathbf{k}} h_{-\mathbf{k}}\rangle)$. This approach can be viewed as an ad hoc abridgement of Herring's extended-TFM theory. Holloway described the resulting integral equations as "corresponding to the statistical evolution of a stochastic variable governed by a modified Langevin equation in which topography provides a steady driving force". It should be noted that the Markov assumption again requires the estimation of a characteristic triad interaction $\theta_{\mathbf{kpq}}$, a scalar of proportionality.

The work described above led to great insight into the effect of random topography in determining spectra of transient vorticity variance, however in order to examine the effect of mean topography on the structures of the mean flows a closure theory based on single realization topography must be implemented. The incorporation of topography

with a nonzero mean would also enable insight into the problem of parameterizing the subgrid-scale effects of the interaction between the turbulent eddies and the mean topography, however, an inhomogeneous closure is required. The most important investigations of inhomogeneous closures, previous to Frederiksen [91], are due to Kraichnan and are contained in two important papers where both diagonal [92] and nondiagonal [85] cases are examined. In Kraichnan's 1972 paper [85] a generalized version of Orszag's EDQNM was compared to the nonstationary inhomogeneous form of the DIA with a mean shearing velocity. In the discussion it was demonstrated that the general non-diagonal form of the inhomogeneous DIA was not computationally tractable and that some form of diagonalization was required. These issues motivated Frederiksen to formulate his QDIA [91]. Importantly in an earlier version of the quasi-diagonal approximation Kraichnan found that the resulting equations were not realizable for the case with thermal convection however, the QDIA of Frederiksen is realizable on the diagonal elements with the question of whether the off-diagonal elements are realizable remaining open. The salient features of the relevant theories discussed above are presented in table 3.1.

Table 3.1: Closure theories for geophysical flow

Closure theory	Comments
extended TFM, DIA	• Herring 1977 [93]
	• Random topography with zero mean
	• homogeneous theory
	• non-Markovian
	• good qualitative agreement with some quantitative differences between TFM and DIA
	• not Galilean invariant
hybrid TFM-DIA	• Holloway 1978 [101]
	• Random topography with zero mean
	• homogeneous theory

continued on next page

continued from previous page	
Closure theory	Comments
	• Markovian
	• much simpler theory than Herring's extended TFM
	• close agreement with the extended TFM
	• employs a characteristic triad interaction time $\theta_{\mathbf{kpq}}$
QDIA, CUQDIA	• J.S. Frederiksen 1999 (QDIA) [91],
	T.J. O'Kane and J.S. Frederiksen 2002 (CUQDIA) [102]
	• incorporates topography with non-zero mean
	• quasi-diagonal approximation
	• generalization of Kraichnan's approach to Boussinesq turbulence [92]
	• very complex set of integro-differential equations
	with large numbers of interaction coefficients
	• requires formal restart procedure to render
	computationally tractable
IDIA	• R.H. Kraichnan 1972 [85]
	• inhomogeneous theory
	• no assumptions of quasi-diagonality
	• computationally intractable

3.2 2-D flow on an f-plane

The evolution equation for two dimensional flow over a fixed topography on a periodic f-plane $(0 \leq x \leq 2\pi)$, $(0 \leq y \leq 2\pi)$ is simply the nondimensional barotropic vorticity equation which takes the form

$$\frac{\partial \zeta}{\partial t} = -J(\psi, \zeta + h) + \nu_0 \nabla^2 \zeta + f^0 \tag{3.1}$$

where f^0 is the bare forcing and ν_0 the bare viscosity. The Jacobian is defined as

$$J(\psi, \zeta) = \frac{\partial \psi}{\partial x}\frac{\partial \zeta}{\partial y} - \frac{\partial \psi}{\partial y}\frac{\partial \zeta}{\partial x}. \tag{3.2}$$

The vorticity is the Laplacian of the streamfunction

$$\zeta = \bigtriangledown^2 \psi. \tag{3.3}$$

We make the assumption that the variation in the topography, $\triangle H$, is small, and define h to be the spatial variation of the height of the topography relative to the total depth, D, in units of the Coriolis parameter f.

We may write Eq. 3.1 in spectral form via

$$\zeta(\mathbf{x}, t) = \sum_{\mathbf{k}} \zeta_{\mathbf{k}}(t) \exp i\mathbf{k} \cdot \mathbf{x} \tag{3.4}$$

where

$$\zeta_{\mathbf{k}}(t) = \frac{1}{(2\pi)^2} \int_0^{2\pi} d^2\mathbf{x} \;\; \zeta(\mathbf{x}, t) \exp -i\mathbf{k} \cdot \mathbf{x} \tag{3.5}$$

and $\mathbf{x} = (x, y), \mathbf{k} = (k_x, k_y)$. The spectral vorticity equation with a more general dissipation where $\nu_0 \rightarrow \nu_0(k)$ is

$$\begin{aligned} (\frac{\partial}{\partial t} + \nu_0(k)k^2)\zeta_{\mathbf{k}}(t) = \sum_{\mathbf{p}} \sum_{\mathbf{q}} \delta(\mathbf{k} + \mathbf{p} + \mathbf{q}) \\ \times [K(\mathbf{k}, \mathbf{p}, \mathbf{q})\zeta_{-\mathbf{p}}\zeta_{-\mathbf{q}} + A(\mathbf{k}, \mathbf{p}, \mathbf{q})\zeta_{-\mathbf{p}}h_{-\mathbf{q}}] + f^0_{\mathbf{k}} \end{aligned} \tag{3.6}$$

where $k = (k_x^2 + k_y^2)^{1/2}$ and $\zeta_{-\mathbf{k}}$ is conjugate to $\zeta_{\mathbf{k}}$.

The interaction coefficients, derived in Appendix II, are governed by the following relationships

$$A(\mathbf{k}, \mathbf{p}, \mathbf{q}) = -(p_x q_y - p_y q_x)/p^2, \tag{3.7}$$

$$\begin{aligned} K(\mathbf{k}, \mathbf{p}, \mathbf{q}) &= \frac{1}{2}\left[A(\mathbf{k}, \mathbf{p}, \mathbf{q}) + A(\mathbf{k}, \mathbf{q}, \mathbf{p})\right] \\ &= \frac{1}{2}(p_x q_y - p_y q_x)(p^2 - q^2)/p^2 q^2 \end{aligned} \tag{3.8}$$

where

$$\delta(\mathbf{k} + \mathbf{p} + \mathbf{q}) = \begin{cases} 1 & \text{if } \mathbf{k}{+}\mathbf{p}{+}\mathbf{q}{=}0, \\ 0 & \text{otherwise} \end{cases} \tag{3.9}$$

and

$$K(\mathbf{k}, \mathbf{p}, \mathbf{q}) + K(\mathbf{p}, \mathbf{q}, \mathbf{k}) + K(\mathbf{q}, \mathbf{k}, \mathbf{p}) = 0. \tag{3.10}$$

For an ensemble of flows satisfying Eq. 3.6, we may express the vorticity $\zeta_{\mathbf{k}}$ in terms of the ensemble mean $\langle\zeta_{\mathbf{k}}\rangle$ and the deviation from the ensemble mean $\hat{\zeta}_{\mathbf{k}}$

$$\zeta_{\mathbf{k}} = \langle\zeta_{\mathbf{k}}\rangle + \hat{\zeta}_{\mathbf{k}}. \tag{3.11}$$

Hence we may write equations for the ensemble mean

$$\begin{aligned}(\frac{\partial}{\partial t} + \nu_0(k)k^2)\langle\zeta_{\mathbf{k}}\rangle = \\ \sum_{\mathbf{p}}\sum_{\mathbf{q}} \delta(\mathbf{k}+\mathbf{p}+\mathbf{q})K(\mathbf{k},\mathbf{p},\mathbf{q})\left[\langle\zeta_{-\mathbf{p}}\rangle\langle\zeta_{-\mathbf{q}}\rangle + C_{-\mathbf{p}-\mathbf{q}}(t,t)\right] \\ + \sum_{\mathbf{p}}\sum_{\mathbf{q}} \delta(\mathbf{k}+\mathbf{p}+\mathbf{q})A(\mathbf{k},\mathbf{p},\mathbf{q})\langle\zeta_{-\mathbf{p}}\rangle h_{-\mathbf{q}} + \langle f^0_{\mathbf{k}}\rangle\end{aligned} \tag{3.12}$$

and the deviation

$$\begin{aligned}(\frac{\partial}{\partial t} + \nu_0(k)k^2)\hat{\zeta_{\mathbf{k}}} = \\ \sum_{\mathbf{p}}\sum_{\mathbf{q}} \delta(\mathbf{k}+\mathbf{p}+\mathbf{q})K(\mathbf{k},\mathbf{p},\mathbf{q})\left[\langle\zeta_{-\mathbf{p}}\rangle\hat{\zeta}_{-\mathbf{q}} + \hat{\zeta}_{-\mathbf{p}}\langle\zeta_{-\mathbf{q}}\rangle + \hat{\zeta}_{-\mathbf{p}}\hat{\zeta}_{-\mathbf{q}} - C_{-\mathbf{p}-\mathbf{q}}(t,t)\right] \\ + \sum_{\mathbf{p}}\sum_{\mathbf{q}} \delta(\mathbf{k}+\mathbf{p}+\mathbf{q})A(\mathbf{k},\mathbf{p},\mathbf{q})\hat{\zeta}_{-\mathbf{p}}h_{-\mathbf{q}} + \hat{f}^0_{\mathbf{k}}\end{aligned} \tag{3.13}$$

with $f^0_{\mathbf{k}} = \langle f^0_{\mathbf{k}}\rangle + \hat{f}^0_{\mathbf{k}}$ and the two-point cumulant in Eqs. 3.12 and 3.13 determined by

$$C_{-\mathbf{p}-\mathbf{q}}(t,s) = \langle\hat{\zeta}_{-\mathbf{p}}(t)\hat{\zeta}_{-\mathbf{q}}(s)\rangle \tag{3.14}$$

3.3 Quasi-diagonal DIA closure equations

The derivation of the closure equations (without restart terms) can be found in Frederiksen [91] and we only present an outline here. In order to obtain the closure equations, the vorticity is expanded in a perturbation series to find the zeroth order and first order terms. We write the solution to the first order equation for $\hat{\zeta}^{(1)}_{\mathbf{k}}$ in terms of the response or Green's function $R^{(0)}_{\mathbf{k}}(t,s)$, and express the two-time cumulant to first order.

The initial $\hat{\zeta}_{\mathbf{k}}(t_0)$ are assumed to have a multivariate Gaussian distribution[1], implying

$$\langle\hat{\zeta}_{\mathbf{k}}(t_0)\hat{\zeta}_{-\mathbf{l}}(t_0)\rangle = \delta_{\mathbf{kl}}\langle\hat{\zeta}_{\mathbf{k}}(t_0)\hat{\zeta}_{-\mathbf{k}}(t_0)\rangle. \tag{3.15}$$

[1]The important point is that the QDIA is diagonal to first order in contrast to the nondiagonal IDIA [85].

We now apply a quasi-diagonal approximation such that

$$\langle\hat{\zeta}^0_{\mathbf{k}}(t)\hat{\zeta}^0_{-\mathbf{l}}(\acute{t})\rangle = \delta_{\mathbf{kl}}\langle\hat{\zeta}^0_{\mathbf{k}}(t)\hat{\zeta}^0_{-\mathbf{k}}(\acute{t})\rangle. \tag{3.16}$$

Thus, to zeroth order, $C_{\mathbf{k-l}}(t,\acute{t})$ is diagonal with the nondiagonal contribution contained in the first-order terms. We may now determine $C^1_{\mathbf{k-l}}(t,\acute{t})$ after which we renormalize by setting the expansion parameter $\lambda \to 1$, and setting $R^0_{\mathbf{kk}} \to R_{\mathbf{kk}}$, $C^0_{\mathbf{k-k}} \to C_{\mathbf{k-k}}$, and $C^1_{\mathbf{k-l}} \to C_{\mathbf{k-l}}$.

After renormalization [91] we find that we may write the off-diagonal two-point cumulant in terms of diagonal cumulant and response functions

$$\begin{aligned} C_{\mathbf{k-l}}(t,\acute{t}) = \int_{t_0}^{t} ds\ \ R_{\mathbf{kk}}(t,s)C_{\mathbf{l-l}}(s,\acute{t}) \\ \times[A(\mathbf{k},-\mathbf{l},\mathbf{l}-\mathbf{k})h_{(\mathbf{k-l})} + 2K(\mathbf{k},-\mathbf{l},\mathbf{l}-\mathbf{k})\langle\zeta_{(\mathbf{k-l})}(s)\rangle] \\ + \int_{t_0}^{\acute{t}} ds\ \ R_{\mathbf{-l-l}}(\acute{t},s)C_{\mathbf{k-k}}(t,s) \\ \times[A(-\mathbf{l},\mathbf{k},\mathbf{l}-\mathbf{k})h_{(\mathbf{k-l})} + 2K(-\mathbf{l},\mathbf{k},\mathbf{l}-\mathbf{k})\langle\zeta_{(\mathbf{k-l})}(s)\rangle]. \end{aligned} \tag{3.17}$$

In a similar way, the off-diagonal response function

$$R_{\mathbf{kl}}(t,\acute{t}) = \langle\frac{\partial\hat{\zeta}_{\mathbf{k}}(t)}{\partial\hat{f}_{\mathbf{l}}(\acute{t})}\rangle \tag{3.18}$$

can also be represented in the form

$$\begin{aligned} R_{\mathbf{kl}}(t,\acute{t}) = \int_{\acute{t}}^{t} ds\ \ R_{\mathbf{kk}}(t,s)R_{\mathbf{ll}}(s,\acute{t}) \\ \times[A(\mathbf{k},-\mathbf{l},\mathbf{l}-\mathbf{k})h_{(\mathbf{k-l})} + 2K(\mathbf{k},-\mathbf{l},\mathbf{l}-\mathbf{k})\langle\zeta_{(\mathbf{k-l})}(s)\rangle]. \end{aligned} \tag{3.19}$$

The end result of this procedure is the determination of the two-point cumulant and the diagonal two-time and single-time cumulants. Hence we may write

$$\begin{aligned} (\frac{\partial}{\partial t} + \nu_0(k)k^2)\langle\zeta_{\mathbf{k}}\rangle = \\ \sum_{\mathbf{p}}\sum_{\mathbf{q}}\delta(\mathbf{k}+\mathbf{p}+\mathbf{q})K(\mathbf{k},\mathbf{p},\mathbf{q})\langle\zeta_{-\mathbf{p}}(t)\rangle\langle\zeta_{-\mathbf{q}}(t)\rangle + \\ \sum_{\mathbf{p}}\sum_{\mathbf{q}}\delta(\mathbf{k}+\mathbf{p}+\mathbf{q})A(\mathbf{k},\mathbf{p},\mathbf{q})\langle\zeta_{-\mathbf{p}}(t)\rangle h_{-\mathbf{q}} \\ -\int_{t_0}^{t} ds\ \ \eta_{\mathbf{k}}(t,s)\langle\zeta_{\mathbf{k}}(s)\rangle + h_{\mathbf{k}}\int_{t_0}^{t} ds\ \ \chi_{\mathbf{k}}(t,s) + \langle f^0_{\mathbf{k}}(t)\rangle \end{aligned} \tag{3.20}$$

where

$$\eta_{\mathbf{k}}(t,s) = -4\sum_{\mathbf{p}}\sum_{\mathbf{q}}\delta(\mathbf{k}+\mathbf{p}+\mathbf{q})K(\mathbf{k},\mathbf{p},\mathbf{q}) \times K(-\mathbf{p},-\mathbf{q},-\mathbf{k})R_{-\mathbf{p}}(t,s)C_{-\mathbf{q}}(t,s) \tag{3.21}$$

and

$$\chi_{\mathbf{k}}(t,s) = 2\sum_{\mathbf{p}}\sum_{\mathbf{q}}\delta(\mathbf{k}+\mathbf{p}+\mathbf{q})K(\mathbf{k},\mathbf{p},\mathbf{q}) \times A(-\mathbf{p},-\mathbf{q},-\mathbf{k})R_{-\mathbf{p}}(t,s)C_{-\mathbf{q}}(t,s). \tag{3.22}$$

Here we have employed the abbreviation

$$R_{\mathbf{k}}(t,t') \equiv R_{\mathbf{kk}}(t,t') \tag{3.23}$$

$$C_{\mathbf{k}}(t,t') \equiv C_{\mathbf{k}-\mathbf{k}}(t,t'). \tag{3.24}$$

The two-point cumulant takes the form

$$\sum_{\mathbf{p}}\sum_{\mathbf{q}}\delta(\mathbf{k}+\mathbf{p}+\mathbf{q})K(\mathbf{k},\mathbf{p},\mathbf{q})C_{-\mathbf{p}-\mathbf{q}}(t,t) = -\int_{t_0}^{t} ds\ \ \eta_{\mathbf{k}}(t,s)\langle\zeta_{\mathbf{k}}(s)\rangle + h_{\mathbf{k}}\int_{t_0}^{t} ds\ \ \chi_{\mathbf{k}}(t,s) \tag{3.25}$$

with the two-time cumulant given as

$$\begin{aligned}(\frac{\partial}{\partial t}+\nu_0(k)k^2)C_{\mathbf{k}}(t,\acute{t}) &= \sum_{\mathbf{p}}\sum_{\mathbf{q}}\delta(\mathbf{k}+\mathbf{p}+\mathbf{q})A(\mathbf{k},\mathbf{p},\mathbf{q})C_{-\mathbf{p}-\mathbf{k}}(t,\acute{t})h_{-\mathbf{q}} \\ &+\sum_{\mathbf{p}}\sum_{\mathbf{q}}\delta(\mathbf{k}+\mathbf{p}+\mathbf{q})K(\mathbf{k},\mathbf{p},\mathbf{q})\left[2\langle\zeta_{-\mathbf{q}}(t)\rangle C_{-\mathbf{p}-\mathbf{k}}(t,\acute{t})\right. \\ &\left.+\langle\hat{\zeta}_{-\mathbf{q}}(t)\hat{\zeta}_{-\mathbf{p}}(t)\hat{\zeta}_{-\mathbf{k}}(\acute{t})\rangle\right]+\int_{t_0}^{\acute{t}} ds\ \ F^0_{\mathbf{k}}(t,s)R_{-\mathbf{k}}(\acute{t},s).\end{aligned} \tag{3.26}$$

The non-diagonal elements of the two-time cumulant expressed in terms of the diagonal elements in the quasi-diagonal approximation gives

$$\begin{aligned}(\frac{\partial}{\partial t}+\nu_0(k)k^2)C_{\mathbf{k}}(t,\acute{t}) &= \int_{t_0}^{\acute{t}} ds\ \ \left[S_{\mathbf{k}}(t,s)+P_{\mathbf{k}}(t,s)+F^0_{\mathbf{k}}(t,s)\right]R_{-\mathbf{k}}(\acute{t},s) \\ &-\int_{t_0}^{t} ds\ \ \left[\eta_{\mathbf{k}}(t,s)+\pi_{\mathbf{k}}(t,s)\right]C_{-\mathbf{k}}(\acute{t},s)\end{aligned} \tag{3.27}$$

where

$$F^0_{\mathbf{k}}(t,s) = \langle \hat{f}^0_{\mathbf{k}}(t)\hat{f}^{0*}_{\mathbf{k}}(s)\rangle, \tag{3.28}$$

$$\begin{aligned} S_{\mathbf{k}}(t,s) = 2\sum_{\mathbf{p}}\sum_{\mathbf{q}} &\delta(\mathbf{k}+\mathbf{p}+\mathbf{q})K(\mathbf{k},\mathbf{p},\mathbf{q}) \\ &\times K(-\mathbf{k},-\mathbf{p},-\mathbf{q})C_{-\mathbf{p}}(t,s)C_{-\mathbf{q}}(t,s), \end{aligned} \tag{3.29}$$

$$\begin{aligned} P_{\mathbf{k}}(t,s) = \sum_{\mathbf{p}}\sum_{\mathbf{q}} &\delta(\mathbf{k}+\mathbf{p}+\mathbf{q})C_{-\mathbf{p}}(t,s) \\ &\times \left[2K(\mathbf{k},\mathbf{p},\mathbf{q})\langle\zeta_{-\mathbf{q}}(t)\rangle + A(\mathbf{k},\mathbf{p},\mathbf{q})h_{-\mathbf{q}}\right] \\ \times \left[2K(-\mathbf{k},-\mathbf{p},-\mathbf{q})\langle\zeta_{\mathbf{q}}(s)\rangle\right. &+ \left. A(-\mathbf{k},-\mathbf{p},-\mathbf{q})h_{\mathbf{q}}\right], \end{aligned} \tag{3.30}$$

and

$$\begin{aligned} \pi_{\mathbf{k}}(t,s) = -\sum_{\mathbf{p}}\sum_{\mathbf{q}} &\delta(\mathbf{k}+\mathbf{p}+\mathbf{q})R_{-\mathbf{p}}(t,s) \\ &\times \left[2K(\mathbf{k},\mathbf{p},\mathbf{q})\langle\zeta_{-\mathbf{q}}(t)\rangle + A(\mathbf{k},\mathbf{p},\mathbf{q})h_{-\mathbf{q}}\right] \\ \times \left[2K(-\mathbf{p},-\mathbf{k},-\mathbf{q})\langle\zeta_{\mathbf{q}}(s)\rangle\right. &+ \left. A(-\mathbf{p},-\mathbf{k},-\mathbf{q})h_{\mathbf{q}}\right]. \end{aligned} \tag{3.31}$$

The equation for the response function takes a similar form.

$$\begin{aligned} &(\frac{\partial}{\partial t} + \nu_0(k)k^2)R_{\mathbf{k}}(t,\acute{t}) \\ &= -\int_{\acute{t}}^{t} ds \;\; \left[\eta_{\mathbf{k}}(t,s) + \pi_{\mathbf{k}}(t,s)\right] R_{\mathbf{k}}(s,\acute{t}) \end{aligned} \tag{3.32}$$

with $R_{\mathbf{k}}(t,t) = 1$.

Finally the single-time cumulant takes the form:

$$\begin{aligned} &(\frac{\partial}{\partial t} + 2\nu_0(k)k^2)C_{\mathbf{k}}(t,t) \\ &= 2Re\int_{t_0}^{t} ds \left[S_{\mathbf{k}}(t,s) + P_{\mathbf{k}}(t,s) + F^0_{\mathbf{k}}(t,s)\right] R_{-\mathbf{k}}(t,s) \\ &\quad -2Re\int_{t_0}^{t} ds \left[\eta_{\mathbf{k}}(t,s) + \pi_{\mathbf{k}}(t,s)\right] C_{-\mathbf{k}}(t,s) \end{aligned} \tag{3.33}$$

3.4 Non-Gaussian cumulants and cumulant updates

The QDIA, like other non-Markovian closure theories, may be computationally expensive for long time integrations because of the time-history integrals which need to be evaluated between the initial and final times. The cumulant update restart procedure consists of integrating the QDIA forward for a time, calculating the two- and three-point terms at this time and then using these in the new initial conditions for further integration. In principle, knowledge of all higher order cumulants should be available, but to be consistent with the approximations of the QDIA, only the two- and three-point cumulants are needed. The crucial information contained in the three-point term is that of the non-Gaussian covariances accumulated in the time-history integrals.

The three-point cumulant is effectively the homogeneous component of the closure equations while the two-point terms arise due to the inhomogeneity produced by the presence of topography and mean field. If we follow the argument of Rose [103] and suppose that the initial two- and three-point cumulants are non-zero then we are confronted with the in principle non-vanishing of other higher order cumulants (≥ 3). These higher order cumulants arise due to the nonlinearity in the expansion parameter λ. To see this, let us consider the inhomogeneous QDIA two-time cumulant equation

$$\begin{aligned}(\frac{\partial}{\partial t} + \nu_0(k)k^2)C_{\mathbf{k}}(t,\acute{t}) = \\ \int_{t_0}^{\acute{t}} ds \;\; \left[S_{\mathbf{k}}(t,s) + P_{\mathbf{k}}(t,s) + F^0_{\mathbf{k}}(t,s)\right] R_{-\mathbf{k}}(\acute{t},s) \\ - \int_{t_0}^{t} ds \;\; \left[\eta_{\mathbf{k}}(t,s) + \pi_{\mathbf{k}}(t,s)\right] C_{-\mathbf{k}}(\acute{t},s).\end{aligned} \tag{3.34}$$

When $\zeta_{\mathbf{k}}(0)$ is Gaussian, we may write the nonlinear noise $S_{\mathbf{k}}$, nonlinear damping $\eta_{\mathbf{k}}$ and inhomogeneous contributions, $P_{\mathbf{k}}$ and $\pi_{\mathbf{k}}$ as a power series[2] in λ ie

$$S = \alpha_n\lambda^n, \quad \eta = \beta_n\lambda^n \quad P = \gamma_n\lambda^n \quad \pi = \sigma_n\lambda^n \qquad n = 2,3,\ldots, \tag{3.35}$$

where $\alpha_n, \beta_n, \gamma_n$ and σ_n consist of finite products of R and C. It is the dependence of these terms on the exact R and C that constitutes a propagator renormalized expansion[3].

[2] As the P and π terms are composed of $\eta_{\mathbf{p}}$, $\eta_{\mathbf{q}}$, $\chi_{\mathbf{p}}$ and $\chi_{\mathbf{q}}$ terms, and the evolution equation for $\langle\zeta_{\mathbf{k}}\rangle$ consists of $\eta_{\mathbf{k}}$, $\chi_{\mathbf{k}}$ components then in essence only the S, η and χ terms involve the power series.

[3] The DIA is truncated at $O(\lambda^2)$.

We can now clearly see that for non-vanishing two- and three-point cumulants Eqs. 3.35 convert to multiple power series in λ and all non-vanishing initial cumulants. Hence in order to be consistent with the approximations of the DIA we need only consider the two- and three-point cumulants. In the following two sections we will explicitly derive the restart terms.

3.4.1 Derivation of the three-point restart terms

The three-point restart terms are of the same form as found in Rose [103] and discussed in detail by Frederiksen, Davies and Bell [104]. A short derivation of these terms has been included here for completeness. Consider the barotropic vorticity equation in the following form

$$\frac{\partial \zeta_i}{\partial t} = D_{ij}\zeta_j + \frac{1}{2}\lambda_{ijk}\zeta_j\zeta_k + f_i^0 \tag{3.36}$$

where D_{ij} is a dissipation operator, f_i^0 the bare forcing and where the coefficient λ determines the nonlinear interactions. For f_i^0 and $\zeta(t_0)$ Gaussian we may now write the statistics of Eq. 3.36 as

$$(\delta_{ij}\frac{\partial}{\partial t} - D_{ij})R_{jk}(t,\acute{t}) = -\int_{\acute{t}}^{t} ds\ \ \tilde{\eta}_{ij}(t,s)R_{jk}(s,\acute{t}) \tag{3.37}$$

where $R_{jk}(t,t) = \delta_{jk}$ with δ_{jk} the Kronecker delta function, and

$$\begin{aligned}(\delta_{ij}\frac{\partial}{\partial t} - D_{ij})C_{jk}(t,\acute{t}) = &-\int_{t_0}^{t} ds\ \ \tilde{\eta}_{ij}(t,s)C_{jk}(\acute{t},s) \\ &+\int_{t_0}^{\acute{t}} ds\ \ [F_{ij}^0(t,s) + \tilde{S}_{ij}(t,s)]R_{kj}(\acute{t},s)\end{aligned} \tag{3.38}$$

with $C_{jk}(t_0,t_0)$ specified. The cumulant and response functions are defined as $C_{ij}(t,\acute{t}) = \langle\hat{\zeta}_i(t)\hat{\zeta}_j(\acute{t}\rangle$ and $R_{ij} = \langle\frac{\partial\hat{\zeta}_i(t)}{\partial\hat{f}_j(\acute{t})}\rangle$. The tilde over the η and S terms denotes these as exact quantities. The DIA truncates the expansion in $\tilde{\eta}$ and $\tilde{S}$ at $O(\lambda^2)$ such that from Eq. 3.37 we have

$$(\delta_{ij}\frac{\partial}{\partial t} - D_{ij})R_{jk}(t,\acute{t}) = \int_{\acute{t}}^{t} ds\ \ [\lambda_{ikl}R_{km}(t,s)C_{ln}(t,s)\lambda_{mnj}]R_{jk}(s,\acute{t}) \tag{3.39}$$

and from Eq. 3.38

$$(\delta_{ij}\frac{\partial}{\partial t} - D_{ij})C_{jk}(t,\acute{t}) = \int_{t_0}^{t} ds\ \ [\lambda_{ikl}R_{km}(t,s)C_{ln}(t,s)\lambda_{mnj}]C_{jk}(\acute{t},s)$$

$$+\int_{t_0}^{\acute{t}} ds\ \ [\frac{1}{2}\lambda_{ikl}C_{km}(t_0,t_0)C_{ln}(t_0,t_0)\lambda_{jmn} + \frac{1}{2}\lambda_{ikl}C_{km}(t,s)C_{ln}(t,s)\lambda_{jmn}]R_{kj}(\acute{t},s). \quad (3.40)$$

For clarity we use the following notation

$$-\eta_{jk}^{DIA}(t,\acute{t}) = \lambda_{jlm}R_{ln}(t,\acute{t})C_{mo}(t,\acute{t}))\lambda_{nok} \quad (3.41)$$

$$S_{jk}^{DIA}(t,\acute{t}) = \frac{1}{2}\lambda_{jlm}C_{ln}(t,\acute{t})C_{mo}(t,\acute{t})\lambda_{kno}. \quad (3.42)$$

The three-point and higher cumulants arise due to the nonlinearity λ; thus, in order to be consistent with the DIA approximation we need only the three-point term as it has order $O(\lambda)$. Thus to $O(\lambda^2)$

$$\eta_{jk} = \eta_{jk}^{DIA} \quad (3.43)$$

$$S_{jk}(t,\acute{t}) = S_{jk}^{DIA}(t,\acute{t}) + \frac{1}{2}\lambda_{jlm}R_{ln}(t,t_0)R_{mo}(t,t_0)C_{nok}^3(t_0,t_0,t_0)\delta(\acute{t})$$
$$+\frac{1}{2}\delta(t)C_{jlm}^3(t_0,t_0,t_0)R_{ln}(\acute{t},t_0)R_{mo}(\acute{t},t_0)\lambda_{kno} \quad (3.44)$$

with the last term in Eq. 3.44 making no contribution by causality and where

$$C_{ijk}^3(t_0,t_0,t_0) = \langle\hat{\zeta}_i(t_0)\hat{\zeta}_j(t_0)\hat{\zeta}_k(t_0)\rangle. \quad (3.45)$$

The final result is that

$$(\delta_{ij}\frac{\partial}{\partial t} - D_{ij})C_{jk}(t,\acute{t}) = -\int_{t_0}^{t} ds\ \ \eta_{ij}^{DIA}(t,s)C_{jk}(s,\acute{t})$$
$$+\int_{t_0}^{\acute{t}} ds\ \ [F_{ij}^0(t,s) + S_{ij}^{DIA}(t,s)]R_{kj}(\acute{t},s)$$
$$+\frac{1}{2}\lambda_{ilm}R_{ln}(t,t_0)R_{mo}(t,t_0)R_{jk}(\acute{t},t_0)C_{noj}^3(t_0,t_0,t_0) \quad (3.46)$$

where for $t = \acute{t} = T$

$$C_{klm}^3(T,T,T) = R_{kn}(T,t_0)R_{lo}(T,t_0)R_{mp}(T,t_0)C_{nop}^3(t_0,t_0,t_0)$$
$$+\int_{t_0}^{T} ds\ \ R_{kn}(T,s)C_{lo}(T,s)C_{mp}(T,s)\lambda_{nop}$$
$$+\int_{t_0}^{T} ds\ \ C_{kn}(T,s)R_{lo}(T,s)C_{mp}(T,s)\lambda_{opn}$$
$$+\int_{t_0}^{T} ds\ \ C_{kn}(T,s)C_{lo}(T,s)R_{mp}(T,s)\lambda_{pno}. \quad (3.47)$$

In the notation of the preceding section Eqs. 3.46 and 3.47 become

$$(\frac{\partial}{\partial t}+\nu_0(k)k^2)C_k(t,\acute{t}) = \int_{t_0}^{\acute{t}} ds\ \ [F_k^0(t,s)+S_k(t,s)]R_k(\acute{t},s) - \int_{t_0}^{t} ds\ \ \eta_k(t,s)C_k(\acute{t},s)$$
$$+\sum_{\mathbf{p}}\sum_{\mathbf{q}}\delta(\mathbf{k}+\mathbf{p}+\mathbf{q})K(\mathbf{k},\mathbf{p},\mathbf{q})\tilde{K}^3_{-\mathbf{q},-\mathbf{p},-\mathbf{k}}(t_0,t_0,t_0)R_p(t,t_0)R_q(t,t_0)R_k(\acute{t},t_0) \quad (3.48)$$

and

$$\tilde{K}^3_{-\mathbf{q},-\mathbf{p},-\mathbf{k}}(T,T,T) = K^{3Dyn}_{-\mathbf{q},-\mathbf{p},-\mathbf{k}}(T,T,T)$$
$$+\tilde{K}^3_{-\mathbf{q},-\mathbf{p},-\mathbf{k}}(t_0,t_0,t_0)R_p(T,t_0)R_q(T,t_0)R_k(T,t_0) \quad (3.49)$$

with

$$\sum_{\mathbf{p}}\sum_{\mathbf{q}}\delta(\mathbf{k}+\mathbf{p}+\mathbf{q})K(\mathbf{k},\mathbf{p},\mathbf{q})K^{3Dyn}_{-\mathbf{q},-\mathbf{p},-\mathbf{k}}(t,t,\acute{t})$$
$$= -\int_{t_0}^{t} ds\ \ \eta_k^{DIA}(t,s)C_k(\acute{t},s) + \int_{t_0}^{\acute{t}} ds\ \ S_k^{DIA}(t,s)R_k(\acute{t},s) \quad (3.50)$$

3.4.2 Perturbative derivation of two-point restart terms

Let us now derive in detail the two-point restart terms using a perturbative approach. Suppose we expand $\hat{\zeta}_{\mathbf{k}}$ in a perturbation series

$$\hat{\zeta}_{\mathbf{k}}(t) = \hat{\zeta}^0_{\mathbf{k}}(t) + \lambda\hat{\zeta}^1_{\mathbf{k}}(t) + \ldots \quad (3.51)$$

To zero order we have from Eq. 3.6

$$(\frac{\partial}{\partial t}+\nu_0(k)k^2)\hat{\zeta}^0_{\mathbf{k}}(t) = \hat{f}^0_{\mathbf{k}}(t) + \delta(t-t_0)\hat{\zeta}^0_{\mathbf{k}}(t_0) \quad (3.52)$$

with solution

$$\hat{\zeta}^0_{\mathbf{k}}(t) = R_{\mathbf{k}}(t,t_0)\hat{\zeta}^0_{\mathbf{k}}(t_0) + \int_{t_0}^{t} dsR^0_{\mathbf{k}}(t,s)\hat{f}^0_{\mathbf{k}}(s). \quad (3.53)$$

To order λ we have

$$(\frac{\partial}{\partial t}+\nu_0(k)k^2)\hat{\zeta}^1_{\mathbf{k}}(t) = \sum_{\mathbf{p}}\sum_{\mathbf{q}}\delta(\mathbf{k}+\mathbf{p}+\mathbf{q})A(\mathbf{k},\mathbf{p},\mathbf{q})\hat{\zeta}^0_{-\mathbf{p}}h_{-\mathbf{q}}$$
$$+\sum_{\mathbf{p}}\sum_{\mathbf{q}}\delta(\mathbf{k}+\mathbf{p}+\mathbf{q})K(\mathbf{k},\mathbf{p},\mathbf{q})$$
$$\times[\langle\zeta_{-\mathbf{p}}\rangle\hat{\zeta}^0_{-\mathbf{q}} + \langle\zeta_{-\mathbf{q}}\rangle\hat{\zeta}^0_{-\mathbf{p}} + \hat{\zeta}^0_{-\mathbf{p}}\hat{\zeta}^0_{-\mathbf{q}} - \langle\hat{\zeta}^0_{-\mathbf{p}}\hat{\zeta}^0_{-\mathbf{q}}\rangle] + \delta(t-t_0)\hat{\zeta}^1_{\mathbf{k}}(t_0) \quad (3.54)$$

Thus

$$\hat{\zeta}^1_{\mathbf{k}}(t) = \hat{\zeta}^{1(Dyn)}_{\mathbf{k}}(t) + R^0_{\mathbf{k}}(t,t_0)\hat{\zeta}^1_{\mathbf{k}}(t_0) \tag{3.55}$$

where

$$\begin{aligned}\hat{\zeta}^{1(Dyn)}_{\mathbf{k}}(t) = \int_{t_0}^{t} ds R^0_{\mathbf{k}}(t,s) \Bigg[\sum_{\mathbf{p}} \sum_{\mathbf{q}} \delta(\mathbf{k}+\mathbf{p}+\mathbf{q}) A(\mathbf{k},\mathbf{p},\mathbf{q}) \hat{\zeta}^0_{-\mathbf{p}}(s) h_{-\mathbf{q}} \\ + \sum_{\mathbf{p}} \sum_{\mathbf{q}} \delta(\mathbf{k}+\mathbf{p}+\mathbf{q}) K(\mathbf{k},\mathbf{p},\mathbf{q}) \\ \times [\langle \zeta_{-\mathbf{p}}(s)\rangle \hat{\zeta}^0_{-\mathbf{q}}(s) + \langle \zeta_{-\mathbf{q}}(s)\rangle \hat{\zeta}^0_{-\mathbf{p}}(s) + \hat{\zeta}^0_{-\mathbf{p}}(s)\hat{\zeta}^0_{-\mathbf{q}}(s) - \langle \hat{\zeta}^0_{-\mathbf{p}}(s)\hat{\zeta}^0_{-\mathbf{q}}(s)\rangle] \Bigg]\end{aligned} \tag{3.56}$$

Finally

$$\begin{aligned} C^1_{\mathbf{k}-\mathbf{l}}(t,\acute{t}) &= \langle \hat{\zeta}^{1(Dyn)}_{\mathbf{k}}(t)\hat{\zeta}^0_{-\mathbf{l}}(\acute{t})\rangle + \langle \hat{\zeta}^0_{\mathbf{k}}(t)\hat{\zeta}^{1(Dyn)}_{-\mathbf{l}}(\acute{t})\rangle \\ &+ R^0_{\mathbf{k}}(t,t_0)\langle \hat{\zeta}^1_{\mathbf{k}}(t_0)\hat{\zeta}^0_{-\mathbf{l}}(\acute{t})\rangle + R^0_{-\mathbf{l}}(\acute{t},t_0)\langle \hat{\zeta}^0_{\mathbf{k}}(t)\hat{\zeta}^1_{-\mathbf{l}}(t_0)\rangle \\ &= \langle \hat{\zeta}^{1(Dyn)}_{\mathbf{k}}(t)\hat{\zeta}^0_{-\mathbf{l}}(\acute{t})\rangle + \langle \hat{\zeta}^0_{\mathbf{k}}(t)\hat{\zeta}^{1(Dyn)}_{-\mathbf{l}}(\acute{t})\rangle \\ &+ R^0_{\mathbf{k}}(t,t_0)R^0_{-\mathbf{l}}(\acute{t},t_0)\langle \hat{\zeta}^1_{\mathbf{k}}(t_0)\hat{\zeta}^0_{-\mathbf{l}}(t_0)\rangle \\ &+ R^0_{\mathbf{k}}(t,t_0)R^0_{-\mathbf{l}}(\acute{t},t_0)\langle \hat{\zeta}^0_{\mathbf{k}}(t_0)\hat{\zeta}^1_{-\mathbf{l}}(t_0)\rangle \\ &= \langle \hat{\zeta}^{1(Dyn)}_{\mathbf{k}}(t)\hat{\zeta}^0_{-\mathbf{l}}(\acute{t})\rangle + \langle \hat{\zeta}^0_{\mathbf{k}}(t)\hat{\zeta}^{1(Dyn)}_{-\mathbf{l}}(\acute{t})\rangle \\ &+ R^0_{\mathbf{k}}(t,t_0)R^0_{-\mathbf{l}}(\acute{t},t_0)C_{\mathbf{k}-\mathbf{l}}(t_0,t_0). \end{aligned} \tag{3.57}$$

Thus, after renormalizing Eq. 3.57 we have for $t \geq \acute{t} \geq T$

$$\begin{aligned} C_{\mathbf{k}-\mathbf{l}}(t,\acute{t}) = \int_T^t ds \quad & R_{\mathbf{k}}(t,s)C_{-\mathbf{l}}(\acute{t},s)[A(\mathbf{k},-\mathbf{l},\mathbf{l}-\mathbf{k})h_{\mathbf{k}-\mathbf{l}} \\ & + 2K(\mathbf{k},-\mathbf{l},\mathbf{l}-\mathbf{k})\langle \zeta_{\mathbf{k}-\mathbf{l}}(s)\rangle] \\ + \int_T^{\acute{t}} ds \quad & C_{\mathbf{k}}(t,s)R_{-\mathbf{l}}(\acute{t},s)[A(-\mathbf{l},\mathbf{k},\mathbf{l}-\mathbf{k})h_{\mathbf{k}-\mathbf{l}} \\ & 2K(-\mathbf{l},\mathbf{k},\mathbf{l}-\mathbf{k})\langle \zeta_{\mathbf{k}-\mathbf{l}}(s)\rangle] \\ & + R_{\mathbf{k}}(t,T)R_{-\mathbf{l}}(\acute{t},T)C_{\mathbf{k}-\mathbf{l}}(T,T). \end{aligned} \tag{3.58}$$

We note that these terms have an equivalent derivation via the fluctuation-dissipation theorem which has been included in appendix III.

3.5 Cumulant update quasi-diagonal DIA closure equations

Incorporating the results of the preceding sections we may write the full set of cumulant update quasi-diagonal DIA closure equations (CUQDIA). Hence we may write equations for the mean-field

$$\begin{aligned}(\frac{\partial}{\partial t}+\nu_0(k)k^2)\langle\zeta_{\mathbf{k}}\rangle = \sum_{\mathbf{p}}\sum_{\mathbf{q}}\delta(\mathbf{k}+\mathbf{p}+\mathbf{q})\\ \times[K(\mathbf{k},\mathbf{p},\mathbf{q})\langle\zeta_{-\mathbf{p}}(t)\rangle\langle\zeta_{-\mathbf{q}}(t)\rangle + A(\mathbf{k},\mathbf{p},\mathbf{q})\langle\zeta_{-\mathbf{p}}(t)\rangle h_{-\mathbf{q}}\\ +K(\mathbf{k},\mathbf{p},\mathbf{q})\tilde{K}^{(2)}_{-\mathbf{p},-\mathbf{q}}(0,0)R_{-\mathbf{p}}(t,0)R_{-\mathbf{q}}(t,0)]\\ -\int_{t_0}^{t}ds\ \ \eta_{\mathbf{k}}(t,s)\langle\zeta_{\mathbf{k}}(s)\rangle + h_{\mathbf{k}}\int_{t_0}^{t}ds\ \ \chi_{\mathbf{k}}(t,s)+\langle f^0_{\mathbf{k}}(t)\rangle.\end{aligned} \tag{3.59}$$

We find that the two-time cumulant satisfies

$$\begin{aligned}(\frac{\partial}{\partial t}+\nu_0(k)k^2)C_{\mathbf{k}}(t,\acute{t})\\ =\int_{t_0}^{\acute{t}}ds\ \ \left[S_{\mathbf{k}}(t,s)+P_{\mathbf{k}}(t,s)+F^0_{\mathbf{k}}(t,s)\right]R_{-\mathbf{k}}(\acute{t},s)\\ -\int_{t_0}^{t}ds\ \ \left[\eta_{\mathbf{k}}(t,s)+\pi_{\mathbf{k}}(t,s)\right]C_{-\mathbf{k}}(\acute{t},s)\\ +\sum_{\mathbf{p}}\sum_{\mathbf{q}}\delta(\mathbf{k}+\mathbf{p}+\mathbf{q})\\ \times\Big[K(\mathbf{k},\mathbf{p},\mathbf{q})\tilde{K}^{(3)}_{-\mathbf{q},-\mathbf{p},-\mathbf{k}}(0,0,0)R_{-\mathbf{q}}(t,0)R_{-\mathbf{p}}(t,0)R_{-\mathbf{k}}(\acute{t},0)\\ +[2K(\mathbf{k},\mathbf{p},\mathbf{q})\langle\zeta_{-\mathbf{q}}(t)\rangle + A(\mathbf{k},\mathbf{p},\mathbf{q})h_{-\mathbf{q}}]\\ \times\tilde{K}^{(2)}_{-\mathbf{p},-\mathbf{k}}(0,0)R_{-\mathbf{p}}(t,0)R_{-\mathbf{k}}(\acute{t},0)\Big].\end{aligned} \tag{3.60}$$

Here the bare noise is assumed to be white:

$$F^0_{\mathbf{k}}(t,s)=\langle\hat{f}^0_{\mathbf{k}}(t)\hat{f}^{0*}_{\mathbf{k}}(s)\rangle = F^0_{\mathbf{k}}(t)\delta(t-s) \tag{3.61}$$

where δ is the Dirac delta function. The restart terms are calculated at time $t=\acute{t}=T$ through the relationships

$$\begin{aligned}\tilde{K}^{(2)}_{-\mathbf{p},-\mathbf{k}}(T,T) = K^{(2)Dyn}_{-\mathbf{p},-\mathbf{k}}(T,T)\\ +\tilde{K}^{(2)}_{-\mathbf{p},-\mathbf{k}}(0,0)R_{-\mathbf{p}}(T,0)R_{-\mathbf{k}}(T,0),\end{aligned} \tag{3.62}$$

$$\begin{aligned}\tilde{K}^{(3)}_{-\mathbf{q},-\mathbf{p},-\mathbf{k}}(T,T,T) = K^{(3)Dyn}_{-\mathbf{q},-\mathbf{p},-\mathbf{k}}(T,T,T)\\ +\tilde{K}^{(3)}_{-\mathbf{q},-\mathbf{p},-\mathbf{k}}(0,0,0)R_{-\mathbf{q}}(T,0)R_{-\mathbf{p}}(T,0)R_{-\mathbf{k}}(T,0)\end{aligned} \tag{3.63}$$

where

$$K^{(2)Dyn}_{-\mathbf{p},-\mathbf{k}}(t,\acute{t}) = \int_{t_0}^{t} ds \;\; R_{-\mathbf{p}}(t,s)C_{-\mathbf{k}}(\acute{t},s) \times [A(-\mathbf{p},-\mathbf{k},-\mathbf{q})h_{\mathbf{q}} + 2K(-\mathbf{p},-\mathbf{k},-\mathbf{q})\langle\zeta_{\mathbf{q}}(s)\rangle] + \int_{t_0}^{\acute{t}} ds \;\; R_{-\mathbf{k}}(\acute{t},s)C_{-\mathbf{p}}(t,s) \times [A(-\mathbf{k},-\mathbf{p},-\mathbf{q})h_{\mathbf{q}} + 2K(-\mathbf{k},-\mathbf{p},-\mathbf{q})\langle\zeta_{\mathbf{q}}(s)\rangle] , \tag{3.64}$$

$$\sum_{\mathbf{p}}\sum_{\mathbf{q}} \delta(\mathbf{k}+\mathbf{p}+\mathbf{q})K(\mathbf{k},\mathbf{p},\mathbf{q})K^{(2)Dyn}_{-\mathbf{p},-\mathbf{q}}(t,t) = -\int_{t_0}^{t} ds \;\; \eta_{\mathbf{k}}(t,s)\langle\zeta_{\mathbf{k}}(s)\rangle + h_{\mathbf{k}}\int_{t_0}^{t} ds \;\; \chi_{\mathbf{k}}(t,s). \tag{3.65}$$

and

$$\sum_{\mathbf{p}}\sum_{\mathbf{q}} \delta(\mathbf{k}+\mathbf{p}+\mathbf{q})K(\mathbf{k},\mathbf{p},\mathbf{q})K^{(3)Dyn}_{-\mathbf{q},-\mathbf{p},-\mathbf{k}}(t,t,\acute{t}) = \int_{t_0}^{\acute{t}} ds \;\; S_{\mathbf{k}}(t,s)R_{-\mathbf{k}}(\acute{t},s) - \int_{t_0}^{t} ds \;\; \eta_{\mathbf{k}}(t,s)C_{-\mathbf{k}}(\acute{t},s). \tag{3.66}$$

The single time cumulant is obtained from the fact that

$$\frac{\partial C_{\mathbf{k}}(t,t)}{\partial t} = \lim_{\acute{t}\to t}\left(\frac{\partial C_{\mathbf{k}}(t,\acute{t})}{\partial t} + \frac{\partial C_{\mathbf{k}}(t,\acute{t})}{\partial \acute{t}}\right) \tag{3.67}$$

and $C_{\mathbf{k}}(t,\acute{t}) = C_{\mathbf{k}}(\acute{t},t)$. Thus the single-time cumulant satisfies the equation

$$\begin{aligned}(\frac{\partial}{\partial t} + 2\nu_0(k)k^2)C_{\mathbf{k}}(t,t) &= 2Re\int_{t_0}^{t} ds \;\; \left[S_{\mathbf{k}}(t,s) + P_{\mathbf{k}}(t,s) + F^0_{\mathbf{k}}(t,s)\right] R_{-\mathbf{k}}(t,s) \\ &\quad -2Re\int_{t_0}^{t} ds \;\; \left[\eta_{\mathbf{k}}(t,s) + \pi_{\mathbf{k}}(t,s)\right] C_{-\mathbf{k}}(t,s) \\ &\quad +2Re\sum_{\mathbf{p}}\sum_{\mathbf{q}} \delta(\mathbf{k}+\mathbf{p}+\mathbf{q}) \\ &\quad \times \Big[K(\mathbf{k},\mathbf{p},\mathbf{q})\tilde{K}^{(3)}_{-\mathbf{q},-\mathbf{p},-\mathbf{k}}(0,0,0)R_{-\mathbf{q}}(t,0)R_{-\mathbf{p}}(t,0)R_{-\mathbf{k}}(t,0) \\ &\quad + [2K(\mathbf{k},\mathbf{p},\mathbf{q})\langle\zeta_{-\mathbf{q}}(t)\rangle + A(\mathbf{k},\mathbf{p},\mathbf{q})h_{-\mathbf{q}}] \\ &\quad \times\tilde{K}^{(2)}_{-\mathbf{p},-\mathbf{k}}(0,0)R_{-\mathbf{p}}(t,0)R_{-\mathbf{k}}(t,0)\Big]\end{aligned} \tag{3.68}$$

The equation for the response function takes the form:

$$\begin{aligned}(\frac{\partial}{\partial t} + \nu_0(k)k^2)R_{\mathbf{k}}(t,\acute{t}) &= -\int_{\acute{t}}^{t} ds \;\; \left[\eta_{\mathbf{k}}(t,s) + \pi_{\mathbf{k}}(t,s)\right] R_{\mathbf{k}}(s,\acute{t})\end{aligned} \tag{3.69}$$

with $R_{\mathbf{k}}(t,t) = 1$ and where for $t < \acute{t}$ we have $R_{\mathbf{k}}(t,\acute{t}) = 0$. Thus the inhomogeneous cumulant update QDIA equations require that we integrate up to some time $t = \acute{t} = T$ and calculate the two- and three-point cumulants through the relations Eqs. 3.62 to 3.66. The procedure may now be performed as often as required by simply replacing $\tilde{K}^2_{-\mathbf{p},-\mathbf{k}}(0,0)$, $\tilde{K}^2_{-\mathbf{p},-\mathbf{q}}(0,0)$ and $\tilde{K}^3_{-\mathbf{q},-\mathbf{p},-\mathbf{k}}(0,0,0)$ with the quantities $\tilde{K}^2_{-\mathbf{p},-\mathbf{k}}(T,T)$, $\tilde{K}^2_{-\mathbf{p},-\mathbf{q}}(T,T)$ and $\tilde{K}^3_{-\mathbf{q},-\mathbf{p},-\mathbf{k}}(T,T,T)$.

3.5.1 Integral conservation laws

As we have assumed that the variation in the topography, $\triangle H$, is small, the potential vorticity may be written as

$$q = \bigtriangledown^2 \psi + h \tag{3.70}$$

The evolution equation, which again describes the flow over a fixed topography on an f-plane in terms of the enstrophy, is simply

$$\frac{dq}{dt} + J(\psi, q) = 0 \tag{3.71}$$

with J the Jacobian. The evolution equation represents the advection of potential vorticity which implies the conservation of all integrals of the form

$$\int \int F(q) \; dx \, dy \tag{3.72}$$

with $F(q)$ any arbitrary function of q. This results holds for periodic boundary conditions by Eq. 3.71 and the periodicity of q.

The most important integral invariants are those that are quadratic in ψ [105, 9, 13] namely i) the total kinetic energy

$$\begin{aligned} E &= \frac{1}{2} \int \int (\bigtriangledown \psi)^2 \; dx \, dy \\ &= \frac{1}{2} \sum_{\mathbf{k}} k^2 \langle |\psi_{\mathbf{k}}|^2 \rangle \\ &= \frac{1}{2} \sum_{\mathbf{k}} (C_{\mathbf{k}}(t,\acute{t})/k^2 + \langle \zeta_{\mathbf{k}}(t) \rangle \langle \zeta^*_{\mathbf{k}}(\acute{t}) \rangle / k^2) \end{aligned} \tag{3.73}$$

and ii) the potential enstrophy

$$\begin{aligned} Q &= \frac{1}{2}\int\int(\zeta+h)^2 \; dx\, dy \\ &= \frac{1}{2}\sum_{\mathbf{k}}\langle|\zeta_{\mathbf{k}}+h_{\mathbf{k}}|^2\rangle \\ &= \langle|\zeta_{\mathbf{k}}-\langle\zeta_{\mathbf{k}}\rangle|^2\rangle + |\langle\zeta_{\mathbf{k}}\rangle+h_{\mathbf{k}}|^2 \\ &= \frac{1}{2}\sum_{\mathbf{k}}\left[(\langle\zeta_{\mathbf{k}}(t)\rangle+h_{\mathbf{k}})(\langle\zeta_{\mathbf{k}}(\acute{t})\rangle+h_{\mathbf{k}})^* \right. \\ &\qquad \left. +C_{\mathbf{k}}(t,\acute{t})\right]. \end{aligned} \tag{3.74}$$

The existence of these quadratic invariants implies stability for the stationary state

$$\mu\psi = q \tag{3.75}$$

as demonstrated by Arnold [106], with μ a constant of proportionality.

3.6 Summary

Having briefly reviewed the historical development of the theories that precede Frederiksen's QDIA [91] we proceeded to formulate the cumulant update QDIA deriving the three-point restart terms in an analogous manner to Rose [103] and the two-point terms via both a perturbative method and a method based on the fluctuation-dissipation theorem. In the next chapter we will develop numerical and computational methods to implement the QDIA, CUQDIA and also a model for the direct numerical simulation of the barotropic vorticity equation.

Chapter 4

Computational methodology

In this chapter, the numerical methodology developed to implement the CUQDIA equations of the preceding chapter is presented. This work represents a generalization of the homogeneous codes developed by Frederiksen and Davies [107, 108, 28] and was developed using the homogeneous closure code (without topography) of Frederiksen, Davies and Bell [104] as a starting point. As well the DNS code for flow over topography is an extension of DNS code (without topography) developed by the same authors. Initially the basic structure of the code is outlined. Section 4.2 deals with the generation of the circularly truncated wave number space and the required interaction coefficients and their selection rules. The DNS, closures and mean-field calculations use a predictor-corrector scheme which is derived in section 4.3. This is followed by a brief discussion about estimating errors (section 4.3.1). In the CUQDIA, the subsequent restarts in the closure and mean-field equations use non-Gaussian initial conditions, represented by three-point terms, and as well restarts of two-point terms (involving the topographic forcing and mean-fields). The time-history integrals in the closure and mean-field equations are discretized via the trapezoidal rule. The implementation of the restart procedure and method of evaluation of the integrals is described in section 4.4.

As shown in the previous chapter, the CUQDIA represents a large and complex system of integro-differential equations that pose a significant computational challenge. As an initial test of the numerical model, diagnostic tests, based primarily on analysis at canonical equilibrium are discussed in section 4.5. In section 4.6, the model used in the

direct numerical simulation of the barotropic vorticity equation (Eq. 3.6) in discrete space is presented. The use of closure calculations formulated for continuous wavenumbers [38] is generally employed to enable high wavenumber calculations via logarithmic discretization of wavenumber space. In the present discussion discrete closures are used in order to avoid any discrepancies arising from the use of differing wavenumber formulations and discretizations and to incorporate the mean-field equation which is naturally represented in discrete wavenumber space. As noted by Frederiksen et al [104], the use of discrete spectra in closures allows not only the incorporation of all interactions, both local and nonlocal, but also enables the detection of systematic errors in the closures. There is as a consequence no ambiguity due to different formulations involving discrete or continuous spectra. Finally, in section 4.7, the conversion routine for transforming the results from spectral to physical space is discussed.

4.1 Structure of the CUQDIA code

In this section the structure of the main program `di2ens2.f`, which is used to calculate the CUQDIA closure equations, is discussed. Throughout, the following discussion Fig. 4.1, in which a flow diagram of the code is depicted, will be refered to. The initial sections of the code simply read in the required parameters, logical statements, forcing and viscosity constants etc, which are then used to generate the initial fields. These are in turn sent to subroutines `eqout1.f, ensedgns.f, enseqout1.f, dgns0.f, etc` where the diagnostic quantities, viz., energy, enstrophy, streamfunction etc, are calculated. The most important of the input parameters is the information about the circularly truncated wavenumber space that are set up by the `planar1.f` program.

Once this is completed, the outer do loop is entered into, which runs through the specified number of restarts followed by the inner do loop which runs through the time steps. The transient field $C_{\mathbf{k}}(t, \acute{t})$ predictor step is now implemented. The integral terms in Eq. 3.27 and Eq. 3.20 are calculated in subroutine `deriv.f`. If any restart terms are present these are added on at this point. Next, the non-integral terms on the righthand side of Eq. 3.20 are calculated in the subroutine `enserhs.f` followed by the implementation of

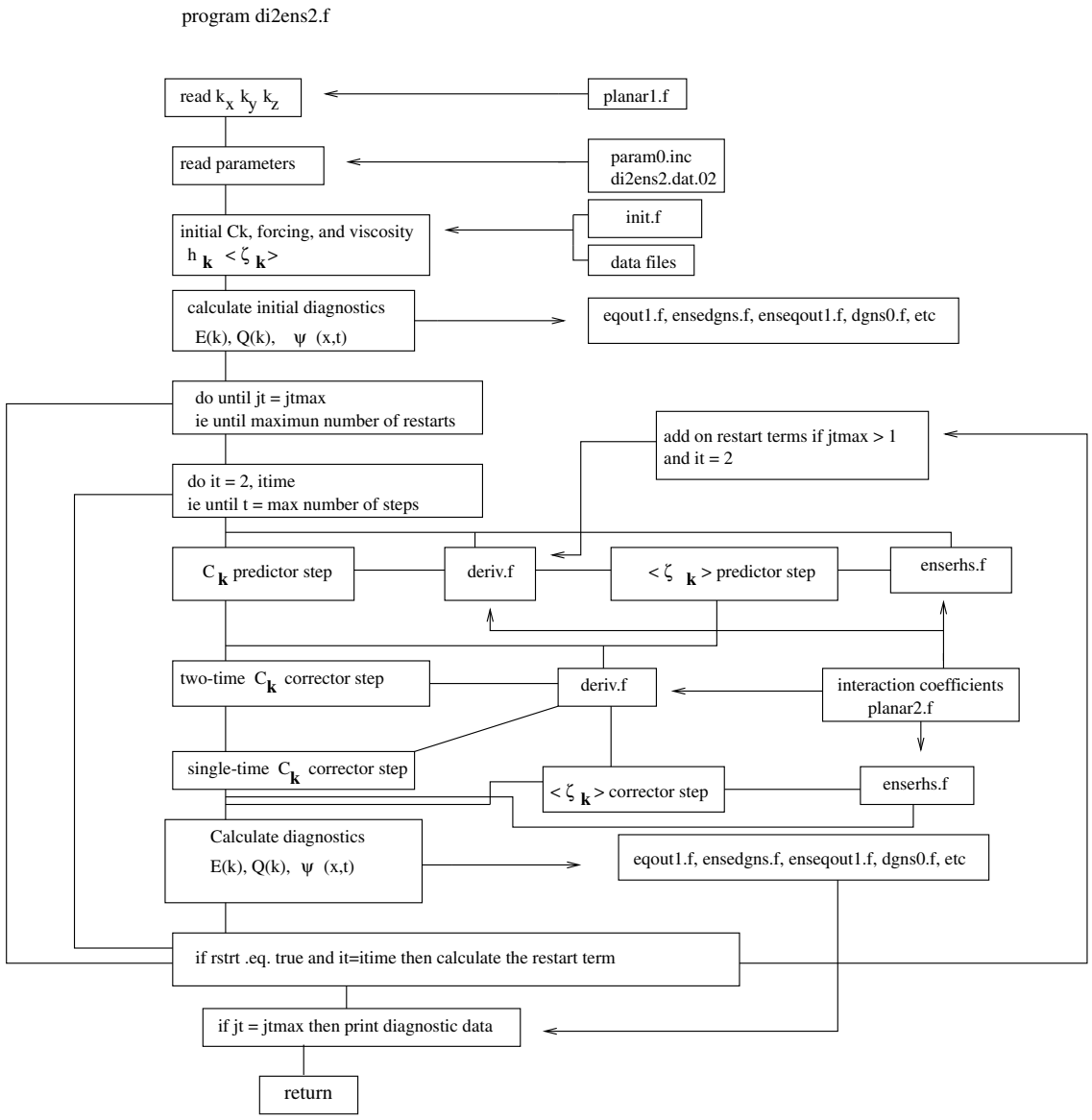

Figure 4.1: Flow diagram of the structure of the main program `di2ens2.f` which implements the CUQDIA closure equations.

the mean-field predictor step. A similar procedure is followed at the corrector step. The next step is to decide if a restart is to take place at $t = \acute{t} = T$ and if so the restart terms are calculated in `deriv.f`. Finally the diagnostics are calculated and printed.

4.2 Discrete *k*-space interaction coefficients

The interaction coefficients and their wavenumber triad selectors are generated on the circularly truncated half-space in the subroutine `planar1.f` by first running over the righthand plane and then backwards over the lefthand plane. The wave number triad selectors `mslct` and `lslct` are then generated with the appropriate skip out implemented, for example when $p_x q_y = p_y q_x$, in order to minimize the number of interaction coefficients required. These minimized triad selectors and the discrete space parameters are then passed to the subroutine `planar2.f` where the required interaction coefficients are generated. The code uses the following equivalences:

$$\begin{aligned}
\texttt{r4(nmb4)} &= K(\mathbf{k},\mathbf{p},\mathbf{q}) \\
\texttt{b4(nmb4)} &= K(-\mathbf{p},-\mathbf{q},-\mathbf{k}) \\
\texttt{tr4(nmb4)} &= A(\mathbf{k},\mathbf{p},\mathbf{q}) \\
\texttt{tb4(nmb4)} &= A(-\mathbf{p},-\mathbf{q},-\mathbf{k}) \\
\texttt{t24(nmb4)} &= A(-\mathbf{p},-\mathbf{k},-\mathbf{q}).
\end{aligned} \tag{4.1}$$

The half-space coefficients may then be used to generate the whole space via the conjugacy property of the mean-field, cumulant and response functions. The number of interaction coefficients increases rapidly as resolution increases and are therefore stored on tape and read into the main subroutine `di2ens2.f` as needed in order to reduce memory requirements. Although these subroutines are not included in the thesis examples of the output are included below for the C3 truncated case. The subroutine `planar1.f` generates the discrete k-space where `k1`= k_x, `k2`= k_y, $k = \sqrt{k_x^2 + k_y^2}$.

Table 4.1: C3 discrete k-halfspace

nk(k1,k2)	k1	k2	k
1	0	1	1.000E+00
2	0	2	2.000E+00
3	0	3	3.000E+00
4	1	-2	2.236E+00
5	1	-1	1.414E+00
6	1	0	1.000E+00
7	1	1	1.414E+00
8	1	2	2.236E+00
9	2	-2	2.828E+00
10	2	-1	2.236E+00
11	2	0	2.000E+00
12	2	1	2.236E+00
13	2	2	2.828E+00
14	3	0	3.000E+00

The routine `planar2.f` generates the triad selectors and interaction coefficients in the following form where `n1`= k_x, `m1`= p_x, `l1`= q_x, `n2`= k_y, etc.

Table 4.2: Triad selectors and b4 coefficients

nm	n1	n2	m	l	m1	m2	l1	l2	b4(nsn)
1	0	1	4	19	-1	2	1	-1	-0.25
2	0	1	5	20	-1	1	1	0	0.E+0
3	0	1	6	21	-1	0	1	1	-0.25
4	0	1	7	22	-1	-1	1	2	-0.4

5	0	1	9	24	-2	2	2	-1	-0.8
6	0	1	10	25	-2	1	2	0	-0.75
etc				etc					etc

4.3 Predictor-corrector scheme

In this section, the predictor-corrector algorithm used to evolve $C_{\mathbf{k}}$, $R_{\mathbf{k}}$ and $\langle\zeta_{\mathbf{k}}\rangle$ is described. This algorithm was first developed by Kraichnan[109] and has become the standard for DIA-type calculations. Important features of the scheme are that it conserves energy exactly at equilibrium, demonstrates good stability properties for large timesteps and as well handles linear terms exactly. The error associated with the predictor-corrector scheme is $O((\triangle t))^3$.

In order to derive this method let equations 3.20, 3.27, and 3.32 be written in the form

$$(\frac{d}{dt} + \nu_n)\langle\zeta_n(t)\rangle = M_n(t) \tag{4.2}$$

$$(\frac{d}{dt} + \nu_n)C_n(t,\acute{t}) = S_n(t,\acute{t}) \tag{4.3}$$

$$(\frac{d}{dt} + \nu_n)R_n(t,\acute{t}) = H_n(t,\acute{t}) \tag{4.4}$$

where $n = k_n$ and $M_n(t)$, $S_n(t,\acute{t})$ and $H_n(t,\acute{t})$ represent the righthand side of equations 3.20, 3.27, and 3.32 respectively. Alternately, one can consider M_n, S_n and H_n to be source terms that are functionals of the statistical variables. The first step is to discretize the time-history integrals in M_n, S_n and H_n using the trapezoidal rule. We next discretize the time interval $t \in [t_0, t_f]$ into intervals $\triangle t_i (i = 1, \ldots, N)$ which for our purposes are uniform, and where t_0 is the initial time and t_f is the time at the end of the interval.

Let us derive the scheme for the response function as the argument that follows applies equally to C_n, and $\langle\zeta_n\rangle$. Now from Eq. 4.4 we have

$$\exp(-\nu_n t)\frac{d}{dt}[R_n(t,\acute{t})\exp(\nu_n t)]$$

$$= \exp(-\nu_n t)[\frac{d}{dt}R_n(t,\acute{t}) + \nu_n R_n(t,\acute{t})]\exp(\nu_n t) \tag{4.5}$$

$$\therefore \frac{d}{dt}[R_n(t,\acute{t})\exp(\nu_n t)] = \exp(\nu_n t)H_n(t,\acute{t}). \tag{4.6}$$

We now replace $H_n(t, \acute{t})$ by the approximate value

$$\overline{H}_n(\acute{t}) = \frac{1}{2}[H_n(t_i, \acute{t}) + H_n(t_{i-1}, \acute{t})] \tag{4.7}$$

over the interval $\triangle t_i$ so that

$$\frac{d}{dt}[R_n(t, \acute{t}) \exp(\nu_n t)] \doteqdot \exp(\nu_n t)\overline{H}_n(\acute{t}). \tag{4.8}$$

Then we integrate over $\triangle t_i$ and find

$$\int_{t_{i-1}}^{t_i} dt \frac{d}{dt}[R_n(t, \acute{t}) \exp(\nu_n t)] = \int_{t_{i-1}}^{t_i} dt \exp(\nu_n t)\overline{H}_n(\acute{t}) \tag{4.9}$$

$$= \overline{H}_n(t_i, t_j)\frac{[\exp(\nu_n t_i) - \exp(\nu_n t_{i-1})]}{\nu_n} \tag{4.10}$$

and consequently

$$R_n(t_i, t_j) \exp(\nu_n t_i) - R_n(t_{i-1}, t_j) \exp(\nu_n t_{i-1}) = \overline{H}_n(t_i, t_j)\frac{[\exp(\nu_n t_i) - \exp(\nu_n t_{i-1})]}{\nu_n}. \tag{4.11}$$

We also note that

$$\int_{t_{i-1}}^{t_i} d(R_n(t, \acute{t}) \exp(\nu_n t)) = R_n(t_i, t_j) \exp(\nu_n t_i) - R_n(t_{i-1}, t_j) \exp(\nu_n t_{i-1}) \tag{4.12}$$

and hence

$$R_n(t_i, t_j) = R_n(t_{i-1}, t_j) \exp(-\nu_n \triangle t_i) + \frac{\overline{H}_n(t_i, t_j)}{\nu_n}[1 - \exp(-\nu_n \triangle t_i)] \tag{4.13}$$

where $\triangle t_i = t_i - t_{i-1}$. Finally we have

$$R_n(t_i, t_j) = R_n(t_{i-1}, t_j) \exp(-\nu_n \triangle t_i) + \frac{1}{2\nu_n}[1 - \exp(-\nu_n \triangle t_i)][H_n(t_i, t_j) + H_n(t_{i-1}, t_j)] \tag{4.14}$$

with initial values $R(t_i, t_i) = 1$.

Similarly, we find

$$C_n(t_i, t_j) = C_n(t_{i-1}, t_j) \exp(-\nu_n \triangle t_i) + \frac{1}{2\nu_n}[1 - \exp(-\nu_n \triangle t_i)][S_n(t_i, t_j) + S_n(t_{i-1}, t_j)] \tag{4.15}$$

for $(i > j)$ and initial conditions $C_n(t_0, t_0) = C_n(0, 0)$. The diagonal values $C_n(t_i, t_i)(i > 0)$ are similarly obtained using the single-time cumulant equation 3.33 where

$$(\frac{d}{dt} + 2\nu_n)C_n(t, \acute{t}) = 2Re(S_n(t, \acute{t})). \tag{4.16}$$

This gives

$$C_n(t_i, t_j) = C_n(t_{i-1}, t_j)\exp(-2\nu_n \triangle t_i)$$
$$+\frac{1}{2\nu_n}[1 - \exp(-2\nu_n \triangle t_i)][S_n(t_i, t_j) + S_n(t_{i-1}, t_j)]. \tag{4.17}$$

Finally, the terms for the mean-field complete the implicit integration scheme

$$\langle\zeta_n(t_i)\rangle = \langle\zeta_n(t_{i-1})\rangle\exp(-\nu_n \triangle t_i)$$
$$+\frac{1}{2\nu_n}[1 - \exp(-\nu_n \triangle t_i)][M_n(t_i) + M_n(t_{i-1})]. \tag{4.18}$$

We implement this scheme in the normal way generating "predictor" values for $C_n(t_i, t_j)$, $R_n(t_i, t_j)$ and $\langle\zeta_n(t_i)\rangle$ $(j < i)$ at the i^{th} step by replacing $S_n(t_i, t_j)$, $S_n(t_i, t_i)$, $H_n(t_i, t_j)$ and $M_n(t_i)$ on the righthand side of equations 4.14, 4.15, 4.17 and 4.18 with $S_n(t_{i-1}, t_j)$, $S_n(t_{i-1}, t_{i-1})$, $H_n(t_{i-1}, t_j)$ and $M_n(t_{i-1})$. The "corrector" values are generated by evaluating $S_n(t_i, t_j)$, $S_n(t_i, t_i)$, $H_n(t_i, t_j)$ and $M_n(t_i)$ with the replacement of all "predictor" values for R, C and $\langle\zeta\rangle$ with an argument t_i appearing in the sums of the trapezoidal rule. The $(i + 1)^{th}$ step is then begun using the "corrector" values of R, C and $\langle\zeta\rangle$ to compute S_n, H_n and M_n. At canonical equilibrium the off-diagonal elements of the covariance matrix vanish (as the time-history integrals cancel) and the system becomes diagonal with $S_n(t_i, t_j) = 0$ and $M_n(t_i) = 0$.

4.3.1 Error estimates

Kraichnan[109] noted that the DIA equations for isotropic turbulence were sufficiently complex that the only feasible error estimate was to compare calculations with various truncation limits and finite-difference intervals. He also noted that errors originated from three primary sources i) truncation to a finite k range, ii) discretizing of k and iii) discretizing of t. Our system is significantly more complex than the isotropic case and has a further source of possible error arising from the use of a formal restart procedure. It

is possible to disregard the discretizing of k as a source of possible error as the model has been developed using a discrete wavenumber space for both the DNS and CUQDIA code. This avoids the error source arising due to the use of logarithmic discretization of continuous k space (an approach commonly used to reach high wavenumbers). As stated before, discrete wavenumber space allows the incorporation of all interactions both local and nonlocal (which are not included when using logarithmic discretization) while also allowing unambiguous comparison of the DNS and CUQDIA results with differences attributable to systematic errors in the closures. Frederiksen et al. [104] noted that nonlocal interactions may be particularly important in the case of two-dimensional turbulence and that differences between discrete DNS and continuous closures may be significant in cases where the larger scales contain a significant amount of energy. Thus truncation to a finite k range and the discretizing of t emerge as the main sources of error.

4.4 Implementing the restart procedure

In this section, the implementation of the restart routine and integro-differential equations, as evaluated in the subroutine `deriv.f`, is discussed. As this subroutine represents a crucial portion of the numerical implementation, it will be considered in some detail. The overall structure of this subroutine is given in figures 4.2, 4.3 and 4.4.

The initial restart values are either zeroed or read in from disk if a previous calculation is to be continued. If $t = \acute{t} = T$ the calculation of the restart terms is carried out. Also, it is possible to simply zero the offdiagonal elements of the covariance matrix and begin the calculation again with the diagonal terms as the new initial conditions. The interaction coefficients and restart values which are numerous, are stored on tape in order to reduce memory requirements and are read in as needed. If it is decided to calculate the cumulant updates the logical parameter `rstrt` is set to true and preparation is made to read the interaction coefficients and previous restart values. In order to select the nonzero triads the triad selection rules must be used, so that an appropriate $\mathbf{p}$ and $\mathbf{q}$ is selected for each $\mathbf{k}$, which are read in via the `mslct(n)` and `lslct(n)` functions. The nonzero initial restart values are also read in at this point.

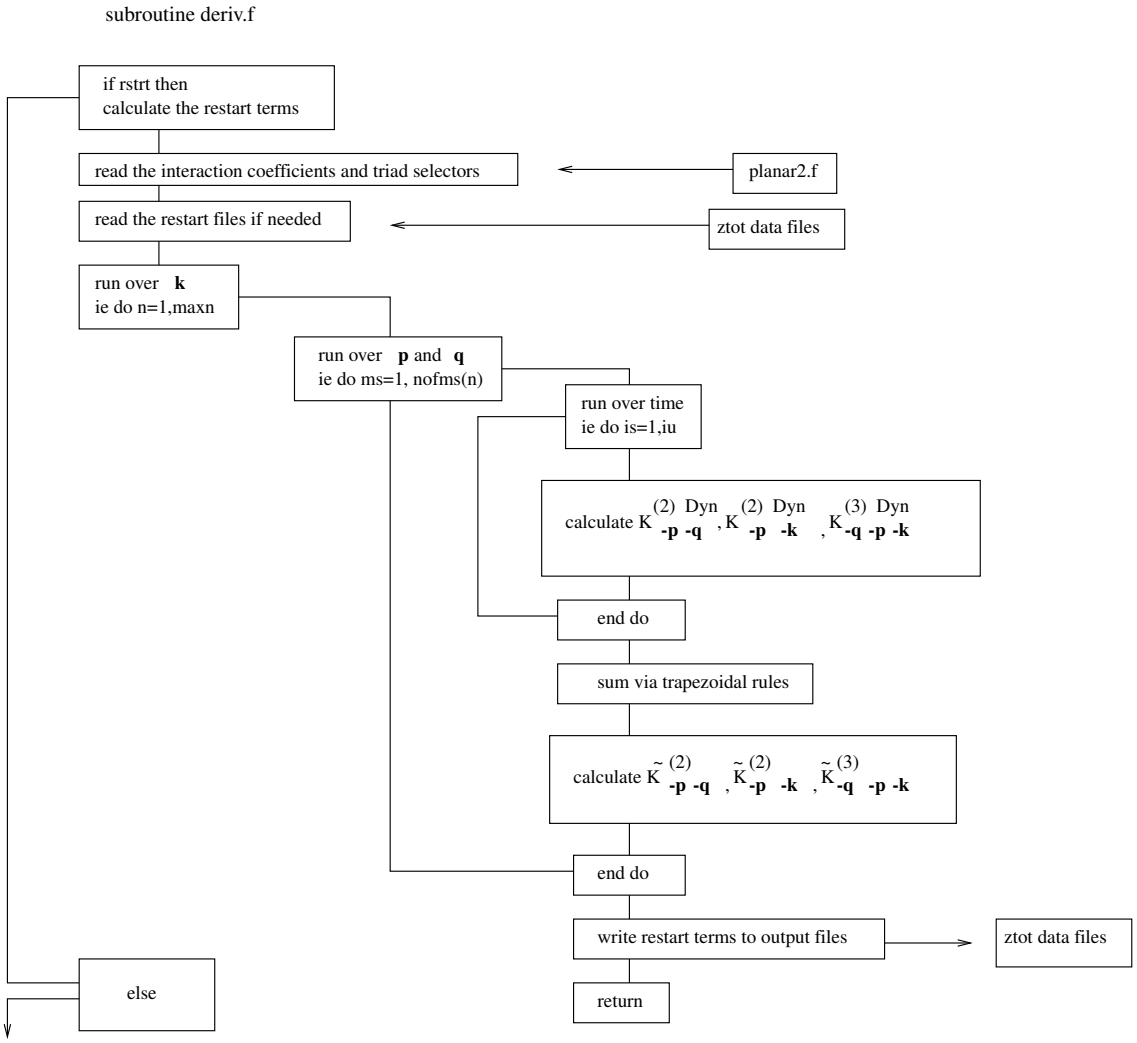

Figure 4.2: Flow diagram of the structure of the initial section of the subroutine `deriv.f` which calculates the restart equations.

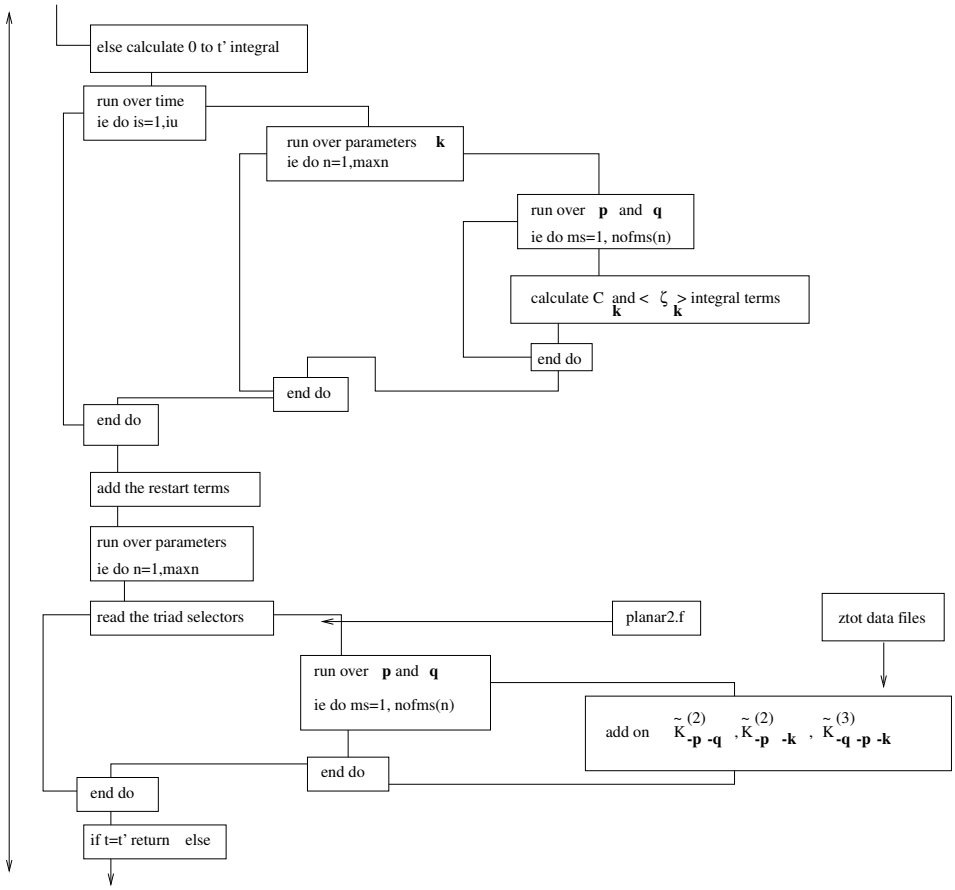

Figure 4.3: Flow diagram of the structure of the middle section of the subroutine `deriv.f`.

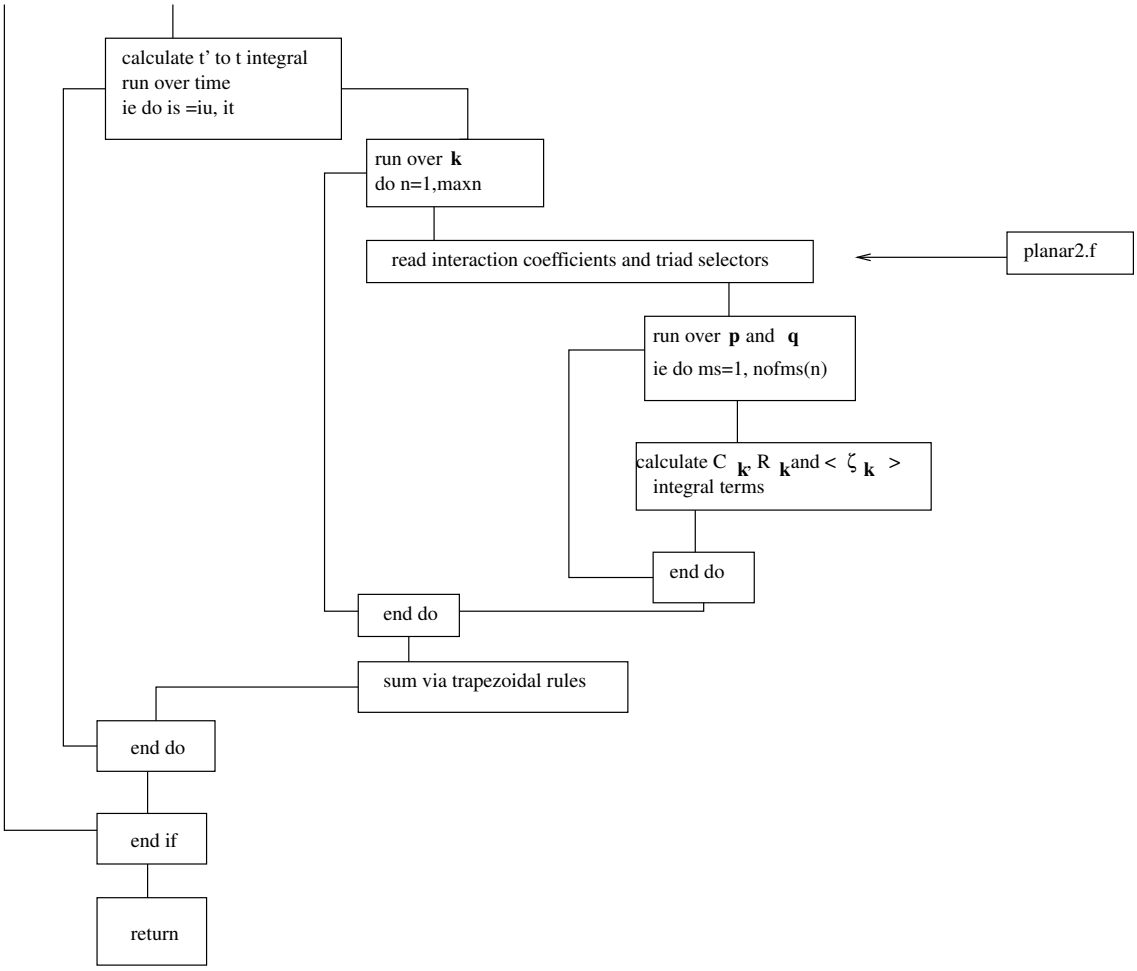

Figure 4.4: Flow diagram of the structure of the final section of the subroutine `deriv.f`.

The next step is to loop through the triads and integrate from $\int_{t_0}^{\acute{t}} ds$ using the trapezoidal method. Now the terms comprising the three-point homogeneous contributions $S_{\mathbf{k}}$ and $\eta_{\mathbf{k}}$, the two-point inhomogeneous contributions $P_{\mathbf{k}}$ and $\pi_{\mathbf{k}}$, and the mean-field terms $\eta_{\mathbf{k}}$ and $\chi_{\mathbf{k}}$ are calculated separately. Finally the restart term is updated before returning from the last call at this timestep. This completes the calculation of the elements of the two-time covariance matrix which is repeated at each successive timestep. It remains to evaluate the $\int_{t_0}^{\acute{t}}$ integral. This operation essentially takes the same form as the restart integrals; however the order of the integration do loops must be changed to run through the temporal arguments first and then through the triads. It is now possible to calculate $C_{\mathbf{k}}(t,\acute{t})$ and the integrals
$\int_{t_0}^{\acute{t}} ds \quad \eta_{\mathbf{k}}(t,s)\langle\zeta_{\mathbf{k}}(s)\rangle + h_{\mathbf{k}} \int_{t_0}^{\acute{t}} ds \quad \chi_{\mathbf{k}}(t,s)$.
As the model is running over the half space, the whole space values are generated via conjugacy and finally summed using the trapezoidal rule.

The final step in the restart calculation involves adding on the restart sums to the $\int_{t_0}^{\acute{t}} ds$ integrals. That is, once again loop through the parameters and triads and simply add the restart terms, after which conjugacy is invoked and the results scaled by the timestep `del`. The last section of the subroutine `deriv.f` is the calculation of the $\int_{\acute{t}}^{t} ds$ integrals, including the response function $R_{\mathbf{k}}$. The approach is to proceed as for the $\int_{t_0}^{\acute{t}} ds$ integration with s running from $\acute{t}$ to t. Also, it is only required to integrate over terms containing $\eta_{\mathbf{k}}(t,s)$ and $\pi_{\mathbf{k}}(t,s)$ in the cumulant equation. The integration is again carried out using the trapezoidal rule. Finally the results of the integrations, that is the values for $R_{\mathbf{k}}(t,\acute{t})$, $C_{\mathbf{k}}(t,\acute{t})$ and the integral terms in $\langle\zeta_{\mathbf{k}}(t)\rangle$ namely $\int_{t_0}^{t} ds \quad \eta_{\mathbf{k}}(t,s)\langle\zeta_{\mathbf{k}}(s)\rangle + h_{\mathbf{k}} \int_{t_0}^{t} ds \quad \chi_{\mathbf{k}}(t,s)$ are then passed to the predictor-corrector scheme contained in the main body of the program.

4.5 Diagnostic tests

As stated in the introduction to this chapter, the implementation of the CUQDIA equations represents a computational and numerical challenge. Canonical equilibrium does, however, offer the opportunity to "debug" the numerical routines via the wealth of ana-

lytic tests that may be derived for this special case. The crucial point is that, at canonical equilibrium (but not in general), we have the fluctuation-dissipation theorem (FDT) [57, 58, 60, 65]. Thus we can replace the equation for the second-order two-time cumulant (or the response function equation) with the FDT. To see this, we restate the equilibrium solution for the two-time cumulant (which is unchanged from the homogeneous case) as

$$C_{\mathbf{k}}(t,\acute{t}) = C_{\mathbf{k}}^{eq} = \frac{k^2}{a+bk^2} \tag{4.19}$$

and note the mean field expression is given by

$$\langle \zeta_{\mathbf{k}}(t) \rangle = \langle \zeta_{\mathbf{k}}^{eq} \rangle = -bh_{\mathbf{k}} C_{\mathbf{k}}^{eq}. \tag{4.20}$$

Now, using the FDT, we can write

$$\begin{aligned} C_{\mathbf{k}}(t,\acute{t})\theta(t-\acute{t}) &= R_{\mathbf{k}}(t,\acute{t})C_{\mathbf{k}}(\acute{t},\acute{t}) \\ &= R_{\mathbf{k}}(t,\acute{t})C_{\mathbf{k}}^{eq} \end{aligned} \tag{4.21}$$

with $\theta(t-\acute{t})$ the Heavyside step function, which is identically zero for $t < \acute{t}$ and unity otherwise. The point to be made is that after the formal renormalization the off-diagonal two point cumulant in the QDIA closure is now expressed in terms of diagonal cumulant and response functions. That is,

$$\begin{aligned} C_{\mathbf{k}-\mathbf{l}}(t,\acute{t}) = \int_{t_0}^{t} ds \quad & R_{\mathbf{k}\mathbf{k}}(t,s)C_{\mathbf{l}-\mathbf{l}}(s,\acute{t})[A(\mathbf{k},-\mathbf{l},\mathbf{l}-\mathbf{k})h_{(\mathbf{k}-\mathbf{l})} \\ & +2K(\mathbf{k},-\mathbf{l},\mathbf{l}-\mathbf{k})\langle\zeta_{(\mathbf{k}-\mathbf{l})}(s)\rangle] \\ + \int_{t_0}^{\acute{t}} ds \quad & R_{-\mathbf{l}-\mathbf{l}}(\acute{t},s)C_{\mathbf{k}-\mathbf{k}}(t,s)[A(-\mathbf{l},\mathbf{k},\mathbf{l}-\mathbf{k})h_{(\mathbf{k}-\mathbf{l})} \\ & +2K(-\mathbf{l},\mathbf{k},\mathbf{l}-\mathbf{k})\langle\zeta_{(\mathbf{k}-\mathbf{l})}(s)\rangle]. \end{aligned} \tag{4.22}$$

Substitution of the FDT result (Eq. 4.21) into Eq. 4.22 gives

$$\begin{aligned} & C_{-\mathbf{l}}^{eq}[A(\mathbf{k},-\mathbf{l},\mathbf{l}-\mathbf{k})h_{(\mathbf{k}-\mathbf{l})} + 2K(\mathbf{k},-\mathbf{l},\mathbf{l}-\mathbf{k})\langle\zeta_{(\mathbf{k}-\mathbf{l})}^{eq}(s)\rangle] \\ & +C_{\mathbf{k}}^{eq}[A(-\mathbf{l},\mathbf{k},\mathbf{l}-\mathbf{k})h_{(\mathbf{k}-\mathbf{l})} + 2K(-\mathbf{l},\mathbf{k},\mathbf{l}-\mathbf{k})\langle\zeta_{(\mathbf{k}-\mathbf{l})}^{eq}(s)\rangle] = 0. \end{aligned} \tag{4.23}$$

It then follows that the off-diagonal elements of the equal-time cumulants vanish ($C_{\mathbf{k}-\mathbf{l}}(t,t) = 0$) for $\mathbf{l} \neq \mathbf{k}$ resulting in the exact cancellation of the homogeneous and inhomogeneous integral terms in Eq. 3.27 as well as the mean-field integrals in Eq. 3.20.

Thus, with canonical equilibrium initial values, the system must remain stationary regardless of the strength of the topographic and mean-field terms. Figure 4.5 represents an equilibrium calculation (inviscid unforced) demonstrating that the QDIA closure model successfully maintains the canonical equilibrium as a stationary solution. The contours of the mean-field in physical space for a system that has evolved to equilibrium were found to be parallel to those of the topography in accordance with the minimum enstrophy principle [9] (not shown). We note that for white, bare random noise forcing, the equilibrium forcing conditions are given by

$$F^{eq} = 2\nu_0(k)k^2 C^{eq}_{\mathbf{k}} \tag{4.24}$$

$$\langle f^{eq}_{\mathbf{k}} \rangle = \nu_0(k)k^2 \langle \zeta^{eq}_{\mathbf{k}} \rangle \tag{4.25}$$

where $C^{eq}_{\mathbf{k}}$ and $\langle \zeta^{eq}_{\mathbf{k}} \rangle$ are defined in Eqs. 4.19 and 4.20 respectively and where the model displays comparable results to those in Fig. 4.5. Another important test is that at equilibrium the restart terms become exact; that is, the time history integral are identically zero. As a further test we have also verified the interaction coefficients by "hard wiring" the FDT into the code for equilibrium initial conditions.

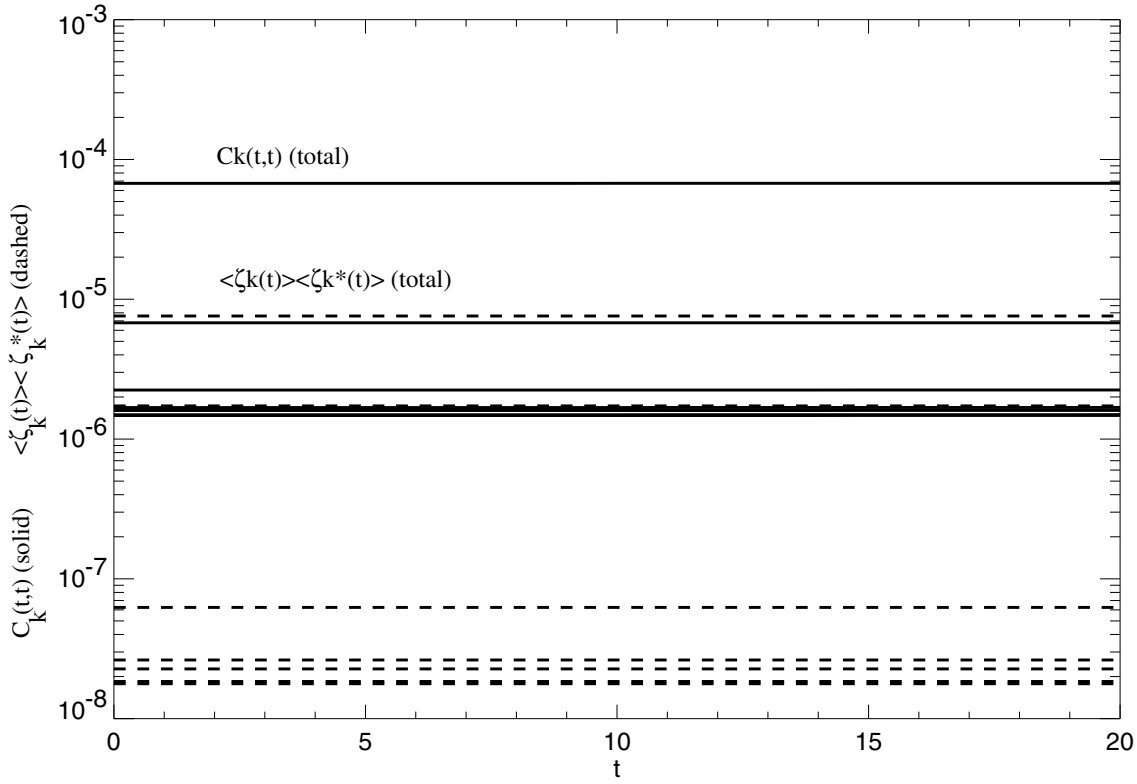

Figure 4.5: Spectral equilibrium calculation. The system has been initialized with the following canonical equilibrium conditions:

topographic amplitude squared $|h_{\mathbf{k}}|^2 = 0.01 \times C_{\mathbf{k}}^{eq}$,

mean vorticity $\langle \zeta_{\mathbf{k}}(0) \rangle = -bh_{\mathbf{k}} C_{\mathbf{k}}^{eq}$,

twice enstrophies $C_{\mathbf{k}}(0,0) = C_{\mathbf{k}}^{eq} = \frac{k^2}{a+bk^2}$,

$a = -5.969 \times 10^5$,

$b = 7.444 \times 10^5$,

$\triangle t = 1/8 \ \ days$,

and displays a stationary solution for all time. Due to degeneracy only the first 6 modes need be displayed.

4.6 Direct numerical simulation

The calculation of the spectral form of the barotropic vorticity equation eqn 3.6 is straight forward with the structure of the main program `ens2.f` depicted in Fig. 4.6. The DNS code, including topographic terms, was developed from the DNS code, without topography, of Frederiksen, Davies and Bell [104]. The input parameters are read in and an ensemble of realizations (a Gaussian distribution) with the required mean is generated. The next step is to loop through the time steps implementing the predictor-corrector scheme via the subroutine `etstep.f`. The right-hand side of the equation is calculated in `erhs.f` where the interaction coefficients are read in as needed. The final step is to then average over the realizations, calculate and save the diagnostic data and print the output.

4.7 Physical space conversion routine

The conversion of the mean-field spectral solutions of the CUQDIA equations to physical space is performed by a discrete 2-D Fourier transform that has been nested in the main body of the code (`di2ens2.f`). This function is used extensively in the chapters dealing with the Rossby wave experiments. In order to make the transformation from spectral to physical space a grid is generated (a grid of 50×50 has been used although $2n$ grid-points for n spectral terms are sufficient for an exact representation). Lastly the topography and the initial streamfunction $\psi_{\mathbf{k}} = -\zeta_{\mathbf{k}}/k^2$ are generated on the same grid. The output is then written to a file to be processed as plots using IDL. For the doubly periodic plane the physical space fields take the form

$$\zeta(\mathbf{x},t) = \sum_{\mathbf{k}} \zeta_{\mathbf{k}} \exp(i\mathbf{k}\cdot\mathbf{x}) \tag{4.26}$$

with

$$\zeta_{\mathbf{k}}(t) = \frac{1}{2\pi^2}\int_0^{2\pi} \quad d^2\mathbf{x}\zeta(\mathbf{x},t)\exp(-i\mathbf{k}\cdot\mathbf{x}) \tag{4.27}$$

where $\mathbf{x} = (x,y)$ and $\mathbf{k} = (k_x,k_y)$ and the integrals over space may be replaced by sums.

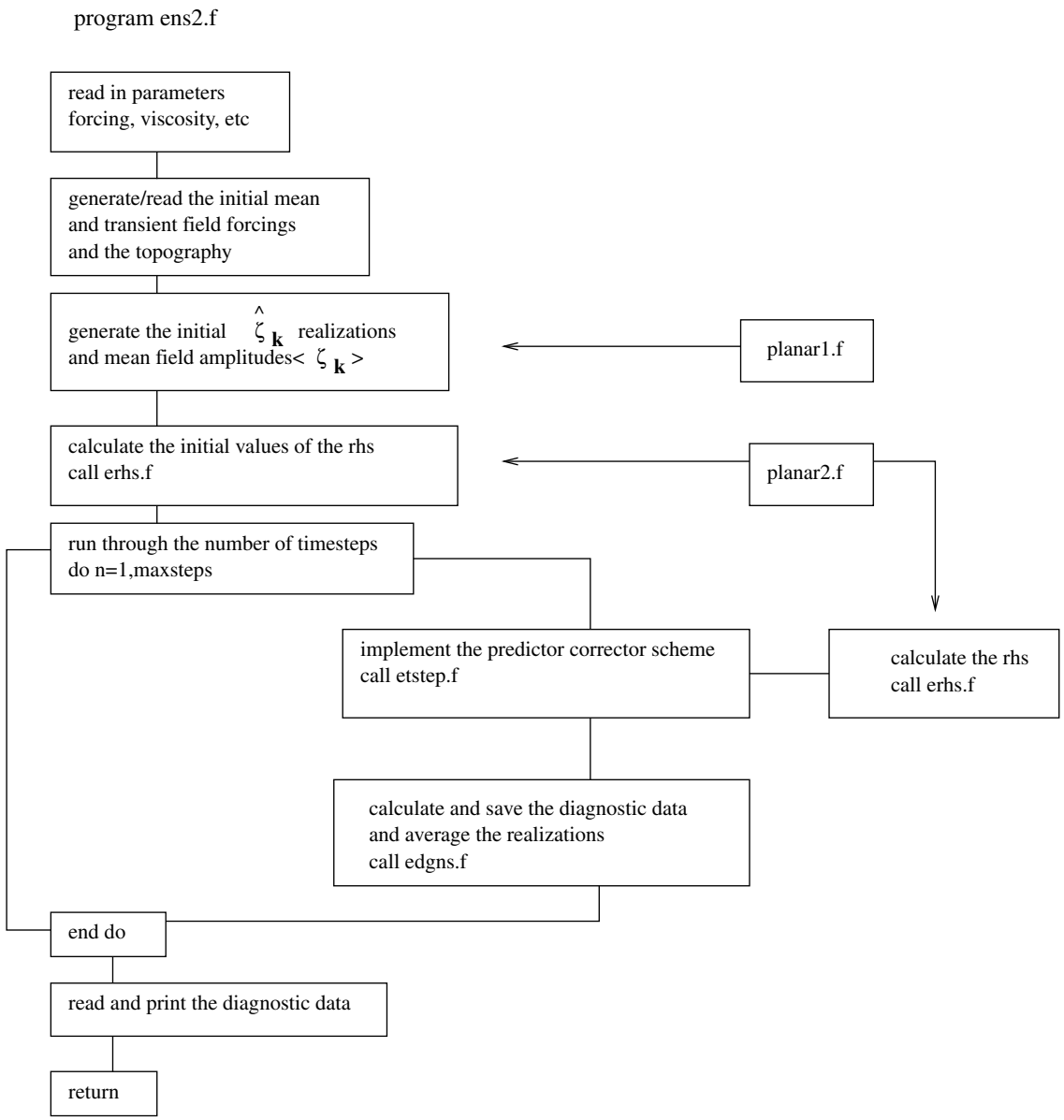

Figure 4.6: Flow diagram of program `ens2.f` for the direct calculation of the spectral form of the barotropic vorticity equation, eqn 3.6.

4.8 Summary

In this chapter the numerical models developed to examine the relative merits of the QDIA inhomogeneous closure equations as compared to DNS have been described. As well the stationarity of initial canonical equilibrium solutions within the closure has been established. In the following chapter the closure and DNS models will be used to investigate both the dynamics and spectra of geophysical flow over topography for a variety of topographies and resolutions from low to medium Reynolds number.

Chapter 5

Numerical experiments

Behold the heaven, the earth, the sea;
all that is bright in them or above them;...
all have form because all have number.
Take away number and they will be nothing...

St Augustine

In this chapter we describe detailed comparisons of the QDIA and CUQDIA closure with DNS for inviscid unforced, viscous decay and forced dissipative flows over a wide variety of topographies and resolutions. First the DNS sampling problem will be described in detail with the specific case of the evolution of a single triad in wavenumber space developed to unambiguously compare the closure to DNS. Next calculations for circular truncation at $k = 3$ (C3) are presented in order to detail the evolution of the modes. This is followed by a comprehensive study of the parameter space at C16 allowing investigation of the performance of the closure in the energy containing range of wavenumbers. The bulk of this chapter concerns studies at resolutions from C16 to C64 at very low, low and moderate Reynolds number. Very low Reynolds number studies allow testing of the accuracy of the closure when strong topographic and mean-field amplitudes are present but without the added complication of strong turbulence effects. The higher Reynolds number studies are then used in order to investigate the presence of spurious convection effects in

the closure transient-field at the smaller scales. As previously mentioned the use of discrete rather than continuous spectra, discussed below, allows the unambiguous attribution of errors and allows us to avoid the problem of the omission of nonlocal interactions that occurs for logarithmic discretization; however, the computational task required to reach high wavenumbers is significantly increased [109, 81, 84]. We follow the approach of Frederiksen, Davies and Bell [104] and formulate the closure and DNS on the doubly periodic domain so that comparison of the closures to DNS means that any differences are solely due to systematic errors in the closures. Thus we avoid any ambiguity arising from different formulations between discrete and continuous spectra. Also Herring and McWilliams [110] found that when the large scales contain an appreciable amount of energy the differences between discrete DNS integrations and continuous closures may be significant.

Before proceeding with the numerical comparison of the closure to DNS, and in order to provide some context for the numerical experiments contained in this chapter, let us first undertake a more detailed discussion of the two most important previous studies in this area. In chapter 3 we briefly discussed the studies of Herring [93] and Holloway [101]. As these works motivate this current study let us consider each in more detail. As stated previously, Holloway's free decay closure employed a modified test-field model where the decorrelation time, θ, of the triplet moment is given approximately as

$$(3\theta_{\mathbf{kpq}})^{-2} \backsimeq \nu_{\mathbf{k}}\mu(k) + \int_0^k Z(p)dp + \int_0^k p^2 H(p)dp - \int_0^k (1 - \frac{p^2}{k^2})R(p)dp \qquad (5.1)$$

for $k \gtrsim k_0$. As usual $\nu_{\mathbf{k}}$ is the linear viscosity with $\mu(k)$ the deformation rate; the strain rate at k due to larger eddies is described via the term containing the single-time second moments of the vorticity $Z(k)$. The term containing the topographic variance $H(k)$ gives the decorrelation effect of topographic Rossby waves, while the final term describes the reduction in wavelike restoring forces, which occur when the flow lies near the contours of constant potential enstrophy, via the vorticity-topography correlation $R(k)$ (note this is not the response function of previous chapters).

Holloway's disequilibrium theory resulted in a pair of equations for the coupled evolution of $Z_{\mathbf{k}}(t) = \langle \zeta_{\mathbf{k}}(t)\zeta_{-\mathbf{k}}(t)\rangle$, $R_{\mathbf{k}}(t) = \langle \zeta_{\mathbf{k}}(t)h_{-\mathbf{k}}\rangle$ and $H(k) = \langle h_{\mathbf{k}}h_{-\mathbf{k}}\rangle$, ie.,

$$(\frac{\partial}{\partial t} + 2\nu_{\mathbf{k}})\langle \zeta_{\mathbf{k}}\zeta_{-\mathbf{k}}\rangle = F_{\mathbf{k}} - 2\eta_{\mathbf{k}}\langle \zeta_{\mathbf{k}}\zeta_{-\mathbf{k}}\rangle + 2\sigma_{\mathbf{k}}\langle \zeta_{\mathbf{k}}h_{-\mathbf{k}}\rangle \tag{5.2}$$

$$(\frac{\partial}{\partial t} + 2\nu_{\mathbf{k}})\langle \zeta_{\mathbf{k}}h_{-\mathbf{k}}\rangle = -\eta_{\mathbf{k}}\langle \zeta_{\mathbf{k}}h_{-\mathbf{k}}\rangle + \sigma_{\mathbf{k}}\langle h_{\mathbf{k}}h_{-\mathbf{k}}\rangle \tag{5.3}$$

where $F_{\mathbf{k}}$, $\eta_{\mathbf{k}}$ and $\sigma_{\mathbf{k}}$ include any external forcings and involve expressions for the weighted sums over spectra of ζ and h.

Holloway considered ensembles of random topography with zero mean value as well as ensemble averages over realizations of the flow. As seen in Eqs. 5.2 and 5.3 this approach results in a closure with approximately the same level of complexity as that for homogeneous turbulence. Holloway compared the total vorticity variance Z and the vorticity-topography correlation R to numerical simulations of geostrophic eddies for a variety of topographic interactions and dissipative mechanisms, as well as differing strengths of eddy-fields. The theory also predicts spectra of variance $\overline{Z}(k)$ for the steady part of the flow field, however this was not compared to DNS. The squared topographies considered by Holloway were of the form $k^2/(1+k^3)$, $k^2/(1+k^4)$ and $k^3e^{-2/3k}$, with an initial vorticity variance of the form k^5e^{-k}.

Although overall quantitative agreement was found, the Holloway closure tended to underpredict vorticity variance $Z(k)$ in higher wavenumbers, an effect ascribed to the choice of the triad interaction time, θ, chosen so that realizable statistics were observed. As well there was an underprediction of the correlation $R(k)$ at small wavenumbers which was unexplained. Holloway [14] subsequently extended this theory to incorporate large-scale zonal flow and the β-effect in order to investigate topographic stress on large-scale mean flows.

Herring [93] studied the complimentary problem of two-dimensional rotating turbulent flow above random topography driven by stationary random forcing. Using an extended non-Markovian test-field model Herring undertook a qualitative look at the influence of topography on the statistics of the flow and also investigated a static component in the energy spectrum of stationary turbulence induced by topographic effects. Two topographic spectra were employed with amplitudes squared of $H_0/(1 + k^4)$ and $H_0k/(1 + k^3)$ for

resolution $0 \leqslant k \leqslant 64$. In his study the extended-TFM was compared to the standard DIA, finding qualitative agreement. These idealized problems were crucial to the development of an understanding of the manner by which random topography determines the spectra of transient vorticity variance and hold a central place in homogeneous closure theory. In order that the effect of the mean topography on the structures of the mean flows be examined single realization topography is required and that is the focus of the numerical studies that follow.

5.1 The sampling problem for DNS

As we can specify exactly the initial state of the mean and transient fields in the CUQDIA experiment we must also have corresponding initial fields for the DNS. The simplest non-trivial case that we will consider is that where the initial-transient field is nonzero and the initial mean-field is zero. In the presence of topography the generated mean-field arises due to the interaction of the field with the topography. For such initial conditions an exact calculation requires that the system must satisfy homogeneity in the first instance, which in turn requires a specific number of realizations with specific symmetry properties in the discrete case.

Consider the homogeneous case in the absence of topography:

$$\langle \zeta_{-\mathbf{p}} \zeta_{-\mathbf{q}} \rangle = \delta_{\mathbf{p},\mathbf{q}} \langle \zeta_{\mathbf{p}} \zeta_{-\mathbf{p}} \rangle \tag{5.4}$$

therefore

$$\frac{d}{dt}\langle \zeta_{\mathbf{k}} \rangle = \sum_{\mathbf{p}} \sum_{\mathbf{q}} \delta(\mathbf{k}+\mathbf{p}+\mathbf{q}) K(\mathbf{k},\mathbf{p},\mathbf{q}) \langle \zeta_{-\mathbf{p}} \zeta_{-\mathbf{q}} \rangle = 0. \tag{5.5}$$

The homogeneous field requires the satisfaction of reflection symmetries for both real and imaginary components (as well as conjugacy). Consider a 2-component field comprising $\zeta_{\mathbf{p}}$ and $\zeta_{\mathbf{q}}$. In order to satisfy the reflection symmetries we require 4 symmetries for each component, that is $(1, i, -1, -i)\zeta_{\mathbf{p}}$ and $(1, i, -1, -i)\zeta_{\mathbf{q}}$, so that the field must be averaged

over 16 realizations if the ensemble average is to vanish exactly. Thus

$$\begin{aligned}\langle\zeta_{\mathbf{p}}\zeta_{\mathbf{q}}\rangle = \\ \frac{1}{16}[\zeta_{\mathbf{p}}\zeta_{\mathbf{q}} + i\zeta_{\mathbf{p}}\zeta_{\mathbf{q}} - \zeta_{\mathbf{p}}\zeta_{\mathbf{q}} - i\zeta_{\mathbf{p}}\zeta_{\mathbf{q}} \\ +\zeta_{\mathbf{p}}i\zeta_{\mathbf{q}} + i\zeta_{\mathbf{p}}i\zeta_{\mathbf{q}} - \zeta_{\mathbf{p}}i\zeta_{\mathbf{q}} - i\zeta_{\mathbf{p}}i\zeta_{\mathbf{q}} \\ -\zeta_{\mathbf{p}}\zeta_{\mathbf{q}} + i\zeta_{\mathbf{p}}(-i)\zeta_{\mathbf{q}} + (-1)\zeta_{\mathbf{p}}(-1)\zeta_{\mathbf{q}} + (-i)\zeta_{\mathbf{p}}(-1)\zeta_{\mathbf{q}} \\ +\zeta_{\mathbf{p}}(-i)\zeta_{\mathbf{q}} + i\zeta_{\mathbf{p}}(-i)\zeta_{\mathbf{q}} + (-1)\zeta_{\mathbf{p}}(-i)\zeta_{\mathbf{q}} + (-i)\zeta_{\mathbf{p}}(-i)\zeta_{\mathbf{q}}] \\ = 0 \end{aligned} \tag{5.6}$$

It is then easy to see that the total number of realizations needed to generate a truly homogeneous field is 4 *to the power of the number points in the domain of wavenumbers.* Therefore for $k = 3$ and circular truncation there are 28 parameters so we require an ensemble of 4^{28} realizations. We can however halve the number of points in wavenumber space by running over the half space and employing conjugacy to map to the rest of the field, thus halving the number of interaction coefficients and dramatically reducing the required number of realizations to $4^{14} = 268,435,456$. Unfortunately 4^{14} represents an insurmountable computational challenge. An alternate is to consider $k = 2$ with a requirement of 4096 realizations. $k = 2$ unfortunately has no nontrivial interactions [111] which is immediately evident from the interaction coefficients which only have two nonzero components of equal magnitude but opposite sign for any given triad.

In order to rigorously test our model we finally chose to run a single triad calculation requiring 4^3 realizations, to compare the CUQDIA to DNS. We note that alternate strategies to the sampling problem are required for higher resolution studies and these are addressed in subsequent sections.

5.2 Triad calculation

Figure 5.2 describes the evolution of the absolute mean $\langle\zeta_{\mathbf{k}}(t)\rangle\langle\zeta_{-\mathbf{k}}(t)\rangle$ and transient $\langle\hat{\zeta}_{\mathbf{k}}(t)\hat{\zeta}_{-\mathbf{k}}(t)\rangle$ fields for a single triad (see Fig. 5.1 and table 5.1) for a forced viscid calculation. Rather than use the more general form of the viscosity, $\nu_0(k)k^2$, as employed in the theoretical development, instead the form of the viscosity used in all numeric studies

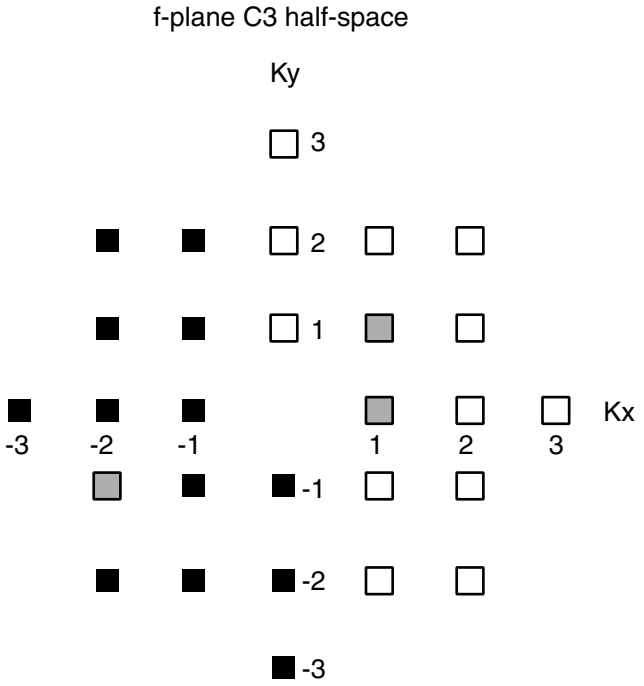

truncation	interaction coefficients	total points
C3	180 x 5 sets	14
C16	183384 x 5 sets	398
C64	48383760 x 5 sets	12852

Figure 5.1: Diagram depicting circular truncation of k=3 wavenumber space and separation into halfspace partitions (black and white). Grey denotes the triad used in the calculations depicted in Figs. 5.2, and 5.3.

will be $\nu_0(k) = \hat{\nu}$, where $\hat{\nu}$ is the nondimensional viscosity. The initial fields are chosen such that $\langle \zeta_{\mathbf{k}}(t_0) \rangle = 0$. This choice of initial conditions allows the explicit construction of a homogeneous initial field $\zeta_{\mathbf{k}}$. For a single triad 64 realizations (4^3) are needed with the symmetry properties specified in section 5.1. The system was forced from an initial nonequilibrium state, in which most of the enstrophy was contained in the $\zeta_{(-2,-1)}$ mode, toward the canonical equilibrium state via forcings given in table 5.2. It is quite evident from Fig. 5.2 that the modes of the respective fields appear to behave in a similar manner for both DNS and CUQDIA. Figure 5.3 shows clearly that this is indeed the case, including in the early period of the evolution from timesteps 0-50, where one might reasonably expect to see some deviation. As well the CUQDIA closely matches with the time averaged DNS results from timesteps 160-320. The obvious difference between the DNS and closure triad calculations arise due to the sampling of the forcing. The strong stochastic noise in the DNS can be eliminated via a time average, as evident in Fig. 5.3, although it should also be possible to eliminate these fluctuations by choosing the random forcings to obey similar relationships to the initial conditions.

Table 5.1: Triad calculation initial conditions.

$C_{(1,0)}$	$C_{(1,1)}$	$C_{(-2,-1)}$	total
1.9634E-7	3.7424E-7	2.6722E-4	2.6779E-4
$\langle \zeta_{k_{(1,0)}} \rangle$	$\langle \zeta_{k_{(1,1)}} \rangle$	$\langle \zeta_{k_{(-2,-1)}} \rangle$	total
0.0	0.0	0.0	0.0

Table 5.2: Triad calculation parameters.

$\triangle$ t	$\hat{\nu}$	a	b	$\lvert h_{\mathbf{k}} \rvert^2$	$F_{\mathbf{k}}$	$\langle f_{\mathbf{k}} \rangle$
1.1136	1.8579E-2	-5.969E+5	7.444E+5	$\frac{a+bk^2}{k^2b^2}$	$2\hat{\nu}k^2C^{eq}_{\mathbf{k}}$	$-\frac{1}{2}bh_{\mathbf{k}}F_{\mathbf{k}}$

The purpose of the triad calculation was not so much to undertake a rigorous comparison of DNS to closure, although the comparison is favorable, but rather to show the origin of the DNS sampling error and demonstrate one approach that can be taken in

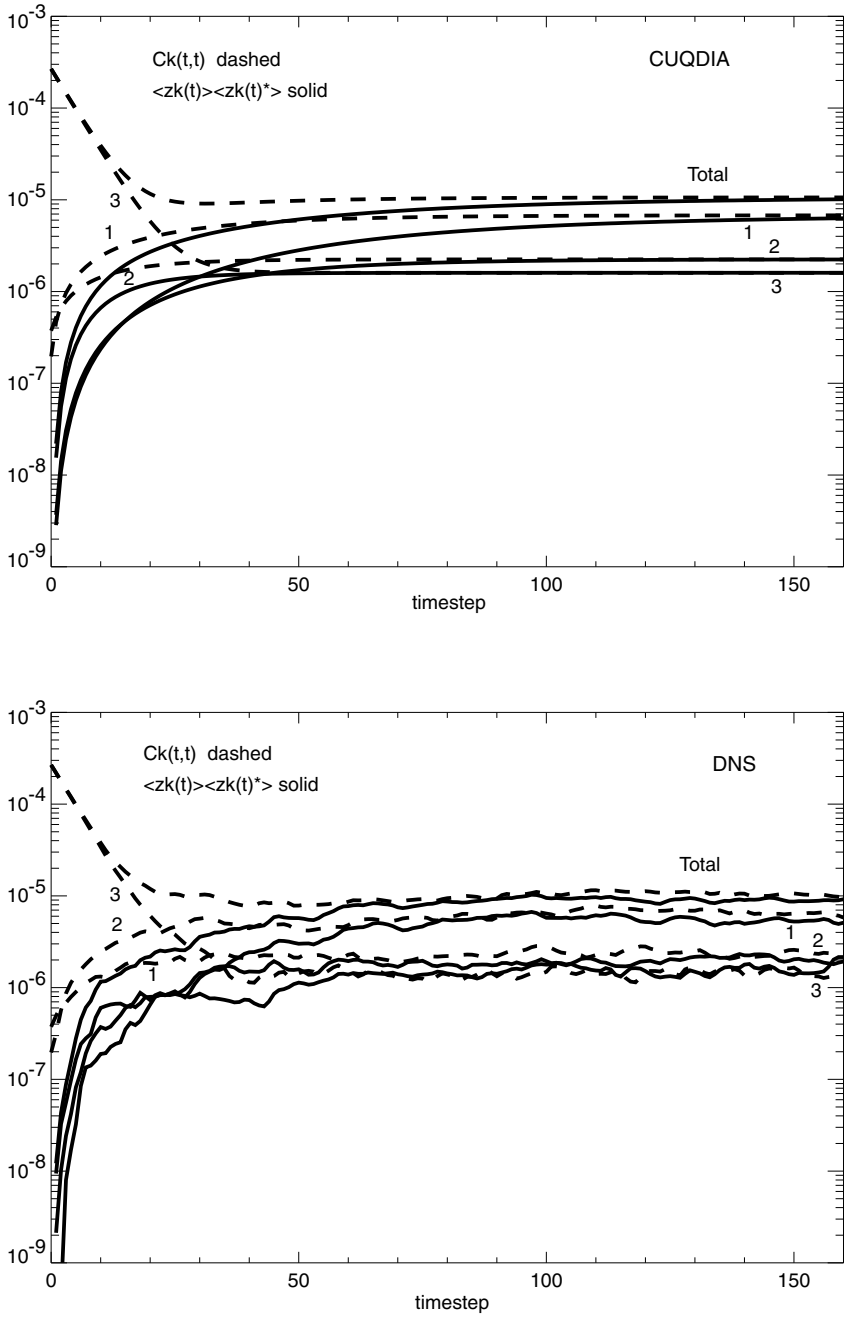

Figure 5.2: The evolution of the mean (solid) and transient (dashed) twice enstrophies for a single triad with forcing and dissipation are depicted for the CUQDIA closure (top). The results shown are for an initially zero mean field with topography chosen such that at equilibrium the mean and transient fields are of equal magnitude. Results represent an ensemble average of 64 realizations where the ensemble is initially homogeneous. The CUQDIA results are with cumulant updates every 10 timesteps. (bottom) The DNS results are displayed for the same parameters and initial conditions. Parameters are given in tables 5.1 and 5.2.

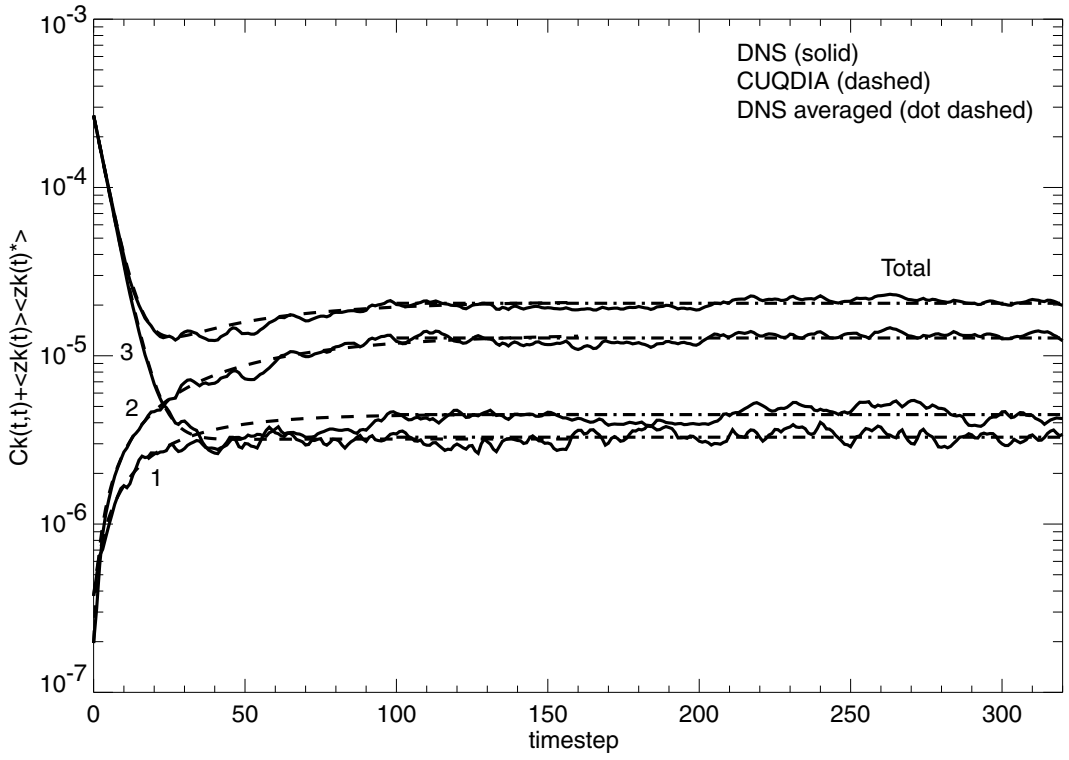

Figure 5.3: Total fields for DNS and CUQDIA: The total fields for both CUQDIA (dashed) and DNS (solid) are compared with a time average of the DNS (dot dashed) taken after stable behavior (equilibrium) has been attained. A time average of the modes from timesteps 160-320, is then taken in order to average out the stochastic noise due to strong random forcing. The CUQDIA results are shown to be in excellent agreement with the time average.

order to eliminate it. As noted this involves the explicit construction of the initial DNS field at a resolution where it is reasonable to do so. In the following section we examine the evolution of the closure modes in more detail for inviscid, viscous decay and forced dissipative cases at C3 resolution.

5.3 C3 experiments

In this section we examine the dynamics of the CUQDIA and QDIA closure compared to DNS at resolution C3. As Kells and Orszag [111] noted C3 has sufficient degrees of freedom such that the systems are mixing. Table 5.3 shows the initial transient (twice) enstrophies $C_{\mathbf{k}}(0,0)$ and mean (twice) enstrophies $\langle\zeta_{\mathbf{k}}(0)\rangle\langle\zeta_{-\mathbf{k}}(0)\rangle$ hereafter refered to as the transient and mean field enstrophies. At C3 resolution the system has 28 components with degeneracy (the number of system components with the same enstrophy) given in table 5.5. The labels given to the components in table 5.5 refer to Figs. 5.5 (bottom) and 5.7. The nondimensional DNS and closure equations have been scaled by typical meteorological time and space scales, namely, a length scale of half the earth's radius, $3.185610 \times 10^6 m$, and a time scale of $(\sqrt{2}\Omega)^{-1}$ where $\Omega = 7.292 \times 10^{-5} s^{-1}$ is the earth's angular velocity. Throughout, the closure equations are initialized using Gaussian initial conditions. The cumulant update procedure uses the non-Gaussian terms which build up with time in the new initial conditions for subsequent restarts steps as detailed in sections 3.4 and 3.5. All C3 DNS calculations represent an ensemble average over 5000 realizations with the real and imaginary parts of $\zeta_{\mathbf{k}}(0)$ having a joint Gaussian distribution.

Table 5.3: Initial conditions for C3 calculations.

$C_{(1,0)}$	$C_{(2,0)}$	$C_{(3,0)}$	$C_{(1,-2)}$	$C_{(1,-1)}$	$C_{(2,-2)}$	total
1.9634E-7	6.8372E-7	1.2664E-6	2.6716E-4	3.7414E-7	1.1677E-6	2.1523E-3
$\langle\zeta\rangle\langle\zeta^*\rangle_{(1,0)}$	$\langle\zeta\rangle\langle\zeta^*\rangle_{(2,0)}$	$\langle\zeta\rangle\langle\zeta^*\rangle_{(3,0)}$	$\langle\zeta\rangle\langle\zeta^*\rangle_{(1,-2)}$	$\langle\zeta\rangle\langle\zeta^*\rangle_{(1,-1)}$	$\langle\zeta\rangle\langle\zeta^*\rangle_{(2,-2)}$	total
1.1663E-11	4.5713E-10	8.9954E-10	5.4295E-8	1.0050E-10	7.8884E-12	2.6094E-7

Table 5.4: Figure 5.4, 5.5 and 5.6 parameters.

$\triangle$ t	$\hat{\nu}$	a	b	$\lvert h_{\mathbf{k}}\rvert^2$	$F_{\mathbf{k}}$	$\langle f_{\mathbf{k}}\rangle$
2.2272	1.8579E-2	-5.969E+5	7.444E+5	$\frac{a+bk^2}{k^2b^2}$	$2\hat{\nu}k^2C^{eq}_{\mathbf{k}}$	$-b\hat{\nu}k^2h_{\mathbf{k}}C^{eq}_{\mathbf{k}}$

Table 5.5: $\zeta(k_x,k_y)^{label}_{degeneracy}$

$\zeta(1,0)^1_4$	$\zeta(2,0)^2_4$	$\zeta(3,0)^3_4$	$\zeta(1,-2)^4_8$	$\zeta(1,-1)^5_4$	$\zeta(2,-2)^6_4$

Table 5.6: C3 inviscid unforced parameters.

$\triangle$ t	$\hat{\nu}$	a	b	$\lvert h_{\mathbf{k}}\rvert^2$	$F_{\mathbf{k}}$	$\langle f_{\mathbf{k}}\rangle$
8.9088	0	-5.969E+5	7.444E+5	$\frac{a+bk^2}{k^2b^2}$	0	0

Table 5.7: C3 viscid unforced parameters.

$\triangle$ t	$\hat{\nu}$	a	b	$\lvert h_{\mathbf{k}}\rvert^2$	$F_{\mathbf{k}}$	$\langle f_{\mathbf{k}}\rangle$
2.2272	1.8579E-4	-5.969E+5	7.444E+5	$\frac{a+bk^2}{k^2b^2}$	0	0

The first case we consider is for forced dissipative flow. The random forcing is determined by

$$F_{\mathbf{k}} = 2\hat{\nu}k^2C^{eq}_{\mathbf{k}} \tag{5.7}$$

with the mean forcing determined by

$$\langle f_{\mathbf{k}}\rangle = \hat{\nu}k^2\langle\zeta^{eq}_{\mathbf{k}}\rangle = -\frac{1}{2}bh_{\mathbf{k}}F_{\mathbf{k}} \tag{5.8}$$

such that the system is forced to canonical equilibrium, as was done in the triad calculation. The nondimensional viscosity used is 1.8579×10^{-2}. A comparison of the early evolution of the fields between DNS and CUQDIA is given in Fig. 5.4 in which two particular initialization schemes are considered as follows. The first (top) is for the particular case

where the initial CUQDIA fields are exact so that the slight initial differences between the closure and DNS mean fields are a result of the DNS sampling error [1], specifically in the earliest period (0-15 timesteps) when the mean field is being generated via eddy-topography interactions. Figure 5.4 (bottom) shows the same case now with the closure initialized with the sampled DNS fields. We are now able to observe very close agreement in even the earliest time periods. In Fig. 5.5 we show the dynamics over a 20 day period for both the mean and transient (twice) enstrophy components (top) and the total (twice) enstrophies (bottom) (1 day has a nondimensional value equal to 8.9088). Close agreement is shown at all time periods as the system evolves from a nonequilibrium state toward canonical equilibrium under the effects of forcing and viscosity. A comparison of the QDIA and CUQDIA (Fig. 5.6) with the CUQDIA employing restarts at every 20 timesteps shows close agreement. The QDIA and CUQDIA results have not been superimposed as the agreement is very close (up to 6 significant figures). The CUQDIA was found to dramatically reduce computation times. We also note that an ensemble average of 5000 realizations in the DNS calculation cannot ensure isotropy in the 28 components of the C3 truncation resulting in a maximum relative error in the twice enstrophies of approximately 3 percent [104].

The closures were found to perform very well when both forcing and dissipation are present. However, a more stringent test is to consider the performance of the closure for inviscid unforced or purely viscid flows. These cases are considered in Fig. 5.7 with parameters given in tables 5.6 and 5.7. The inviscid unforced calculation, Fig. 5.7 (top), is again started with the same disequilibrium state as that used in the viscid forced calculations and is evolved over an 80 day period with timesteps of 1 day. The closure calculation is without cumulant updates (QDIA), in order that the dynamics may be compared directly to the DNS without the possibility of information being lost at the restart step. The closure clearly captures the initial growth and decay phase of the total twice enstrophies. This is also the period in which the mean field is being generated (0-20 days). The erroneous oscillations evident between days 20 and 40 are very similar to those reported in the study of closure theories for severely truncated two-dimensional homogeneous turbulence with-

[1] For 5000 realizations the DNS sampling error is approximately at the level of 0.01 percent

out mean-fields or topography by Frederiksen, Davies and Bell [104]. These oscillations result in the QDIA under-predicting the crossover time for the decaying twice enstrophy component (1,-2) and the two strongest increasing twice enstrophy components (3,0) and (2,-2). In general it was found that the QDIA oscillations were somewhat reduced in amplitude relative to those present in the DIA indicating that the presence of topography, and consequently a mean-field, acts to damp erroneous oscillations observed in the dynamics of the eddies. Since such oscillations are a feature of the DIA it is reasonable to assume that they arise due to the treatment of the triple cumulant term. The viscid calculation in Fig. 5.7 (bottom), was run with a reduced timestep (1/4 days) in order to ensure stability and displays similar dynamics to the inviscid unforced experiment. Both cases are in close agreement with DNS in the early (0-15 days) and later (40-80 days) periods with most divergence due to the oscillatory phase in the closure occurring between 15 and 40 days.

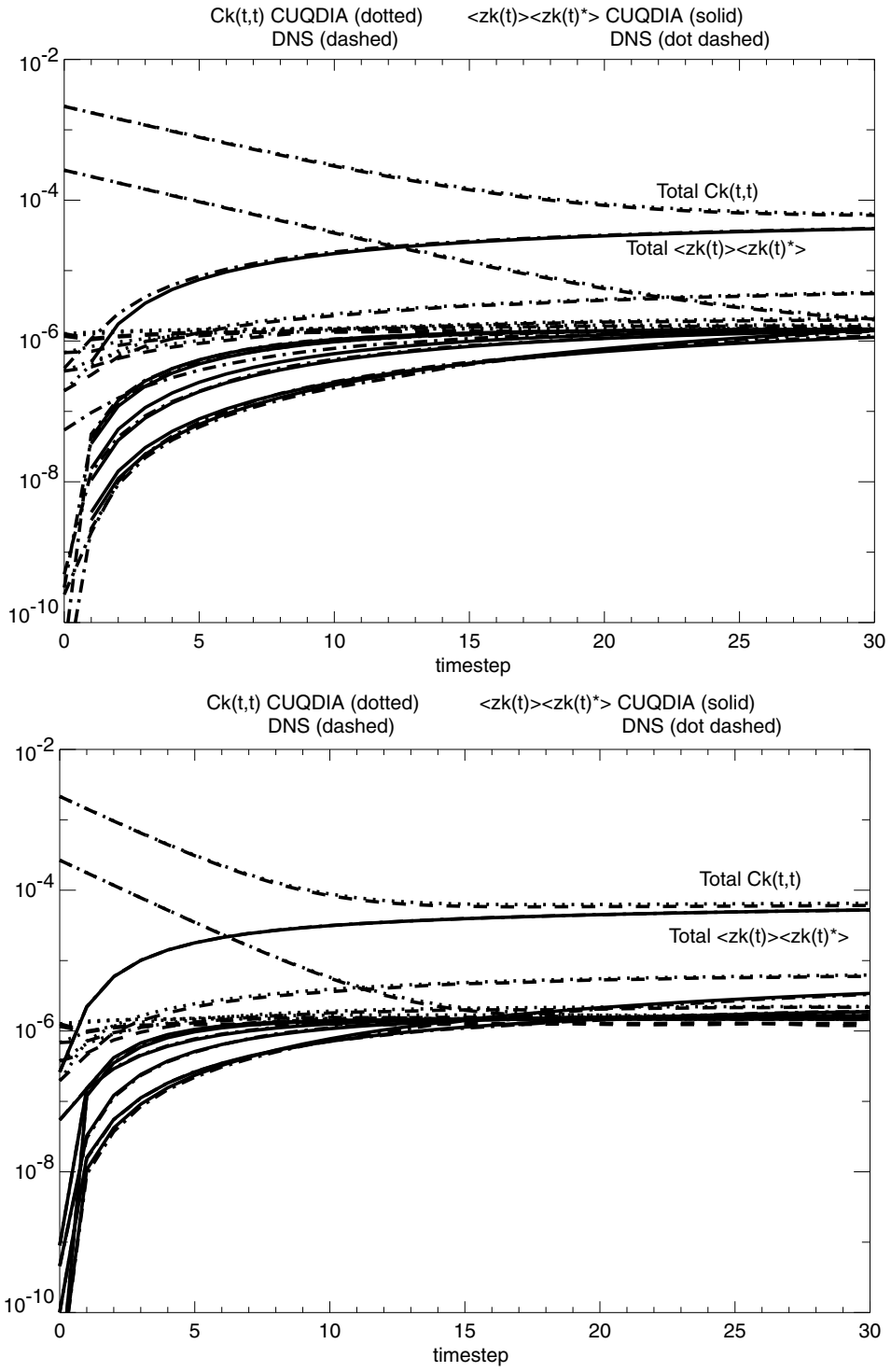

Figure 5.4: (top) Detailed comparison of the early evolution of the fields corresponding to the regime where the transients dominate. The error in the DNS mean field arising from an inexact initial homogeneous field are obvious. The initial DNS field is given in table 5.3 with the relevant parameters are found in table 5.4. (bottom) Comparison of the early evolution of the fields where the CUQDIA fields are initialized with the generated DNS fields.

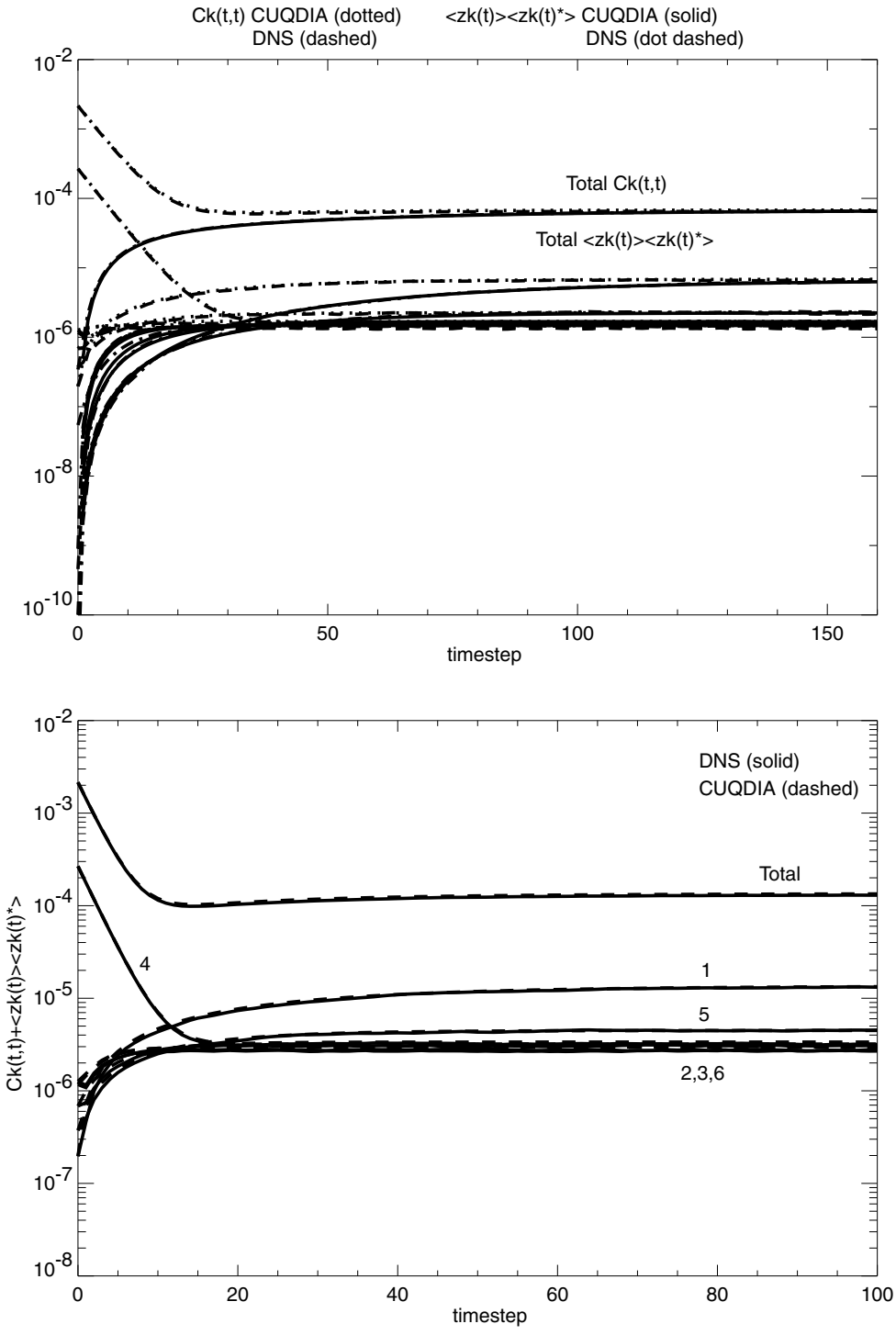

Figure 5.5: (top) Evolution over 20 days with parameters as for Fig. 5.4. (bottom) Comparison of C3 results for the CUQDIA and QDIA calculations for the viscid forced case considered in the preceding Fig. 5.4. The CUQDIA employs restarts at every 20 timesteps demonstrating excellent agreement with the QDIA results.

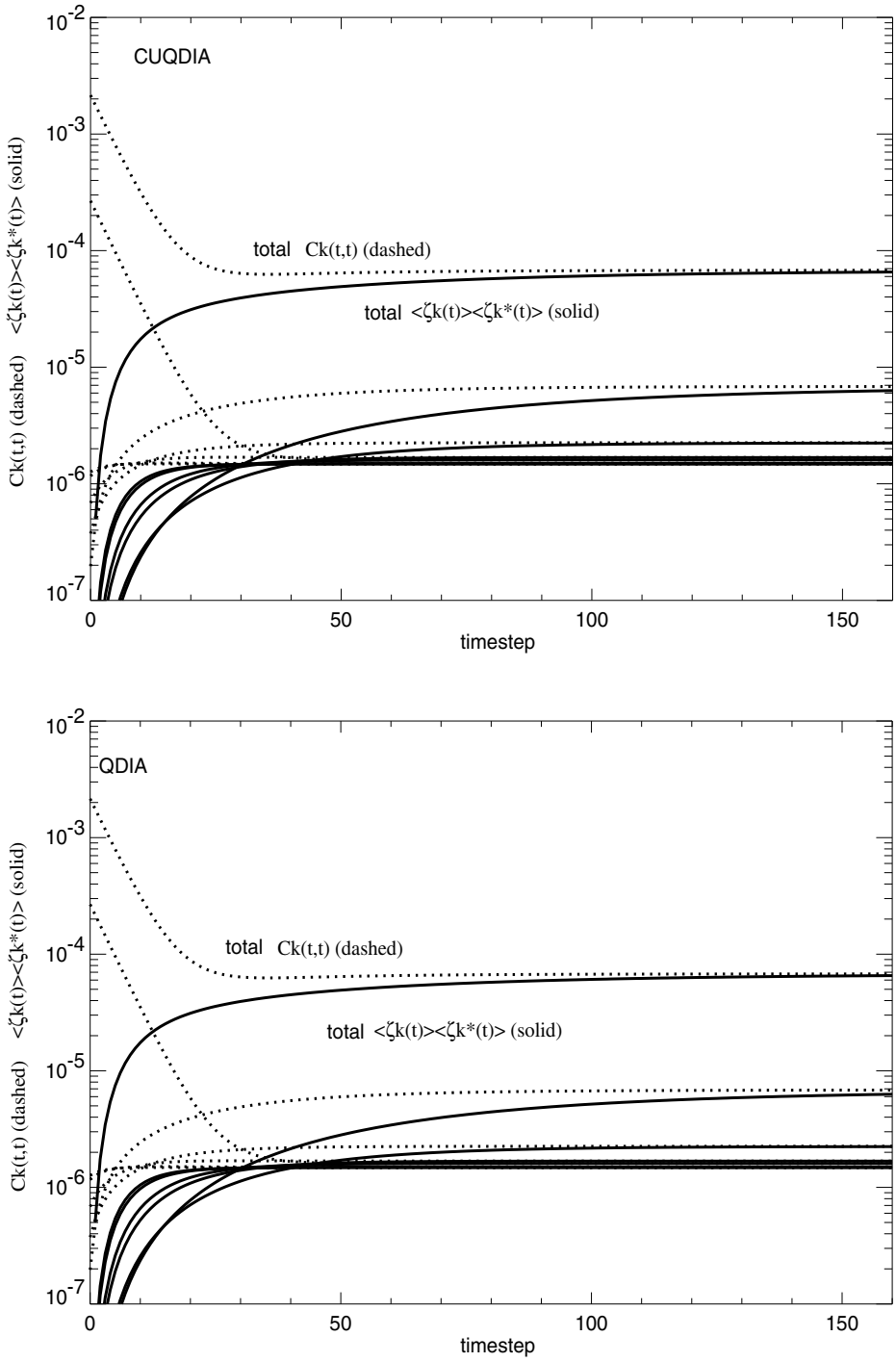

Figure 5.6: Comparison of C3 results for the CUQDIA and QDIA calculations for the viscid forced case considered in the preceding Figs. 5.4 and 5.5. The CUQDIA employs restarts at every 20 timesteps demonstrating excellent agreement with the QDIA results.

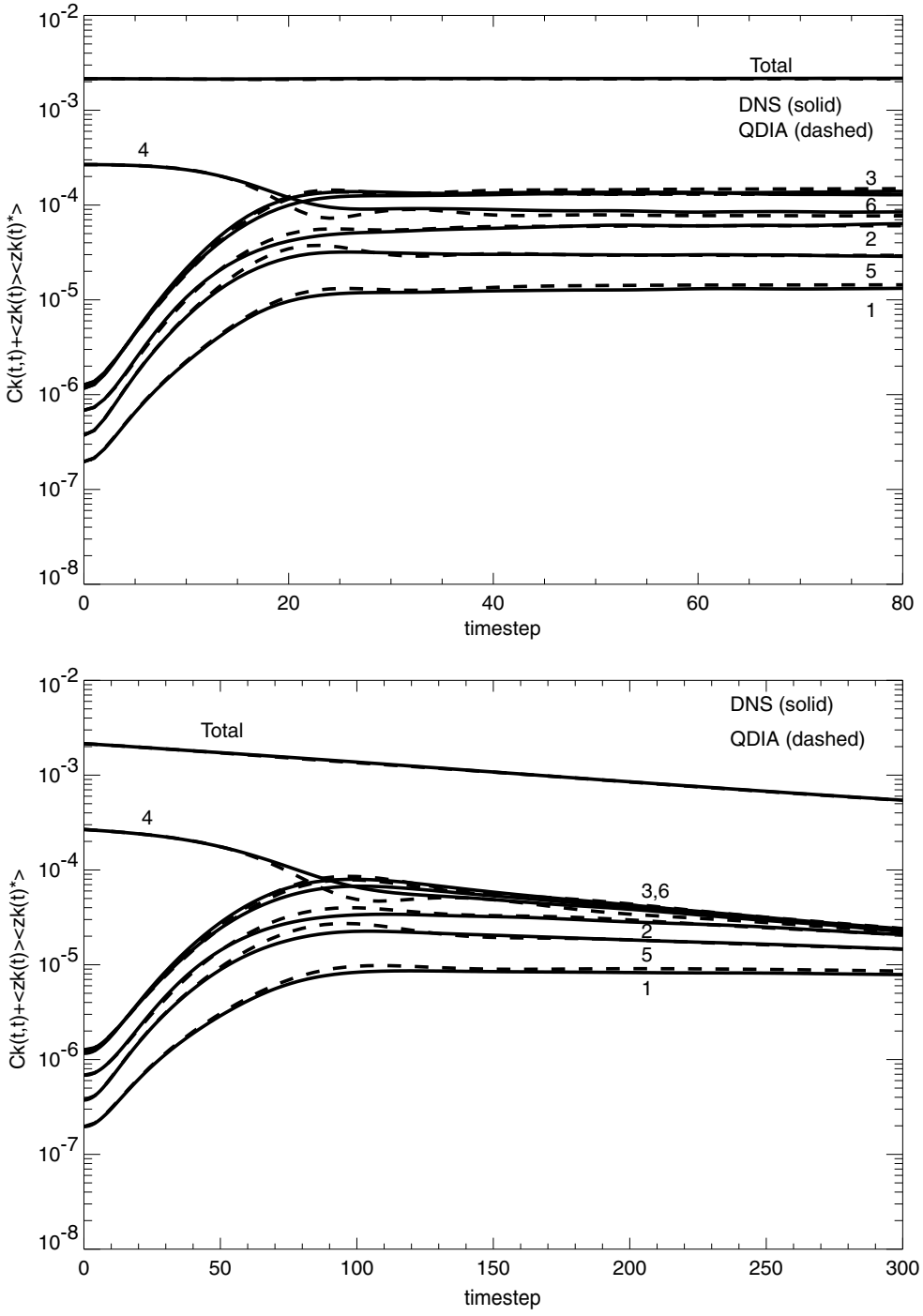

Figure 5.7: (top) Comparison of the total fields for DNS and QDIA in the absence of forcing and viscosity. Parameters are given in table 5.6. (bottom) Comparison of the total fields for DNS and QDIA for the viscid case with parameters as for tables 5.3 and 5.7.

5.4 C16 experiments

In this section a comprehensive study of CUQDIA and DNS results for a variety of topographies are considered for inviscid unforced, viscous decay and forced dissipative cases. The form of the topographies studied are similar to those considered by Herring [93] and Holloway [101], namely

$$|h_{\mathbf{k}}|^2 = \frac{4}{1+k^4}, \frac{4}{1+k^3}, \frac{4k}{1+k^3}, \frac{4k^2}{1+k^3}. \tag{5.9}$$

The difference between the studies presented in this thesis and the previous studies of Herring [93] and Holloway [101] is that whereas they employed ensemble averaging over different realizations of the topography this current study utilizes a mean or single realization topography. In this section single realization random topographies are used where $h_{\mathbf{k}}$ is defined as

$$h_{\mathbf{k}} = |h_{\mathbf{k}}| \times (\cos\phi + i\sin\phi) \tag{5.10}$$

with ϕ the random argument. Various types of random phases have been investigated with no significant quantitative differences found. As well the topography studied previously for the C3 and the triad cases, namely $|h_{\mathbf{k}}|^2 = \frac{a+bk^2}{k^2b^2}$, is included. A variety of initial conditions are also investigated including viscous decay from an initial canonical equilibrium state, inviscid unforced evolution from an initial disequilibrium state and, forced dissipative evolution to canonical equilibrium in which the initial mean-field is zero and the evolved mean field is "spun up" as a result of the interaction of the topography with the transient-field. These low-resolution studies form a basis for a more rigorous study of the effects of topography, resolution and Reynolds number on the evolution of the spectra of the mean and transient fields presented in sections 5.5 and 5.6.

Prognostic DNS and CUQDIA equations are analyzed via the following diagnostics for the i) kinetic energy

$$E(t) = \frac{1}{2}\sum_{\mathbf{k}} \left[C_{\mathbf{k}}(t,t) + \langle\zeta_{\mathbf{k}}(t)\rangle\langle\zeta_{-\mathbf{k}}(t)\rangle\right]/k^2, \tag{5.11}$$

ii) potential enstrophy

$$Q(t) = \frac{1}{2}\left[\sum_{\mathbf{k}} C_{\mathbf{k}}(t,t) + \sum_{\mathbf{k}}(\langle\zeta_{\mathbf{k}}(t)\rangle + h_{\mathbf{k}})(\langle\zeta_{-\mathbf{k}}(t)\rangle + h_{-\mathbf{k}})\right], \tag{5.12}$$

iii) enstrophy

$$F(t) = \frac{1}{2}\left[\sum_{\mathbf{k}} C_{\mathbf{k}}(t,t) + \sum_{\mathbf{k}} \langle\zeta_{\mathbf{k}}(t)\rangle\langle\zeta_{-\mathbf{k}}(t)\rangle\right], \tag{5.13}$$

and iv) palinstrophy

$$P(t) = \frac{1}{2}\sum_{\mathbf{k}} \left[C_{\mathbf{k}}(t,t) + \langle\zeta_{\mathbf{k}}(t)\rangle\langle\zeta_{-\mathbf{k}}(t)\rangle\right] k^2. \tag{5.14}$$

These diagnostic terms are used to calculate band averaged spectra defined as

$$\begin{aligned} E(k_i,t) &= \frac{1}{2}\sum_{\mathbf{k}\in S} \left[C_{\mathbf{k}}(t,t) + \langle\zeta_{\mathbf{k}}(t)\rangle\langle\zeta_{-\mathbf{k}}(t)\rangle\right]/k^2, \\ Q(k_i,t) &= \frac{1}{2}\left[\sum_{\mathbf{k}\in S} C_{\mathbf{k}}(t,t) + \sum_{\mathbf{k}\in S} (\langle\zeta_{\mathbf{k}}(t)\rangle + h_{\mathbf{k}})(\langle\zeta_{-\mathbf{k}}(t)\rangle + h_{-\mathbf{k}})\right], \\ F(k_i,t) &= \frac{1}{2}\left[\sum_{\mathbf{k}\in S} C_{\mathbf{k}}(t,t) + \sum_{\mathbf{k}\in S} \langle\zeta_{\mathbf{k}}(t)\rangle\langle\zeta_{-\mathbf{k}}(t)\rangle\right], \\ P(k_i,t) &= \frac{1}{2}\sum_{\mathbf{k}\in S} \left[C_{\mathbf{k}}(t,t) + \langle\zeta_{\mathbf{k}}(t)\rangle\langle\zeta_{-\mathbf{k}}(t)\rangle\right] k^2. \end{aligned} \tag{5.15}$$

The set S is defined as

$$S = \left[\mathbf{k} | k_i = Int.[k + \frac{1}{2}]\right] \tag{5.16}$$

where the subscript i indicates that the integer part is taken in Eq. 5.16 so that all $\mathbf{k}$ that lie within a given radius band of unit width are summed over. Recall that the DNS results are averaged over a large number of realizations in which the initial conditions are sampled from a Gaussian distribution with specified spectrum and specified mean. All DNS results in the remainder of this chapter are an ensemble average of 100 realizations calculated on the CSIRO Cray-YMP (at resolutions C16 to C48) and CSIRO NEC SX-5 (at resolutions C48 to C64) computers. Only the CUQDIA results up to resolutions C16 were performed on the Cray-YMP with the higher resolution experiments requiring the NEC SX-5.

Before detailing the C16 experiments we will briefly outline the approach taken to sampling the initial DNS fields for subsequent calculations at resolutions C16, C48 and C64. Figure 5.8 depicts an initial energy spectrum with a peak at wavenumber $k = 2$. The initial mean field is specified to be zero in both the closure and DNS. However, the fact

that the DNS represents an ensemble average of 100 realizations with zero mean results in the sampling error manifesting as a nonzero DNS mean field. The transient fields show excellent agreement between DNS and closure however the DNS sampling error is at the level of approximately one percent for 100 realizations. The difference in the initial fields can be compensated for by initializing the CUQDIA with the generated DNS initial fields. However, this approach is only valid for cases where the evolving field is above the level of the DNS sampling error. Higher resolution spectral studies with limited number of realizations require a different line of attack. The approach that works is quite simple; if for every DNS field ζ_i we also include its negative $-\zeta_i$ for $\forall i = 1, \ldots N$ (where N is the number of realizations) then the sampling problem can be minimized. This method is employed in all subsequent calculations. In all Figs. detailing spectra the following convention will be followed:

Total field diagrams; DNS (solid lines), CUQDIA (dotted lines), initial fields (dashed lines)

Component field diagrams: mean field; DNS (dashed lines), CUQDIA (dotted lines), :transient field; DNS (solid lines), CUQDIA (dot dashed).

Figures 5.9 and 5.10 show the evolved total kinetic energy and potential enstrophy for inviscid and viscid cases respectively starting from the initial non-equilibrium spectrum given in Fig. 5.8 and with parameters detailed in tables 5.8 and 5.9. As in the previous low resolution studies, the topography was chosen such that at canonical equilibrium the transient and mean fields were of the equal amplitude. This choice of topography is not very realistic as it is almost flat across all scales. However, it does result in a strong topographic amplitude at the smallest scales thereby ensuring a rigorously test of the closure theory. Once again the initial mean-field is zero. As the closures are started from Gaussian initial conditions the initial three-point cumulants are zero. Subsequent cumulant updates are calculated at every 20 timesteps. The large computational resources required to evaluate the closures for discrete spectra meant that only the more efficient CUQDIA and not the QDIA closures were considered.

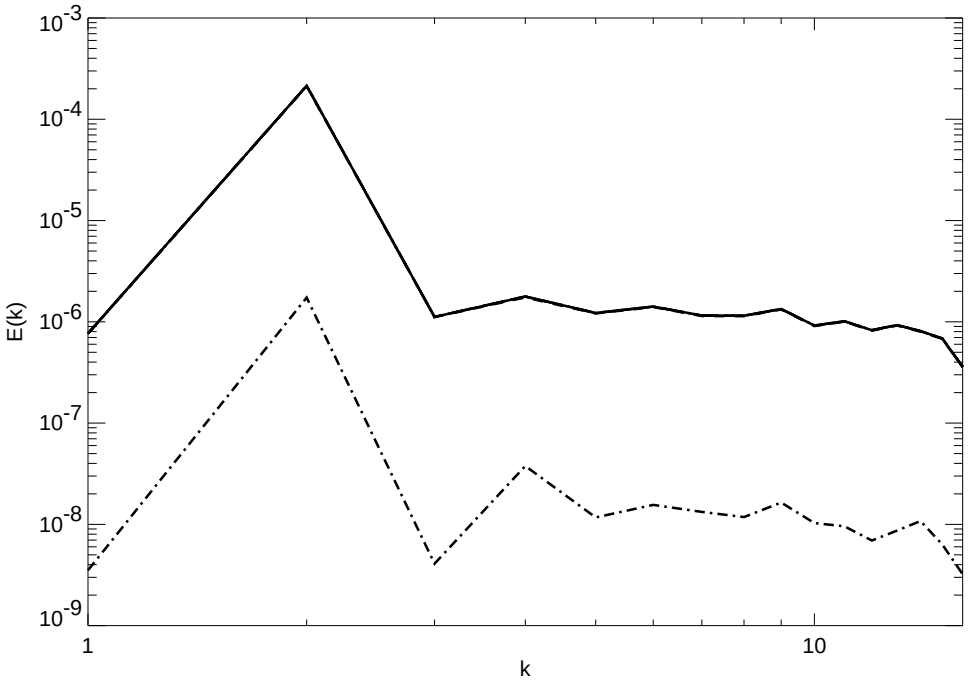

Figure 5.8: The initial energy spectra used in Figs. 5.13 to 5.10 (solid). The (dot dashed) lines represents the initial DNS sampling error when a naive sampling is used rather using positive and negative realizations. The error is approximately 1 percent for 100 realizations.

Table 5.8: C16 parameters for Fig. 5.9.

$\triangle$ t	$\hat{\nu}$	a	b	$\lvert h_{\mathbf{k}}\rvert^2$	$F_{\mathbf{k}}$	$\langle f_{\mathbf{k}} \rangle$
0.11136	0	-5.969E+5	7.444E+5	$\frac{a+bk^2}{k^2b^2}$	0	0

Table 5.9: C16 parameters for Fig. 5.10.

$\triangle$ t	$\hat{\nu}$	a	b	$\lvert h_{\mathbf{k}}\rvert^2$	$F_{\mathbf{k}}$	$\langle f_{\mathbf{k}} \rangle$
0.11136	1.879E-2	-5.969E+5	7.444E+5	$\frac{a+bk^2}{k^2b^2}$	0	0

The CUQDIA and DNS were integrated forward for 300 nondimensional timesteps of $\triangle t = 0.11136$, corresponding to a final time $t = 33.408$, and compared to the statistics of 100 realizations of DNS. The DNS and CUQDIA displayed the same computational stability properties in contrast to the homogeneous CUDIA calculations of Frederiksen and Davies [108] where the closure allowed a far larger time step and was shown to be more stable than DNS. However, the relative stability of the CUQDIA was found to improve as resolution was increased. The total energy and potential enstrophy spectra displayed in Figs. 5.9 and 5.10 demonstrate good agreement with DNS with a slight over-prediction of energy at $k = 4$ for the inviscid calculation (Fig. 5.9). A more systematic over estimation at $k = 3 - 14$ was found for the viscous decay case (Fig. 5.10) but in general the discrepancies are minor given the length of the integration.

Figure 5.11 depicts evolved kinetic energy and potential enstrophy spectra from an initial nonequilibrium state (see table 5.10). The initial spectrum is purely transient, with a large amount of the kinetic energy in the small scales, which decays rapidly due to viscous effects, but also as transient energy is converted into mean energy. The mean field is once again initially zero and is "spun up" as the system evolves. The nondimensional viscosity, $\hat{\nu}$, is chosen in order to guarantee significant decay in the small scales. The spectra are calculated at $t = 0.8$ with cumulant updates at $t = \acute{t} = 20\triangle t$. The initial large-scale Reynolds number is 67.34. The total transient field energy spectra (Fig. 5.11 (bottom)) are in close agreement. As well as being dissipated from the system, energy has been

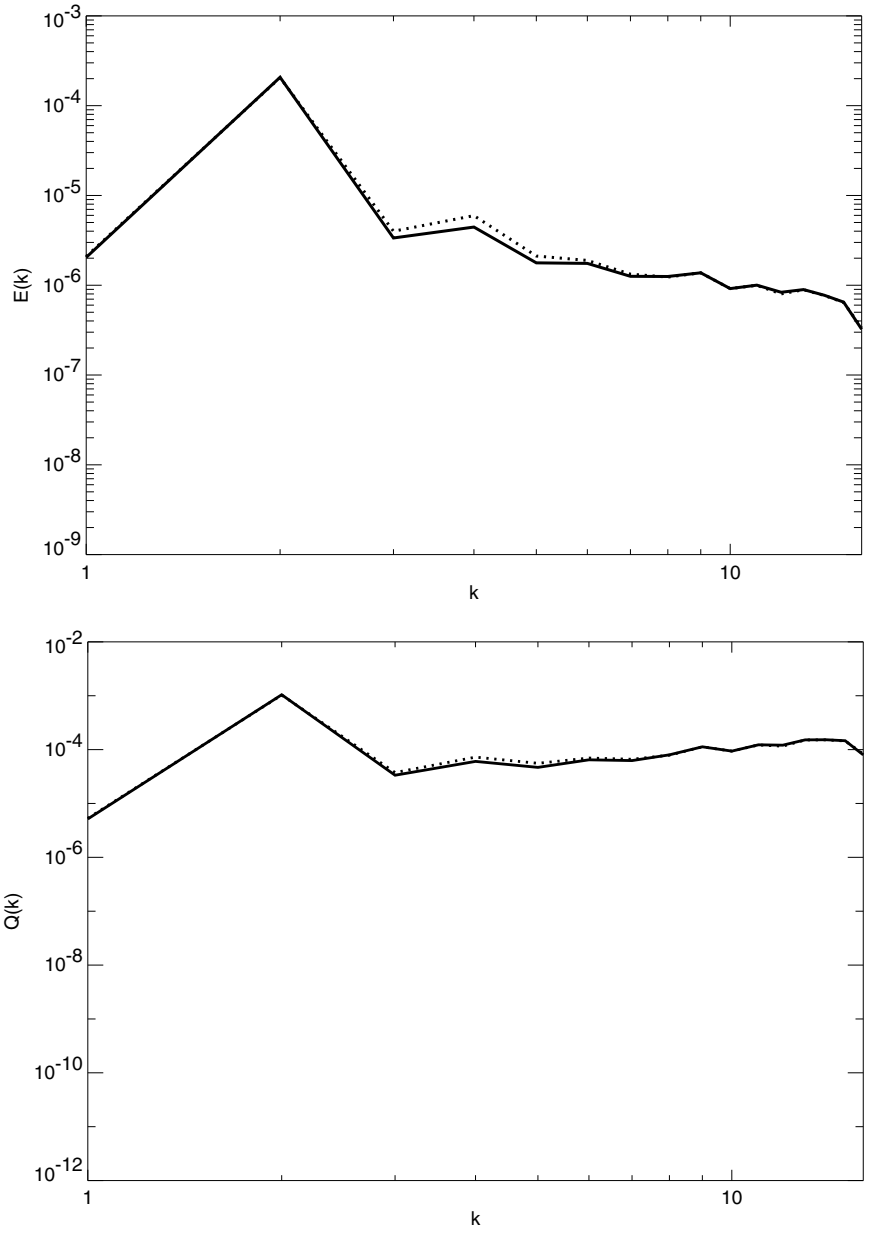

Figure 5.9: (top) Energy spectra after 300 timesteps with restarts at $T = \acute{T} = 20$ where $\triangle t = 0.11136$ for the inviscid unforced case with DNS (solid) and CUQDIA (dotted). (bottom) Potential-enstrophy spectra for $t = 300$ timesteps.

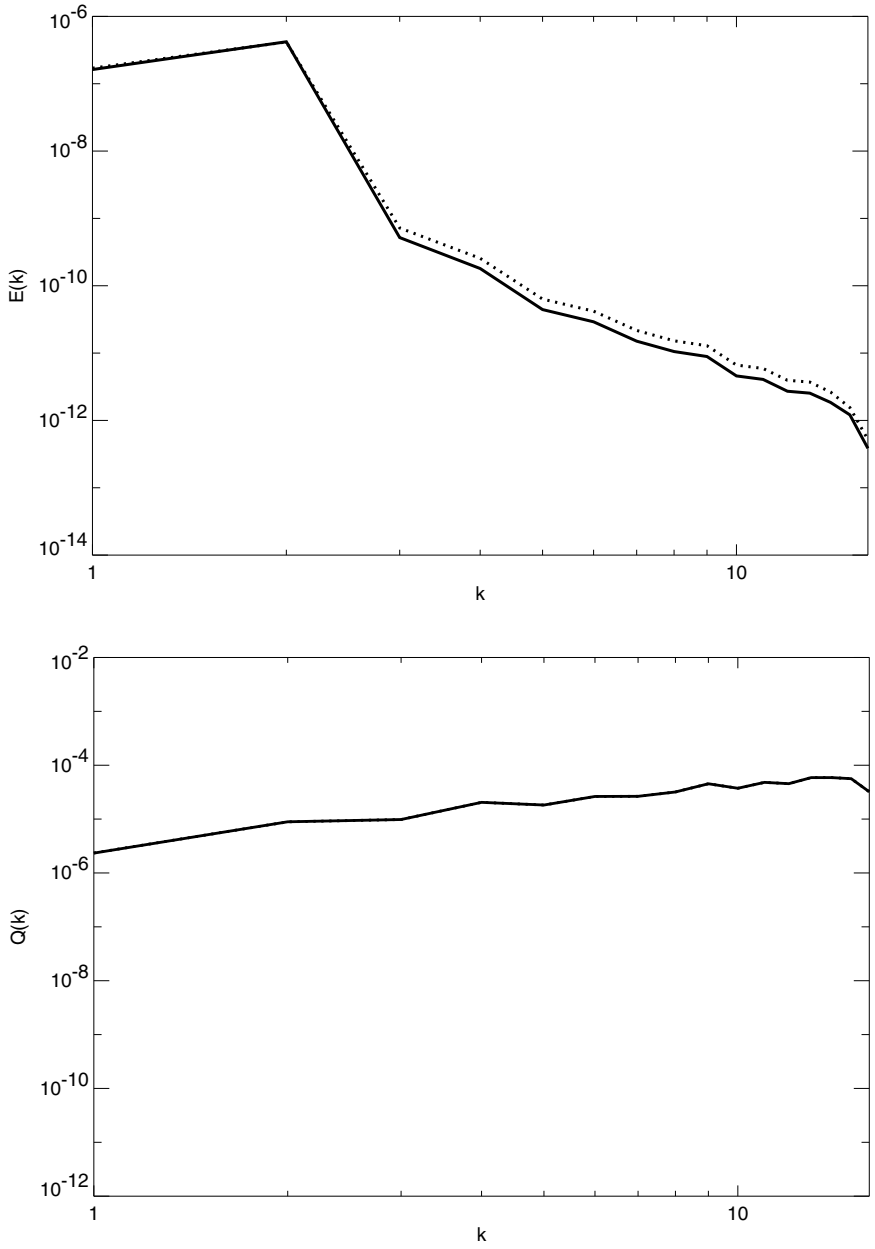

Figure 5.10: (top) Total energy spectra after 300 timesteps with restarts at $T = \acute{T} = 20$ where $\triangle t = 0.11136$ for the viscid unforced case with topography of the form $|h_{\mathbf{k}}|^2 = \frac{a+bk^2}{k^2 b^2}$ where DNS (solid) and CUQDIA (dotted). (bottom) Total potential enstrophy spectra after 300 timesteps corresponding to a nondimensional time of $t = 33.408$. The respective total potential enstrophy spectra are indistinguishable.

transferred from the transient to the generated mean field via the topographic interaction (Eqs. 3.13 and 3.17). The final Reynolds numbers are found to be 41.00 for DNS and 40.00 for the closure. The topography chosen here is typical of those chosen for idealized studies of oceanographic flows [93], Holloway [101]. Similar behavior is displayed in Fig. 5.12, where the amplitude squared of the topography is of the form $4/(1+k^4)$. Again the initial large-scale Reynolds number is found to be 67.34 and the evolved Reynolds number at $t = 0.8$ calculated to be 45.86 for DNS and 44.83 for the CUQDIA. A more detailed investigation of the effect of increasing Reynolds number is contained in sections 5.5 and 5.6.

Table 5.10: Figure 5.11 parameters

$\triangle$ t	$\hat{\nu}$	$C_{\mathbf{k}}(0,0)$	$\lvert h_{\mathbf{k}}\rvert^2$	$\langle\zeta_{\mathbf{k}}(0)\rangle$
0.004	0.025	$0.18 \times k^2$	$\frac{4k^2}{1+k^4}$	0

A topography whose amplitude squared is of the form $4k/(1+k^3)$ (not shown) has also been found to behave in a similar manner to the $4k^2/(1+k^4)$ case, as is to be expected. Various experiments were conducted with squared topographies of the form $4/(1+k^3)$ with a variety of initial conditions and viscosities with the overall result that the closure showed close agreement with DNS in all cases.

Table 5.11: Figure 5.12 parameters

$\triangle$ t	$\hat{\nu}$	$C_{\mathbf{k}}(0,0)$	$\lvert h_{\mathbf{k}}\rvert^2$	$\langle\zeta_{\mathbf{k}}(0)\rangle$
0.004	0.025	$0.18 \times k^2$	$\frac{4}{1+k^4}$	0

Figures 5.13, 5.14 and 5.15 demonstrate spectra for a forced dissipative study that evolved from the initial conditions given in Fig. 5.8 and table 5.12. The system is being forced to an equilibrium state where the mean and transient fields are of equal magnitude. The results for all fields agree except for some slight underestimation of the CUQDIA transient-field at wavenumbers $9 \leqslant k \leqslant 16$ (Fig. 5.14).

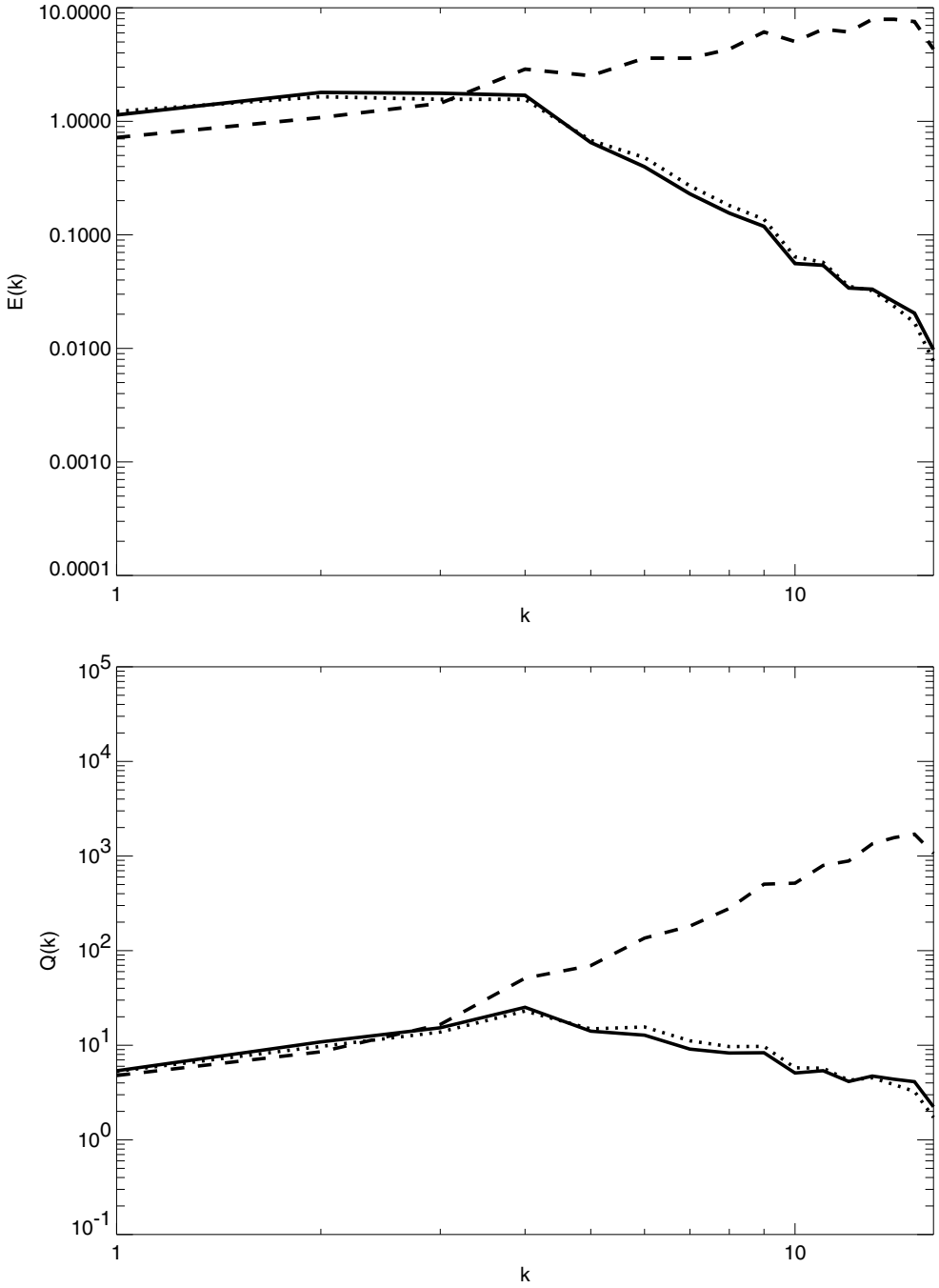

Figure 5.11: (top) Total energy spectra after 200 timesteps with restarts at $T = \acute{T} = 20$ where $\triangle t = 0.004$ for the viscid unforced case where the respective spectra are DNS (solid), CUQDIA (dotted) and the initial spectrum (dashed). The nondimensional viscosity is given by $\hat{\nu} = 0.025$ and the topography (squared) is $|h_{\mathbf{k}}|^2 = \frac{4k^2}{1+k^4}$. (bottom) Total potential-enstrophy spectra after 200 timesteps.

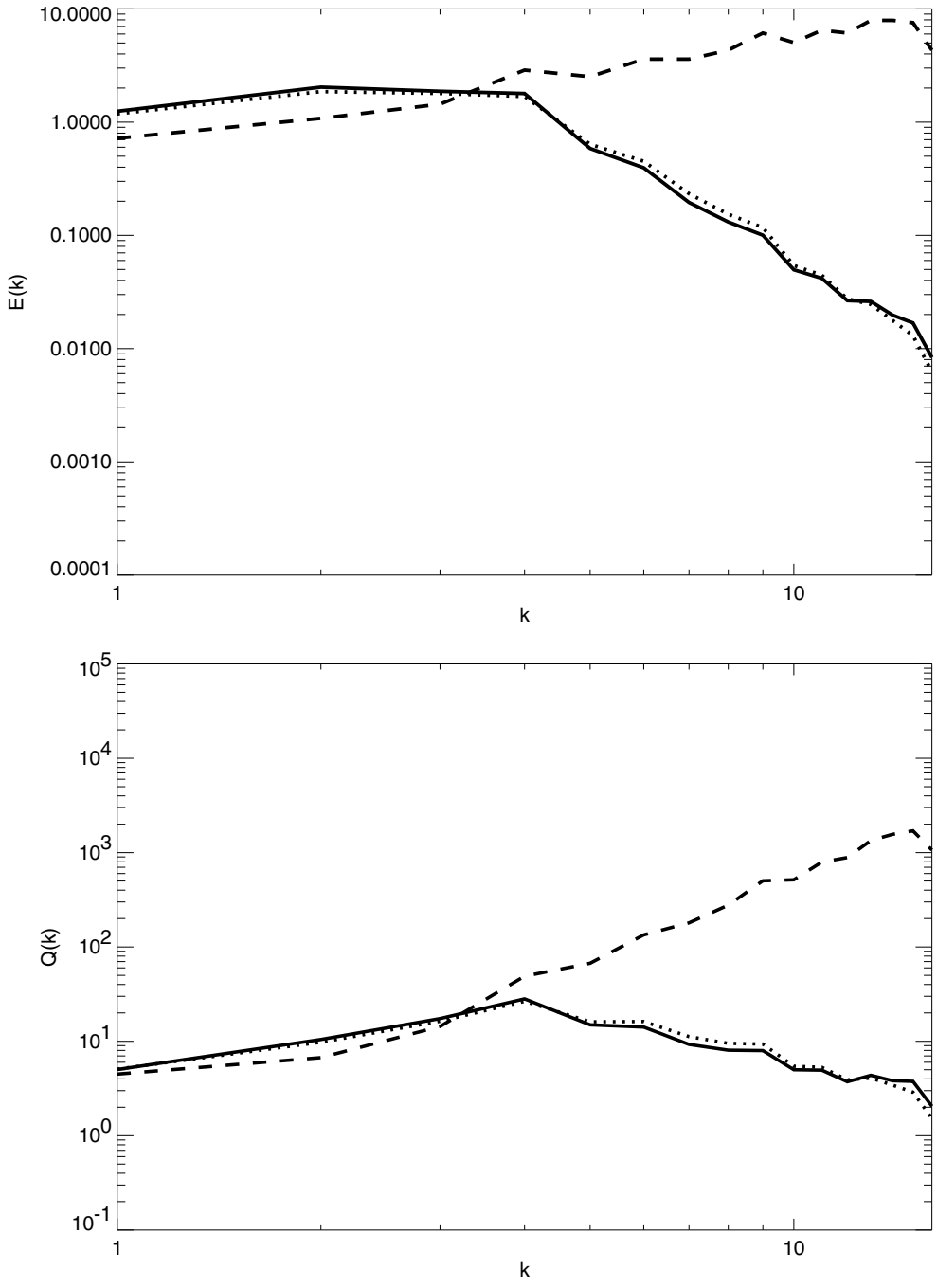

Figure 5.12: (top) Energy spectra after 200 timesteps with restarts at $T = \acute{T} = 20$ where $\triangle t = 0.004$ for the viscid unforced case where the respective spectra are DNS (solid), CUQDIA (dotted) and the initial spectrum (dashed). The nondimensional viscosity is given by $\hat{\nu} = 0.025$ and the topography squared is $|h_{\mathbf{k}}|^2 = \frac{4}{1+k^4}$. (bottom) Total Potential-enstrophy spectra after 200 timesteps.

Table 5.12: C16 parameters for Figs. 5.13 - 5.15.

$\triangle$ t	$\hat{\nu}$	a	b	$\lvert h_{\mathbf{k}}\rvert^2$	$F_{\mathbf{k}}$	$\langle f_{\mathbf{k}} \rangle$
0.11136	1.879E-2	-5.969E+5	7.444E+5	$\frac{a+bk^2}{k^2b^2}$	$2\nu(k)C^{eq}_{\mathbf{k}}$	$-\frac{1}{2}bh_{\mathbf{k}}F^{eq}_{\mathbf{k}}$

Figure 5.15 details the evolution of the total potential enstrophy spectra, where again excellent agreement is demonstrated between DNS and CUQDIA. This particular case was also run with restarts at $T = \acute{T} = 5$ and 10. Systematic under-representation of the cumulants was evident with cumulant updates at every 5 timesteps due to insufficient information about the non-Gaussian cumulants, but overall qualitative agreement with DNS was observed. For restarts at every 10 timesteps results comparable to Figs. 5.13, 5.14 and 5.15 were produced. The obvious conclusion to be drawn here is that as resolution is increased, then the number of timesteps required for a sufficiently representative calculation of those off-diagonal coherences decreases. As will be shown in section 5.5 for C48 and C64 resolution calculations cumulant updates at every 10 timesteps were more than sufficient for reasonable quantitative agreement with DNS in the cases examined.

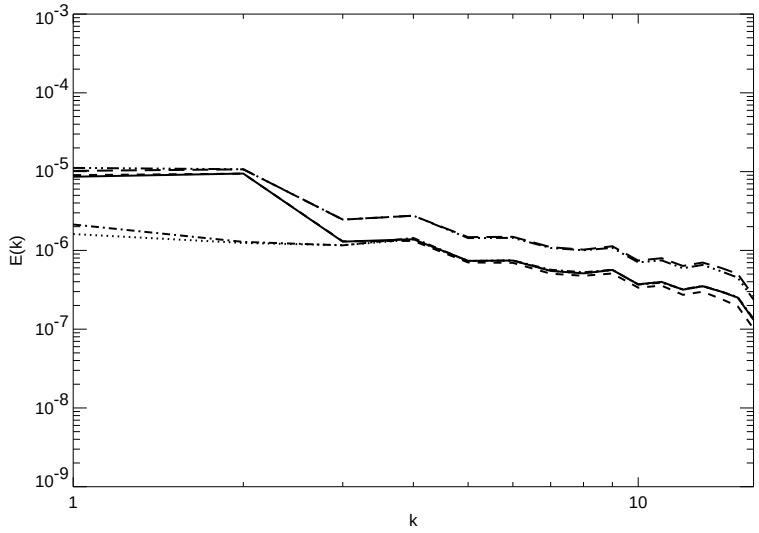

Figure 5.13: Energy spectra after 160 timesteps with restarts at $T = \acute{T} = 20$ where $\triangle t = 0.11136$. Transient energy for DNS (solid) and CUQDIA (short dashed); Mean energy for DNS (dot dashed) and CUQDIA (dotted); Total energy for DNS (long dashed) and CUQDIA (dot dot dot dashed)

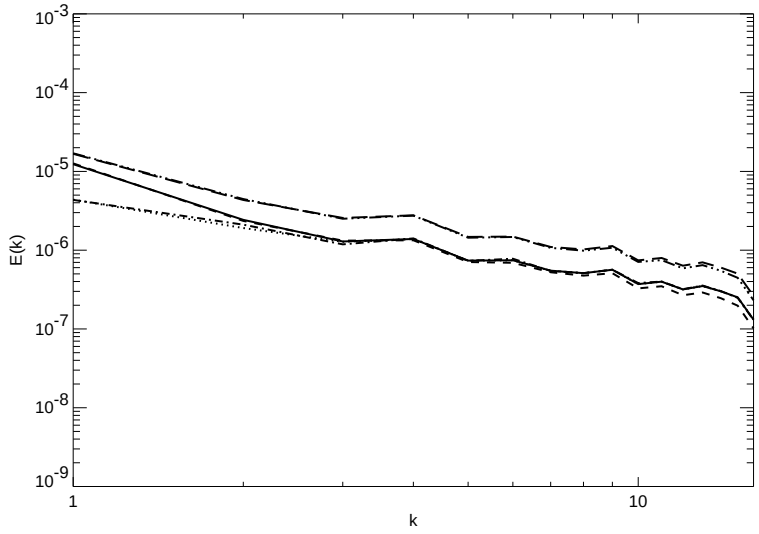

Figure 5.14: Energy spectra after 320 timesteps with restarts at $T = \acute{T} = 20$ where $\triangle t = 0.11136$. Transient energy for DNS (solid) and CUQDIA (short dashed); Mean energy for DNS (dot dashed) and CUQDIA (dotted); Total energy for DNS (long dashed) and CUQDIA (dot dot dot dashed)

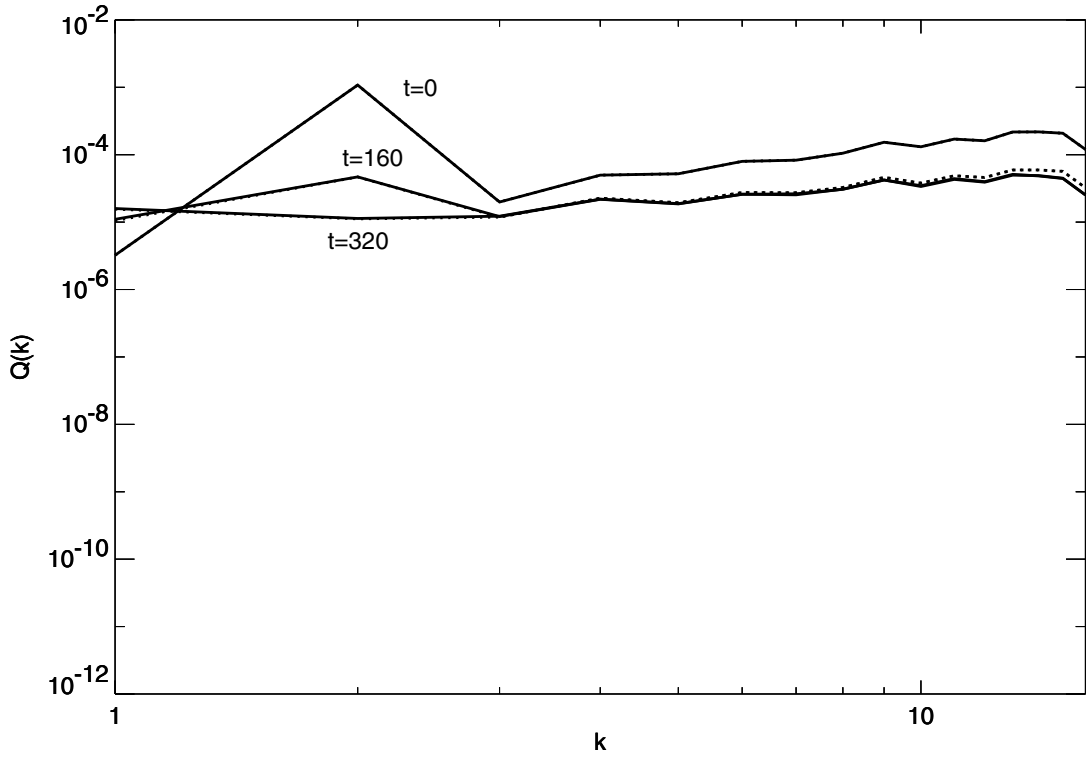

Figure 5.15: Potential-enstrophy spectra for timesteps 0, 160 and 320 with restarts at $T = \acute{T} = 20$ where $\triangle t = 0.11136$ for DNS (solid) and CUQDIA (dashed). Very close agreement is evident.

5.5 Very low Reynolds number turbulence

In this section, we consider viscous decay for cases at or near equilibrium for very low Reynolds number (typically < 1) and for resolutions ranging from C16 to C64. The square of the topographic amplitudes considered in this section are $|h_{\mathbf{k}}|^2 = \frac{16k^2}{(1+k^3)^2}$ and $|h_{\mathbf{k}}|^2 = \frac{a+bk^2}{k^2b^2}$. The purpose of these experiments is to ascertain the validity of the quasi-diagonal closure approach for the incorporation of topography and mean-field in a setting devoid of the effects of strong turbulence. These studies will underpin our later investigations as we progressively incorporate the effects of stronger turbulence. The topographies chosen are markedly different thus providing a strong test of the effect of topography on the accuracy of the model. Throughout this section the restart time will be 20 timesteps and parameters $a = -5.969 \times 10^5$ and $b = 7.444 \times 10^5$.

5.5.1 C16 resolution

Figures 5.16 and 5.17 display viscous decay from canonical equilibrium. The parameters are given in table 5.13. This case was chosen in order to compare and contrast the closure with DNS in a situation where the initial mean and transient fields have the same magnitude. The step size employed was $\triangle t = 0.004$ which is of the same order as that used by Frederiksen and Davies [107, 108], and is small enough to ensure absolute stability and to minimize any error due to timestepping considerations. Restarts are employed at every 20 timesteps.

Table 5.13: Figures 5.16-5.17 parameters

$\triangle$ t	$\hat{\nu}$	$C_{\mathbf{k}}(0,0)$	$\lvert h_{\mathbf{k}}\rvert^2$	$\langle\zeta_{\mathbf{k}}(0)\rangle$
0.004	0.005	$C_{\mathbf{k}}^{eq}$	$\frac{a+bk^2}{b^2k^2}$	$\langle\zeta_{\mathbf{k}}\rangle^{eq}$

Figure 5.16 reveals excellent agreement between the CUQDIA and DNS total energy spectra at all stages of the evolution for both the total energy and the component fields. It is observed that both the mean and transient fields are decaying at the same rate. Thus the mean field always remains the same strength as the transient field. The agree-

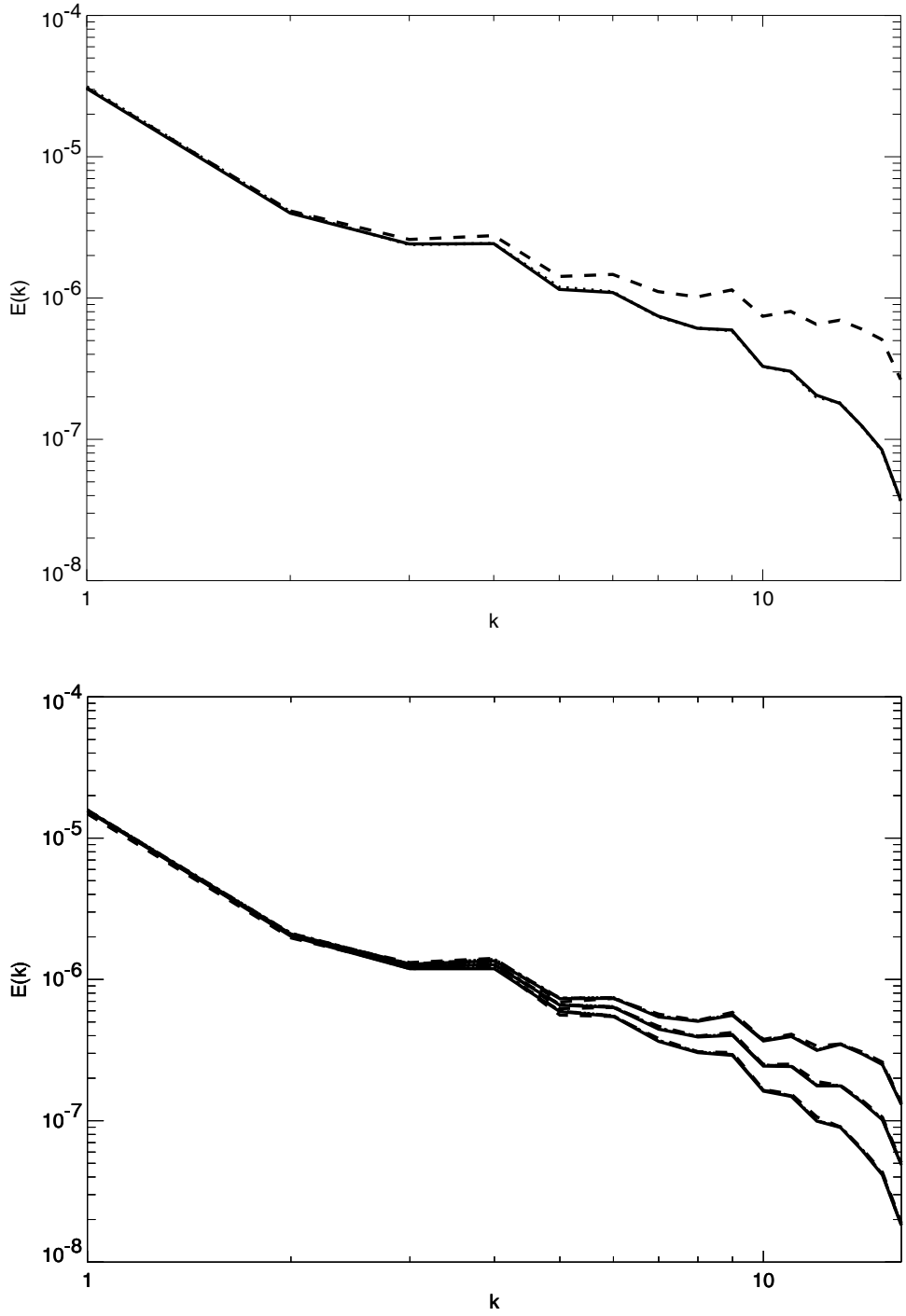

Figure 5.16: (top) Comparison of the total energy for the DNS (solid) and CUQDIA (dotted) calculations after 200 timesteps ($t_f = 0.8$). The initial field is the dashed line. (bottom) Comparison of the component fields at times t = 0, 0.4 and 0.8. Transient energy: DNS (solid) CUQDIA (dot dashed), Mean energy: DNS (dashed) CUQDIA (dotted). Note that the respective DNS and CUQDIA closure fields are almost in exact agreement.

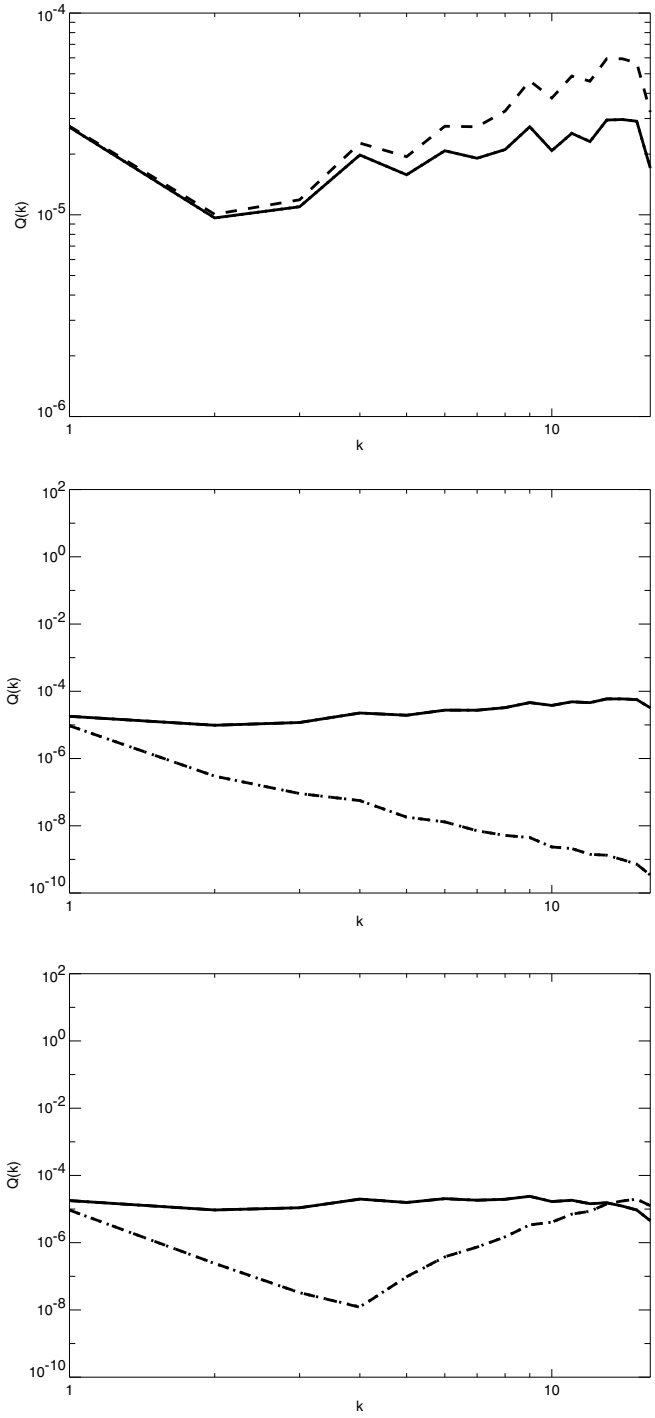

Figure 5.17: (top) Total potential enstrophy for the DNS (solid) and CUQDIA (dotted) calculations at t = 0.8. The initial field is the dashed line. (Middle) Initial Mean and Transient potential enstrophy fields. (bottom) t=0.8 Mean and Transient potential enstrophy fields. Transient enstrophy: DNS (solid), CUQDIA (dot dashed). Mean potential enstrophy $(\langle\zeta_{\mathbf{k}}(t)\rangle + h_{\mathbf{k}})(\langle\zeta_{-\mathbf{k}}(t)\rangle + h_{-\mathbf{k}})$: DNS (dashed), CUQDIA (dotted). Note that the respective DNS and CUQDIA closure fields are almost in exact agreement.

ment is so close that the respective DNS and CUQDIA mean and transient spectra are indistinguishable. In Fig. 5.17 the total potential enstrophy (top) also shows very close agreement as does the mean and transient fields (bottom). The increase in the mean potential enstrophy at the small scales can be readily explained by considering the canonical equilibrium expression for the mean-vorticity $\langle\zeta_{\mathbf{k}}\rangle^{eq} = -bh_{\mathbf{k}}C_{\mathbf{k}}^{eq}$ and the expression for the mean potential enstrophy $(\langle\zeta_{\mathbf{k}}(t)\rangle + h_{\mathbf{k}})(\langle\zeta_{-\mathbf{k}}(t)\rangle + h_{-\mathbf{k}})$. As the mean-vorticity decays at the smallest scales via the enstrophy cascade the mean potential enstrophy becomes dominated by the topographic contribution, which for this particular case is flat across all scales. Thus we see a marked increase in the mean potential enstrophy at the very smallest scales.

Table 5.14: Figures 5.18-5.19 parameters

$\triangle$ t	$\hat{\nu}$	$C_{\mathbf{k}}(0,0)$	$\lvert h_{\mathbf{k}}\rvert^2$	$\langle\zeta_{\mathbf{k}}(0)\rangle$
0.004	0.005	$C_{\mathbf{k}}^{eq}$	$\frac{a+bk^2}{b^2k^2}$	$0.1 \times \langle\zeta_{\mathbf{k}}\rangle^{eq}$

If we now consider the same set of parameters and initial conditions, but with a significantly weaker mean-field $\langle\zeta_{\mathbf{k}}(0)\rangle = 0.1 \times \langle\zeta_{\mathbf{k}}\rangle^{eq}$ (see table 5.14), we see again (Figs. 5.18 and 5.19) that the agreement between closure and DNS is so close that the respective spectra are indistinguishable. Again, the mean and transient energy spectra relax at about the same rate, with the transient and mean potential enstrophy spectra also exhibiting similar behavior to Fig. 5.17.

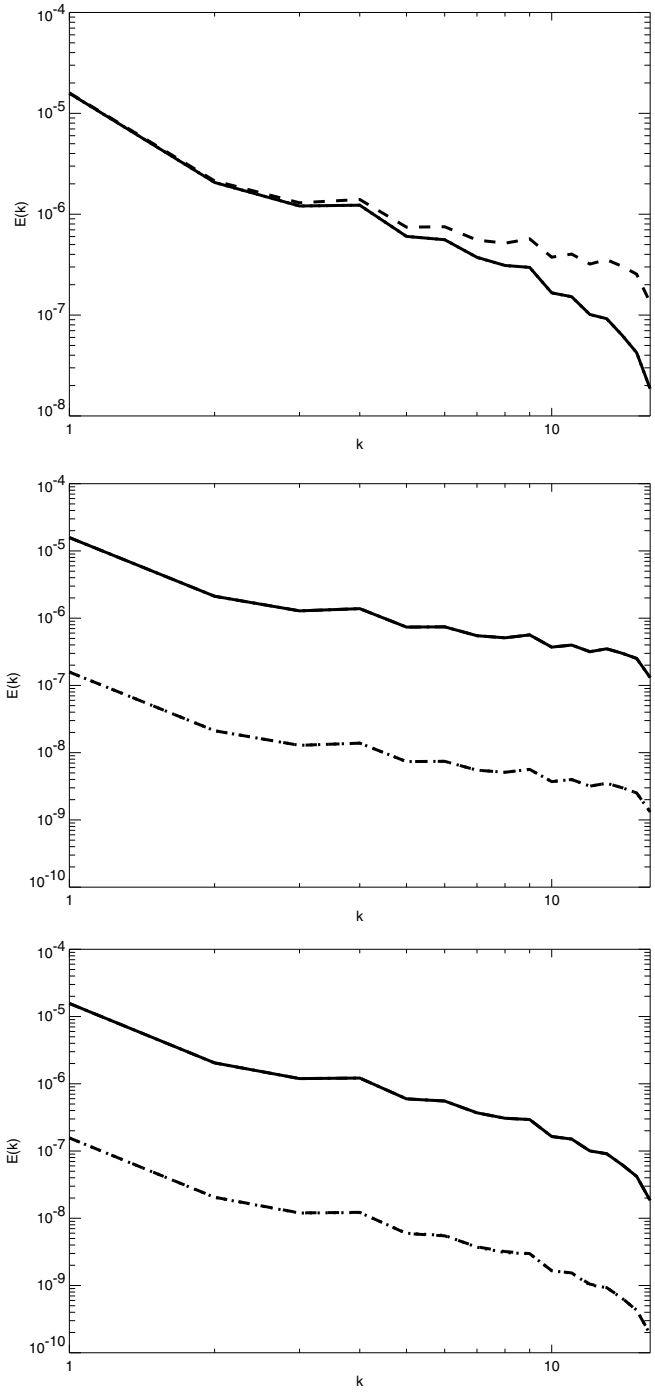

Figure 5.18: (top) Total energy for the DNS (solid) and CUQDIA (dotted) calculations at t = 0.8. The initial field is the dashed line. (Middle) Initial Mean and Transient kinetic energy fields. (bottom) Mean and Transient energy fields at t = 0.8. Note that all CUQDIA energy fields are indistinguishable from DNS. Component field diagrams: mean field; DNS (dashed lines), CUQDIA (dotted lines), :transient field; DNS (solid lines), CUQDIA (dot dashed). Note that the respective DNS and CUQDIA closure fields are almost in exact agreement and are consequently indistinguishable.

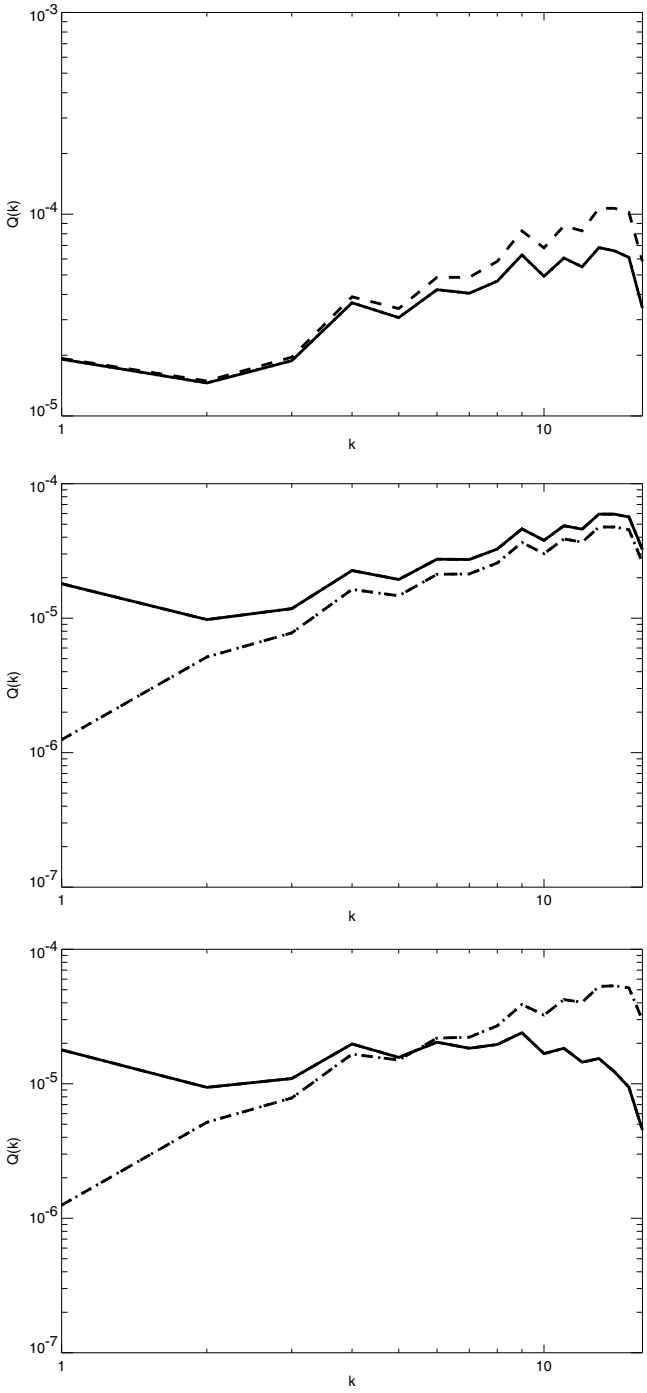

Figure 5.19: (top) Total potential-enstrophy for the DNS (solid) and CUQDIA (dotted) calculations at t = 0.8. The initial field is the dashed line. (Middle) Initial Mean and Transient potential enstrophy fields. (bottom) t = 0.8 Mean and Transient potential enstrophy fields. Component field diagrams: mean field; DNS (dashed lines), CUQDIA (dotted lines), :transient field; DNS (solid lines), CUQDIA (dot dashed). Note that the respective DNS and CUQDIA closure fields are almost in exact agreement and are consequently indistinguishable.

5.5.2 C48 resolution

In this subsection the same experiments as in Figs. 5.18 and 5.19 are repeated at the higher C48 resolution in order to ascertain if increased resolution will adversely effect the model comparisons or to see if the theory breaks down with increased resolution. The experiments were conducted with restart times of $10\triangle t$ and $20\triangle t$ with no observable difference in the results. The close agreement between the results of the closure with these two different restart times is not surprising given that it is expected that for very low Reynolds number the significance of the non-Gaussian cumulants should be greatly reduced. Throughout this subsection the results shown are for cumulant updates at every $10\triangle t$.

In Figs. 5.20 and 5.21 the total field spectra show very close agreement at all scales with only slight underestimation in the closure at the smallest scales evident in the total energy, enstrophy and palinstrophy spectra. Excellent agreement in the mean-field potential enstrophy can be seen in Fig. 5.23 while the transient-field calculation reveals the source of the closure underestimation at wavenumbers $40 \leqslant k \leqslant 48$ in the total field spectra. The small disagreement between DNS and the closure in the transient-fields is again evident at the smallest scales in transient energy spectra (Fig. 5.22), with the transient enstrophy spectra (Fig. 5.24) revealing similar behavior. Even the palinstrophy spectra (Fig. 5.25), which is a much more sensitive test of the smaller scales, demonstrates very close agreement with DNS. Further experiments at this resolution were run for a range of topographies with similar initial conditions again demonstrating extremely close agreement. No obvious defects in the comparisons due to increased resolution were observed apart from some underestimation of closure amplitudes at the smallest scales.

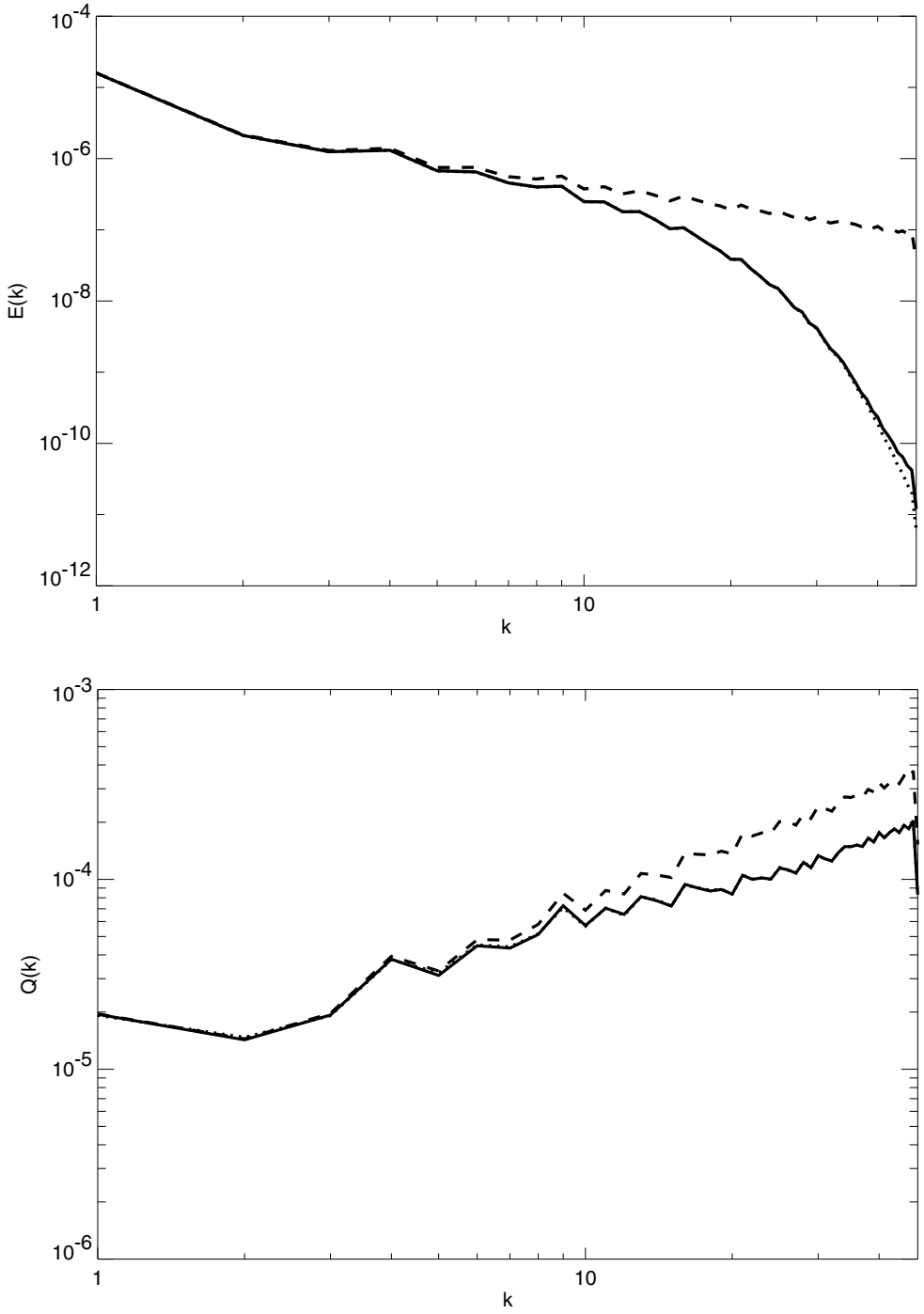

Figure 5.20: (top) Total energy for the DNS (solid) and CUQDIA (dotted) calculations at t = 0.4. The initial field is the dashed line. The parameters are as for table 5.14 however we now implement the restart procedure at every 10 timesteps. (bottom) Total potential-enstrophy for the DNS (solid) and CUQDIA (dotted) calculations at t= 0.4. The initial field is the dashed line.

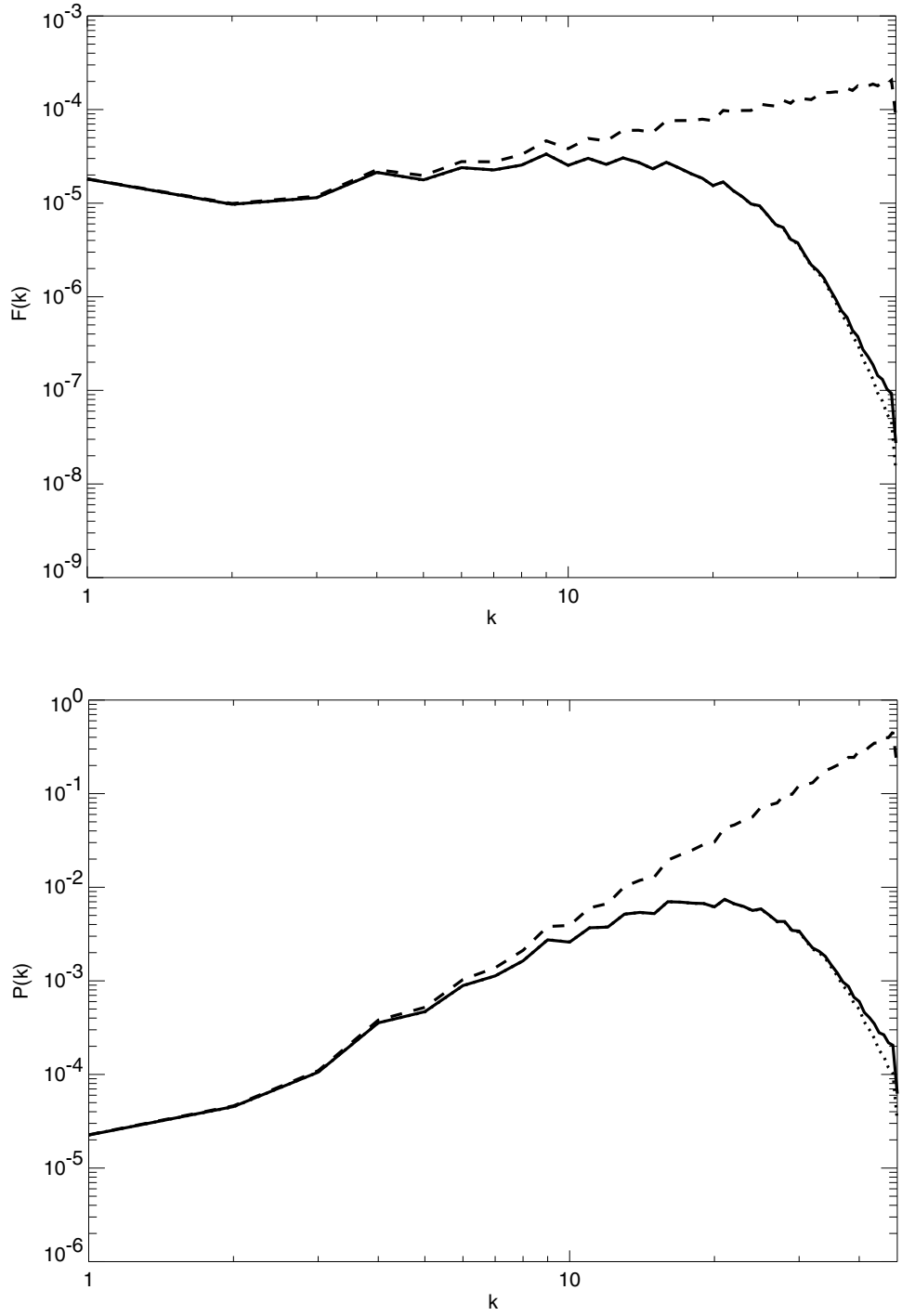

Figure 5.21: (top) As in Fig. 5.20 but for total enstrophy at t = 0.4. (bottom) Total palinstrophy at timestep 100. Total field diagrams; DNS (solid lines), CUQDIA (dotted lines), initial fields (dashed lines).

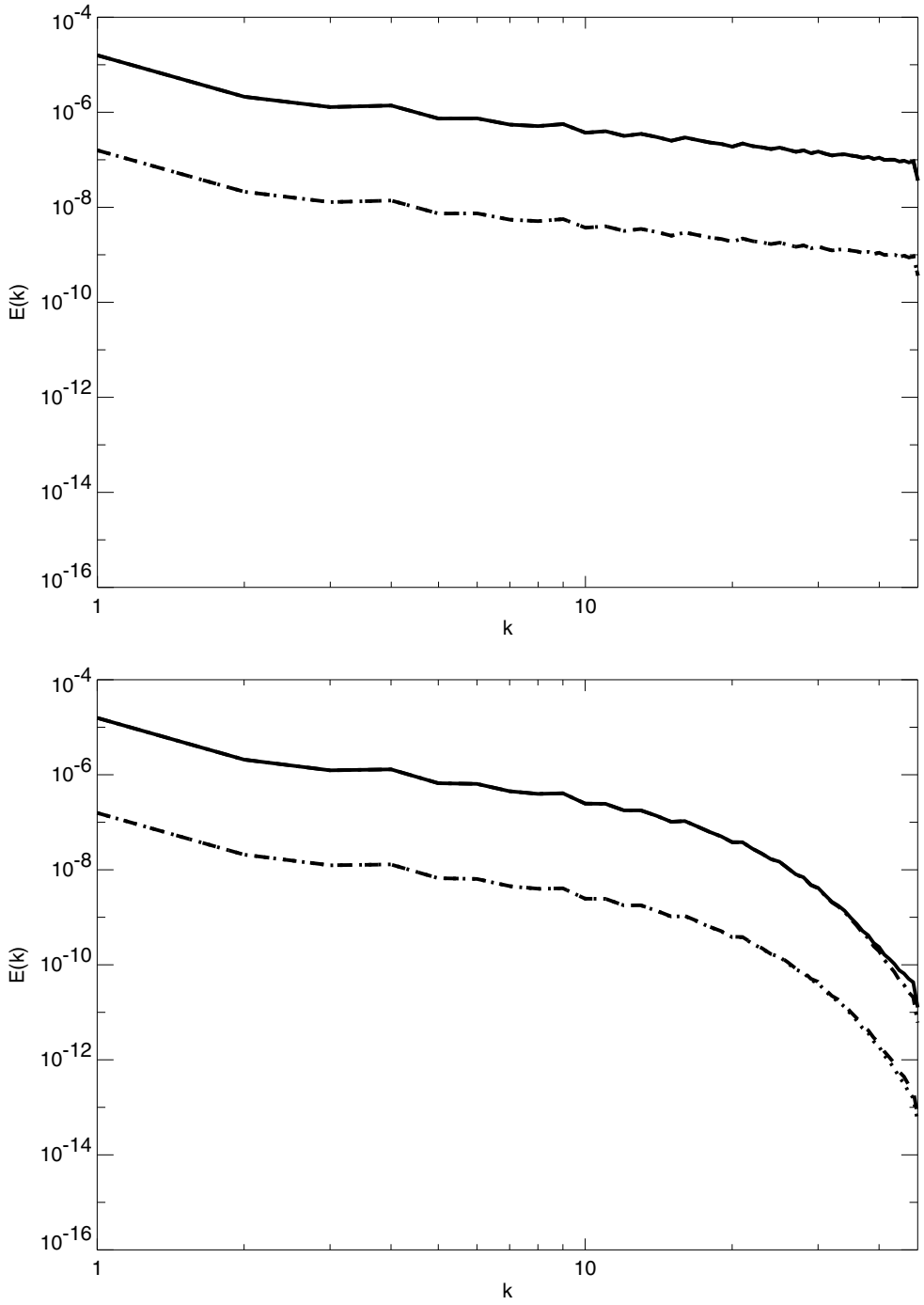

Figure 5.22: (top) Initial mean and transient energy fields. (bottom) Mean and Transient energy fields at t = 0.4. Component field diagrams: mean field; DNS (dashed lines), CUQDIA (dotted lines), :transient field; DNS (solid lines), CUQDIA (dot dashed).

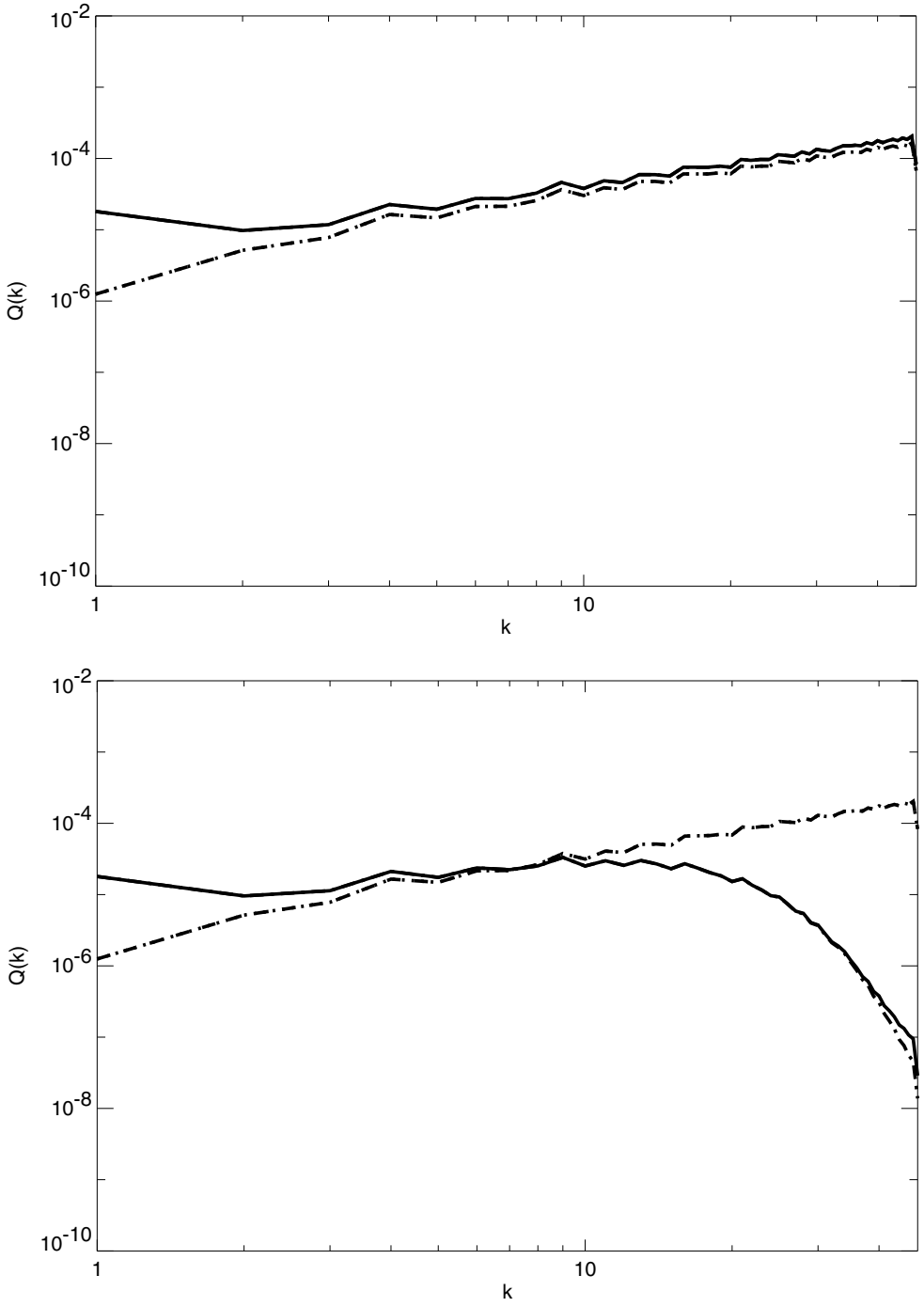

Figure 5.23: (top) Initial mean and transient potential enstrophy spectra. (bottom) Mean and transient enstrophy spectra at t = 0.4. Component field diagrams: mean field; DNS (dashed lines), CUQDIA (dotted lines), :transient field; DNS (solid lines), CUQDIA (dot dashed).

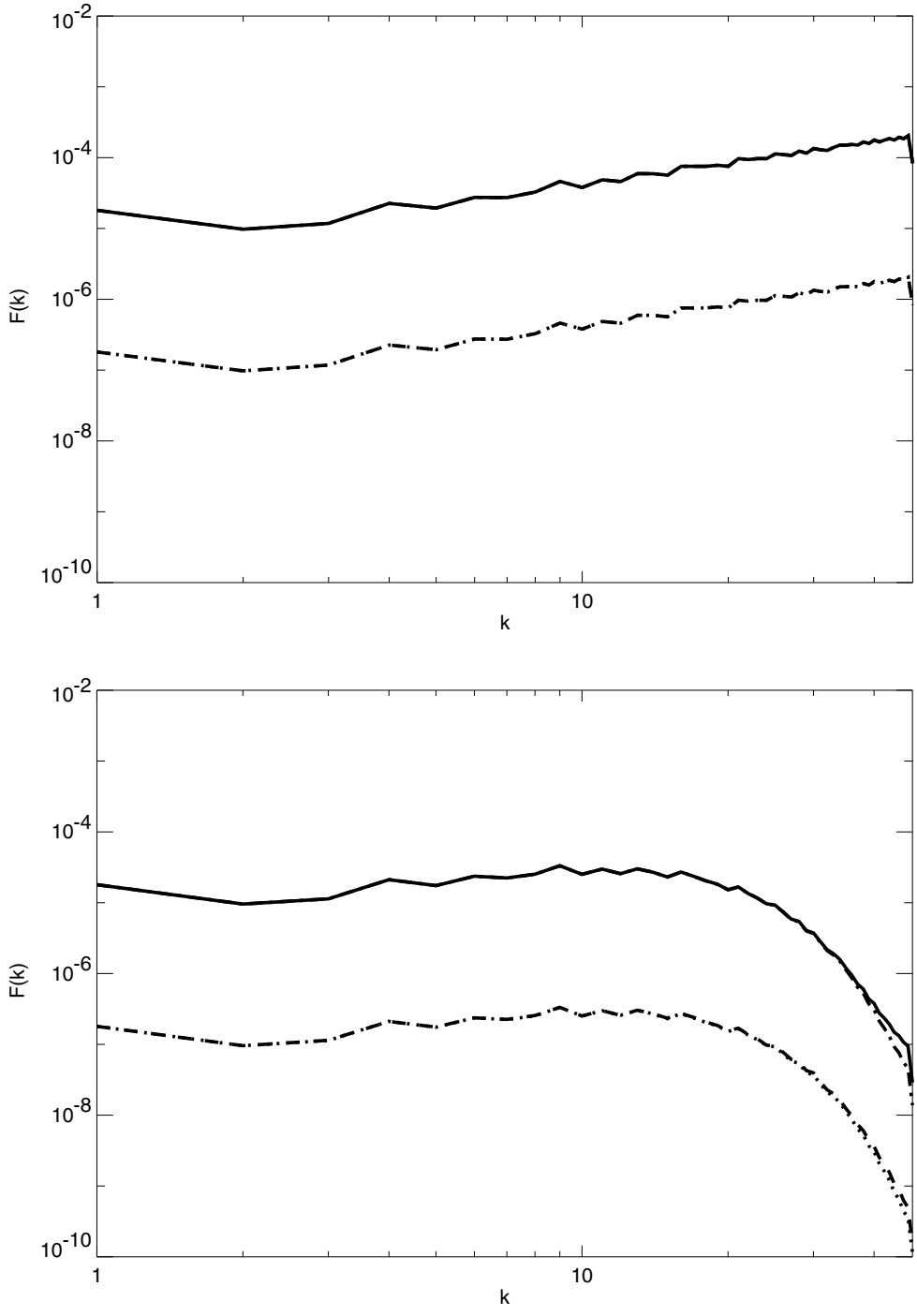

Figure 5.24: (top) Initial Mean and Transient enstrophy spectra. (bottom) t = 0.4 mean and transient enstrophy spectra. Component field diagrams: mean field; DNS (dashed lines), CUQDIA (dotted lines), :transient field; DNS (solid lines), CUQDIA (dot dashed).

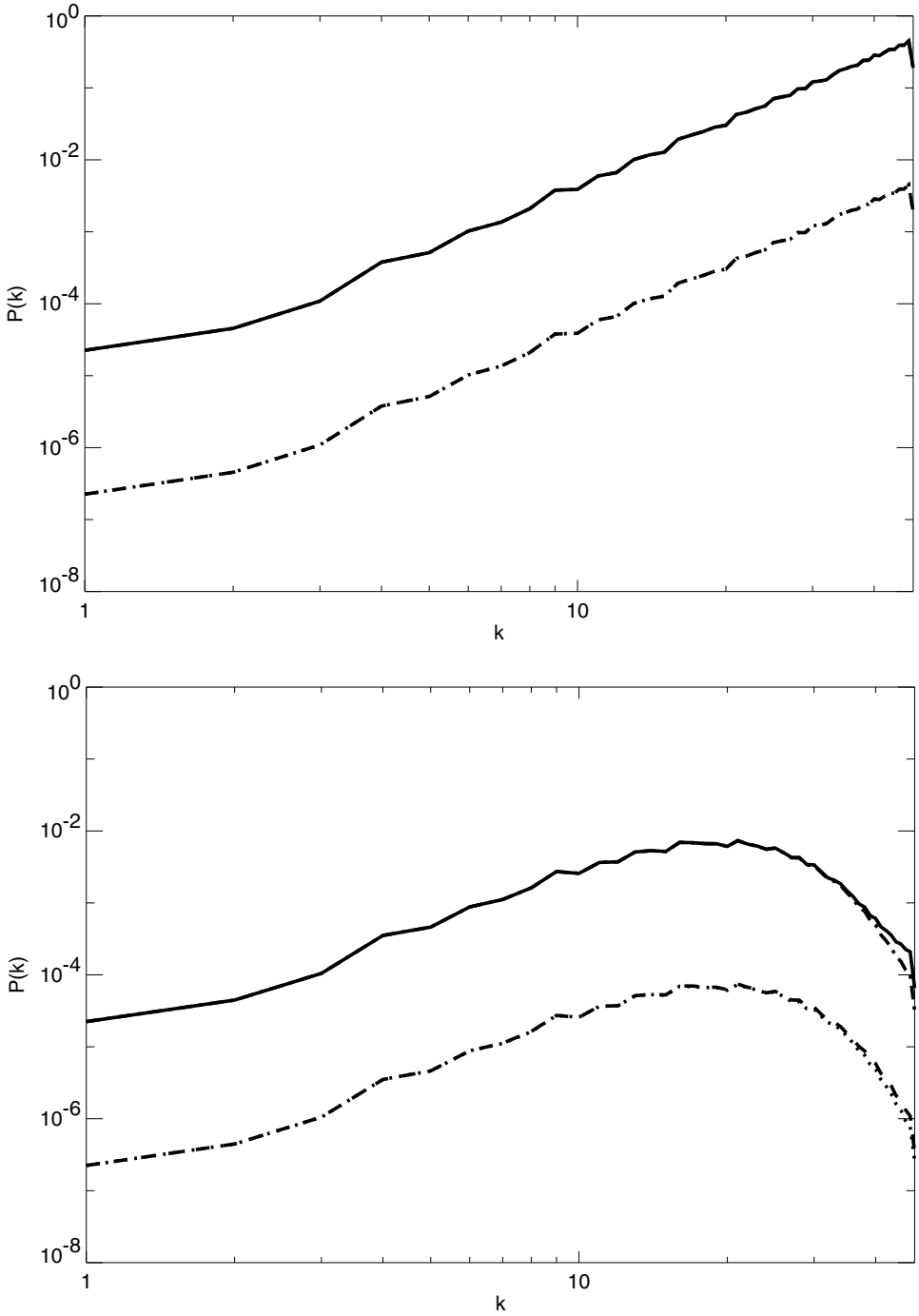

Figure 5.25: (top) Initial mean and transient palinstrophy spectra. (bottom) t = 0.4 mean and transient palinstrophy spectra. Component field diagrams: mean field; DNS (dashed lines), CUQDIA (dotted lines), :transient field; DNS (solid lines), CUQDIA (dot dashed).

5.5.3 C64 experiments

In this section the results of numerical experiments conducted at C64 resolution are presented. These calculations without cumulant updates would represent a very significant computational task due to the long time-history integrals and large memory requirements arising from the large number of points in the domain of discrete wavenumbers as well as the large number of interaction coefficients to be summed over. We consider two particular cases at this resolution. Firstly, in Figs. 5.26 to 5.31 we repeat the case of viscous decay from an initial canonical equilibrium state considered previously at C16 resolution in Figs. 5.16, 5.17 and table 5.13, but now with enstrophy and palinstrophy calculations included in order to gain more detailed comparison with DNS at the smallest scales. Due to the significant evolution observed for inhomogeneous flow over topography, in both the DNS and CUQDIA experiments, we only required relatively short integrations in comparison to previous homogeneous studies. That said, the C64 calculation still takes considerably longer to run ($\backsim$5 times) than for C48. In Fig. 5.32 the palinstrophy spectra for the same case as Figs. 5.26 to 5.31 is shown for C48 resolution run out to $t = 0.4$. This Fig. is included in order to demonstrate the likely behavior of the C64 resolution run at longer time periods. The second case we present is again for viscid relaxation from equilibrium but with a topography whose amplitude squared is given by $|h_{\mathbf{k}}|^2 = 16k^2/(1 + k^3)^2$. For this topography the energy in the mean-field at equilibrium is mostly contained in the larger scales and falls away rapidly in the smaller scales whereas the transient-field energy has a initially flat spectrum (Fig. 5.35). The fields are calculated at a final time of$t = 0.2$. In the calculations restarts at every 10 timesteps were used.

Figures 5.26 and 5.27 depict the total energy, potential enstrophy, enstrophy and palinstrophy for DNS (solid lines) and CUQDIA (dotted lines) respectively. For clarity we restate that the topography has been chosen such that at the initial equilibrium the mean and transient (twice) enstrophies are of equal magnitude. It is apparent from the total field comparisons that the DNS and closure spectra are indistinguishable as are the mean and transient-fields as seen in Figs. 5.28, 5.30 and 5.31. However, we see in Fig. 5.29 (bottom) that, as the total fields decay under dissipation, the DNS and closure mean-fields begin to exhibit increase in the small scales. This is due to the fact that at equilibrium the mean

field and topographies obey the relationship $\langle\zeta_{\mathbf{k}}\rangle^{eq} = -bh_{\mathbf{k}}C_{\mathbf{k}}^{eq}$. Thus as the mean-field decays from the equilibrium state the mean component of the potential enstrophy; that is, $(\langle\zeta_{\mathbf{k}}(t)\rangle + h_{\mathbf{k}})(\langle\zeta_{-\mathbf{k}}(t)\rangle + h_{-\mathbf{k}})$, approaches $h_{\mathbf{k}}h_{-\mathbf{k}}$ at the smallest scales.

Figure 5.32 reveals the palinstrophy spectra at a final time $t = 0.4$ for C48 resolution. Here we see complete agreement between DNS and CUQDIA for the mean-field calculation and slight underestimation of the transient-field palinstrophy at wavenumbers 40 to 48 in the CUQDIA closure. It is expected that the C64 resolution study would begin to show some of this behavior given longer run times.

Figures 5.33 to 5.38 are for the same parameters as the preceding case but with a topographic amplitude (squared) that goes like $1/k^4$. The spectra are calculated at a final time of $t = 0.2$ with the DNS an ensemble average over 100 realizations; the closure cumulant updates occur at every 10 timesteps. The total fields concur very well as do the mean and transient-fields in Figs. 5.35, 5.37 and 5.38. Figure 5.36 also demonstrates close agreement in the potential enstrophy spectra.

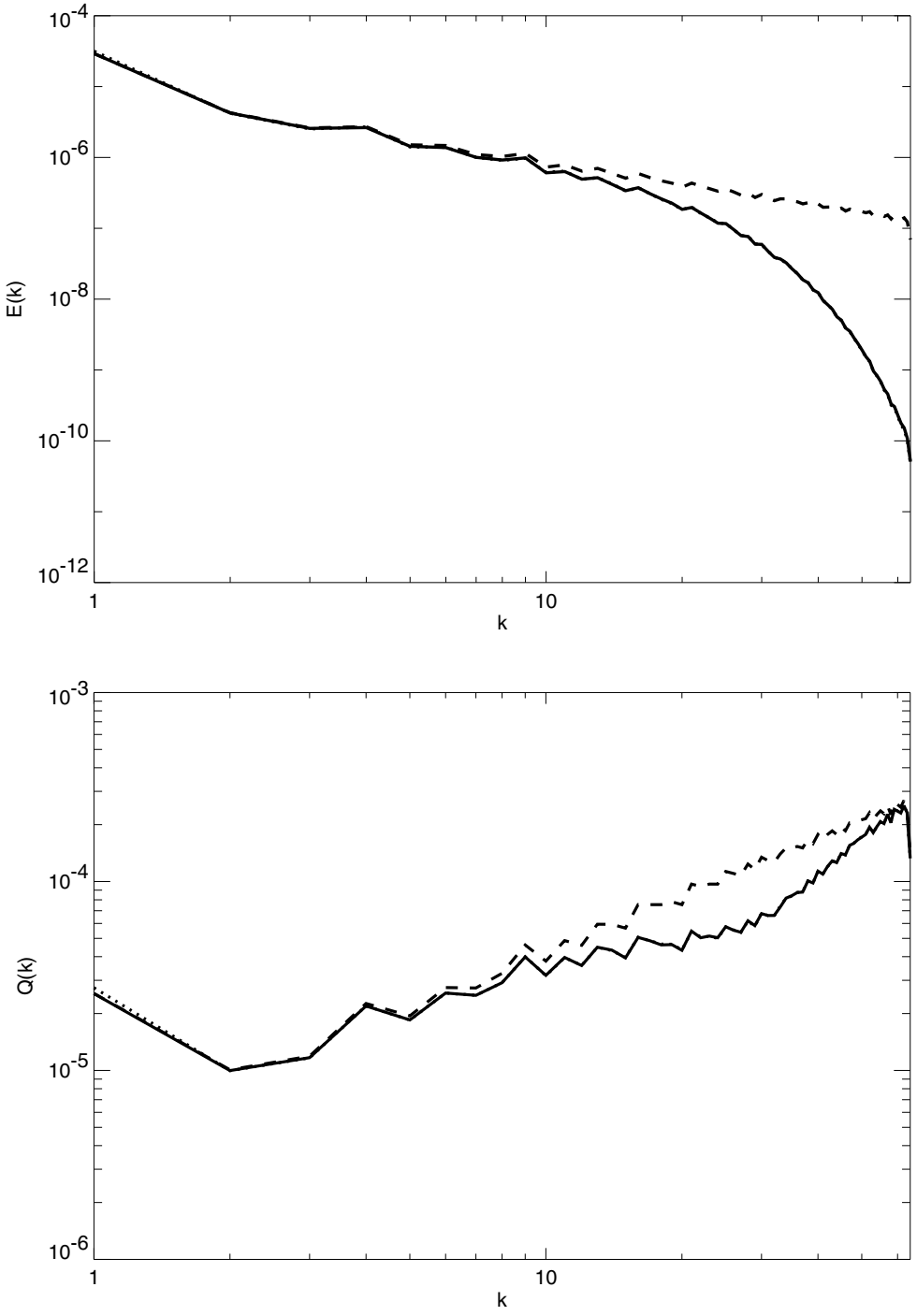

Figure 5.26: (top) Total energy for the DNS (solid) and CUQDIA (dotted) calculations after 45 timesteps. The initial field is the dashed line. The parameters are as for table 5.13 and we again implement the restart procedure at every 10 timesteps. (bottom) Total potential-enstrophy for the DNS (solid) and CUQDIA (dotted) calculations after 45 timesteps. The initial field is the dashed line. Note that the respective DNS and CUQDIA closure fields are almost in exact agreement and are consequently indistinguishable.

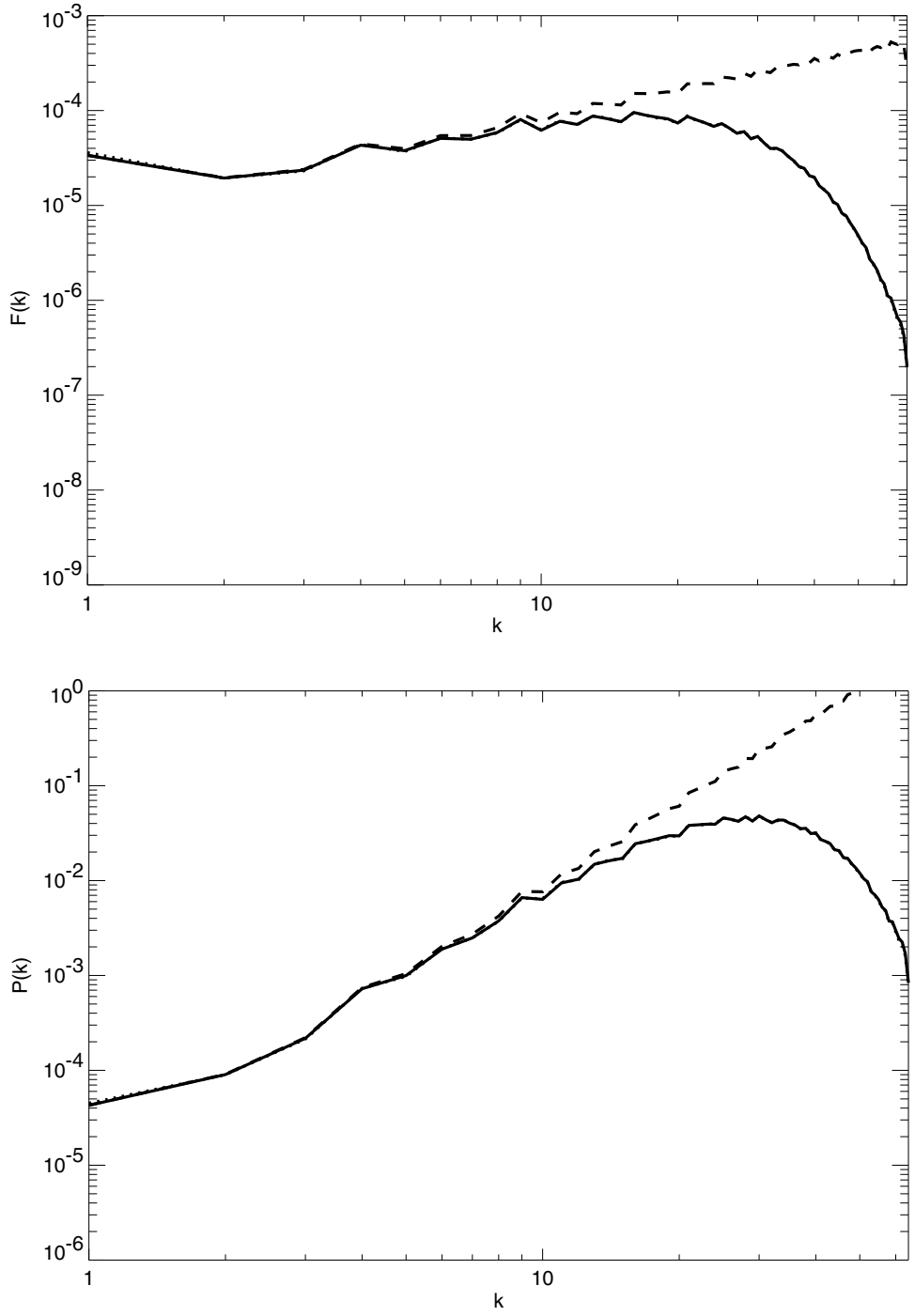

Figure 5.27: (top) Total enstrophy at t=0.18. (bottom) Total palinstrophy at t=0.18. Total field diagrams; DNS (solid lines), CUQDIA (dotted lines), initial fields (dashed lines). Note that the respective DNS and CUQDIA closure fields are almost in exact agreement and are consequently indistinguishable.

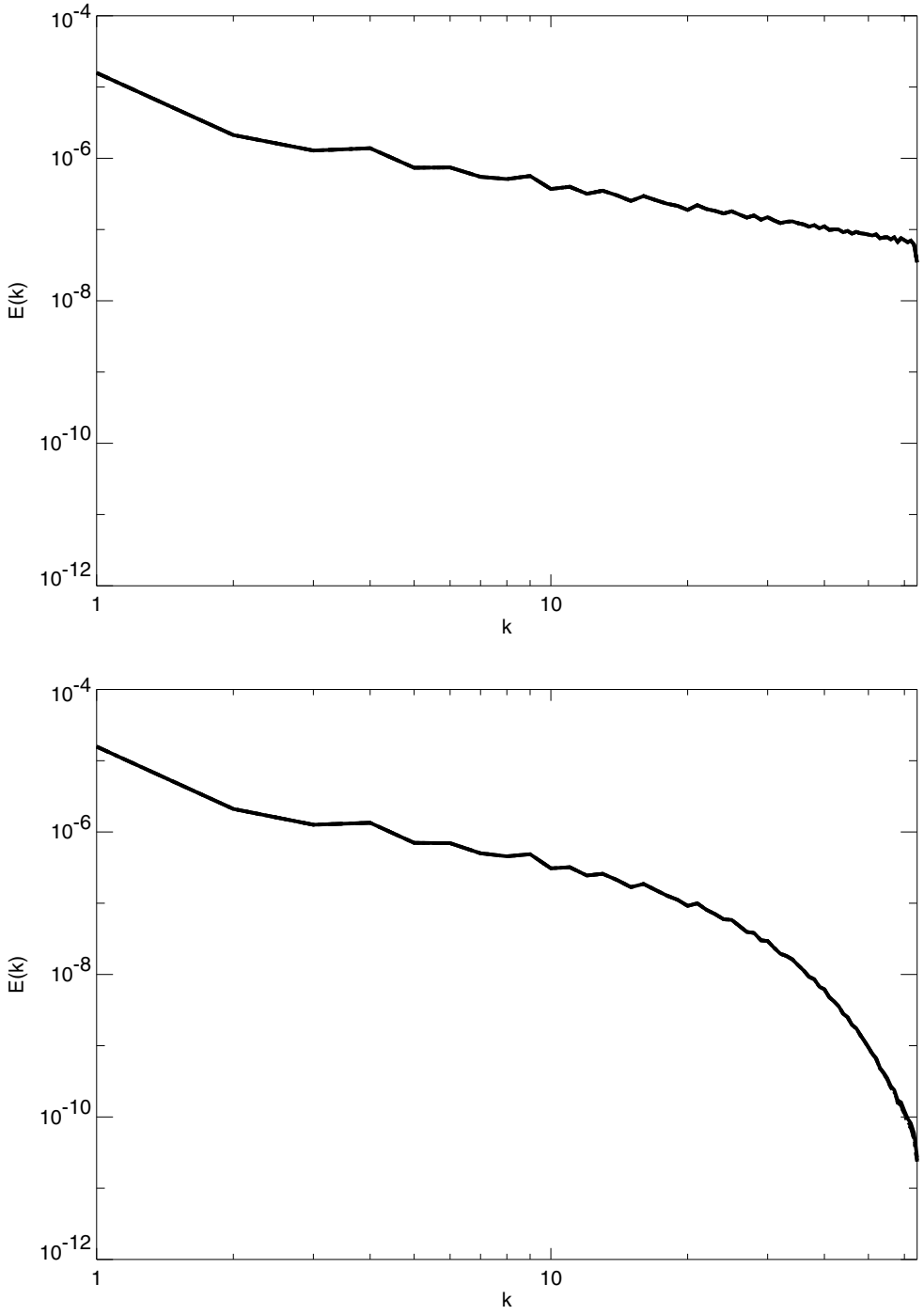

Figure 5.28: (top) Initial Mean and Transient energy fields. (bottom) Mean and Transient energy spectra at t=0.18. Component field diagrams: mean field; DNS (dashed lines), CUQDIA (dotted lines), :transient field; DNS (solid lines), CUQDIA (dot dashed). Note that the respective DNS and CUQDIA closure fields are almost in exact agreement and are consequently indistinguishable.

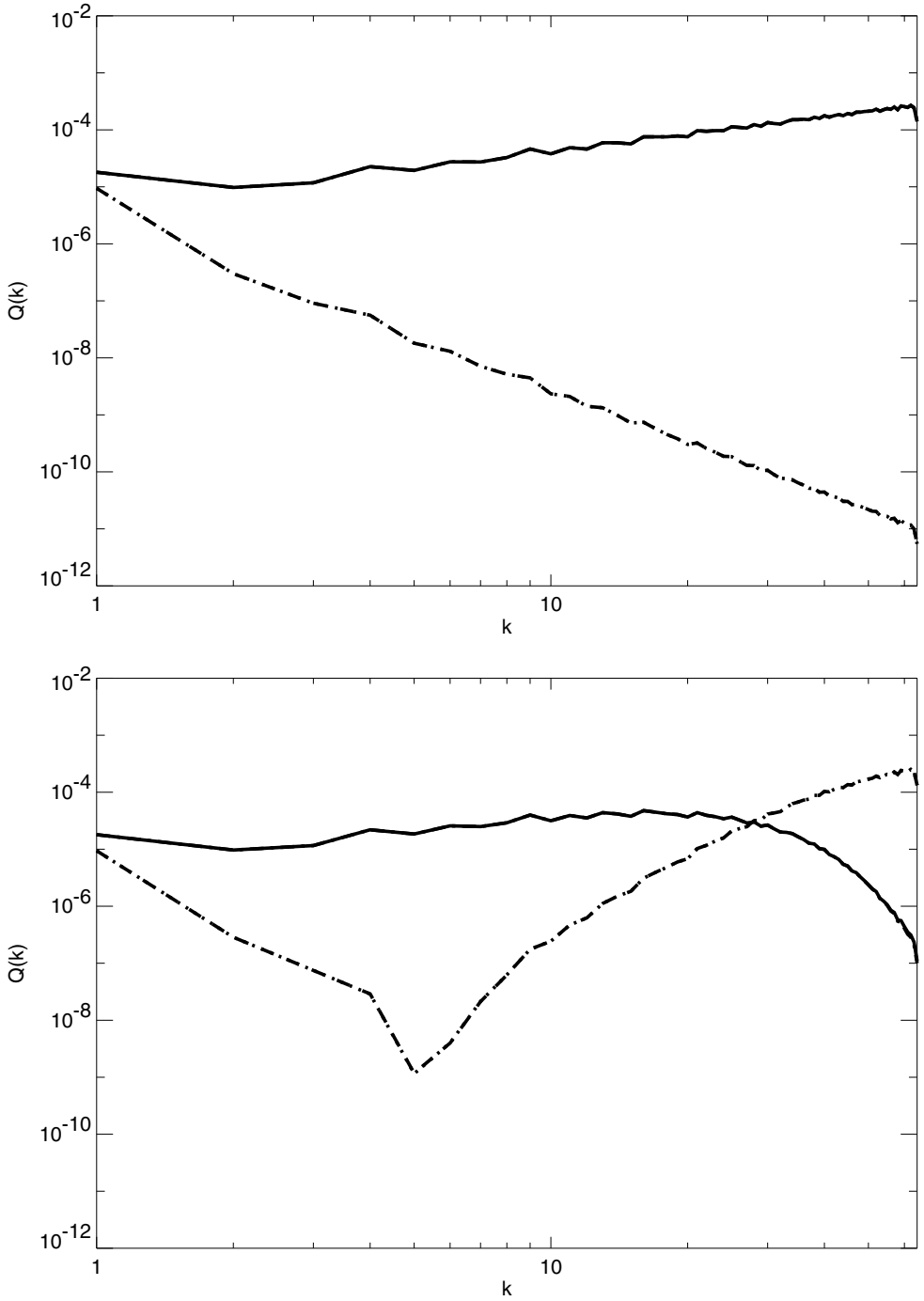

Figure 5.29: (top) Initial Mean and Transient potential enstrophy spectra. (bottom) Mean and Transient potential enstrophy spectra at t=0.18. Component field diagrams: mean field; DNS (dashed lines), CUQDIA (dotted lines), :transient field; DNS (solid lines), CUQDIA (dot dashed). Note that the respective DNS and CUQDIA closure fields are almost in exact agreement and are consequently indistinguishable.

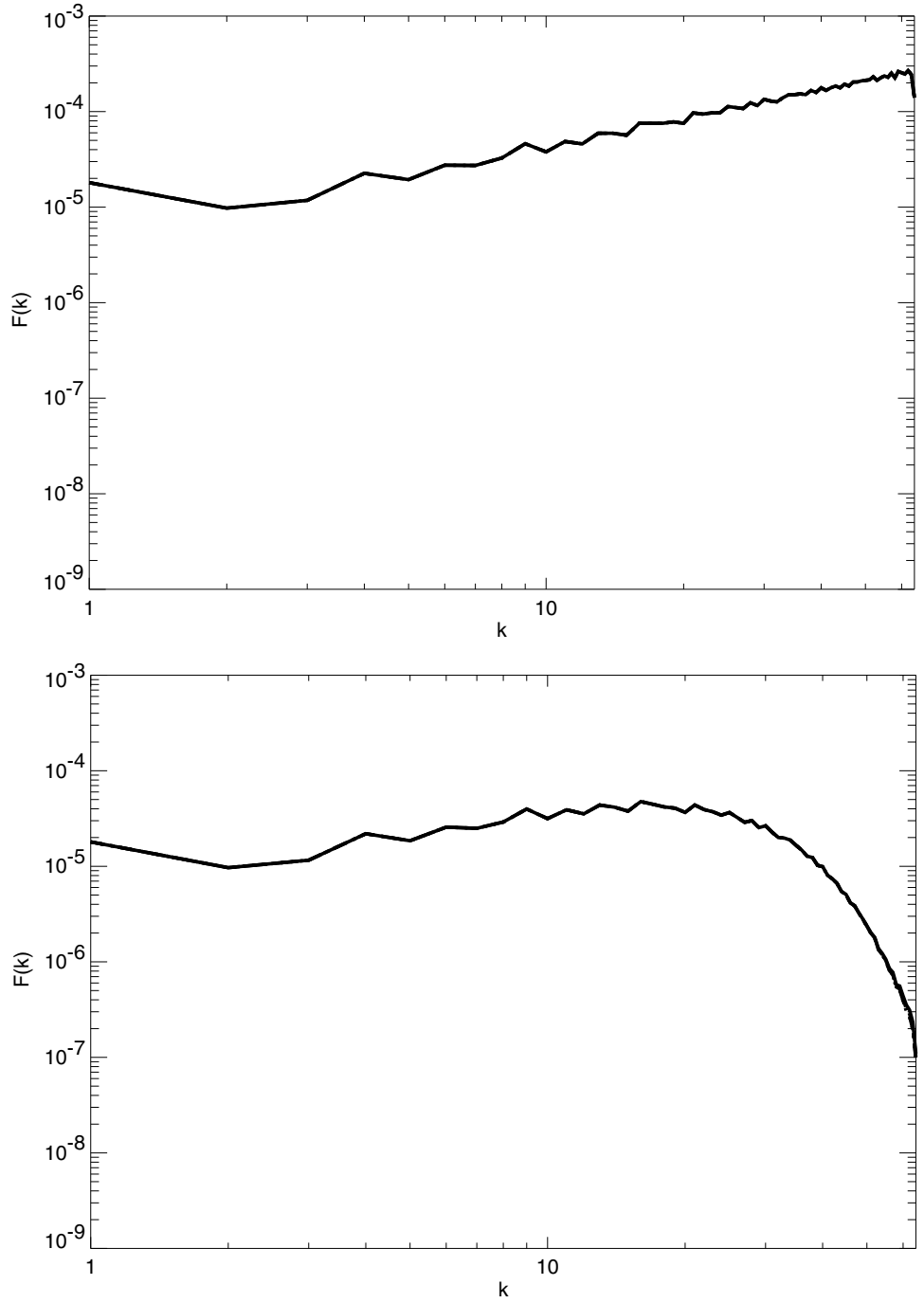

Figure 5.30: (top) Initial Mean and Transient enstrophy spectra. (bottom) Mean and Transient enstrophy spectra at t=0.18. Component field diagrams: mean field; DNS (dashed lines), CUQDIA (dotted lines), :transient field; DNS (solid lines), CUQDIA (dot dashed). Note that the respective DNS and CUQDIA closure fields are almost in exact agreement and are consequently indistinguishable.

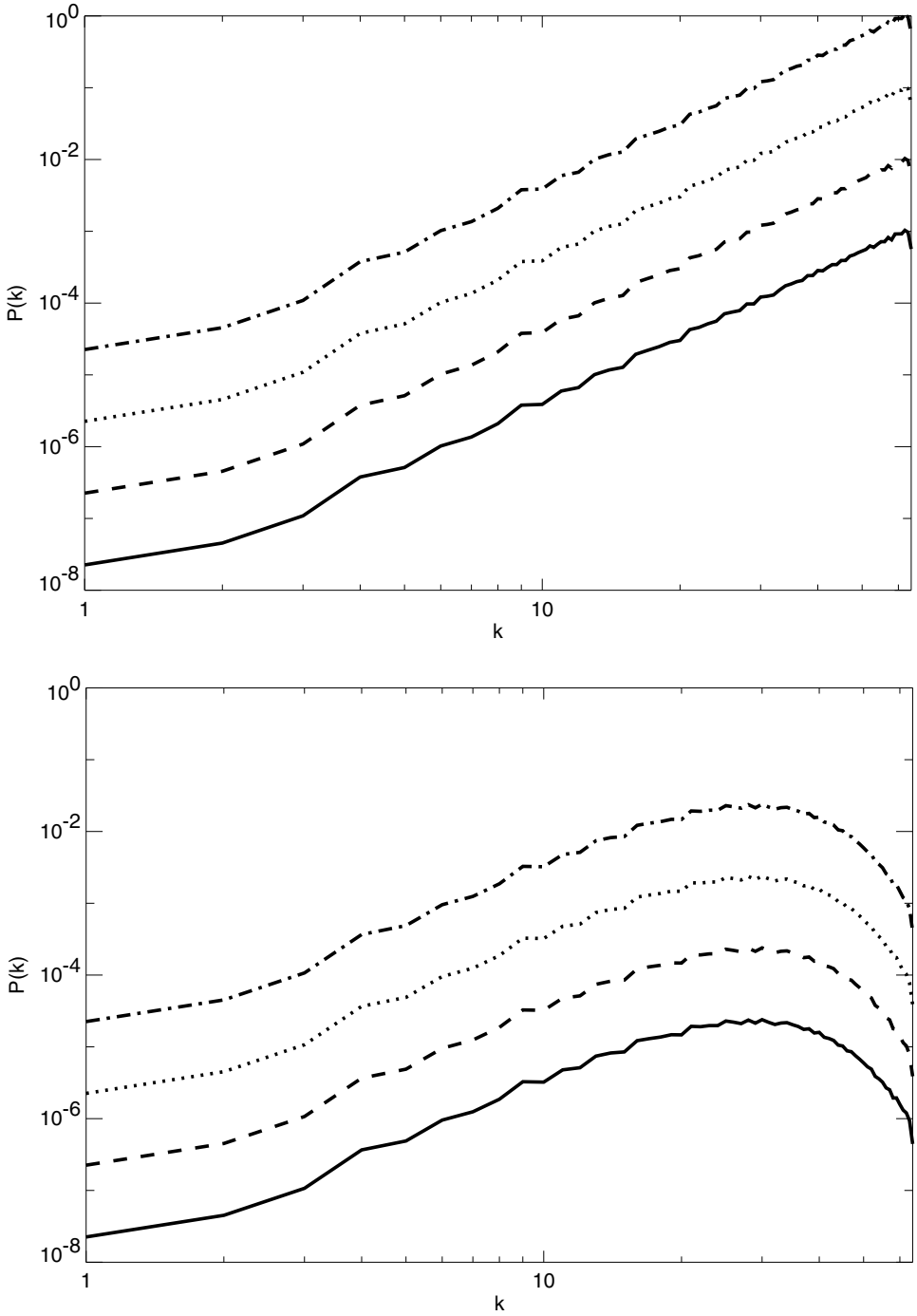

Figure 5.31: (top) Initial Mean and Transient palinstrophy spectra. (bottom) Mean and Transient palinstrophy spectra at t=0.18. The DNS transient palinstrophy spectrum (solid) has been reduced by a factor of 1×10^{-3}, the DNS mean (dashed) reduced by a factor of 1×10^{-2}, the CUQDIA mean (dotted) reduced by a factor of 1×10^{-1} with the CUQDIA transient palinstrophy spectra (dot dashed) is unchanged.

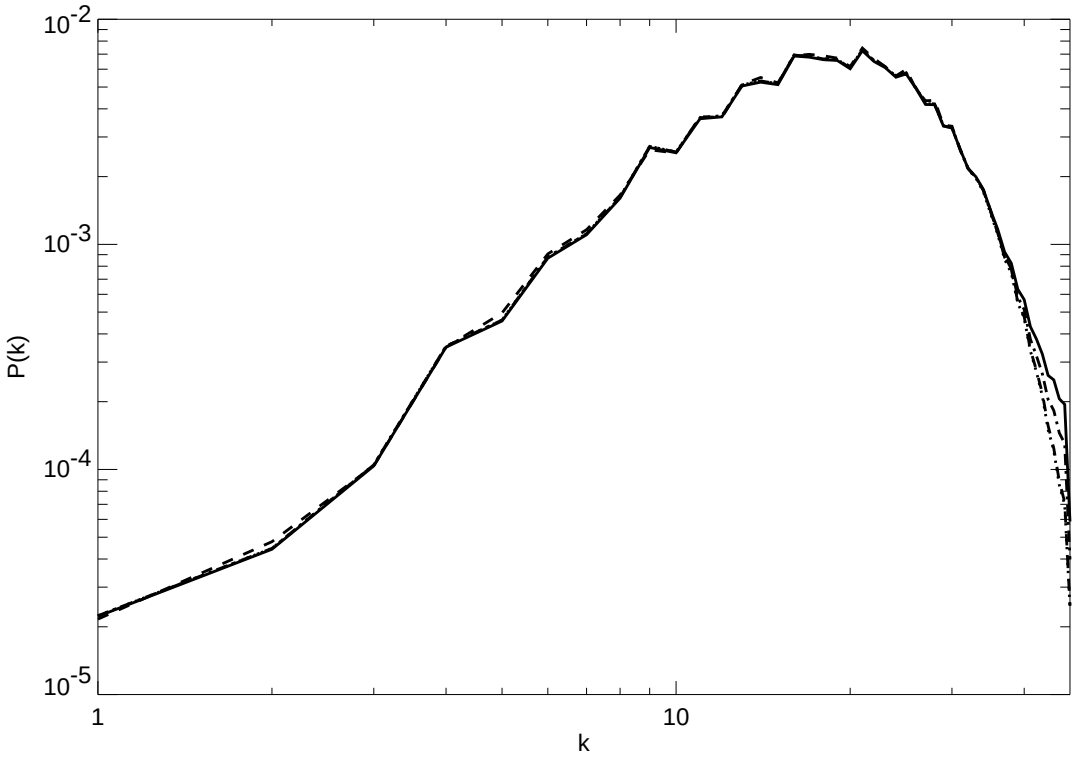

Figure 5.32: The same case as for the preceding figure ie Fig. 5.31 at resolution C48 evolved for 100 timesteps. Note that the CUQDIA transient-field palinstrophy is demonstrating slight spurious convection effects in the smallest scales. Component field diagrams: mean field; DNS (dashed lines), CUQDIA (dotted lines), :transient field; DNS (solid lines), CUQDIA (dot dashed).

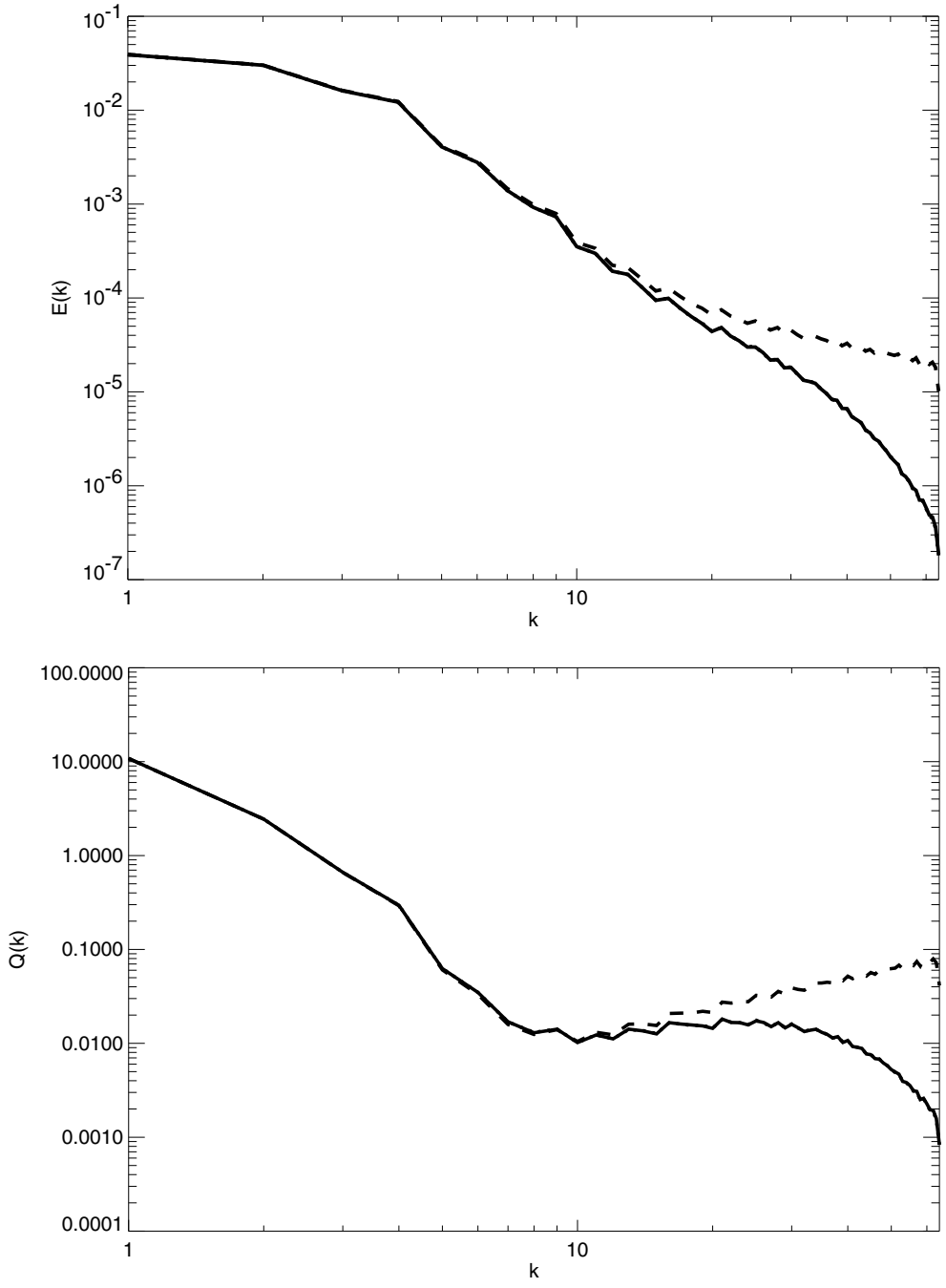

Figure 5.33: (top) Total energy for the DNS (solid) and CUQDIA (dotted) calculations after 50 timesteps. The initial field is the dashed line. The parameters are as for table 5.13 however the amplitude squared of the topography has been modified to $\frac{16k^2}{(1+k^3)^2}$. Restarts occur at every 10 timesteps. (bottom) Total potential-enstrophy for the DNS (solid) and CUQDIA (dotted) calculations after 50 timesteps. The initial field is the dashed line. Note that the respective DNS and CUQDIA closure fields are almost in exact agreement and are consequently indistinguishable.

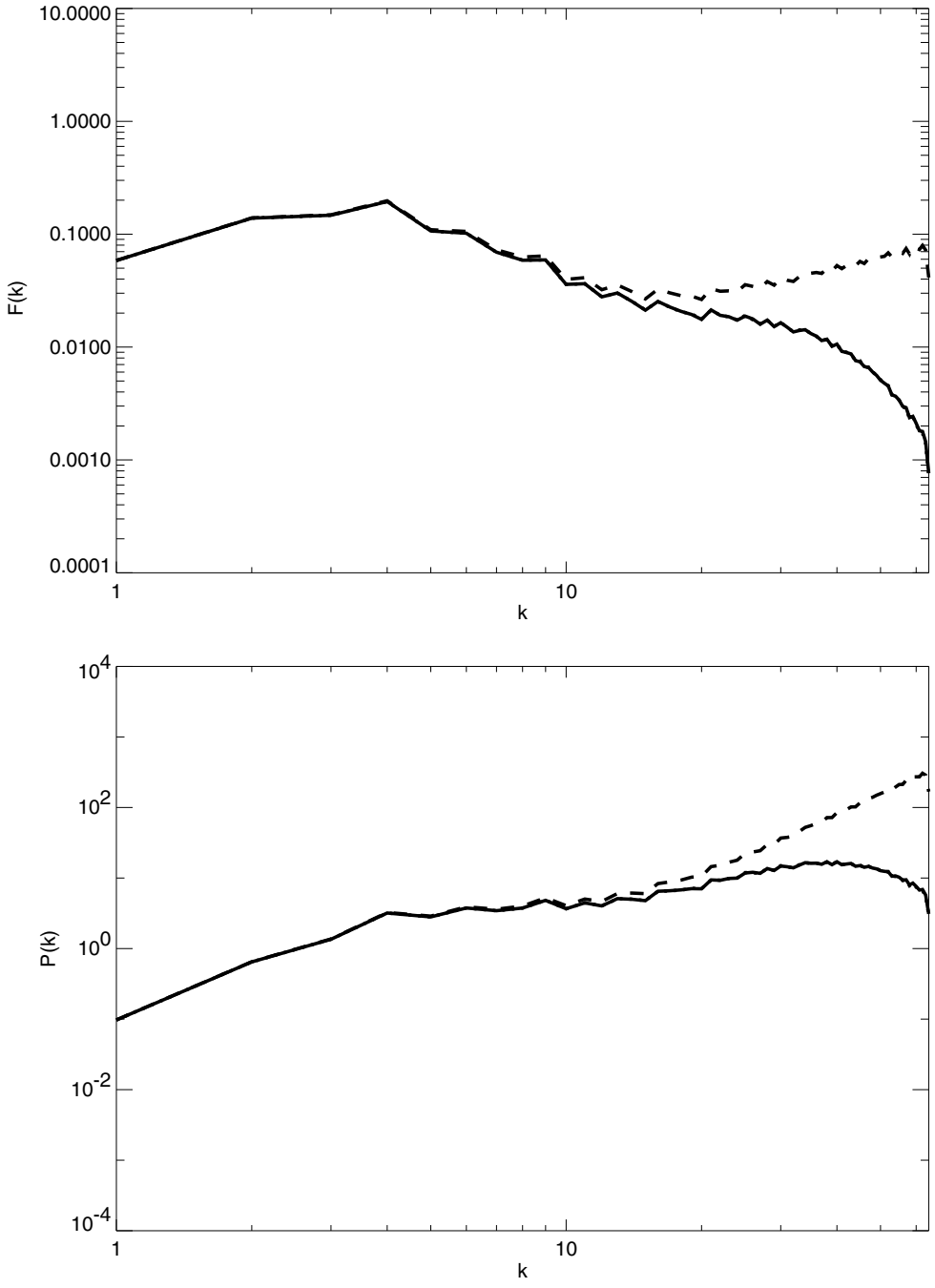

Figure 5.34: (top) Total enstrophy at t=0.2. (bottom) Total palinstrophy at t=0.2. Total field diagrams; DNS (solid lines), CUQDIA (dotted lines), initial fields (dashed lines). Note that the respective DNS and CUQDIA closure fields are almost in exact agreement and are consequently indistinguishable.

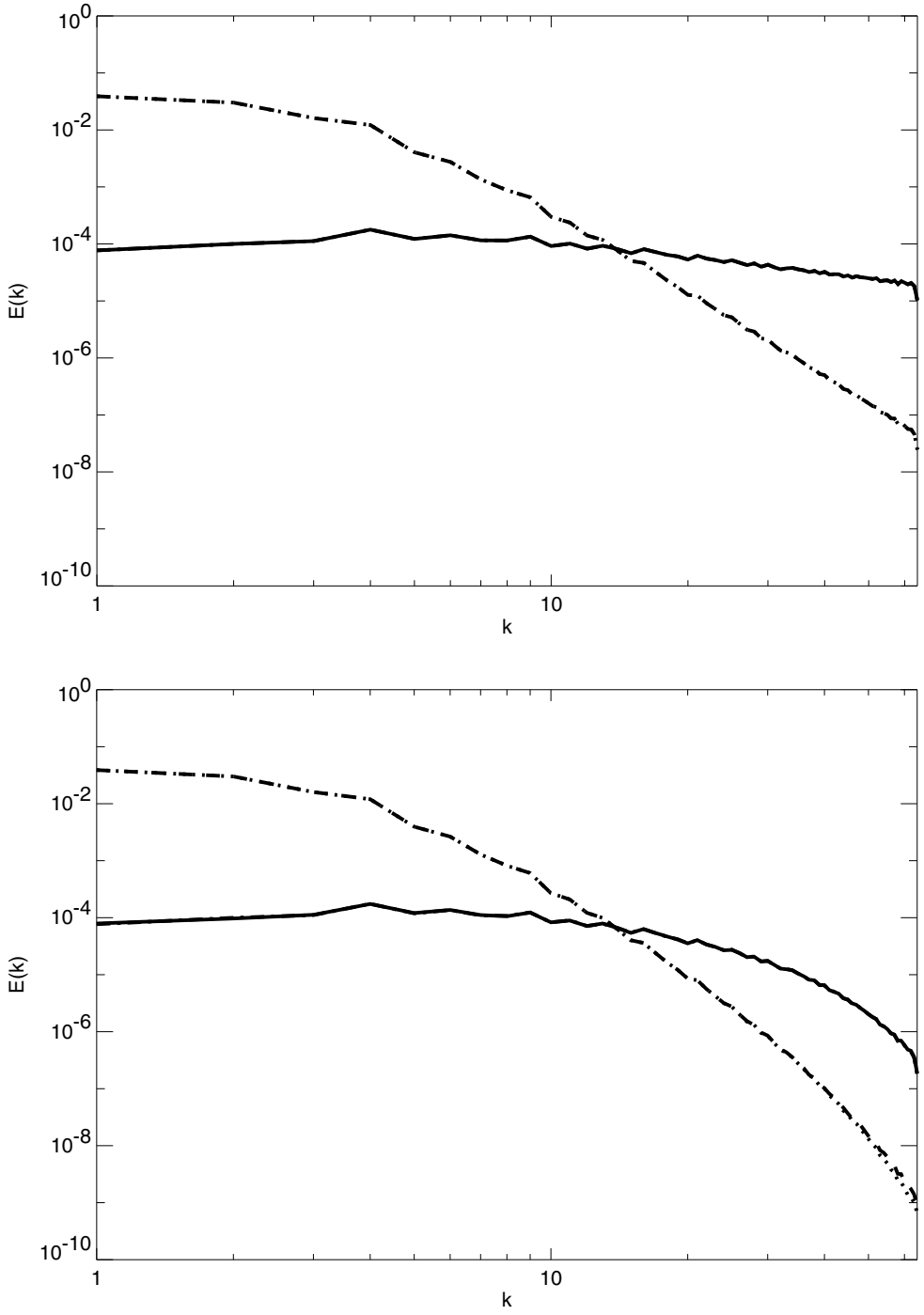

Figure 5.35: (top) Initial Mean and Transient energy fields. (bottom) Mean and Transient energy spectra after 50 timesteps. Component field diagrams: mean field; DNS (dashed lines), CUQDIA (dotted lines), :transient field; DNS (solid lines), CUQDIA (dot dashed). Note that the respective DNS and CUQDIA closure fields are almost in exact agreement and are consequently indistinguishable.

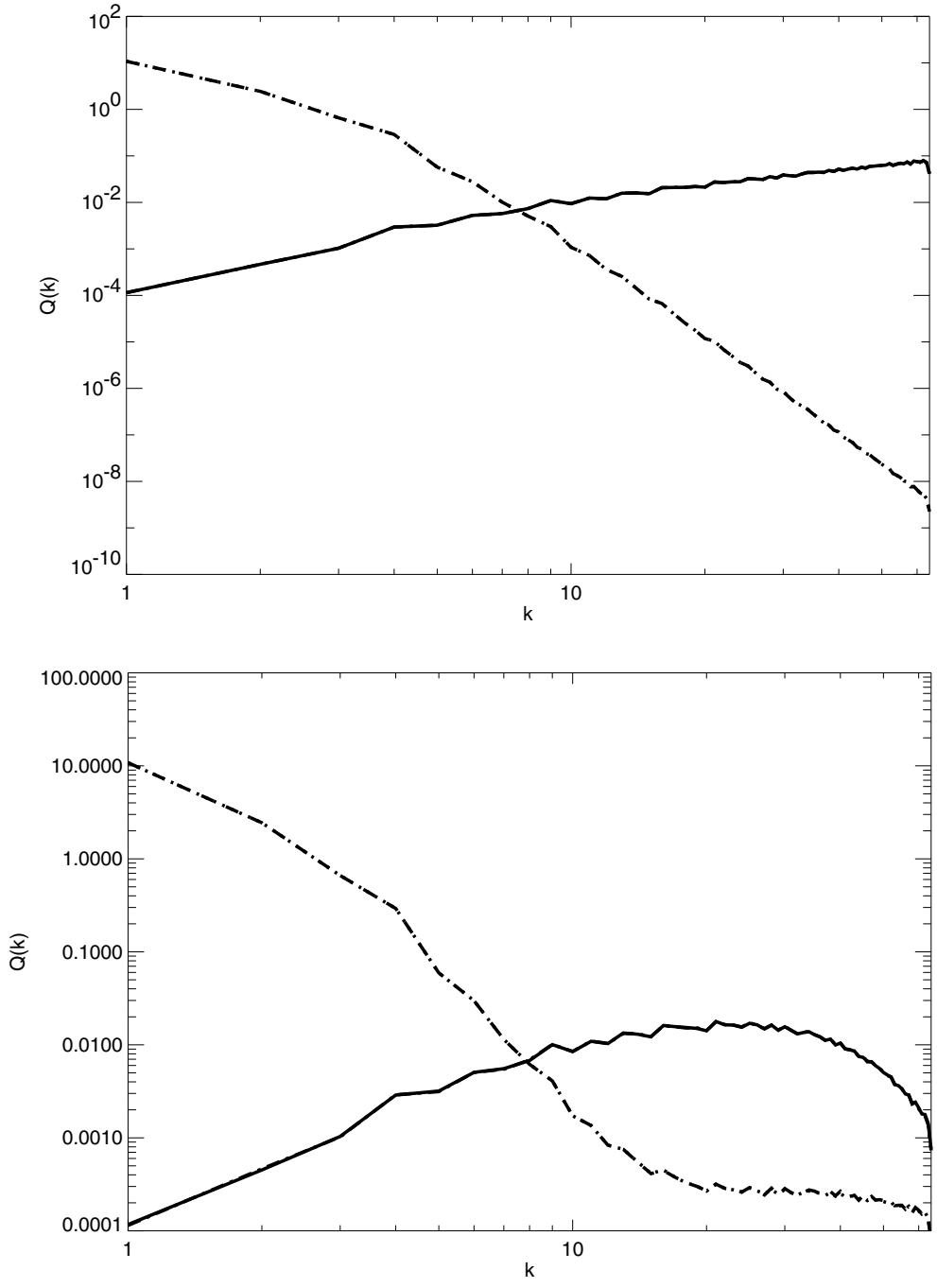

Figure 5.36: (top) Initial Mean and Transient potential enstrophy spectra. (bottom) Mean and Transient potential enstrophy spectra at t=0.2. Component field diagrams: mean field; DNS (dashed lines), CUQDIA (dotted lines), :transient field; DNS (solid lines), CUQDIA (dot dashed). Note that the respective DNS and CUQDIA closure fields are almost in exact agreement and are consequently indistinguishable.

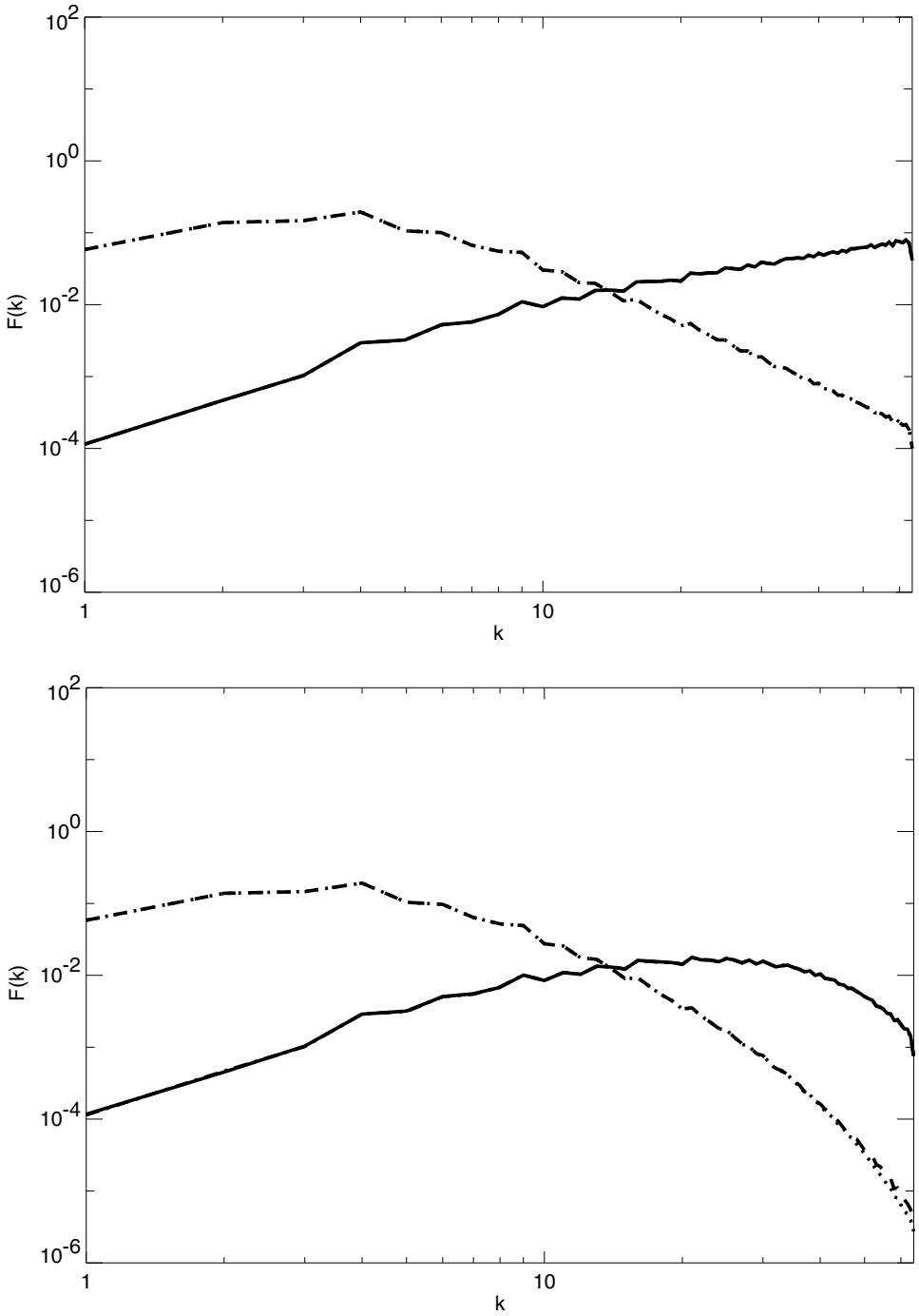

Figure 5.37: (top) Initial Mean and Transient enstrophy spectra. (bottom) Mean and Transient enstrophy spectra at t=0.2. Component field diagrams: mean field; DNS (dashed lines), CUQDIA (dotted lines), :transient field; DNS (solid lines), CUQDIA (dot dashed). Note that the respective DNS and CUQDIA closure fields are almost in exact agreement and are consequently almost indistinguishable.

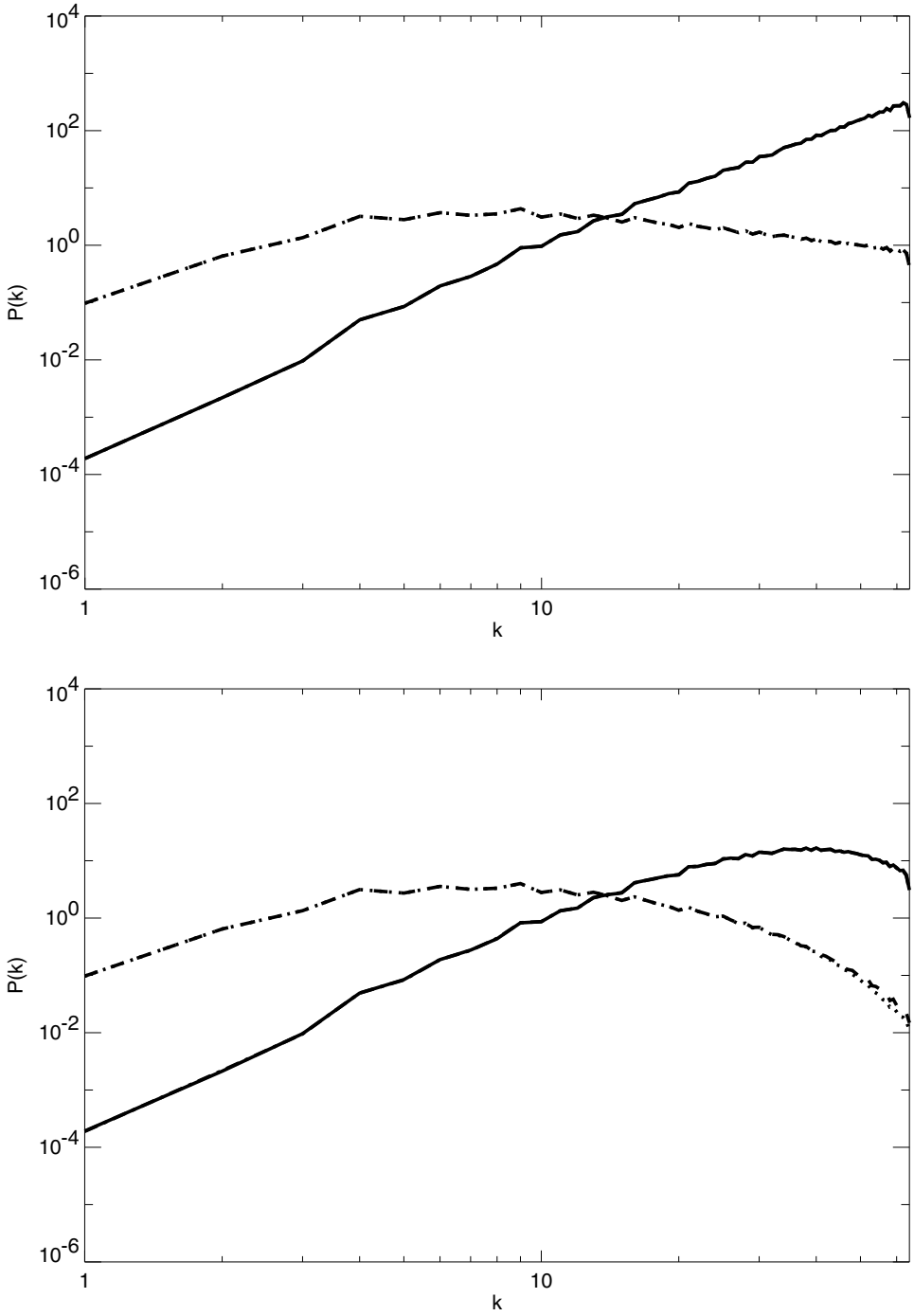

Figure 5.38: (top) Initial Mean and Transient palinstrophy spectra. (bottom) Mean and Transient palinstrophy spectra after 50 timesteps. Component field diagrams: mean field; DNS (dashed lines), CUQDIA (dotted lines), :transient field; DNS (solid lines), CUQDIA (dot dashed). Note that the respective DNS and CUQDIA closure fields are almost in exact agreement and are consequently almost indistinguishable.

5.6 Low to Moderate Reynolds number turbulence

In the experiments of the previous section the Reynolds number was purposely kept low in order to test the closure performance in the absence of strong turbulence effects. In this section we will consider low and moderate Reynolds number turbulence making direct comparisons with the previous isotropic turbulence studies of Herring et al. [112] and Frederiksen and Davies [108]. Our initial transient enstrophy spectra correspond closely to spectra I and II of the Herring et al. [112] paper and exactly to spectra A and B of Frederiksen and Davies [108]. The initial mean enstrophy spectra correspond to an equilibrium mean vorticity field $\langle \zeta_{\mathbf{k}}(0) \rangle = -bh_{\mathbf{k}} \frac{k^2}{a+bk^2}$ for topography of the form $h_{\mathbf{k}}$ and parameters a and b as given in table 5.15. The DNS and closure use nondimesional timesteps of 0.004 or 0.003 and are integrated for 100 timesteps at C48 and 45 timesteps at C64 resolution respectively. Cumulant updates are at every 20 timesteps for the C48 calculation and 10 timesteps for the C64 case. The DNS spectra represent an ensemble average of 100 realizations with standard deviations comparable to those in Figs. 1, 3 and 4 of Frederiksen and Davies [108]. Nondimensional viscosities of $\hat{\nu} = 0.005$ and $\hat{\nu} = 0.0025$ give initial Reynolds number of 61.4 and 304.83 for spectra A and B respectively.

If we denote the right-hand side of the two-time cumulant Eq. 3.60 to be $N_{\mathbf{k}}(t, \acute{t})$ then we have that

$$(\frac{\partial}{\partial t} + \nu(k))C_{\mathbf{k}}(t, \acute{t}) = N_{\mathbf{k}}(t, \acute{t}). \tag{5.17}$$

It is now possible to define the palinstrophy production and enstrophy dissipation as

$$K(t) = \sum_{\mathbf{k}} k^2 N_k(t, t) \tag{5.18}$$

$$\eta(t) = \sum_{\mathbf{k}} \hat{\nu} k^2 C_k(t, t). \tag{5.19}$$

Following [108] and [112] we define the large-scale Reynolds number $R_L(t)$ and the skewness $S_K(t)$ by

$$R_L(t) = \hat{E}/(\hat{\nu}\eta^{1/3}) \tag{5.20}$$

$$S_K(t) = 2K/(\hat{P}\hat{F}^{1/2}). \tag{5.21}$$

Here, the transient energy, enstrophy, and palinstrophy are given by

$$\hat{E}(t) = \frac{1}{2}\sum_{\mathbf{k}} C_{\mathbf{k}}(t,t)/k^2, \tag{5.22}$$

$$\hat{F}(t) = \frac{1}{2}\sum_{\mathbf{k}} C_{\mathbf{k}}(t,t), \tag{5.23}$$

$$\hat{P}(t) = \frac{1}{2}\sum_{\mathbf{k}} C_{\mathbf{k}}(t,t)k^2. \tag{5.24}$$

$$\tag{5.25}$$

These additional diagnostics will be used to compare the DNS and CUQDIA closure and, as well, a closure where the cumulant updates are zeroed at each successive restart step which will be called the ZCUQDIA. The low Reynolds number study starting from spectrum A is performed at C48 resolution. In section 5.6.2 we compare two cases with nearly identical initial conditions but with respective topographies for which $|h_{\mathbf{k}}|^2 = \frac{4k}{(1+k^3)}$ and $|h_{\mathbf{k}}|^2 = \frac{16k^2}{(1+k^3)^2}$. These two cases are intended to identify the effect of the strength of the topography at the small scales on the spectra of the mean and transient fields. Both cases are run at C48 resolution with the $|h_{\mathbf{k}}|^2 = \frac{16k^2}{(1+k^3)^2}$ experiment compared to a higher resolution C64 calculation.

5.6.1 Spectrum A

Table 5.15: Parameters for Figs. 5.39-5.42

$\triangle$ t	$\hat{\nu}$	a	b	$\lvert h_{\mathbf{k}}\rvert^2$	$F_{\mathbf{k}}$	$\langle f_{\mathbf{k}}\rangle$
0.004	0.005	4.824×10^4	2.511×10^3	$16k^2/(1+k^3)^2$	0	0

In the following study of low Reynolds number turbulence the initial transient (twice) enstrophies spectrum used closely corresponds to spectrum I of Herring et al. [112] and exactly to spectrum A of Frederiksen and Davies [108]. This choice of spectrum and viscosity yields an initial large-scale Reynolds number of $R_L(0) = 61.4$. The initial transient

spectrum (Eq. 5.26) is coupled to an initial mean vorticity given in Eq. 5.27:

$$C_{\mathbf{k}}(0,0) = 1.33 \times 10^{-4} k^5 \exp -k^2/32, \tag{5.26}$$

$$\langle \zeta_{\mathbf{k}}(0) \rangle = -bh_{\mathbf{k}} \frac{k^2}{a + bk^2}. \tag{5.27}$$

This study is carried out at C48 resolution where we compare the evolved kinetic energy, palinstrophy, skewness and large-scale Reynolds number. The choice of parameters a and b is the same as Frederiksen and Sawford [95] used to fit the large scales of meteorological flows. These parameters are also the same as those used in a previous study of severely truncated (C3) homogeneous isotropic turbulence without topography or mean flow [104]. The parameters used are given in table 5.15. The choice of nondimensional viscosity is $\hat{\nu} = 0.005$ which again corresponds to that used previously [112, 108].

In Fig. 5.39 we compare the DNS and CUQDIA evolved total energy (top) and total palinstrophy (bottom) at $t = 0.4$, corresponding to 100 timesteps with a nondimensional timestep of $\triangle t = 0.004$. Although only half the time period considered in the earlier studies, the system has been shown to undergo very significant evolution. The rapid evolution of the flow fields can only be attributed to the presence of both topography and a mean-field. The CUQDIA total energy shows excellent agreement with DNS up to $k < 32$ after which the closure slightly under-represents the total energy. A similar picture is evident in the total palinstrophy with some slight over-estimation at wavenumbers 10-20 and underestimation again evident for $k > 32$.

A comparison (Fig. 5.39) with Fig. 1 of Frederiksen and Davies [108] and Figs. 18 and 19 of Herring et al [112] reveals a much more dramatic and rapid increase in the total energy and palinstrophy at the smallest scales when topography and a mean-vorticity are present. This would seem to be due to the relatively large amplitude $\langle \zeta_{\mathbf{k}}(t) \rangle$ and $h_{\mathbf{k}}$ at the small scales forcing the tendency of the transients at the small scales rather rapidly via the $P_{\mathbf{k}}$ and $\pi_{\mathbf{k}}$ terms in the equations for the cumulants (Eqs. 3.27 and 3.33). In Figs. 5.40 and 5.41 we see that this indeed the case. In both the evolved mean and transient energy and palinstrophy spectra it is the transient fields that have undergone rapid increase at the small scales whereas the mean energy and palinstrophy fields have evolved much less significantly. We see very close agreement between the CUQDIA and DNS transient fields

except at the smallest scales and some slight but systematic underestimation of the closure mean fields.

In Fig. 5.42 the DNS and CUQDIA skewness (top) and Reynolds number (bottom) are compared. In Fig. 2c of Frederiksen and Davies [108] it was shown that the discrete closure resulted in a very much improved estimation of the skewness in comparison to the continuous DIA closure (Fig. 12 [112]). For inhomogeneous flow over topography we see that the CUQDIA skewness is under-estimated with final values of $S_K^{CUQDIA}(0.4) = 0.25$ as compared to $S_K^{DNS}(0.4) = 0.41$. This not surprising given that the energy error in the closure for Fig. 5.40 is $O(10^{-4})$ and only $O(10^{-7})$ in Fig. 1a of Frederiksen and Davies [108]. A further comparison of the Reynolds number (Fig. 5.42 bottom) reveals fairly good agreement throughout the evolution to $t = 0.4$.

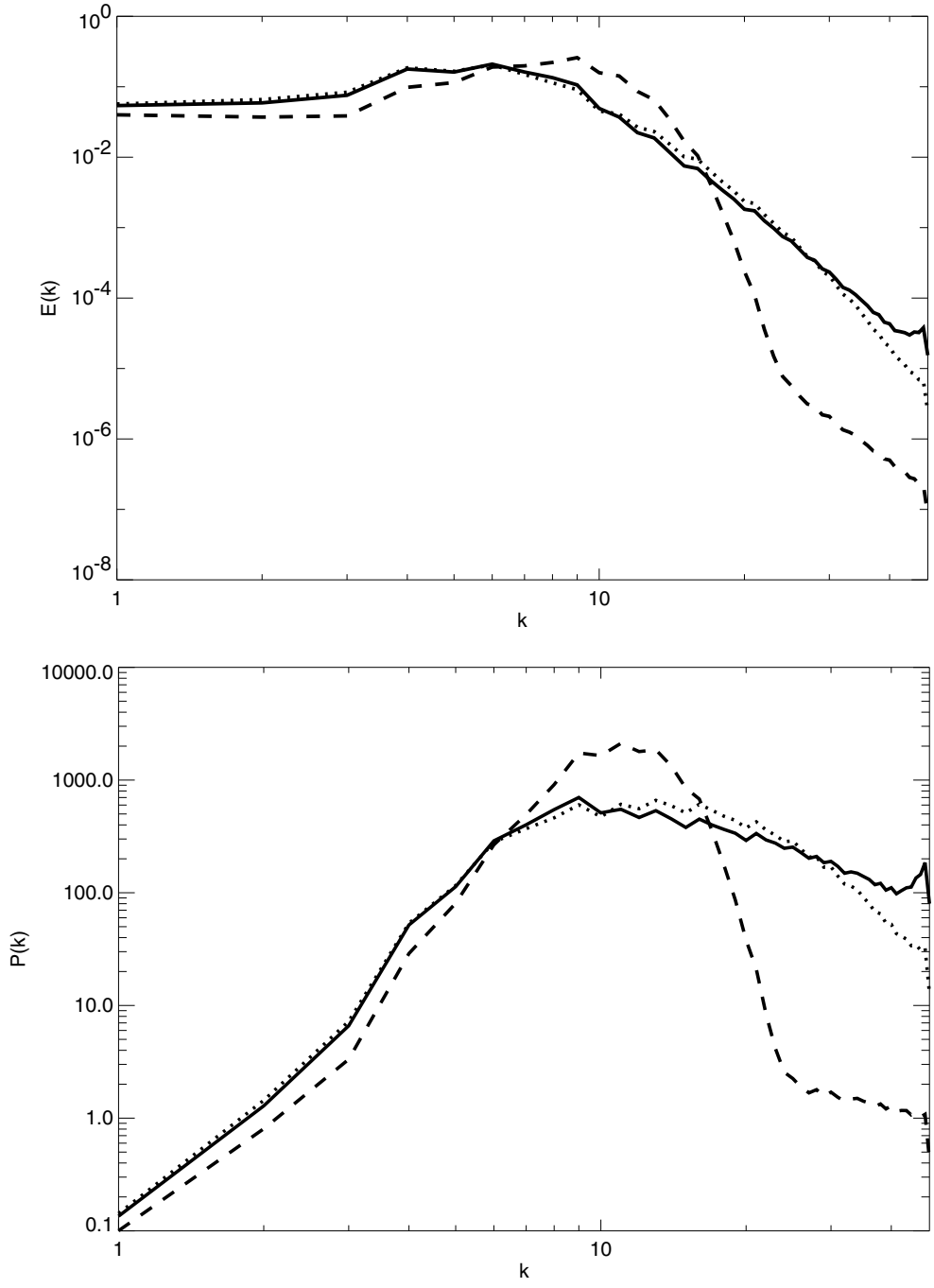

Figure 5.39: C48 resolution spectra. (top) Initial and final (t = 0.4) total kinetic energy spectra. (bottom) Initial and final (t = 0.4) total palinstrophy spectra. The respective spectra are DNS (solid), CUQDIA (dotted) and the initial spectrum (dashed). Cumulant updates occur at every 20 timesteps.

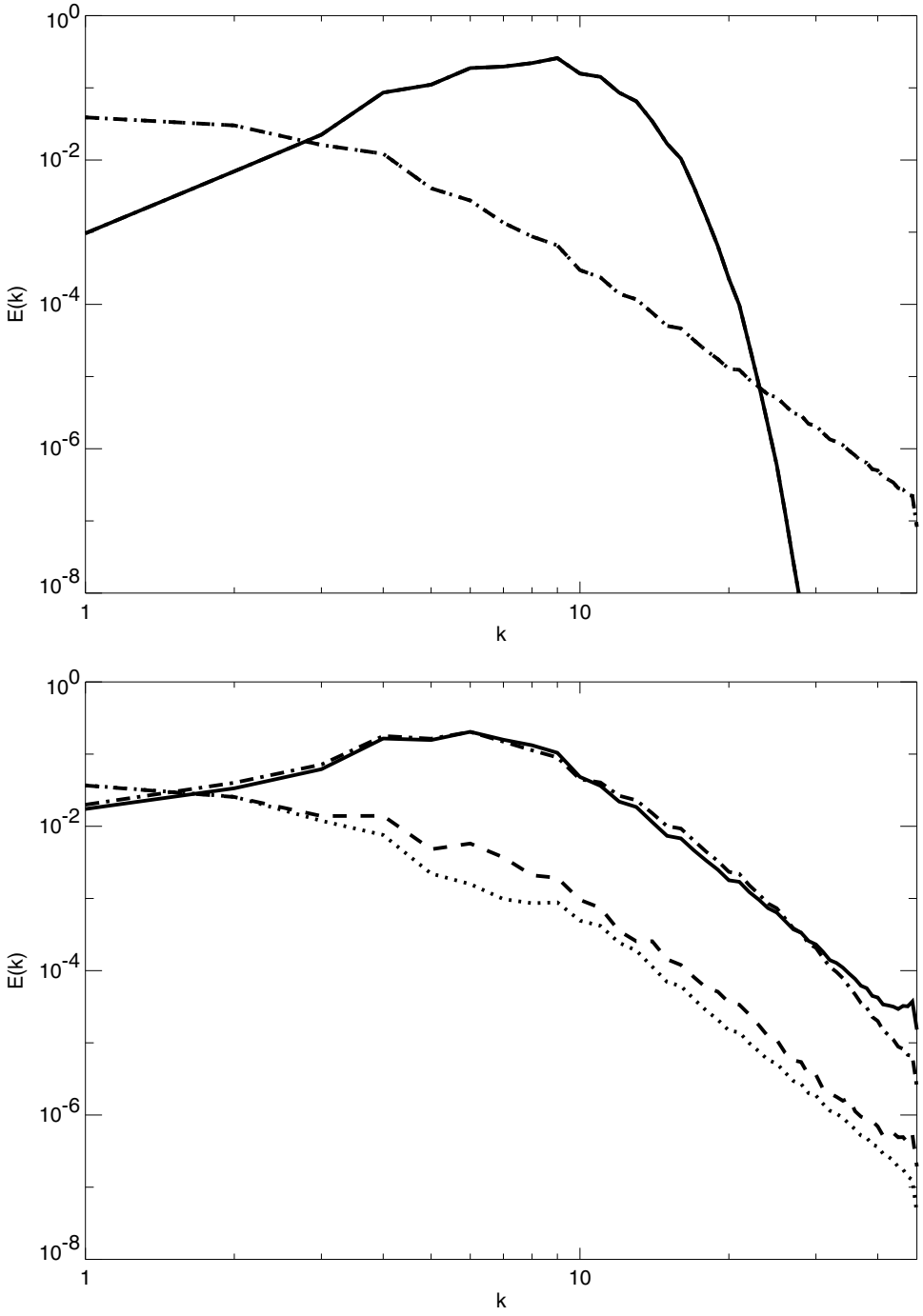

Figure 5.40: C48 resolution spectra. (top) Initial Mean and Transient energy spectra. (bottom) Mean and Transient energy fields at t=0.4. Component field diagrams: mean field; DNS (dashed lines), CUQDIA (dotted lines), :transient field; DNS (solid lines), CUQDIA (dot dashed).

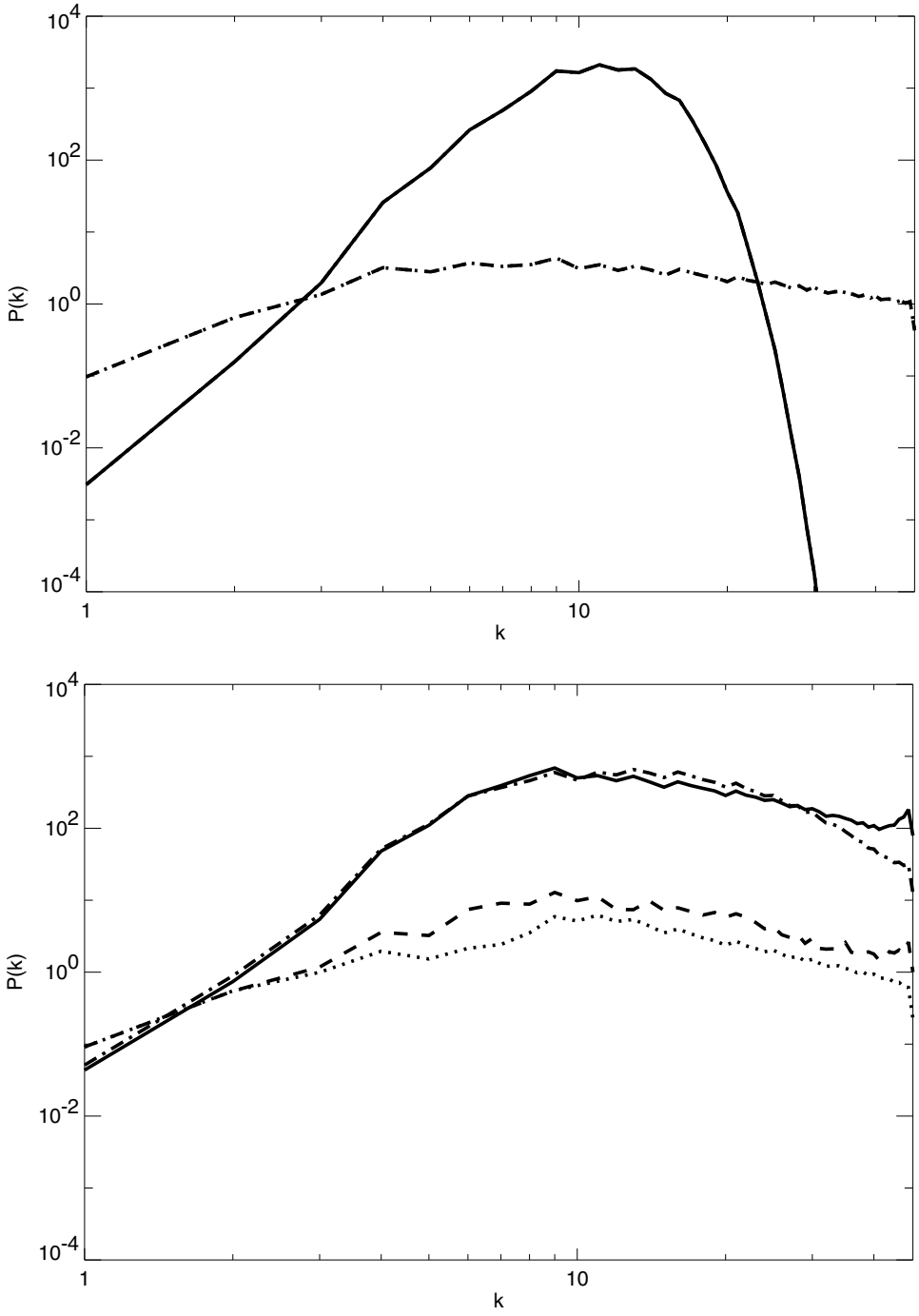

Figure 5.41: C48 resolution spectra. (top) Initial Mean and Transient palinstrophy spectra. (bottom) Mean and Transient palinstrophy spectra at t=0.4. Component field diagrams: mean field; DNS (dashed lines), CUQDIA (dotted lines), :transient field; DNS (solid lines), CUQDIA (dot dashed).

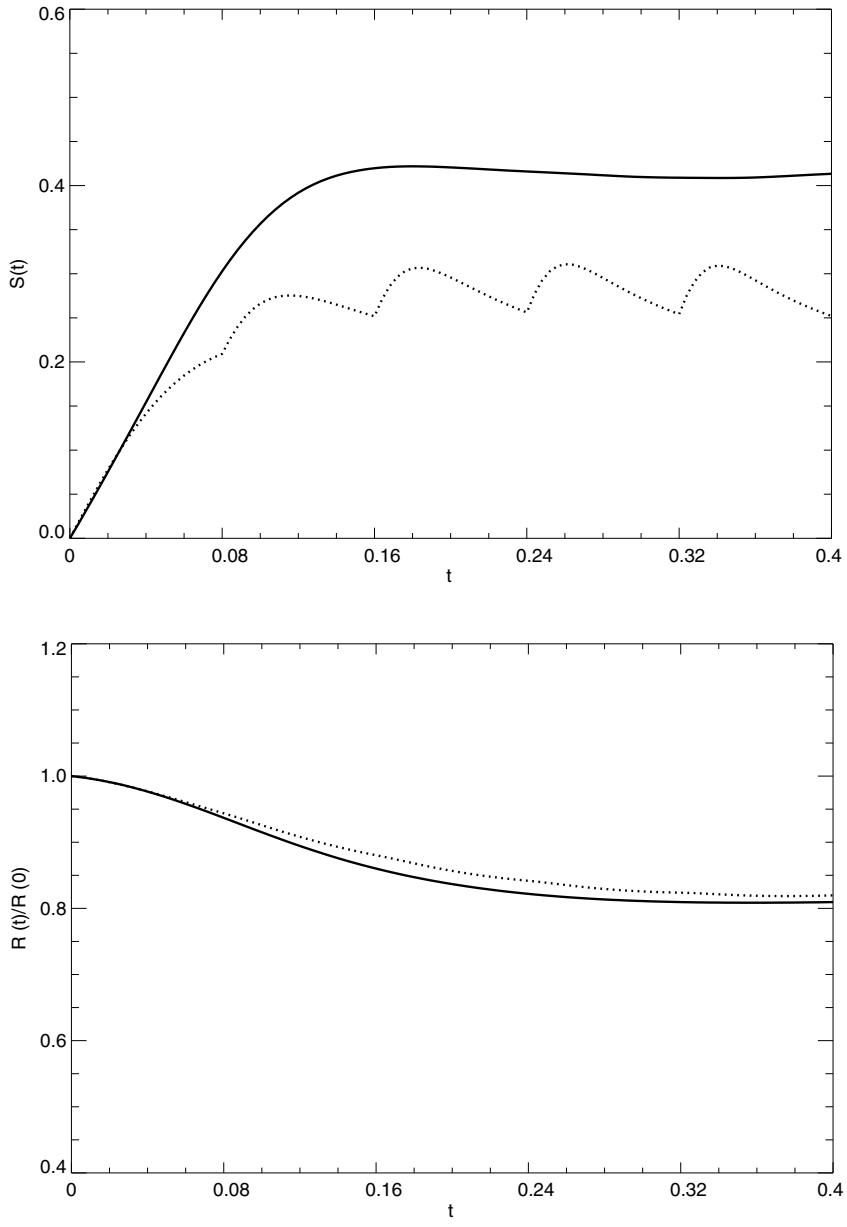

Figure 5.42: (top) Skewness calculated at each successive timestep for C48 resolution. DNS (solid) and CUQDIA (dotted), with restarts calculated at every 20 timesteps. (bottom) $R_L(t)/R_L(0)$ evaluated at times t.

5.6.2 Spectrum B

The next study is at moderate Reynolds number $R_L(0) = 304.8$ and uses the same initial spectrum for the transient enstrophy as spectrum B of Frederiksen and Davies [108] (Eq. 5.28) and is also similar to spectrum II of Herring et al. [112]. The choice of initial mean vorticity (Eq. 5.29) is the same as used in the previous low resolution study with the nondimensional viscosity now set as $\hat{\nu} = 0.0025$. The C48 experiments employ the cumulant update procedure at every 20 timesteps with the C64 calculation using restarts every 10 timesteps. In all experiments in this section we will start with an initial (twice) enstrophy spectrum of

$$C_{\mathbf{k}}(0,0) = 1.8 \times 10^{-1} k^2 \exp -\frac{2}{3}k, \tag{5.28}$$

and an initial mean field

$$\langle \zeta_{\mathbf{k}}(0) \rangle = -bh_{\mathbf{k}} \frac{k^2}{a + bk^2}. \tag{5.29}$$

Two topographies will be considered, firstly a topography whose amplitude squared goes like $1/k^2$ and secondly a topographic amplitude squared that falls away much faster at the small scales ($\approx 1/k^4$). These choices of topography provide a test of the accuracy of the closure with markedly different topographic amplitudes at the small-scales, and consequently differing small-scale eddy-topographic interaction strengths.

In Fig. 5.43 (top) the initial mean and transient spectra are displayed with initial conditions specifying the mean fields given in table 5.16. After a nondimensional evolution period of $t = 0.3$ the evolved mean and transient kinetic energy spectra (Fig. 5.43 bottom) are shown to be in close agreement but for some slight under-estimation of the closure transient field between wavenumbers $20 \leq k \leq 48$, which is also accompanied by some over-estimation for wavenumbers between $7 \leq k \leq 16$.

Table 5.16: Parameters for Figs. 5.43-5.45

$\triangle$ t	$\hat{\nu}$	a	b	$\lvert h_{\mathbf{k}} \rvert^2$	$F_{\mathbf{k}}$	$\langle f_{\mathbf{k}} \rangle$
0.003	0.0025	4.824×10^4	2.511×10^3	$4k/(1+k^3)$	0	0

The mean and transient palinstrophy spectra (Fig. 5.44) show comparable agreement between DNS and the closure transient fields and highlight the very close agreement in the respective mean fields. In Fig. 5.45 it is evident that the closure skewness factor systematically under-estimates the skewness as compared to DNS. The final evolved values are $S_K^{DNS}(0.3) = 1.379$ and $S_K^{CUQDIA}(0.3) = 1.070$ respectively. The temporary increase in the closure skewness factor at the beginning of each update cycle quickly relaxes as the response functions decay. The behavior of the skewness factor for isotropic closures with cumulant updates has been investigated in some detail by Frederiksen and Davies [108]. The CUQDIA closure skewness factor (Fig. 5.45 top) also enables a diagnostic by which the efficiency of the particular choice of restart time $t = \acute{t} = T$ may be judged. That is, by simply observing whether sufficient decay time for the response functions has been allowed over each successive update cycle in order that the skewness return to a value close to that of the closure had cumulant updates not been used. It is clearly evident in Fig. 5.45 (top) that apart from the initial period of rapid increase ($t \in [0, 0.12]$) that a period of $t = \acute{t} = T = 20\triangle t$ is sufficient. In Fig. 5.45 (bottom) the closure is shown to give a reasonable estimate of the evolved Reynolds number with $R_L^{DNS}(0.3) = 164.47$ and $R_L^{CUQDIA}(0.3) = 159.11$.

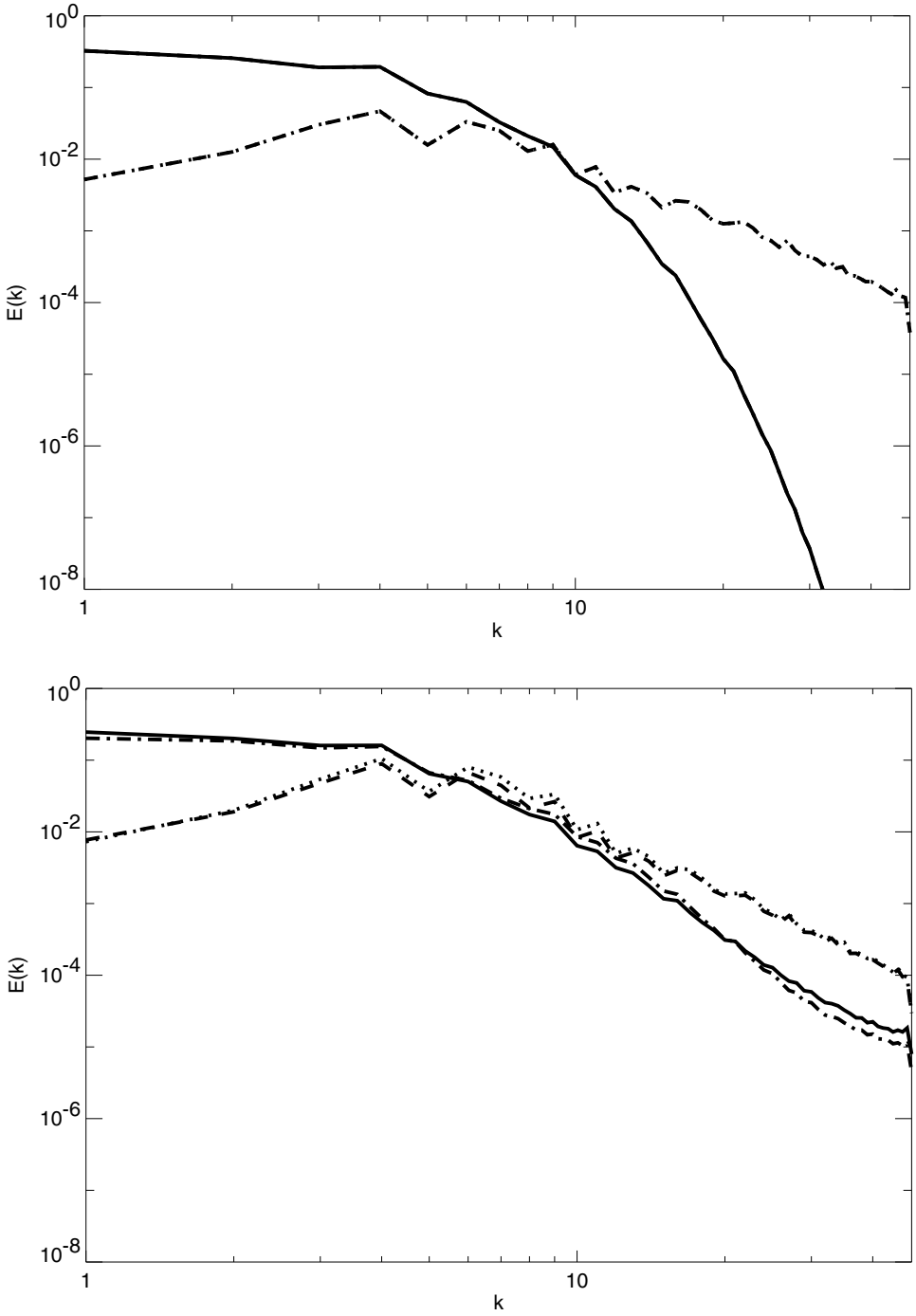

Figure 5.43: C48 resolution spectra. (top) Initial Mean and Transient energy spectra. (bottom) Mean and Transient energy fields at t=0.3. Component field diagrams: mean field; DNS (dashed lines), CUQDIA (dotted lines), :transient field; DNS (solid lines), CUQDIA (dot dashed).

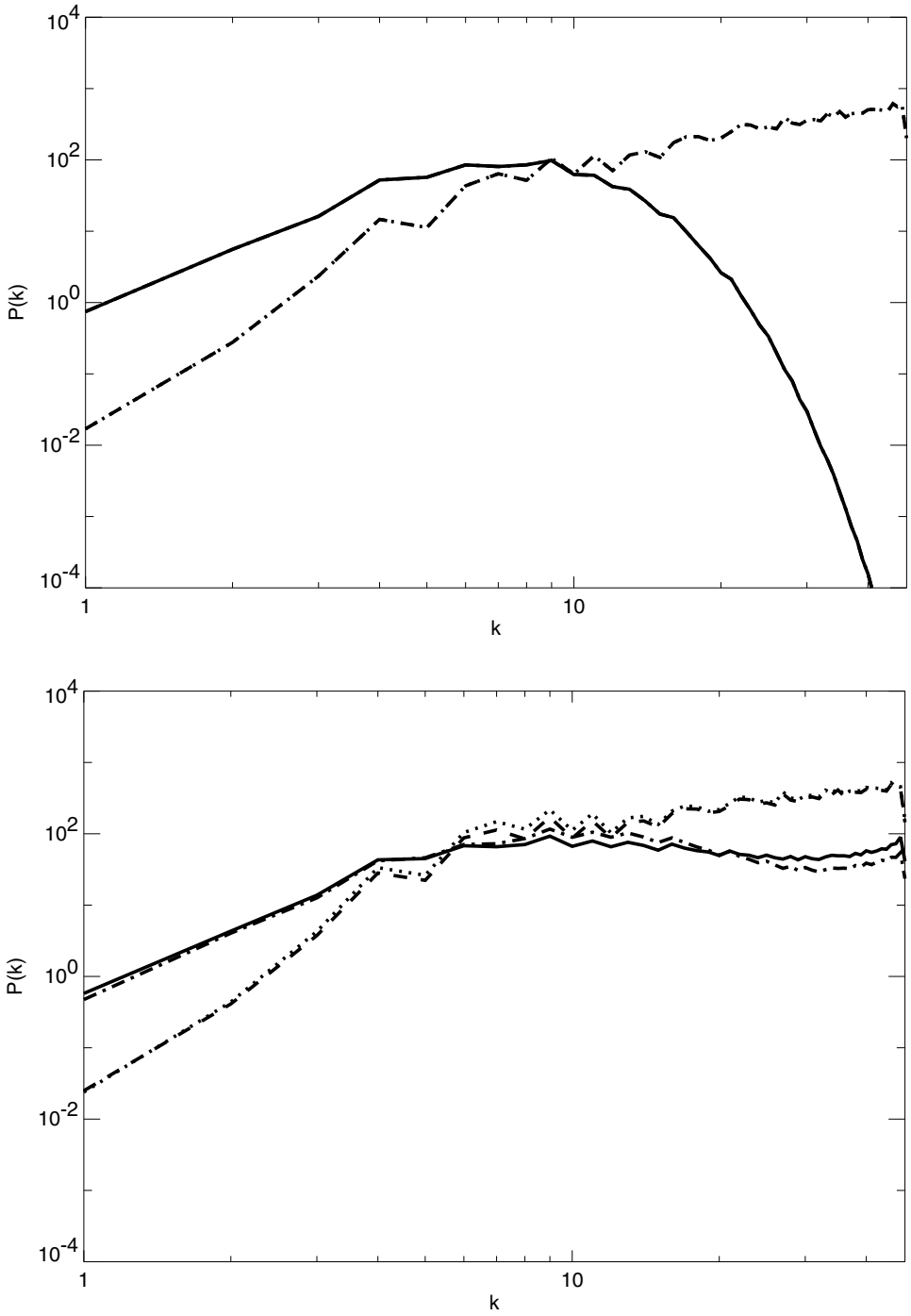

Figure 5.44: C48 resolution spectra. (top) Initial Mean and Transient palinstrophy spectra. (bottom) Mean and Transient palinstrophy spectra at t=0.3. Component field diagrams: mean field; DNS (dashed lines), CUQDIA (dotted lines), :transient field; DNS (solid lines), CUQDIA (dot dashed).

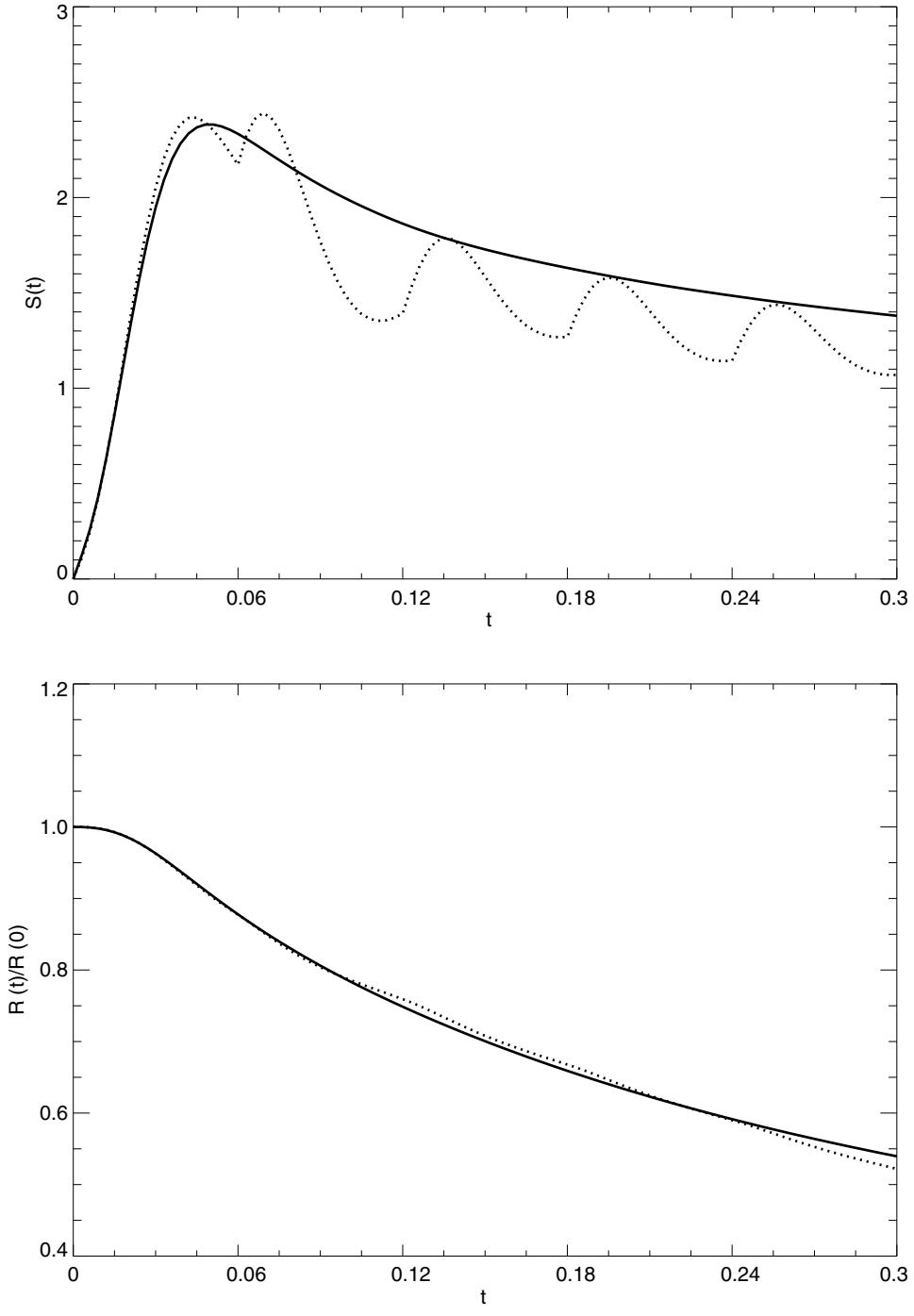

Figure 5.45: (top) Skewness calculated at each successive timestep for C48 resolution. DNS (solid) and CUQDIA (dotted), with restarts calculated at every 20 timesteps. (bottom) $R_L(t)/R_L(0)$ evaluated at times t.

In the second study at C48 resolution the same initial conditions and parameters (but with $\triangle t = 0.004$) are used; however, the topography (squared) now takes the form $|h_{\mathbf{k}}|^2 = 16k^2/(1+k^3)^2$. This choice of topography falls away much more rapidly at the small scales than that used in the previous experiment thus resulting in a significantly reduced initial mean field kinetic energy in the small-scales, as seen in Fig. 5.46 (top). An additional feature of a more rapidly decreasing topographic amplitude is a reduction in the strength of the eddy-topography interaction at the small-scales.

Table 5.17: Parameters for Figs. 5.46-5.51

$\triangle$ t	$\hat{\nu}$	a	b	$\lvert h_{\mathbf{k}}\rvert^2$	$F_{\mathbf{k}}$	$\langle f_{\mathbf{k}} \rangle$
0.004	0.0025	4.824×10^4	2.511×10^3	$16k^2/(1+k^3)^2$	0	0

For $|h_{\mathbf{k}}|^2 = 16k^2/(1+k^3)^2$ both the evolved ($t_f = 0.4$) closure mean kinetic energy (Fig. 5.46 bottom) and mean palinstrophy (Fig. 5.47 bottom) spectra show close agreement with DNS, as was the case when the topography (squared) was of the form $1/k^2$. The transient energy spectra however, have undergone significant increases for $20 < k < 48$ after a period of evolution to $t_f = 0.4$ as compared to the initial spectra; it is also evident that the CUQDIA again underestimates the evolved transient energy for $k > 20$. This is more clearly illustrated in the palinstrophy spectra shown in Fig. 5.47. The failure of the closure to accurately predict the small-scale transient kinetic energy and transient palinstrophy is not surprising given that we know spurious convection effects are inherent in the direct interaction approximation, due to the inaccurate treatment of the three-point cumulant term. These effects were found to be pronounced for this initial transient spectrum in the previous studies of Herring et al [112] and Frederiksen and Davies [108]. As with the low Reynolds study, the most interesting result is that the transient energy and palinstrophy spectra have evolved much more rapidly with a topography and mean vorticity field present in comparison to the previous studies (see Fig. 4 [108] and Figs. 22 and 23 [112]) where they are absent.

It was shown in Figs. 5.43 and 5.44 that the evolved DNS small-scale transient fields remained significantly weaker than the mean-fields; this is an obvious difference to Figs.

5.46 and 5.47 where the evolved small-scale transient fields dominate. The CUQDIA closure was shown to perform significantly better in predicting the evolved transient fields for the case where $|h_{\mathbf{k}}|^2 = \frac{4k}{(1+k^3)}$ than for the case where $|h_{\mathbf{k}}|^2 = \frac{16k^2}{(1+k^3)^2}$. Thus it appears that an increased topographic amplitude, combined with an increased initial mean field, in the small-scales mitigates the tendency of the CUQDIA to generate spurious convection effects. In Fig. 5.48 the evolved DNS and CUQDIA closure large-scale Reynolds number and skewness factor are displayed. We note the close agreement between the DNS and CUQDIA evolved Reynolds numbers and the significant under-estimation of the skewness with the CUQDIA closure. A discussion of these results will be included later but first higher resolution C64 calculations will be presented for the same initial conditions and parameters as for the case that has just been discussed.

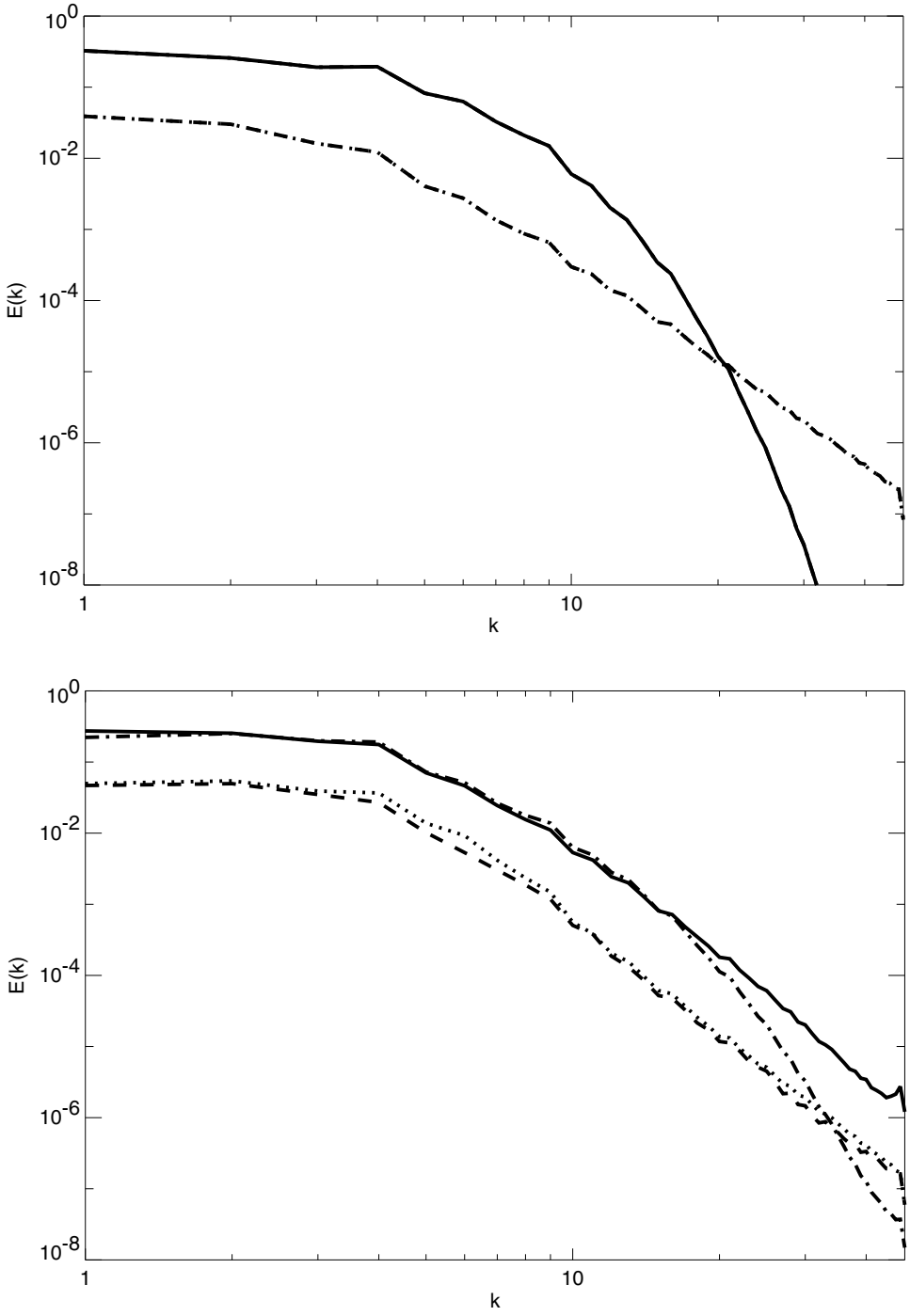

Figure 5.46: C48 resolution spectra. (top) Initial Mean and Transient energy spectra. (bottom) Mean and Transient energy fields at t=0.4. Component field diagrams: mean field; DNS (dashed lines), CUQDIA (dotted lines), :transient field; DNS (solid lines), CUQDIA (dot dashed).

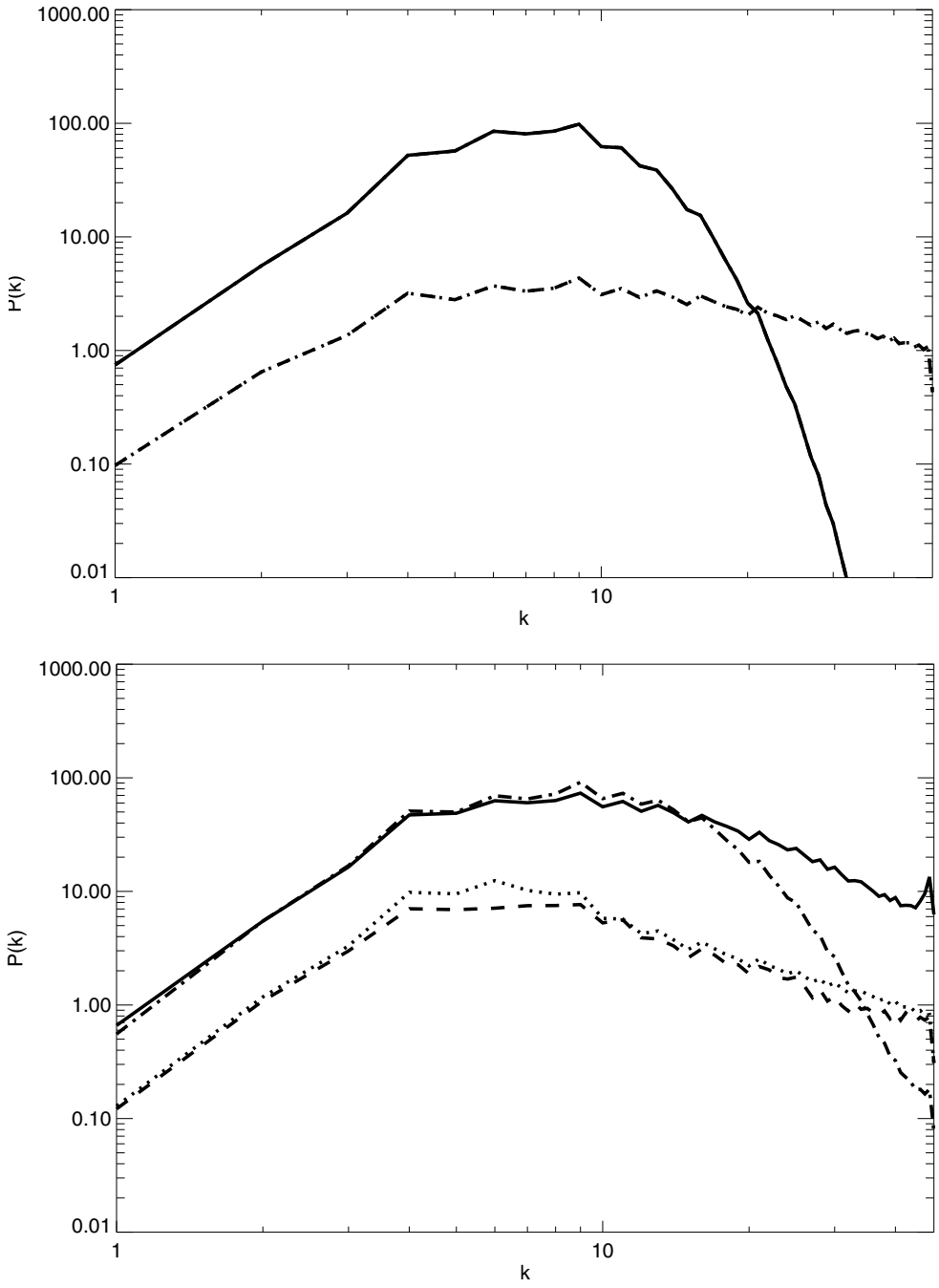

Figure 5.47: (top) C48 resolution. Initial Mean and Transient palinstrophy spectra. (bottom) Mean and Transient palinstrophy spectra at t=0.4. Component field diagrams: mean field; DNS (dashed lines), CUQDIA (dotted lines), :transient field; DNS (solid lines), CUQDIA (dot dashed).

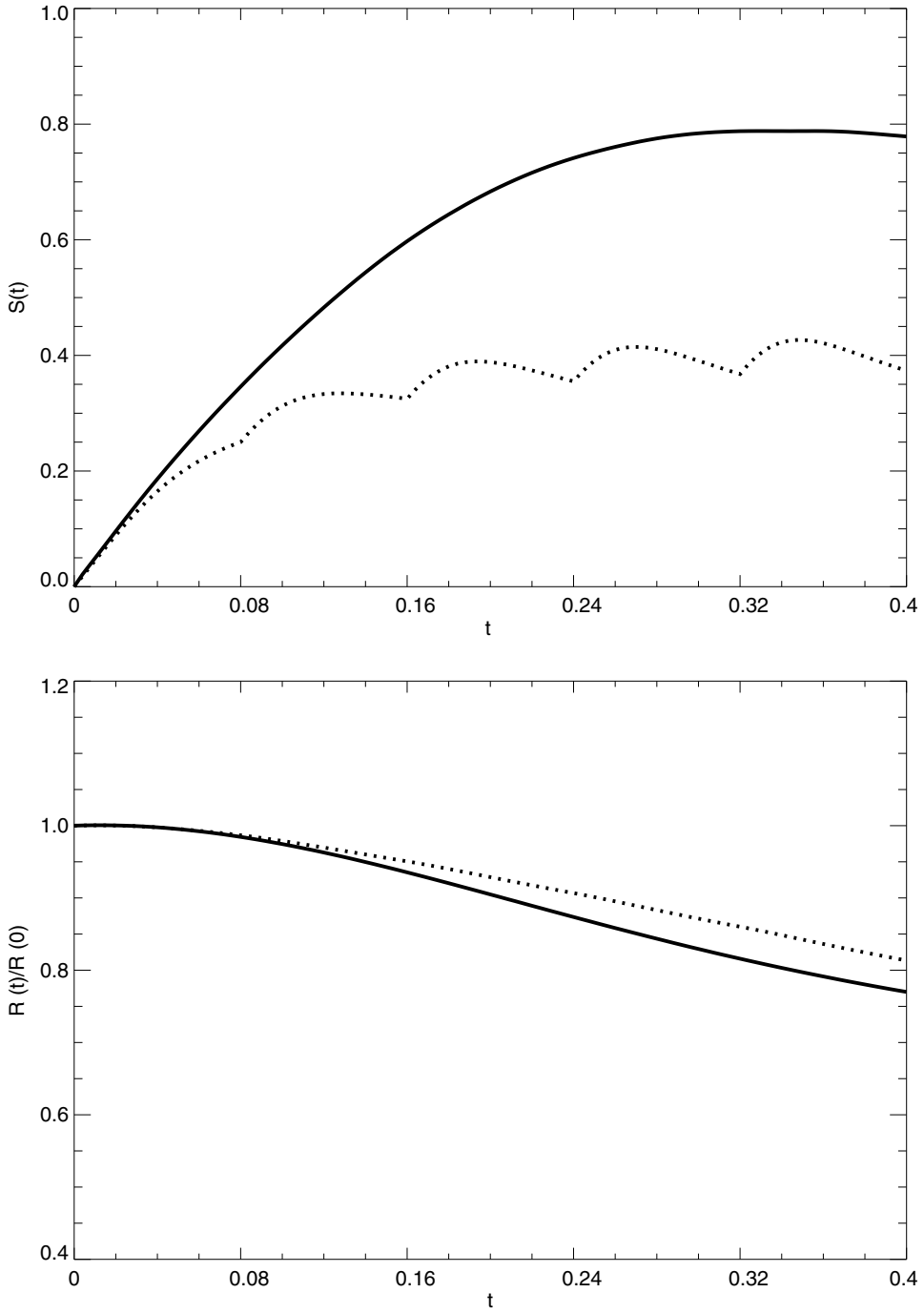

Figure 5.48: (top) Skewness as a function of time for C48 resolution. Shown are results for DNS (solid) and CUQDIA (dotted), with restarts calculated at every 20 timesteps. (bottom) $R_L(t)/R_L(0)$ evaluated at timestep t.

In Figs. 5.49 and 5.50 comparisons are shown between the closure and DNS spectra for times $t_0 = 0$ and $t_f = 0.18$ at C64 resolution. At $t_f = 0.18$ (and after 4 restarts) the evolved DNS and closure mean energy and palinstrophy spectra are still in very close agreement. However, the CUQDIA transient fields at $t_f = 0.18$ show a marked underestimation at scales $k > 20$ which again arises due to spurious convection effects inherent in the direct interaction approximation. The inhomogeneous closure transient energy and palinstrophy spectra at $t_f = 0.18$ are found have comparable magnitudes to those in the isotropic case (Fig. 4 [108]), which were evolved with the same parameters. The obvious difference is that the inhomogeneous case has a nonzero mean vorticity from which enstrophy can be transferred to the transients as the system evolves. This is in contrast to our previous studies (see Figs. 5.28 and 5.31) of viscous decay where both mean and transient fields were seen to decay at approximately similar rates with no preferential transfer of enstrophy from one field to the other. Also of interest is the pronounced "hump" in the DNS spectra at $50 < k < 64$. This phenomena is also observed in Figs. 1, 3 and 4 of [108] however it is much more pronounced in the C64 inhomogeneous DNS calculations (Figs. 5.49 and 5.50) whereas it is significantly reduced at C48 resolution (see Figs. 5.46 and 5.47).

The differences between the transient energy and palinstrophy spectra for the CUQDIA and DNS are comparable to those of the isotropic study of Frederiksen and Davies [108] (Fig. 4) where it was found that the discrete closure was in closer agreement with DNS than the continuous DIA of Herring et al. (Figs. 22 and 23 [112]). The time evolution of the skewness (Fig. 5.51) shows the effect of the cumulant updates at times $t = 0.04, 0.08, 0.12, 0.16$ for the CUQDIA and also (more pronounced) for the ZCUQDIA closure, where the cumulants are zeroed at each restart step. This dramatically illustrates the large amount of information about the non-Gaussian cumulants captured by the cumulant update method. The DNS on the other-hand exactly represents the three-point cumulant.

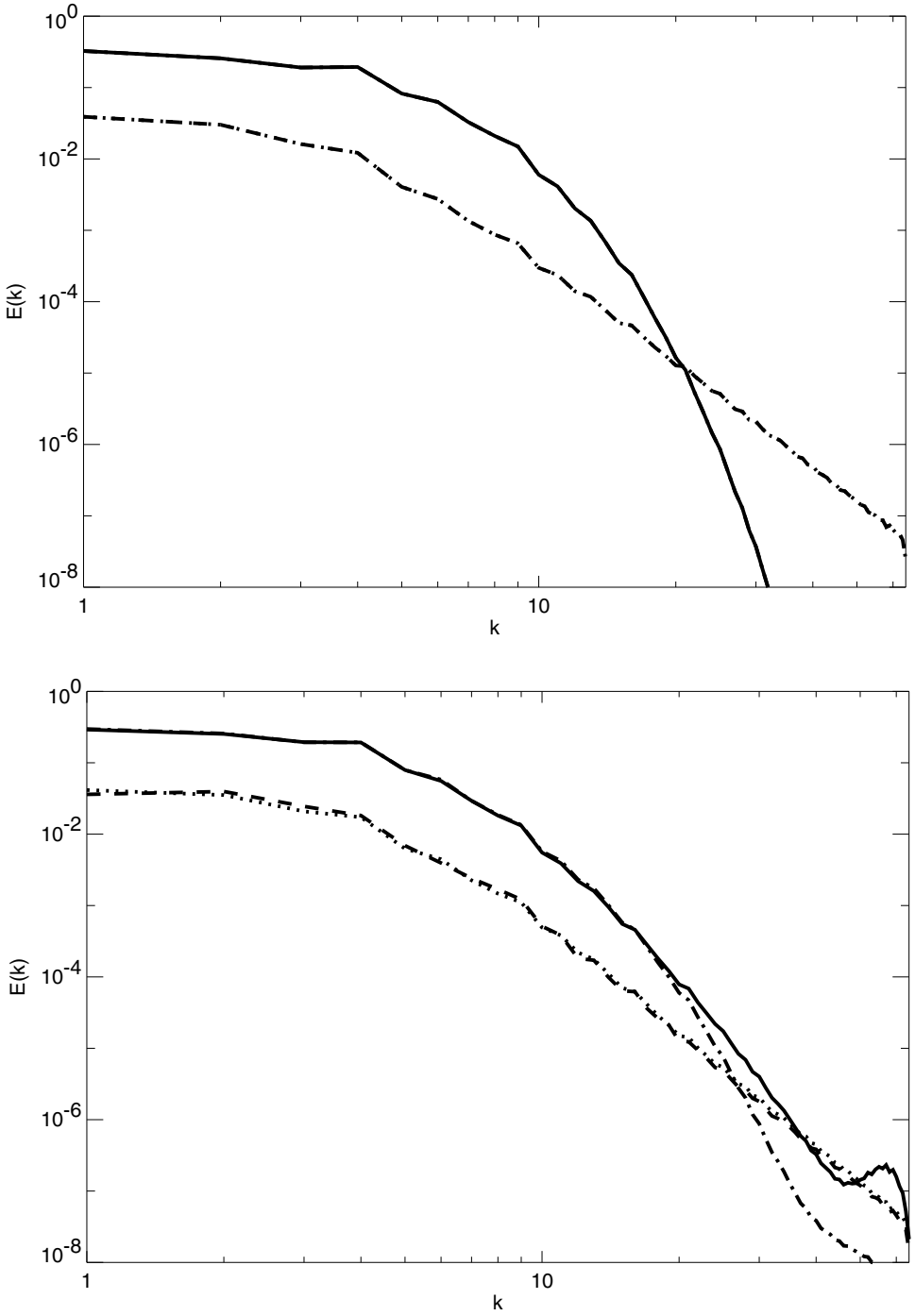

Figure 5.49: C64 resolution spectra. (top) Initial Mean and Transient energy spectra. (bottom) Mean and Transient energy fields at t=0.18. Component field diagrams: mean field; DNS (dashed lines), CUQDIA (dotted lines), :transient field; DNS (solid lines), CUQDIA (dot dashed).

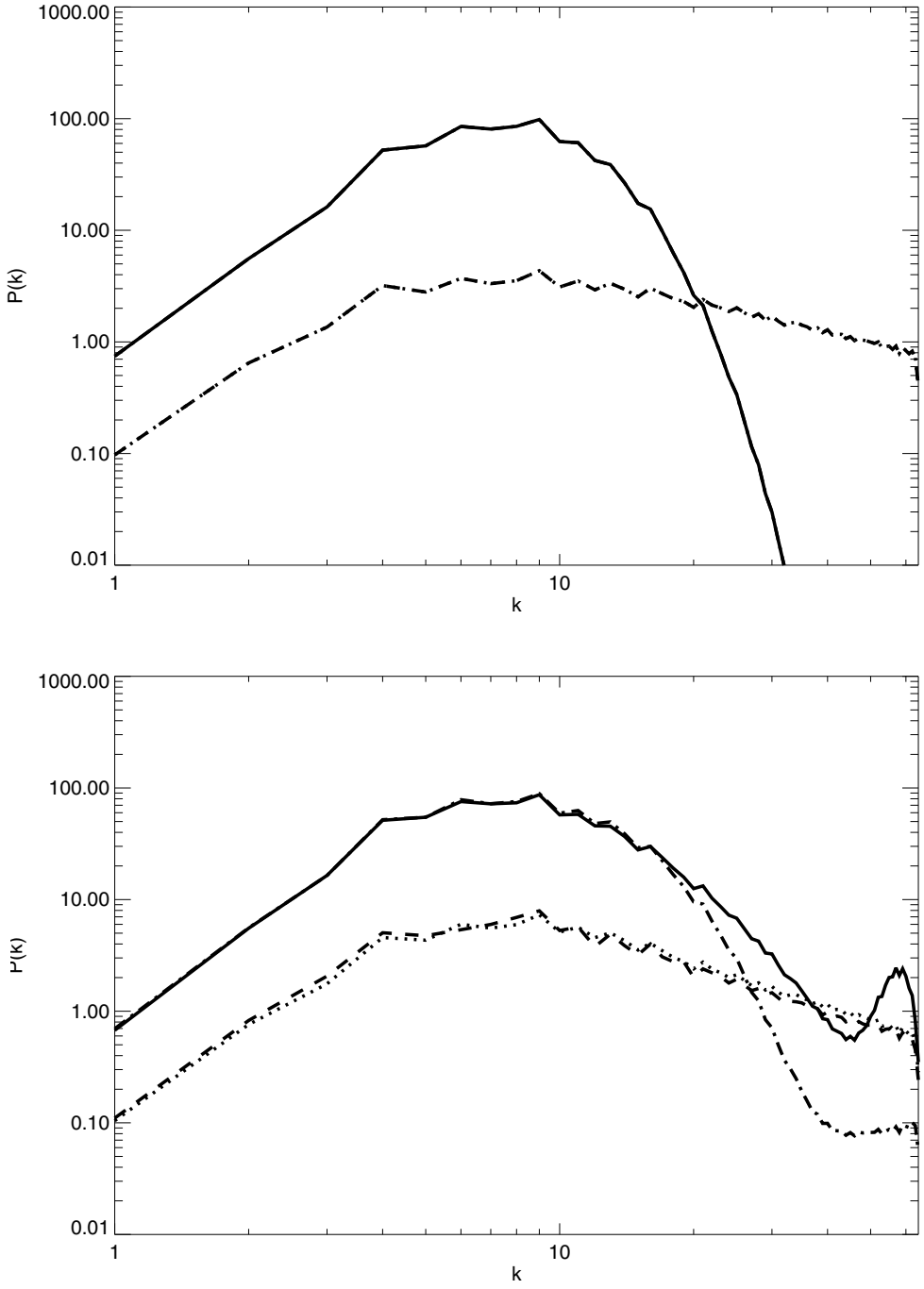

Figure 5.50: C64 resolution spectra. (top) Initial Mean and Transient palinstrophy spectra. (bottom) Mean and Transient palinstrophy spectra at t=0.18. Component field diagrams: mean field; DNS (dashed lines), CUQDIA (dotted lines), :transient field; DNS (solid lines), CUQDIA (dot dashed).

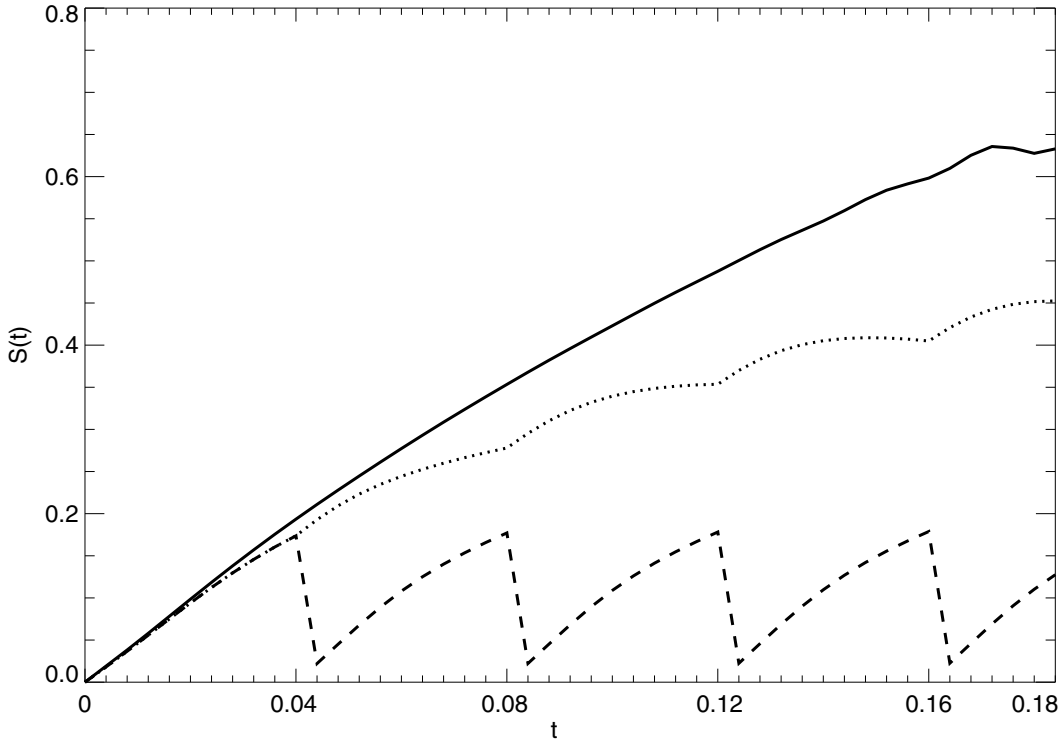

Figure 5.51: C64 resolution skewness calculated as a function of time. Shown are results for DNS (solid) and the CUQDIA (dotted), with restarts calculated at every 10 timesteps. The DNS and CUQDIA closure skewness are also compared with the case where the third order cumulants are zeroed (ZCUQDIA) at each restart step (dashed).

As was observed in the spectrum A study, Frederiksen and Davies [108] (Figs. 3 and 5) found that the discrete DIA and CUDIA closures were very much more accurate in representing of skewness than the continuous DIA ([112] Fig. 16). In the case of the discrete inhomogeneous CUQDIA the skewness has been found to agree with DNS with approximately the same level of confidence (Fig. 5.51) as in the discrete closure isotropic experiment. This is in contrast to the low resolution study of the CUQDIA (Fig. 5.42) where it was shown that the CUQDIA did not estimate the skewness with the same accuracy as the corresponding discrete isotropic CUDIA. However, when the topography was modified to increase the topographic strength at the small-scales the CUQDIA closure was found to much better estimate the skewness factor and large-scale Reynolds number (Fig. 5.45 top).

In Figs. 5.46 and 5.47 energy and palinstrophy spectra were shown for the lower resolution C48 experiment for a run time approximately double that of the C64 case. The longer runtime at C48 allowed a more detailed examination of the evolution of the skewness (Fig. 5.48 top) where we clearly see the under-representation of the skewness and an over-representation of the Reynolds number (Fig. 5.48 bottom). The initial Reynolds number for both C48 and C64 resolutions was found to be $R_L(0) = 304$ with $R_L(0.18)/R_L(0) = 0.9090$ for the C64 DNS calculation and $R_L(0.18)/R_L(0) = 0.9328$ for the C64 CUQDIA results whereas $R_L(0.4)/R_L(0) = 0.7700$ for the C48 DNS calculation and $R_L(0.4)/R_L(0) = 0.8134$ for the C48 CUQDIA. Figure 5.48 (bottom) shows the evolution of $R_L(t)/R_L(0)$ for the C48 case. Interestingly both the C48 and C64 moderate Reynolds number studies show better accuracy in their estimation of the evolved mean energy (Figs. 5.46 and 5.49) than was observed for the low Reynolds number study from spectrum A (Fig. 5.40).

5.7 Summary

Using low resolution studies we have compared the evolution and dynamics of the mean and transient fields for two-dimensional inhomogeneous flow over topography. Close agreement was found between the QDIA closure equations and DNS of the barotropic vorticity

equation for both an inviscid unforced case and cases where either or both viscosity and forcing were present. We also identified the basis of the DNS sampling error and presented methods in order to remove it for subsequent spectral studies. Higher resolution spectral studies at C16, C48 and C64 were carried out over a wide range of topographies and parameter choices. A number of diagnostic quantities were employed in order to investigate the accuracy of the closure equations and close agreement to DNS was demonstrated, especially for the case of viscous decay from an initial canonical equilibrium state. Subsequent experiments at low and moderate Reynolds number revealed an under-representation of the small-scale transient enstrophy due to spurious convection effects in the closure calculation; this is to be expected on the basis of the well-known behavior of the Eulerian DIA closure for isotropic turbulence [109, 112, 108]. The slope of the topography and the strength of the mean field relative to the transient field were found to affect the accuracy with which the closure predicted the small scales of the evolved fields. The closure model has been found to perform significantly better in estimating the evolved small-scale transient field amplitudes when the small-scale amplitudes of both the topography and evolved mean field are strong relative to the evolved transient field amplitude (Figs. 5.43, 5.44 and 5.45). The mean field amplitudes were found to be in close agreement for all three moderate Reynolds number studies with some minor under-estimation found in the low Reynolds number experiment. The cumulant update procedure was further shown to improve the estimation of the skewness for cases where restarts were required. In the next chapter a description will be given of how the CUQDIA may be extended to the β-plane in order to incorporate differential rotation, large-scale zonal flows and Rossby waves.

Chapter 6

Rossby wave turbulence

In this chapter the QDIA and CUQDIA closure models are extended from an f-plane to a β-plane via the inclusion of the so-called β-effect. This work is not intended to be a thorough investigation of all the potential problems of interest for turbulent flow on a β-plane but is designed to show how an efficient and logical extension of both the model and theory to incorporate both large-scale flow and differential rotation may be achieved. In general most studies of geophysical flow over topography on a β-plane have used the "standard" formulation of the barotropic vorticity equation with the standard large-scale zonal flow and differential rotation terms added [113, 114, 13, 115]

$$\frac{\partial \zeta}{\partial t} + J(\psi - Uy, \zeta + h + \beta y) = 0. \tag{6.1}$$

Unfortunately standard β-plane models are in actuality not all that similar to spherical models. Models formulated for spherical geometry incorporate planetary and solid body rotation vorticity terms in a very natural way whereas the standard β-plane only includes the planetary vorticity. In sections 6.1, 6.2, 6.3 and 6.4 a "generalized" β-plane model is developed that is comparable to models formulated using a spherical geometry. The extension of the standard β-plane model to the generalized β-plane is achieved via the addition of a term, $k_0^2 U y$, representing the vorticity associated with the large-scale flow. Note that in general $k_0^2 U << \beta$ for atmospheric flows. It is noted that the difference between the generalized and standard β-plane models can in principle be made as small as would be liked by taking $k_0^2 \to \epsilon$.

An additional advantage of formulating the QDIA closure on the generalized β-plane is that the symmetry properties of the f-plane QDIA closure equations are preserved. The importance of symmetry in Frederiksen's original derivation of the QDIA [91] is in allowing a very compact set of closure equations to be achieved that can be implemented in an obvious way. On the other hand the standard β-plane barotropic vorticity equation (Eq. 6.1) produces a large and "unwieldy" set of closure equations with nonsymmetric interaction coefficients whose implementation represents a significantly more difficult task.

This chapter is begun with a presentation of the generalized β-plane barotropic vorticity equation. As well as providing a one-to-one correspondence to the barotropic vorticity equation in spherical geometry the resulting symmetric form of the closure equations may be implemented simply by the extension of the interaction coefficients and wavenumber space to include a k_{00} mode that acts in an analogous way to the $(0,1)$ mode in spherical geometry. In sections 6.1-6.4.2 closure equations and their interaction coefficients are derived; as well conservation of energy and potential enstrophy equations are considered before deriving canonical equilibrium solutions. After the theory has been described in detail experiments at C3 and C16 resolution are shown for inviscid unforced, viscous decay and forced dissipative flows over a Gaussian topography on the doubly periodic plane. These experiments are intended to show that the β-QDIA and β-CUQDIA numerical models give results that are not only in close agreement with DNS but are consistent with the current knowledge of waves and turbulence on a β-plane.

6.1 Dispersion relations

General geophysical flow over topography is further complicated by the presence of differential rotation and the effects of interaction with the large-scale flow that drives the system. The addition of differential rotation is known as the β-effect. In the presence of the β-effect, linear waves satisfy the dispersion relation for plane transverse waves of the form $\psi \propto e^{-i\mathbf{k}\cdot\mathbf{x}-\omega t}$. Also in contrast to the f-plane, the direction of the large-scale flow U now becomes of increased importance due to the β-effect exciting Rossby waves; that is the development of a downstream Rossby wave-train for eastward initial flow as

opposed to weak transient Rossby waves for westward initial flow. For 2-D turbulent flow over topography there is the added possibility that turbulence may now be converted to waves (this particular aspect has been discussed by Rhines [113]). To reiterate, on the sphere there are two contributions to the vorticity, namely the planetary vorticity and the vorticity of the large-scale solid body rotation flow. The vorticity of the large-scale flow is small compared to the planetary vorticity but important nevertheless, especially so when one considers that the standard β-plane attempts to approximate the large-scale Laplacian on the sphere with a small-scale Laplacian when applied to $U\mu$[1]. In order to incorporate these effects the required "modified" β-plane dispersion relation for planar geometry is derived in such a way that the resulting closure equations and interaction coefficients are in a symmetric form.

Firstly, consider the dispersion relation for linear Rossby waves on the sphere in the presence of solid body rotation zonal flow [11] given by

$$\omega_r = mU - \frac{2m(1+U)}{n(n+1)} \tag{6.2}$$

$$= mU - \frac{\beta_{01}m + n_{01}(n_{01}+1)Um}{n(n+1)} \tag{6.3}$$

where $\beta_{01} = 2$, $n_{01} = 1$, m = zonal wavenumber, and n = total wavenumber. For flow on the sphere the earths' radius A has been used as a length scale and the earths' angular momentum Ω^{-1} as a time scale. [2]. Also the mean streamfunction for solid body rotation is

$$\overline{\psi} = -U\mu \tag{6.4}$$

with μ the sine of the latitude. It is also noted that Frederiksen [11] considered $U = -\sqrt{\frac{3}{2}}\overline{\psi}_{01}$ where $\overline{\psi}_{01}$ is the streamfunction of the solid body rotation. In contrast, when $\overline{\psi} = -\hat{U}y$ the Rossby waves on the standard $\beta-$plane have the dispersion relation

$$\omega_r^{\beta} = k_x\hat{U} - \beta\frac{k_x}{k^2} \tag{6.5}$$

[1]That is, when the small-scale Laplacian is applied to $U\mu$ the result is zero whereas the application of the large-scale Laplacian to $U\mu$ produces a nonzero result

[2]These scalings are also used for the equatorial β-plane

where k_x is the zonal wavenumber and $k^2 = k_x^2 + k_y^2$. On the standard $\beta-$plane, the dimensional β^d is

$$\begin{aligned}\beta^d &= \frac{d}{d\phi}(2\Omega sin\phi)\frac{d\phi}{dy^d} \\ &= \frac{2\Omega cos\phi}{A}\end{aligned} \tag{6.6}$$

which, using the time and length scales above, has the dimensionless form

$$\beta = 2cos\phi. \tag{6.7}$$

A more detailed discussion and derivation of these relationships may be found in the book by Holton [116]. In a planar geometry the standard $\beta-$plane incorporates the planetary vorticity but neglects the vorticity of the large-scale flow which in spherical co-ordinates appears as [117]

$$\nabla^2_{sphere}\overline{\psi} = [\frac{\partial}{\partial\mu}(1-\mu^2)\frac{\partial}{\partial\mu} + \frac{1}{1-\mu^2}\frac{\partial^2}{\partial\lambda^2}]\overline{\psi} \tag{6.8}$$

$$= -2U\mu. \tag{6.9}$$

On an equatorial $\beta-$plane (β_{eq}) it is evident that the $\beta-$plane dispersion relation, including the contribution from the solid body rotation vorticity, by direct comparison to equations 6.2 and 6.3 must be

$$\omega_r^{\beta_{eq}} = k_x U - \frac{2k_x(1+U)}{k^2} \tag{6.10}$$

$$= k_x U - \frac{\beta_{eq}k_x + k_0^2 U k_x}{k^2} \tag{6.11}$$

where $\beta_{eq} = 2$ and $k_0^2 = k_{0_{eq}}^2 = 2$. More generally we would expect the $\beta-$plane dispersion relation to have the form

$$\omega_r^{\beta} = k_x\hat{U} - \frac{\beta k_x + k_0^2\hat{U}k_x}{k^2} \tag{6.12}$$

6.2 The generalized $\beta-$plane vorticity equation

The vorticity equation with the vorticity of the large-scale flow included but neglecting dissipation and forcing, and with $\hat{U} \rightarrow U$, is

$$\frac{\partial\zeta}{\partial t} + J(\psi - Uy, \zeta + h + \beta y + k_0^2 Uy) = 0. \tag{6.13}$$

In order to determine the evolution of the large scale flow U conservation of energy must be considered (see Appendix A, Frederiksen and Frederiksen [115]). This requires that

$$\frac{\partial U}{\partial t} = \frac{1}{S}\int_S h\frac{\partial \psi}{\partial x}\ dS. \tag{6.14}$$

where S is the area of the surface. The kinetic energy is given by

$$E = \frac{1}{2}U^2 + \frac{1}{2}\frac{1}{S}\int_S (\nabla\psi)^2\ dS \tag{6.15}$$

while the potential enstrophy is defined by

$$Q = \frac{1}{2}(k_0 U + \frac{\beta}{k_0})^2 + \frac{1}{2}\frac{1}{S}\int_S (\zeta + h)^2\ dS \tag{6.16}$$

$$= \frac{1}{2}(\zeta_U + h_U)^2 + \frac{1}{2}\frac{1}{S}\int_S (\zeta + h)^2\ dS \tag{6.17}$$

where $\zeta_U = k_0 U$ and $h_U = \frac{\beta}{k_0}$. Equation (6.17) has a similar form to Eq. 5.9 of Carnevale and Frederiksen [13] with the inclusion of the nontrivial term $\frac{1}{2}k_0^2 U^2$ and the trivial constant term $\frac{1}{2}\frac{\beta}{k_0^2}$.

For a large scale flow it is to be expected that k_0 be less than the retained wavenumber of the smallest scale and then either $k_0 < 1$ or if we regard the small scales as periodic on the domain $0 \le x \le \frac{2\pi}{N}$, $0 \le y \le \frac{2\pi}{N}$, where N is an integer which is greater than 1, if $k_0 \ge 1$, ie.,

$$\mathbf{k}[0 \le x \le \frac{2\pi}{N}, 0 \le y \le \frac{2\pi}{N}] = N\mathbf{k}[0 \le x \le 2\pi, 0 \le y \le 2\pi]. \tag{6.18}$$

6.3 Canonical equilibrium theory

This section contains a discussion of the equilibrium statistical mechanics of flow on the generalized β-plane making a direct comparison with the previous study of Carnevale and Frederiksen [13] for flow on the standard β-plane. It will also be shown that in the limit as $k_0 \to 0$ the generalized β-plane reduces to the standard β-plane and thus the nonlinear stability properties developed previously [13] apply. Firstly, consider the stationary contribution by analogy with Eq. 5.10 of Carnevale and Frederiksen [13]. Let $\mu = \mu^{eq} = a/b$ where as before a and b are determined by the prescribed values of E and

Q for the mean energy and potential enstrophy of the ensemble [3]. The simplest nontrivial solution to Eq. 6.13, is the linear relation

$$\mu(\psi^s - U^s y) = \nabla^2\psi^s + \beta y + k_0^2 U^s y + h. \tag{6.19}$$

Thus, the large-scale contributions may be separated and written as

$$\mu = \frac{\beta + k_0^2 U^s}{U^s} \tag{6.20}$$

or

$$U^s = -\frac{\beta}{\mu + k_0^2} = -\frac{k_0 h_U}{\mu + k_0^2}. \tag{6.21}$$

This implies

$$E_U^s = \frac{1}{2}\frac{\beta^2}{(\mu + k_0^2)^2} = \frac{\frac{1}{2}k_0^2|h_U|^2}{(\mu + k_0^2)^2}, \tag{6.22}$$

$$Q_U^s = \frac{1}{2}(k_0 U^s + h_U)^2 = \frac{\frac{1}{2}\mu^2|h_U|^2}{(\mu + k_0^2)^2}. \tag{6.23}$$

The definitions of E^s and Q^s differ from Eqs. 5.12 and 5.12b of Carnevale and Frederiksen [13] only by the terms containing k_0^2. Also,

$$E^s = \frac{\frac{1}{2}k_0^2|h_U|^2}{(\mu + k_0^2)^2} + \frac{1}{2}\sum_{\mathbf{k}} \frac{k^2|h_{\mathbf{k}}|^2}{(\mu + k^2)^2} \tag{6.24}$$

$$Q^s = \frac{\frac{1}{2}\mu^2|h_U|^2}{(\mu + k_0^2)^2} + \frac{1}{2}\sum_{\mathbf{k}} \frac{\mu^2|h_{\mathbf{k}}|^2}{(\mu + k^2)^2} \tag{6.25}$$

where it is noted that

$$E_U = \frac{1}{2}U^2 \tag{6.26}$$

and

$$Q_U = \frac{1}{2}(k_0 U + \frac{\beta}{k_0})^2 = \frac{1}{2}(\zeta_U + h_U)^2. \tag{6.27}$$

[3] The properties of parameters a and b are detailed in Eqs. 3.7a to 3.10 of Carnevale and Frederiksen [13] as well as the monograph of Katz [118]

These are in the standard from for the statistical mechanics developed in section 2 of Frederiksen and Sawford [10]. Thus the transient terms are

$$E_U^T = \frac{\frac{1}{2}}{a + bk_0^2} \tag{6.28}$$

$$Q_U^T = \frac{\frac{1}{2}k_0^2}{a + bk_0^2} \tag{6.29}$$

thereby giving

$$E^T = \frac{\frac{1}{2}}{a + bk_0^2} + \frac{1}{2}\sum_{\mathbf{k}} \frac{1}{a + bk^2} \tag{6.30}$$

$$Q^T = \frac{\frac{1}{2}k_0^2}{a + bk_0^2} + \frac{1}{2}\sum_{\mathbf{k}} \frac{k^2}{a + bk^2}. \tag{6.31}$$

Again the large scale flow simply adds an extra term with $k^2 \to k_0^2$. Also note that with $\zeta_U = k_0 U$ it is found that

$$\langle \zeta_U \rangle = k_0 U^s = \frac{-bk_0^2 h_U}{a + bk_0^2} \tag{6.32}$$

which is in the same form as Eq. 13.1a of Frederiksen [91] with $k^2 \to k_0^2, h_k \to h_U$.

6.3.1 Standard $\beta-$plane

The potential enstrophy for the standard $\beta-$plane (Eq. 5.12b Carnevale and Frederiksen [13]) differs from the generalized case by a constant term $\frac{1}{2}(\beta/k_0)^2$ as well as by the term $\frac{1}{2}k_0^2 U^2$. In order to see how the case incorporating the vorticity of the large-scale flow reduces to the standard $\beta-$plane as $k_0^2 \to 0$ let

$$\tilde{Q}_U = Q_U - \frac{1}{2}(\beta/k_0)^2, \tag{6.33}$$

$$\tilde{Q}_U^s = \frac{\frac{1}{2}\mu^2(\beta/k_0)^2}{(\mu + k_0^2)^2} - \frac{1}{2}(\beta/k_0)^2 \tag{6.34}$$

$$= -\frac{\beta^2\mu + \frac{1}{2}\beta^2 k_0^2}{(\mu + k_0^2)^2}. \tag{6.35}$$

Thus

$$\tilde{Q}_U^s \to -\frac{\beta^2}{\mu}; \quad Q^T \to 0 \tag{6.36}$$

as $k_0^2 \to 0$ in agreement with Carnevale and Frederiksen [13]. It then follows that the connection between nonlinear stability and canonical equilibrium follows as developed in Carnevale and Frederiksen [13] for infinite resolution.

6.4 Closure equations and interaction coefficients

In this section the f-plane CUQDIA closure equations are extended to the β-plane via a symmetric formulation of the interaction coefficients or bare vertex terms. From Eq. 6.13 with dissipation and forcing included, we have in spectral form

$$\begin{aligned}
(\frac{\partial}{\partial t} + \nu_0(k)k^2)\zeta_{\mathbf{k}}(t) &= \sum_{\mathbf{p}\in\mathbf{R}}\sum_{\mathbf{q}\in\mathbf{R}} \delta(\mathbf{k}+\mathbf{p}+\mathbf{q})\left[K(\mathbf{k},\mathbf{p},\mathbf{q})\zeta_{-\mathbf{p}}\zeta_{-\mathbf{q}}\right. \\
&\left. + A(\mathbf{k},\mathbf{p},\mathbf{q})\zeta_{-\mathbf{p}}h_{-\mathbf{q}}\right] + f^0_{\mathbf{k}} - \left[ik_xU(\zeta_{\mathbf{k}}+h_{\mathbf{k}}) + ik_x\psi_{\mathbf{k}}(\beta+k_0^2U)\right] \\
&= \sum_{\mathbf{p}\in\mathbf{R}}\sum_{\mathbf{q}\in\mathbf{R}} \delta(\mathbf{k}+\mathbf{p}+\mathbf{q})\left[K(\mathbf{k},\mathbf{p},\mathbf{q})\zeta_{-\mathbf{p}}\zeta_{-\mathbf{q}} + A(\mathbf{k},\mathbf{p},\mathbf{q})\zeta_{-\mathbf{p}}h_{-\mathbf{q}}\right] + f^0_{\mathbf{k}} \\
&\quad + ik_0\left[\frac{k_x}{k^2} - \frac{k_x}{k_0^2}\right]\zeta_{\mathbf{k}}\zeta_U + ik_0\left[\frac{k_x}{k^2}\zeta_{\mathbf{k}}h_U - \frac{k_x}{k_0^2}\zeta_U h_{\mathbf{k}}\right] \qquad (6.37) \\
&= \sum_{\mathbf{p}\in\mathbf{R}}\sum_{\mathbf{q}\in\mathbf{R}} \delta(\mathbf{k}+\mathbf{p}+\mathbf{q})\left[K(\mathbf{k},\mathbf{p},\mathbf{q})\zeta_{-\mathbf{p}}\zeta_{-\mathbf{q}} + A(\mathbf{k},\mathbf{p},\mathbf{q})\zeta_{-\mathbf{p}}h_{-\mathbf{q}}\right] + f^0_{\mathbf{k}} \\
&\quad + k_0\left[\frac{k_x}{k^2} - \frac{k_x}{k_0^2}\right]\zeta_{\mathbf{k}}\zeta_{-\mathbf{0}} + k_0\left[\frac{k_x}{k^2}\zeta_{\mathbf{k}}h_{-\mathbf{0}} - \frac{k_x}{k_0^2}\zeta_{-\mathbf{0}}h_{\mathbf{k}}\right] \qquad (6.38)
\end{aligned}$$

where ν_0 is the bare viscosity and $f^0_{\mathbf{k}}$ the bare forcing, and where

$$\zeta_{-\mathbf{0}} = i\zeta_U = ik_0U; \quad h_{-\mathbf{0}} = ih_U = i\frac{\beta}{k_0}; \qquad (6.39)$$

$$\zeta_{\mathbf{0}} = \zeta^*_{-\mathbf{0}} = -i\zeta_U; \quad h_{\mathbf{0}} = h^*_{-\mathbf{0}} = -i\frac{\beta}{k_0}. \qquad (6.40)$$

It is now possible to extend the sums over $\mathbf{p}$ and $\mathbf{q}$ to include the vector $\mathbf{0}$ by defining the appropriate interaction coefficients. Note that we do distinguish between $\mathbf{0}$ and $-\mathbf{0}$ in this representation and $\mathbf{R}$ is the points in discrete wavenumber space. We define the interaction coefficient

$$K(\mathbf{k},\mathbf{p},\mathbf{q}) = \frac{\gamma}{2}[p_x\hat{q_y} - \hat{p_y}q_x](p^2-q^2)/p^2q^2 \qquad (6.41)$$

where

$$\hat{q}_y = \begin{cases} 1 & \text{if } \mathbf{q} = \mathbf{0} \text{ or } \mathbf{p} = \mathbf{0}, \\ q_y & \text{otherwise} \end{cases} \tag{6.42}$$

$$\hat{p}_y = \begin{cases} 1 & \text{if } \mathbf{p} = \mathbf{0} \text{ or } \mathbf{q} = \mathbf{0}, \\ p_y & \text{otherwise} \end{cases} \tag{6.43}$$

$$\gamma = \begin{cases} k_0 & \text{if } \mathbf{q} = \mathbf{0} \text{ or } \mathbf{p} = \mathbf{0}, \\ 1 & \text{otherwise.} \end{cases} \tag{6.44}$$

We also let

$$A(\mathbf{k}, \mathbf{p}, \mathbf{q}) = -\gamma(p_x \hat{q_y} - \hat{p_y} q_x)/p^2 \tag{6.45}$$

where $\hat{q_y}$ and $\hat{p_y}$ are defined in Eqs. 6.42 and 6.43 and γ is defined in Eq. 6.44. Finally the spectral form of the barotropic vorticity equation with differential rotation may be written in a compact form as

$$\begin{aligned} (\frac{\partial}{\partial t} + \nu_0(k)k^2)\zeta_{\mathbf{k}}(t) = \sum_{\mathbf{p}\in\mathbf{T}} \sum_{\mathbf{q}\in\mathbf{T}} \delta(\mathbf{k}+\mathbf{p}+\mathbf{q}) \, [K(\mathbf{k},\mathbf{p},\mathbf{q})\zeta_{-\mathbf{p}}\zeta_{-\mathbf{q}} \\ + A(\mathbf{k},\mathbf{p},\mathbf{q})\zeta_{-\mathbf{p}} h_{-\mathbf{q}}] + f^0_{\mathbf{k}} \end{aligned} \tag{6.46}$$

where $\mathbf{T} = \mathbf{R} \cup \mathbf{0}$.

From Eq. 6.14

$$\frac{\partial U}{\partial t} = \frac{1}{(2\pi)^2} \int_0^{2\pi} \int_0^{2\pi} d\mathbf{x} \sum_{\acute{\mathbf{q}}\in\mathbf{R}} h_{\acute{\mathbf{q}}} \exp i\acute{\mathbf{q}} \cdot \mathbf{x} \sum_{\mathbf{q}\in\mathbf{R}} i q_x \psi_{\mathbf{q}} \exp i\mathbf{q} \cdot \mathbf{x} \tag{6.47}$$

$$= \sum_{\mathbf{q}\in\mathbf{R}} i q_x \psi_{\mathbf{q}} h_{-\mathbf{q}}$$

$$= -i \sum_{\mathbf{q}\in\mathbf{R}} \frac{q_x}{q^2} \zeta_{\mathbf{q}} h_{-\mathbf{q}} \tag{6.48}$$

$$= -i \frac{1}{2} \sum_{\mathbf{p}\in\mathbf{R}} \sum_{\mathbf{q}\in\mathbf{R}} \frac{(p_x - q_x)}{p^2} \zeta_{-\mathbf{p}} h_{-\mathbf{q}}. \tag{6.49}$$

Thus

$$\frac{\partial k_0 U}{\partial t} = -ik_0 \sum_{\mathbf{q}\in\mathbf{R}} \frac{q_x}{q^2} \zeta_{\mathbf{q}} h_{-\mathbf{q}} = \frac{\partial \zeta_U}{\partial t} \tag{6.50}$$

which, using $\zeta_{\mathbf{0}} = -i\zeta_U = -ik_0U$, can equivalently be written as

$$\frac{\partial \zeta_{\mathbf{0}}}{\partial t} = -k_0 \sum_{\mathbf{q}\in\mathbf{R}} \frac{q_x}{q^2} \zeta_{\mathbf{q}} h_{-\mathbf{q}} \tag{6.51}$$

and the appropriate interaction coefficients may be defined as

$$A(\mathbf{0},\mathbf{p},\mathbf{q}) = \frac{k_0}{2}(p_x\hat{q_y} - \hat{p_y}q_x)/p^2 \tag{6.52}$$

$$\text{where} \qquad \hat{p}_y = \hat{q}_y = 1. \tag{6.53}$$

This means that

$$\frac{\partial \zeta_{\mathbf{0}}}{\partial t} = \sum_{\mathbf{p}\in\mathbf{R}} \sum_{\mathbf{q}\in\mathbf{R}} \delta(\mathbf{0}+\mathbf{p}+\mathbf{q}) A(\mathbf{0},\mathbf{p},\mathbf{q}) \zeta_{-\mathbf{p}} h_{-\mathbf{q}} \tag{6.54}$$

where

$$K(\mathbf{0},\mathbf{p},\mathbf{q}) = \frac{1}{2}[A(\mathbf{0},\mathbf{p},\mathbf{q}) + A(\mathbf{0},\mathbf{q},\mathbf{p})] \tag{6.55}$$

from which it follows that

$$\sum_{\mathbf{p}\in\mathbf{R}} \sum_{\mathbf{q}\in\mathbf{R}} \delta(\mathbf{0}+\mathbf{p}+\mathbf{q}) K(\mathbf{0},\mathbf{p},\mathbf{q}) \zeta_{-\mathbf{p}} \zeta_{-\mathbf{q}} = 0. \tag{6.56}$$

We can also write

$$\begin{aligned}(\frac{\partial}{\partial t} + \nu_0(k_0)k_0^2)\zeta_{\mathbf{0}}(t) = \sum_{\mathbf{p}\in\mathbf{T}} \sum_{\mathbf{q}\in\mathbf{T}} \delta(\mathbf{0}+\mathbf{p}+\mathbf{q}) \,[K(\mathbf{0},\mathbf{p},\mathbf{q})\zeta_{-\mathbf{p}}\zeta_{-\mathbf{q}} \\ + A(\mathbf{0},\mathbf{p},\mathbf{q})\zeta_{-\mathbf{p}} h_{-\mathbf{q}}] + f_{\mathbf{0}}^0\end{aligned} \tag{6.57}$$

on including drag and forcing in the $\zeta_{\mathbf{0}}$ equation where $\nu_0(k_0)k_0^2 = const.$ In particular terms such as

$$f_{\mathbf{0}}^0 - \nu_0(k_0)k_0^2\zeta_{\mathbf{0}}(t) = \alpha(\overline{\zeta}_{\mathbf{0}} - \zeta_{\mathbf{0}}(t)). \tag{6.58}$$

may be included. In general, the interaction coefficients that couple the field to the topography may be written as

$$A(\mathbf{k},\mathbf{p},\mathbf{q}) = -\gamma(p_x\hat{q_y} - \hat{p_y}q_x)/p^2 \tag{6.59}$$

where

$$\gamma = \begin{cases} \frac{-k_0}{2} & \text{if } \mathbf{k} = \mathbf{0} \\ k_0 & \text{if } \mathbf{q} = \mathbf{0} \text{ or } \mathbf{p} = \mathbf{0} \\ 1 & \text{otherwise} \end{cases} \tag{6.60}$$

$$\hat{q}_y = \begin{cases} 1 & \text{if } \mathbf{k} = 0 \text{ or } \mathbf{p} = 0 \text{ or } \mathbf{q} = 0 \\ q_y & \text{otherwise} \end{cases} \tag{6.61}$$

$$\hat{p}_y = \begin{cases} 1 & \text{if } \mathbf{k} = 0 \text{ or } \mathbf{p} = 0 \text{ or } \mathbf{q} = 0 \\ p_y & \text{otherwise} \end{cases} \tag{6.62}$$

and

$$K(\mathbf{k}, \mathbf{p}, \mathbf{q}) = \frac{1}{2} \left[A(\mathbf{k}, \mathbf{p}, \mathbf{q}) + A(\mathbf{k}, \mathbf{q}, \mathbf{p}) \right]. \tag{6.63}$$

Now consider

$$\begin{aligned} C_{\mathbf{0}}(t, \acute{t}) &= \langle \zeta_{\mathbf{0}}(t) \zeta_{-\mathbf{0}}(\acute{t}) \rangle \\ &= \langle \zeta_{\mathbf{0}}(t) \zeta^*_{\mathbf{0}}(\acute{t}) \rangle \end{aligned} \tag{6.64}$$

as we define $\zeta_{-\mathbf{0}}(\acute{t}) = \zeta^*_{\mathbf{0}}(\acute{t})$. Then

$$\begin{aligned} C_{\mathbf{0}}(t, \acute{t}) &= \langle -ik_0 U (-ik_0 U)^* \rangle \\ &= k_0^2 \langle U(t) U(t) \rangle \end{aligned} \tag{6.65}$$

where U is real, and similarly

$$\begin{aligned} C_{\mathbf{k}-\mathbf{0}}(t, \acute{t}) &= \langle \zeta_{\mathbf{k}}(t) \zeta_{-\mathbf{0}}(\acute{t}) \rangle \\ &= \langle \zeta_{\mathbf{k}}(t) \zeta^*_{\mathbf{0}}(\acute{t}) \rangle. \end{aligned} \tag{6.66}$$

Thus we find that Eqs. 6.46 and 6.57 are of the same form as Eq. 2.3 of Frederiksen [91] and so the closure equations can be immediately written down, taking care with the $\pm\mathbf{0}$ subscripts, and have the same form as those previously considered for the f-plane.

6.4.1 N-periodic flow

The argument is now generalized to consider N-periodic flow on the equatorial $\beta-$plane. It is firstly noted that with the scaling $\mathbf{k} \to \mathbf{k}N$, where $\mathbf{k}$, $\mathbf{p}$, and $\mathbf{q}$ are not equal to $\mathbf{0}$, then

$$\begin{aligned} A(\mathbf{k}N, \mathbf{q}N, \mathbf{p}N) &= A(\mathbf{k}, \mathbf{q}, \mathbf{p}) \\ K(\mathbf{k}N, \mathbf{q}N, \mathbf{p}N) &= K(\mathbf{k}, \mathbf{q}, \mathbf{p}). \end{aligned} \tag{6.67}$$

From the rescaling transformation

$$\left[\frac{k_x}{k^2}\zeta_{\mathbf{k}}(\beta + k_0^2 U) - k_x U(\zeta_{\mathbf{k}} + h_{\mathbf{k}})\right] \xrightarrow{\mathbf{k} \to \mathbf{k}N} \left[\frac{k_x}{k^2}\zeta_{\mathbf{k}}\frac{(\beta + k_0^2 U)}{N} - k_x U N(\zeta_{\mathbf{k}} + h_{\mathbf{k}})\right] \tag{6.68}$$

and Eq. 6.48 with $\mathbf{k} \to \mathbf{k}N$ we have that

$$\frac{\partial U}{\partial t} = \frac{-i}{N}\sum_{\mathbf{q}} \frac{q_x}{q^2}\zeta_{\mathbf{q}} h_{-\mathbf{q}} \tag{6.69}$$

or

$$\frac{\partial UN}{\partial t} = -i\sum_{\mathbf{q}} \frac{q_x}{q^2}\zeta_{\mathbf{q}} h_{-\mathbf{q}}. \tag{6.70}$$

Let $\mathsf{U} = UN$, $\mathsf{k}_{\mathbf{0}}^2 = \frac{k_0^2}{N^2}$, $\mathsf{B} = \frac{\beta}{N}$. Thus with

$$\mathbf{k} \to \mathbf{k}N \tag{6.71}$$

$$U \to \mathsf{U} = UN \tag{6.72}$$

$$k_0 \to \mathsf{k}_0 = \frac{k_0}{N} \tag{6.73}$$

$$\beta \to \mathsf{B} = \frac{\beta}{N} \tag{6.74}$$

we are back to the form of the original set of equations provided

$$\nu_0(k) \to \nu_0(k)N^2. \tag{6.75}$$

6.4.2 Equilibrium conditions

The required equilibrium conditions incorporating large scale flow are simply defined as for the f-plane but with additional $\mathbf{k}_{(0,0)}$ terms

$$C_{\mathbf{0}}^{eq} = \frac{k_0^2}{a + bk_0^2}, \tag{6.76}$$

$$C_{\mathbf{k}}^{eq} = \frac{k^2}{a + bk^2}, \tag{6.77}$$

$$\langle \zeta_{\mathbf{0}} \rangle^{eq} = -bh_{\mathbf{0}} C_{\mathbf{0}}^{eq}, \tag{6.78}$$

$$\langle \zeta_{\mathbf{k}} \rangle^{eq} = -bh_{\mathbf{k}} C_{\mathbf{k}}^{eq}, \tag{6.79}$$

$$h_{\mathbf{0}} = -i\frac{\beta}{k_0}. \tag{6.80}$$

An equilibrium calculation, on the doubly periodic plane for flow over a Gaussian mountain, is depicted in Fig. 6.1 with parameters given in table 6.1. The closure model was found to obey canonical equilibrium exactly with the stability of the equilibrium state independent of the strength of the topography or stepsize. The parameters a and b are typical for meteorological flows and are the same as used in the low resolution f-plane study of homogenous turbulence without topography of Frederiksen, Davies and Bell [104].

Table 6.1: Figure 6.1 parameters

$\triangle t$	a	b	β	k_0^2
0.1	4.824×10^4	2.511×10^3	2	2

6.5 C3 experiments

Before considering the results of the β-plane CUQDIA it is important to point out a further technical complication. That is, although the closure equations have been written in a compact form via the incorporation of the vorticity associated with the large-scale flow, the interaction coefficients that arise due to the inclusion of a $(k_x = 0, k_y = 0)$ mode are significantly larger in number than for the f-plane closure. This is due to two reasons, the first is that there is no longer an equivalency between the $K(\mathbf{k}, \mathbf{p}, \mathbf{q})$ and $K(-\mathbf{k}, -\mathbf{p}, -\mathbf{q})$

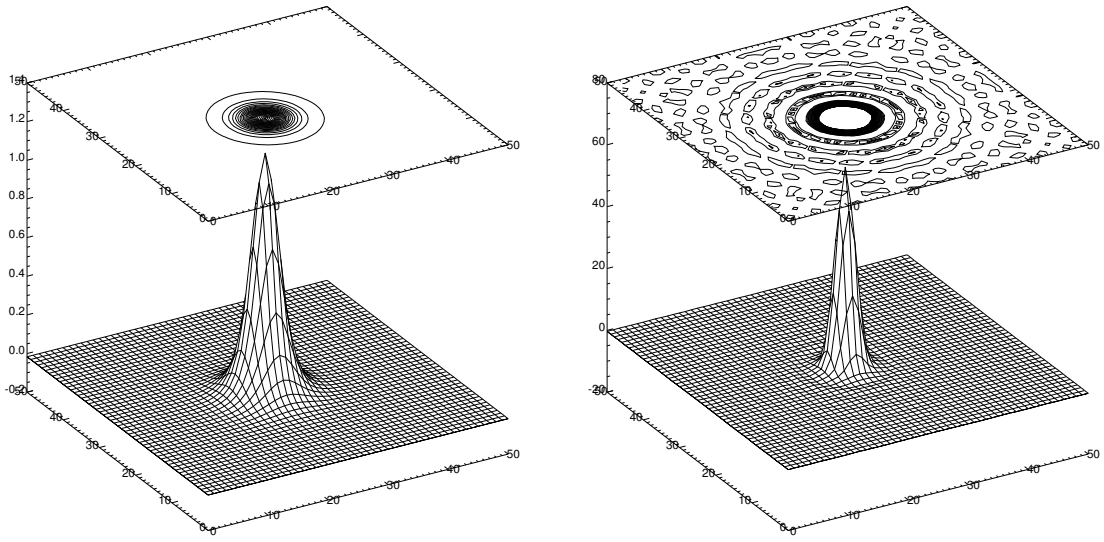

Figure 6.1: The mean stream function (left), excluding the Uy term, and topography (right), for flow on an equatorial β-plane at canonical equilibrium over a nondimensional Gaussian mountain on the doubly periodic plane at C16 resolution. Parameters are given in table 6.1.

interaction coefficients for cases where $\mathbf{k} = \mathbf{0}$, $\mathbf{p} = \mathbf{0}$ or $\mathbf{q} = \mathbf{0}$; thus

$$K(\mathbf{k}, \mathbf{p}, \mathbf{q}) \neq K(-\mathbf{k}, -\mathbf{p}, -\mathbf{q}),$$
$$A(\mathbf{k}, \mathbf{p}, \mathbf{q}) \neq A(-\mathbf{k}, -\mathbf{p}, -\mathbf{q}). \tag{6.81}$$

This results in the number of nonzero interaction coefficients in each of the $K(\mathbf{k}, \mathbf{p}, \mathbf{q})$, $A(\mathbf{k}, \mathbf{p}, \mathbf{q})$, $K(-\mathbf{k}, -\mathbf{p}, -\mathbf{q})$, $A(-\mathbf{k}, -\mathbf{p}, -\mathbf{q})$, $K(-\mathbf{p}, -\mathbf{q}, -\mathbf{k})$, $K(-\mathbf{p}, -\mathbf{k}, -\mathbf{q})$ and $A(-\mathbf{p}, -\mathbf{q}, -\mathbf{k})$ terms being greatly increased. The second and principle reason is essentially one of convenience, that is, in order to allow vectorization the closure code with the $(k_x = 0, k_y = 0)$ mode interaction coefficients included, the model must be run over the whole wavenumber space.

Considering the equatorial β-plane with $\beta = 2$, $k_0^2 = 2$ and N-periodic flow on $[0, 2\pi]$ then this is equivalent to 1-periodic flow on $[0, 2\pi]$ with the conditions as in Eqs. 6.71-6.74 and 6.75. Thus the choice of parameters depends on the choice of separation between the large scale (k_0) and small scales ($\mathbf{k}N$). In Fig. 6.3 we have chosen $\beta = k_0^2 = 2$ and $N = 4$ thus giving $\beta_{2\pi} = 1/2$, $k_{0_{2\pi}}^2 = 1/8$ noting that the specification of ν_0 is somewhat

arbitrary. The initial values of $\pm i0.032389$ for $\langle\zeta_{\mathbf{0}}(0)\rangle$ correspond to westward/eastward initial flow at $15ms^{-1}$ respectively. As for the f-plane experiments, only viscosities of the form $\nu_0(k) = \hat{\nu}$ will be used in the numerical experiments, rather than the more general $\nu_0(k)$. Here $\hat{\nu}$ is the nondimensional viscosity.

Table 6.2: Parameters for figure 6.2 and 6.3

$\triangle t$	a	b	β	k_0^2	N
1.0	2.075×10^5	2.130×10^5	$\frac{1}{2}$	$\frac{1}{8}$	4

Table 6.3: Parameters for figures 6.2 and 6.3

$\hat{\nu}$	$C_{\mathbf{k}}(0,0)$	$C_{\mathbf{0}}(0,0)$	$h_{\mathbf{0}}$	$\langle\zeta_{\mathbf{0}}(0)\rangle$	$\langle\zeta_{\mathbf{k}}(0)\rangle$	f^0
0.0	$C_{\mathbf{k}}^{eq}$	$C_{\mathbf{0}}^{eq}$	$\frac{-i\beta}{k_0}$	$\pm i0.032389$	$-bh_{\mathbf{k}}C_{\mathbf{k}}^{eq}$	0

For flow in which the β-effect is taken into account, Rossby waves may be excited dependent on the direction of the mean flow. In Fig. 6.2 we present the case for eastward flow over a Gaussian mountain at C3 resolution. The topography $h_{\mathbf{k}}$ is the Fourier transform of a nondimensional Gaussian mountain on the doubly periodic plane with maximum height corresponding to a dimensional height of approximately 30 meters (see Fig. 6.4 bottom right). In this case the topography and mean field are considerably weaker than the transient field in order to guarantee stability at such low resolutions with the current relatively large timestep (strong topographies are considered for the C16 cases). For eastward flow the downstream wave pattern excited corresponds to a stationary wave with an elongated circular crest. This downstream stationary Rossby wave develops quickly due to the large value of U. As the system evolves the downstream wave-crest gains in strength as evident in Fig. 6.4 (bottom left). Figure 6.4 (top) shows the evolution of the total (twice) enstrophies for the same modes as previously considered in the C3 f-plane cases (excluding the total and $\zeta_{\mathbf{0}}$ modes) for 50 timesteps with parameters as given in table 6.3 but with $\triangle t = 0.5$. We see excellent agreement between DNS (solid) and CUQDIA (dashed) over a nondimensional time of $t = 50$ for the N-periodic (N=4) calculation.

For westward initial flow (see Fig. 6.3) we have no excitation of Rossby waves with the β-effect reinforcing the trapping of the negative vorticity core (highs in ψ) over the topography. Some small amplitude disturbances are seen to propagate in a principally downstream direction although there is some evidence of the effects of the cyclic symmetry of flow on the doubly periodic plane. These disturbances are transient in nature with the system evolving toward a steady state very similar to the $t = 10$ case in Fig. 6.3. These low resolution studies demonstrate that the closure model is giving results that are broadly in agreement with previous studies of rotating barotropic flow over topography on a β-plane [113, 119, 114] and corresponding studies on the sphere [11, 10].

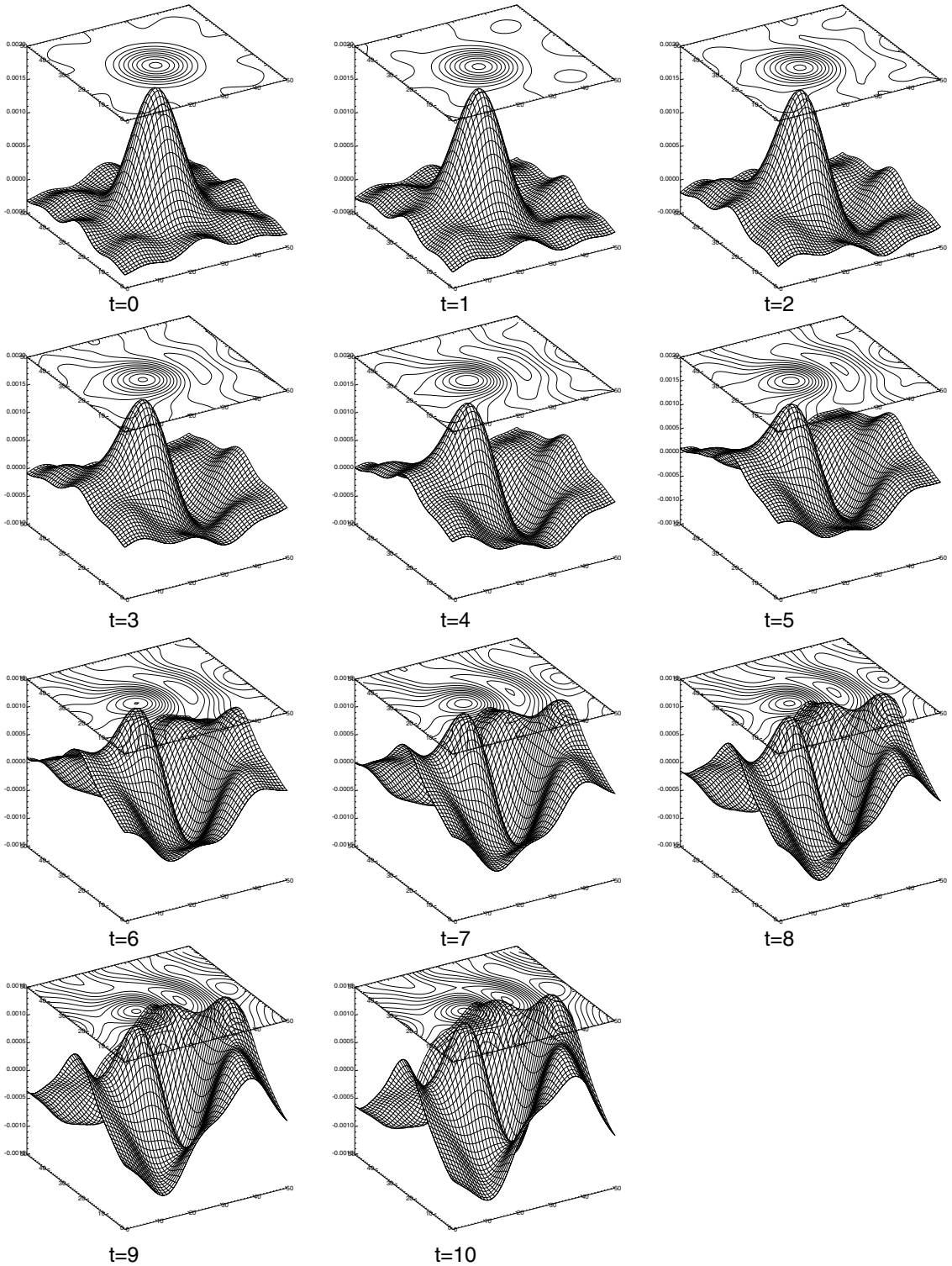

Figure 6.2: Evolution of the QDIA mean streamfunction for eastward initial flow over a Gaussian mountain at C3 resolution: Parameters are given in tables 6.2 and 6.3. The evolution of the mean streamfunction, excluding the Uy contribution, is shown over a nondimensional time of $t = 10$. The downstream stationary Rossby wave of significant amplitude is quickly excited while the lack of any obvious clockwise rotation is expected for inviscid unforced flow.

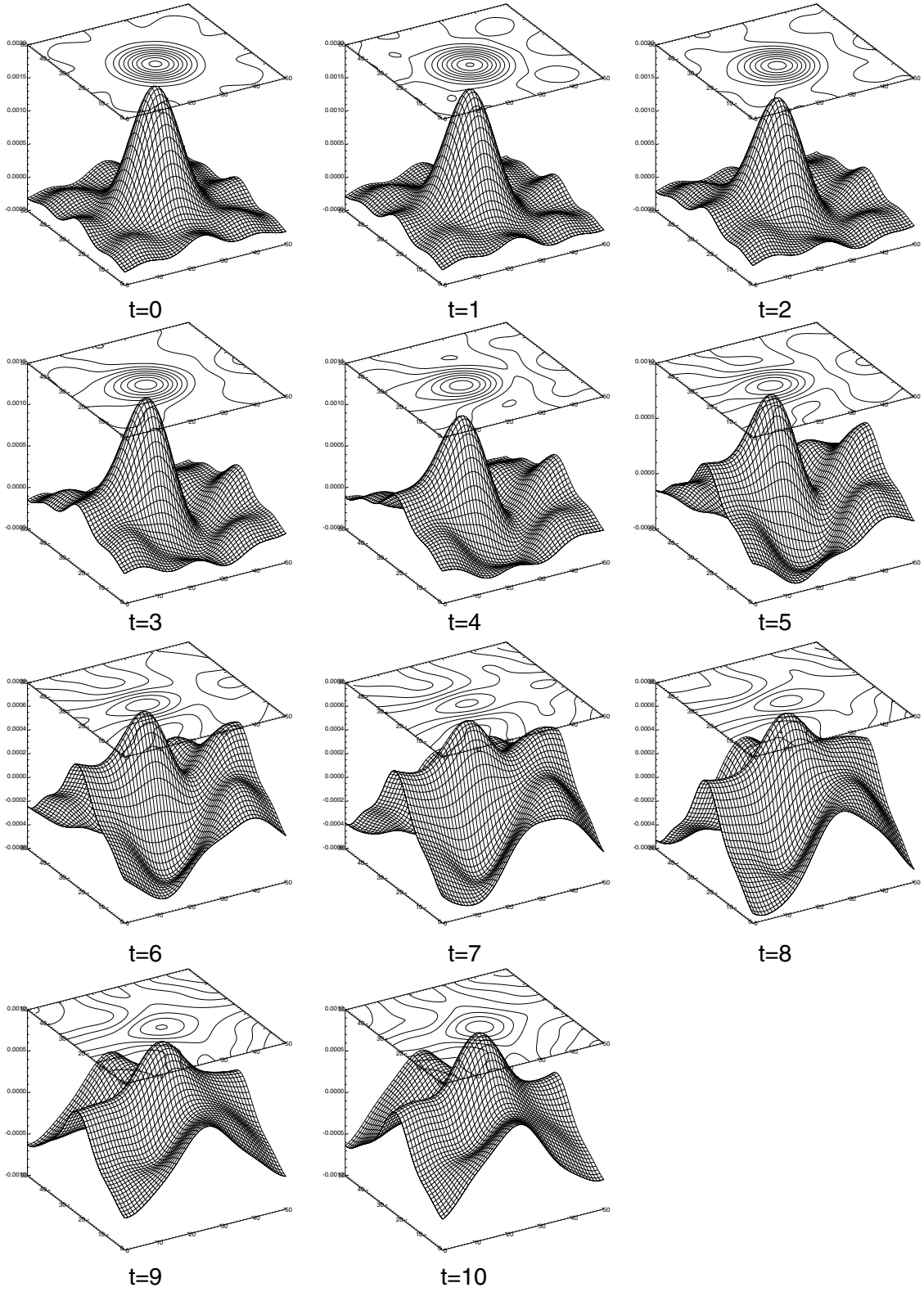

Figure 6.3: Westward initial flow over a Gaussian mountain for C3 resolution: Parameters are as for Fig. 6.3. Flow in the westward direction does not result in significant excitation of Rossby waves with only transient small amplitude Rossby waves apparent.

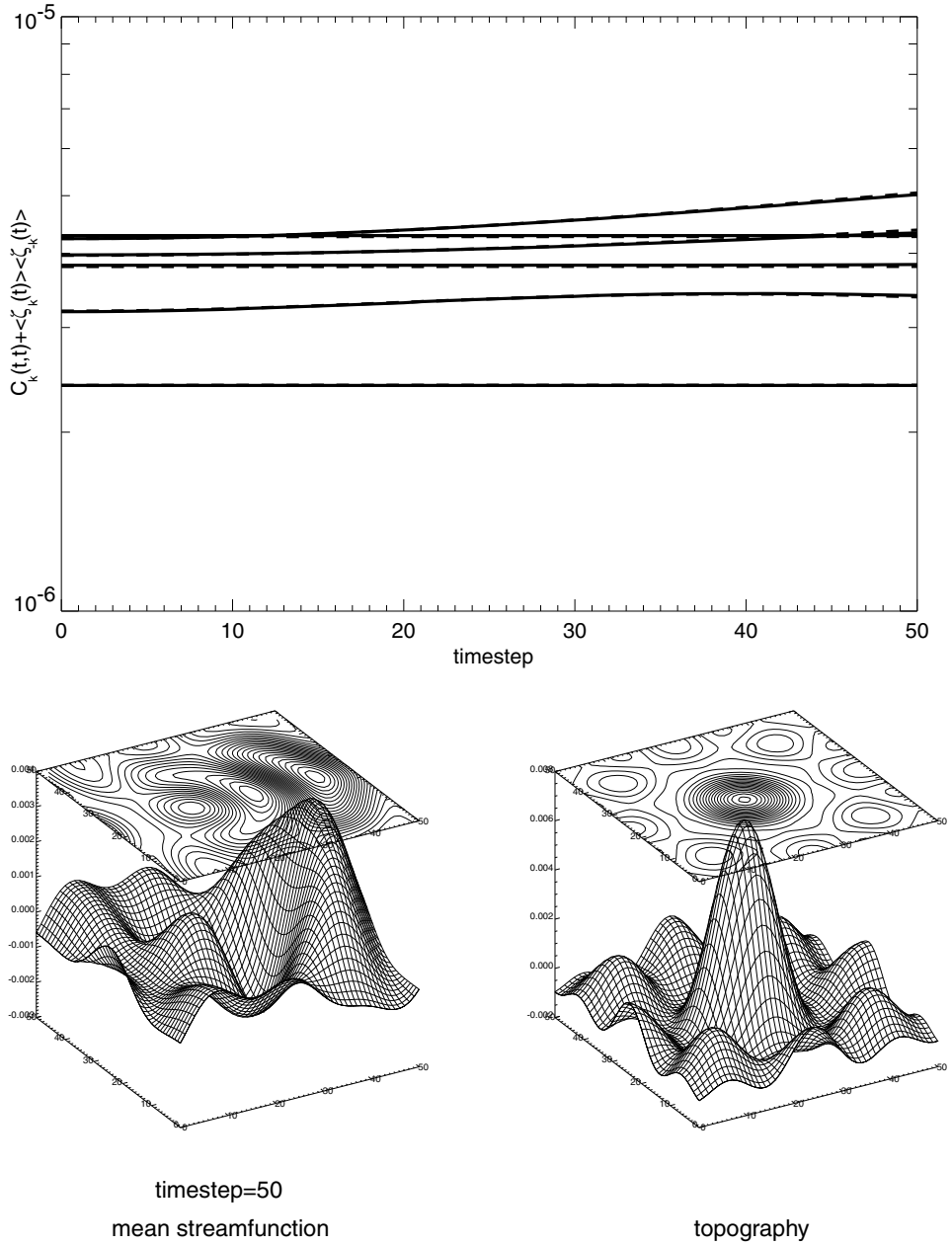

Figure 6.4: (top) The evolution of the total fields for N-periodic flow (N=4) on a β-plane with parameters as for tables 6.2 and 6.3 but with a non-dimensional timestep of 0.5. The total and $\mathbf{k} = \mathbf{0}$ modes are not displayed in order to focus on the modes where there is significant evolution; however they display similar agreement. (bottom) The topography and final state of the mean-field streamfunction after a nondimensional time of 25.

6.6 C16 results

In this section we consider C16 resolution calculations for a flow over a Gaussian mountain whose height in physical space corresponds to 3000 meters. This choice of topography (see Fig. 6.1 left) provides a very strong mean flow component in the two cases that are presented in this section. Again, relatively large time-steps have been used throughout. As in the f-plane study we will use the following convention for the spectral plots:
Total field diagrams; DNS (solid lines), CUQDIA (dotted lines), initial fields (dashed lines)
Component field diagrams: mean field; DNS (dashed lines), CUQDIA (dotted lines), transient field; DNS (solid lines), CUQDIA (dot dashed lines).

Table 6.4: Parameters for Figs. 6.5 to 6.10

$\triangle t$	a	b	β	k_0^2	N
0.1	4.824×10^4	2.511×10^3	$\frac{1}{2}$	$\frac{1}{8}$	4

Table 6.5: Parameters for Figs. 6.5 to 6.10

$\hat{\nu}$	$f_{\mathbf{0}}^0$	$C_{\mathbf{k}}(0,0)$	$C_{\mathbf{0}}(0,0)$	$h_{\mathbf{0}}$	$\langle\zeta_{\mathbf{0}}(0)\rangle$	$\langle\zeta_{\mathbf{k}}(0)\rangle$
0.001	0.0	$C_{\mathbf{k}}^{eq}$	$C_{\mathbf{0}}^{eq}$	$\frac{-i\beta}{k_0}$	$-i0.04305$	$-bh_{\mathbf{k}}C_{\mathbf{k}}^{eq}$

The first case we look at is very similar to the decay from equilibrium cases that we discussed for the f-plane, however we now have an initial large-scale eastward flow at $20ms^{-1}$ (see tables 6.4 and 6.5). The system is evolved for 60 timesteps including 2 restarts for a total nondimensional time of $t = 6.0$. The final energy spectra (Figs. 6.5 top, and 6.7 bottom) show close agreement for the total fields although the CUQDIA slightly overestimates the transient energy at $k > 13$. In Fig. 6.7 close agreement is shown for the evolved mean and transient energy. The relative difference between the mean and transient energy spectra and their crossover point in Fig. 6.7 (bottom) is not dissimilar to those found in the atmosphere and studied by Boer and Shepherd (see Fig.

1a [120]). Comparison of the total potential enstrophy (Fig. 6.5 bottom) also shows close agreement. At $t = 6.0$ the evolved mean potential enstrophy (Fig. 6.8) shows some slight underestimation in the closure while some slight overestimation at scales $8 < k < 12$ is evident in the enstrophy and palinstrophy (Figs. 6.9 and 6.10). Overall all diagnostics compare well even after considerable evolution of the fields.

The second case we will be discussing in detail has parameters given in tables 6.6 and 6.7. This case is again for eastward initial flow at $20ms^{-1}$ but now with a much reduced viscosity and with forcing of the mean large-scale flow $\langle\zeta_{\mathbf{0}}(0)\rangle$ via $\langle f^0_{\mathbf{0}}\rangle$. The result is that energy and enstrophy are forced into the system via the mean large-scale flow term and dissipated via the other modes producing a system that has a very strong mean flow that is forced to stay near $20ms^{-1}$ thereby producing large amplitude Rossby waves. We again implement our restart procedure at $t = \acute{t} = 20\triangle t$ and evolve the system for a nondimendional time of $t = 5.0$. In Figs. 6.11 and 6.12 both the mean and transient energy and palinstrophy spectra are shown to closely agree at all scales.

Table 6.6: Parameters for Figs. 6.11 to 6.14

$\triangle t$	a	b	β	k_0^2	N
0.05	4.824×10^4	2.511×10^3	$\frac{1}{2}$	$\frac{1}{8}$	4

Table 6.7: Parameters for Figs. 6.11 to 6.14

$\hat{\nu}$	$\langle f^0_{\mathbf{0}}\rangle$	$C_{\mathbf{k}}(0,0)$	$C_{\mathbf{0}}(0,0)$	$h_{\mathbf{0}}$	$\langle\zeta_{\mathbf{0}}(0)\rangle$	$\langle\zeta_{\mathbf{k}}(0)\rangle$
0.0001	$-i0.04305\hat{\nu}k_0^2$	$\frac{1}{100}C^{eq}_{\mathbf{k}}$	$\frac{1}{100}C^{eq}_{\mathbf{0}}$	$\frac{-i\beta}{k_0}$	$-i0.04305$	$-bh_{\mathbf{k}}C^{eq}_{\mathbf{k}}$

Figures 6.13 and 6.14 (bottom) reveal the evolution of the mean streamfunction contours from the initial state (6.13 top). We can clearly see evidence of a local clockwise rotation of the negative and positive vorticity structures in the vicinity of the topographic peak. A similar type of effect has been studied in some detail by Verron and Le Provost (Figs. 12a and b [114]).

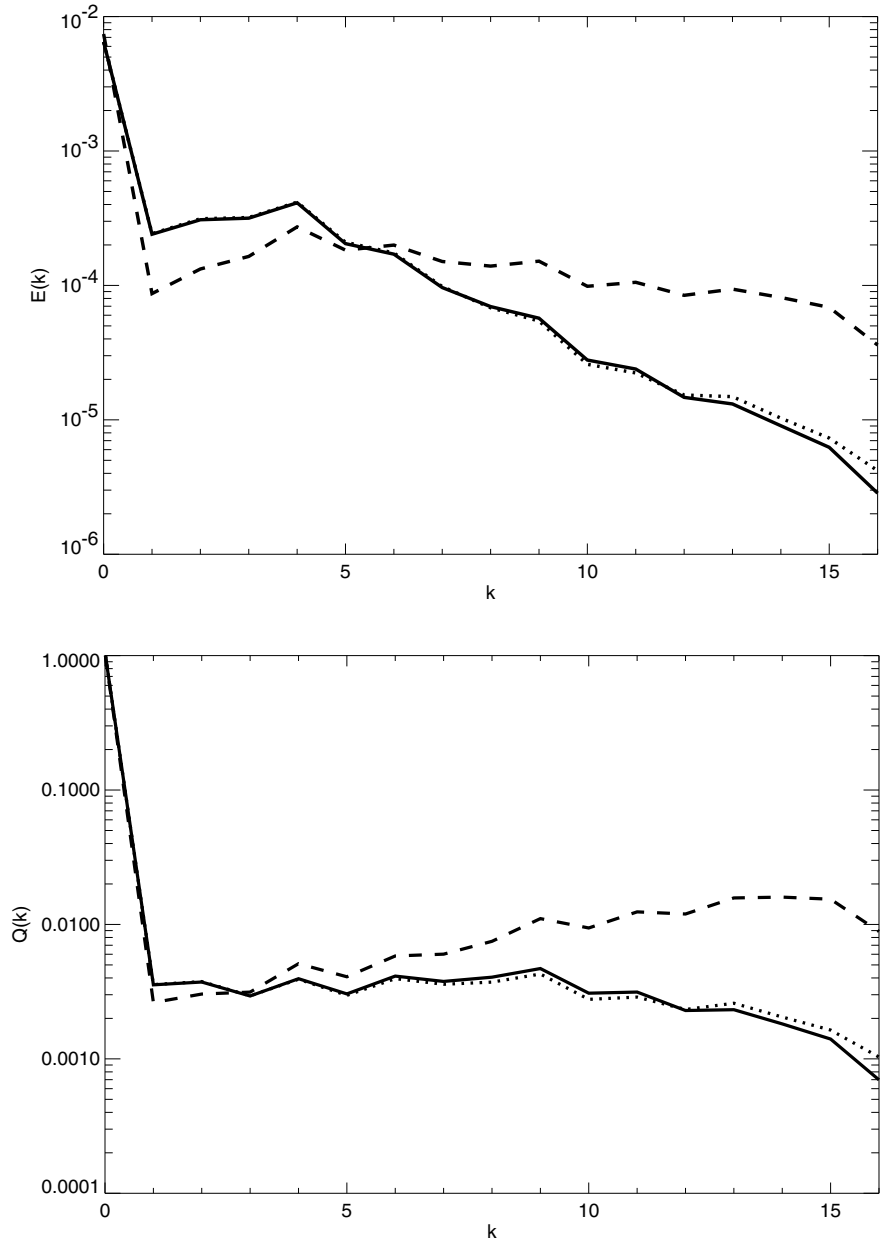

Figure 6.5: The total energy (top) and potential enstrophy spectra (bottom) after 60 timesteps. Total field diagrams; DNS (solid lines), CUQDIA (dotted lines), initial fields (dashed lines).

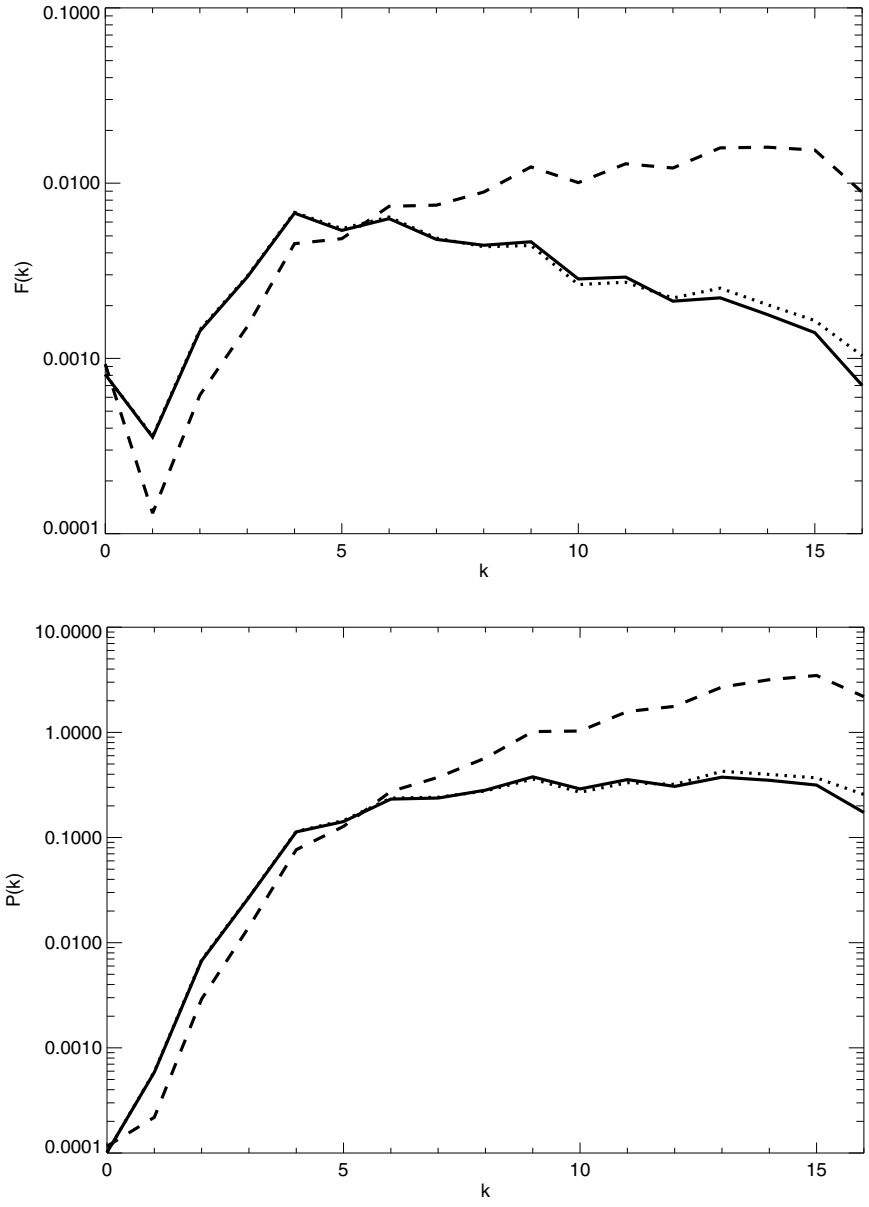

Figure 6.6: The total enstrophy (top) and palinstrophy spectra (bottom) after 60 timesteps and 2 restarts. Total field diagrams; DNS (solid lines), CUQDIA (dotted lines), initial fields (dashed lines).

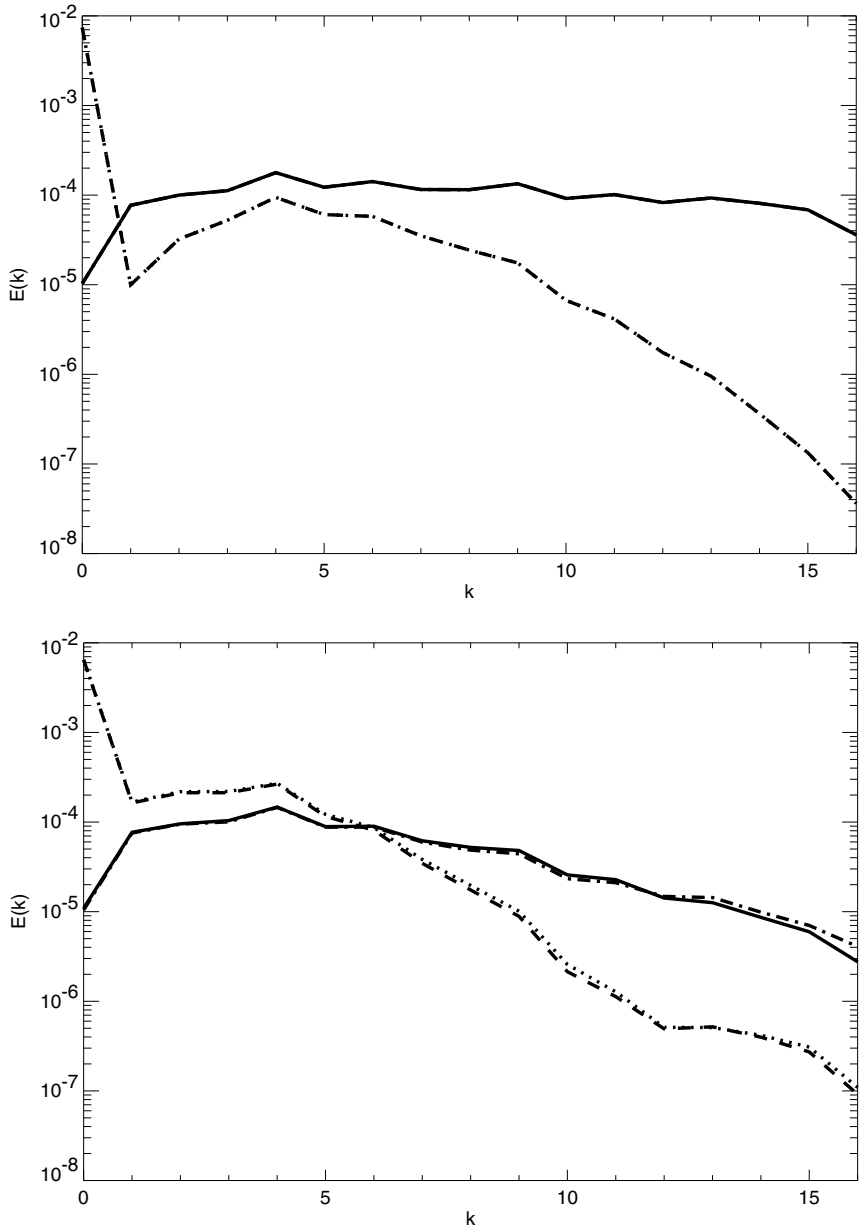

Figure 6.7: (top) The initial mean and transient energy spectra. (bottom) The mean and transient energy spectra at $t = 6.0$. Component field diagrams: mean field; DNS (dashed lines), CUQDIA (dotted lines), :transient field; DNS (solid lines), CUQDIA (dot dashed lines).

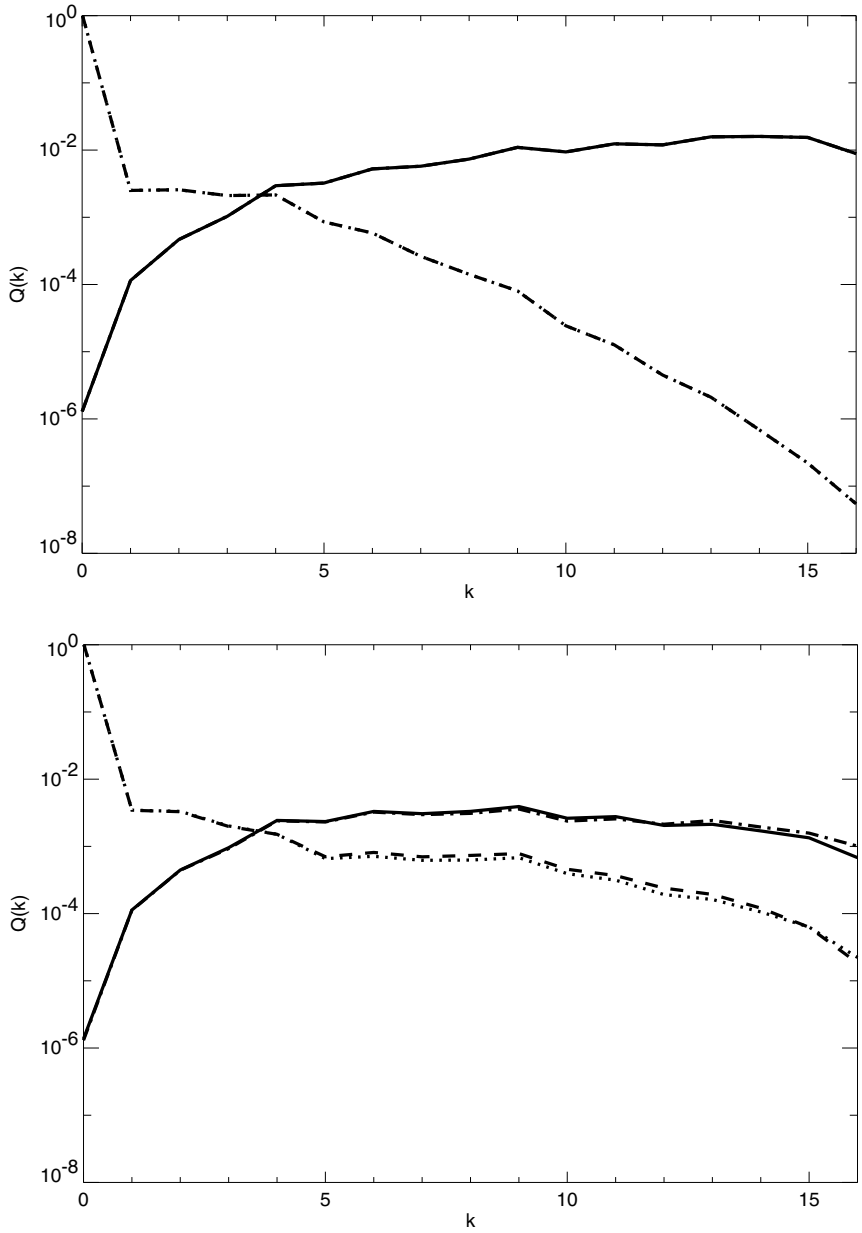

Figure 6.8: (top) The initial mean and transient potential-enstrophy spectra. (bottom) The mean and transient potential-enstrophy spectra at $t = 6.0$. Component field diagrams: mean field; DNS (dashed lines), CUQDIA (dotted lines), :transient field; DNS (solid lines), CUQDIA (dot dashed lines).

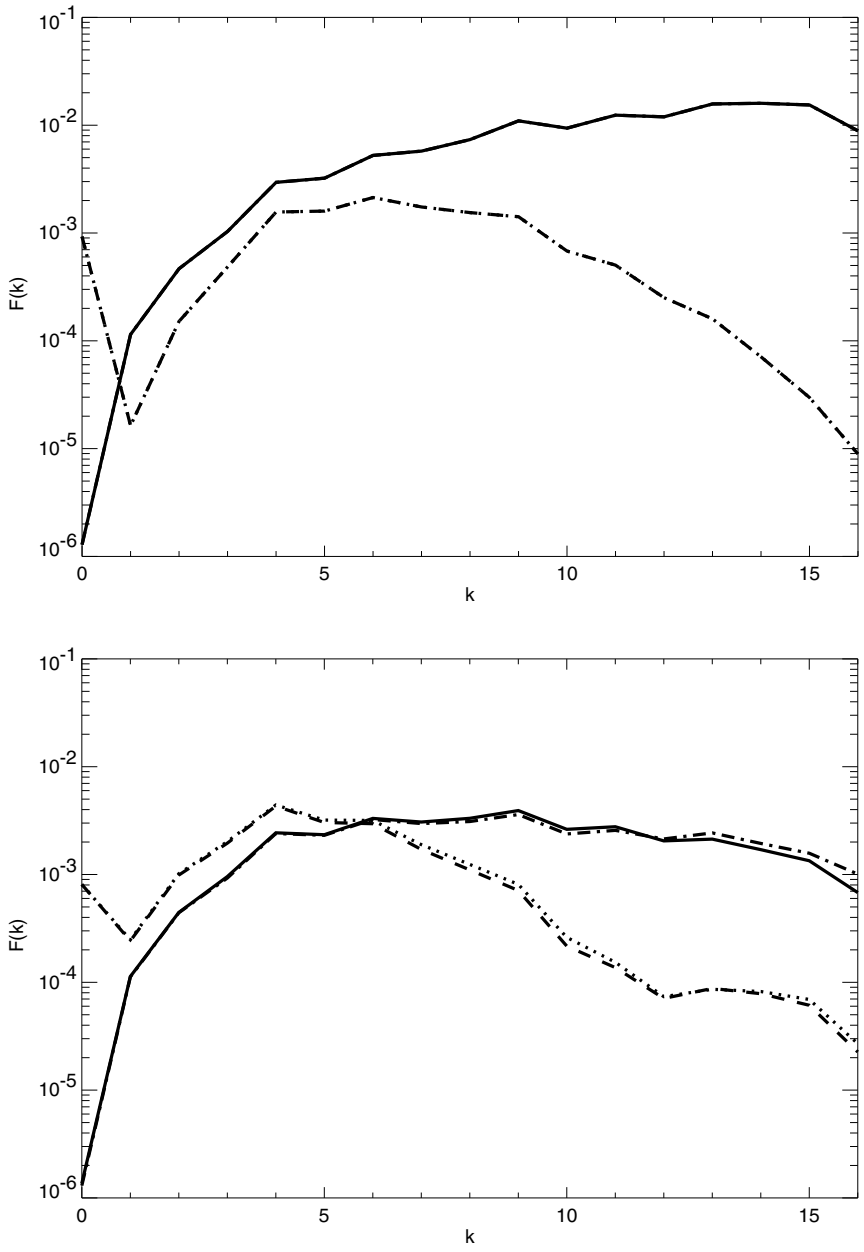

Figure 6.9: (top) The initial mean and transient enstrophy spectra. (bottom) The mean and transient enstrophy spectra after 60 timesteps. Component field diagrams: mean field; DNS (dashed lines), CUQDIA (dotted lines), :transient field; DNS (solid lines), CUQDIA (dot dashed lines).

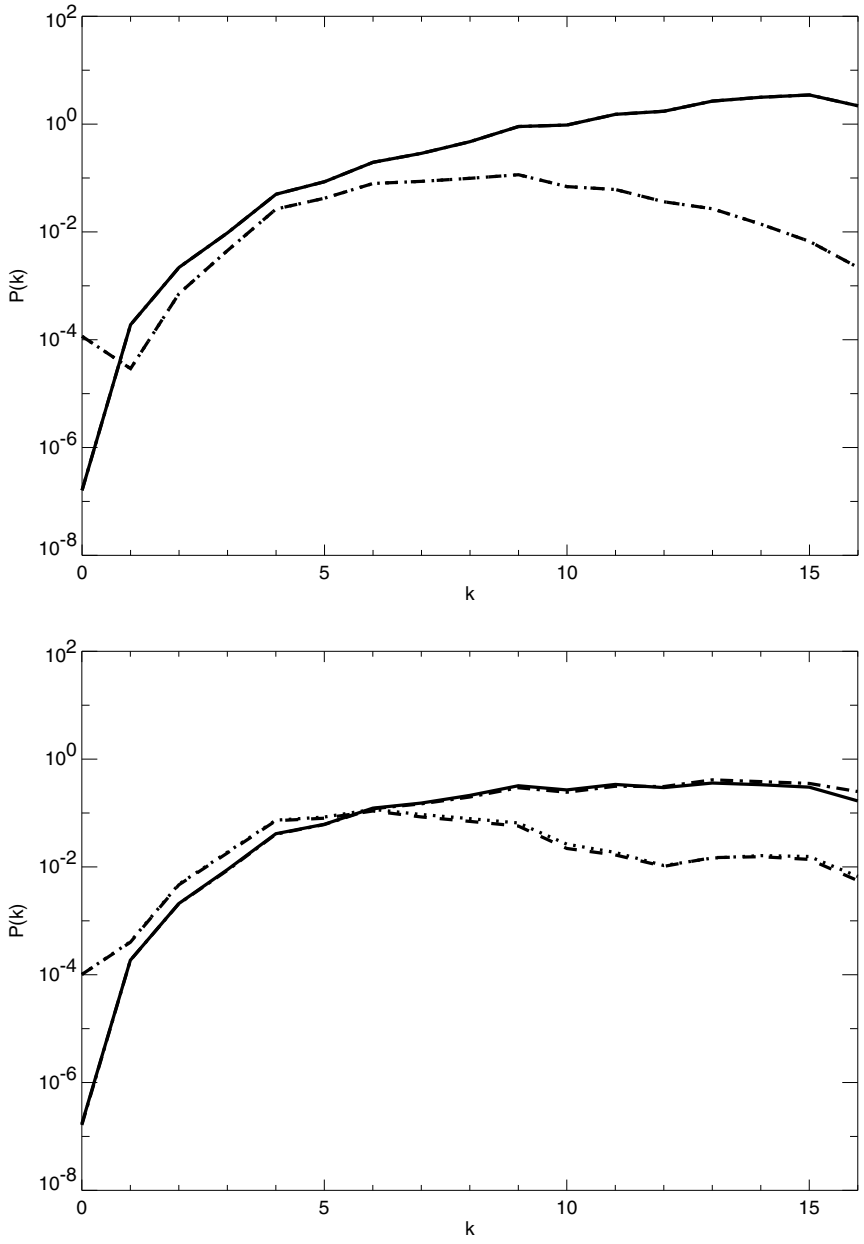

Figure 6.10: (top) The initial mean and transient palinstrophy spectra. (bottom) The mean and transient palinstrophy spectra after 60 timesteps. Component field diagrams: mean field; DNS (dashed lines), CUQDIA (dotted lines), :transient field; DNS (solid lines), CUQDIA (dot dashed lines).

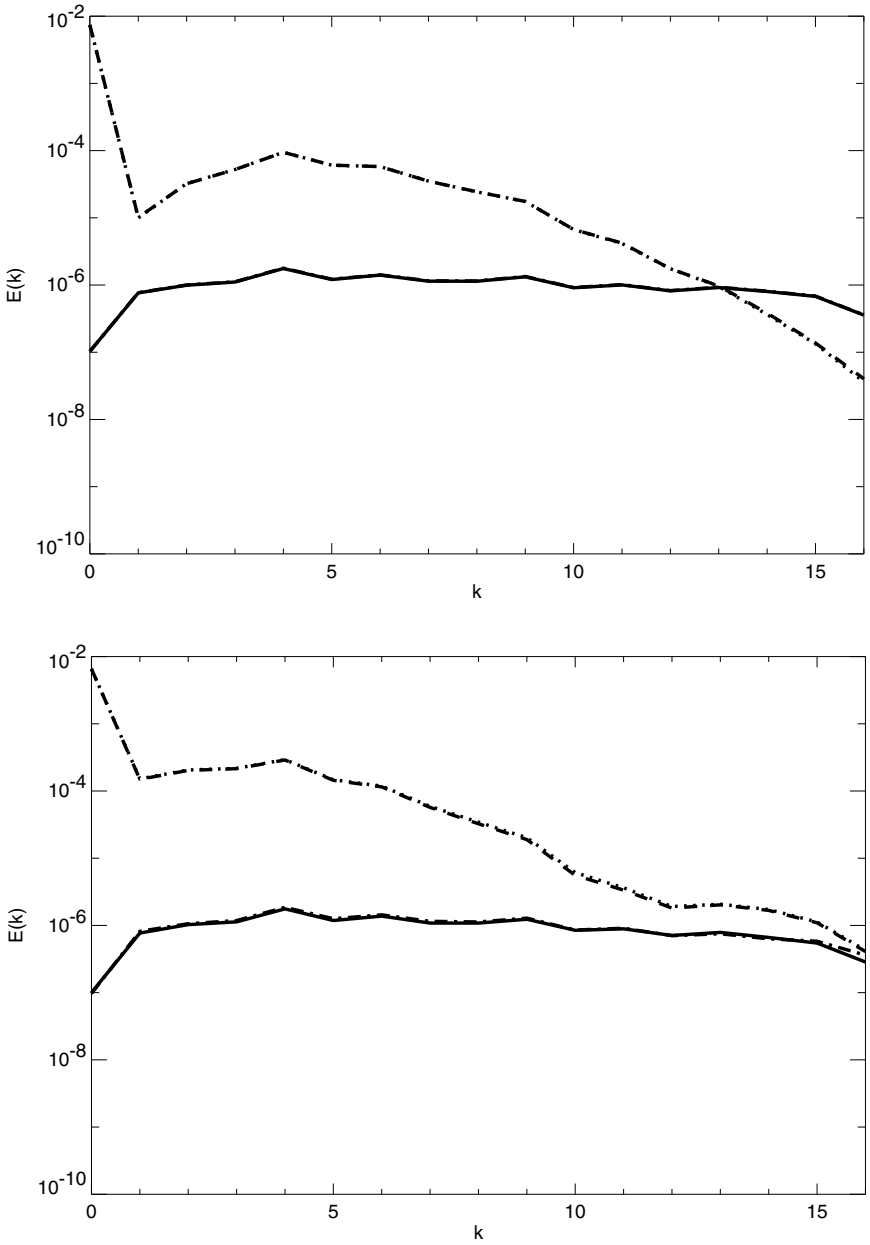

Figure 6.11: (top) The initial mean and transient energy spectra. (bottom) The mean and transient energy spectra after 100 timesteps and 4 restarts. Component field diagrams: mean field; DNS (dashed lines), CUQDIA (dotted lines), :transient field; DNS (solid lines), CUQDIA (dot dashed lines). Note that the respective DNS and CUQDIA mean and transient fields are almost indistinguishable.

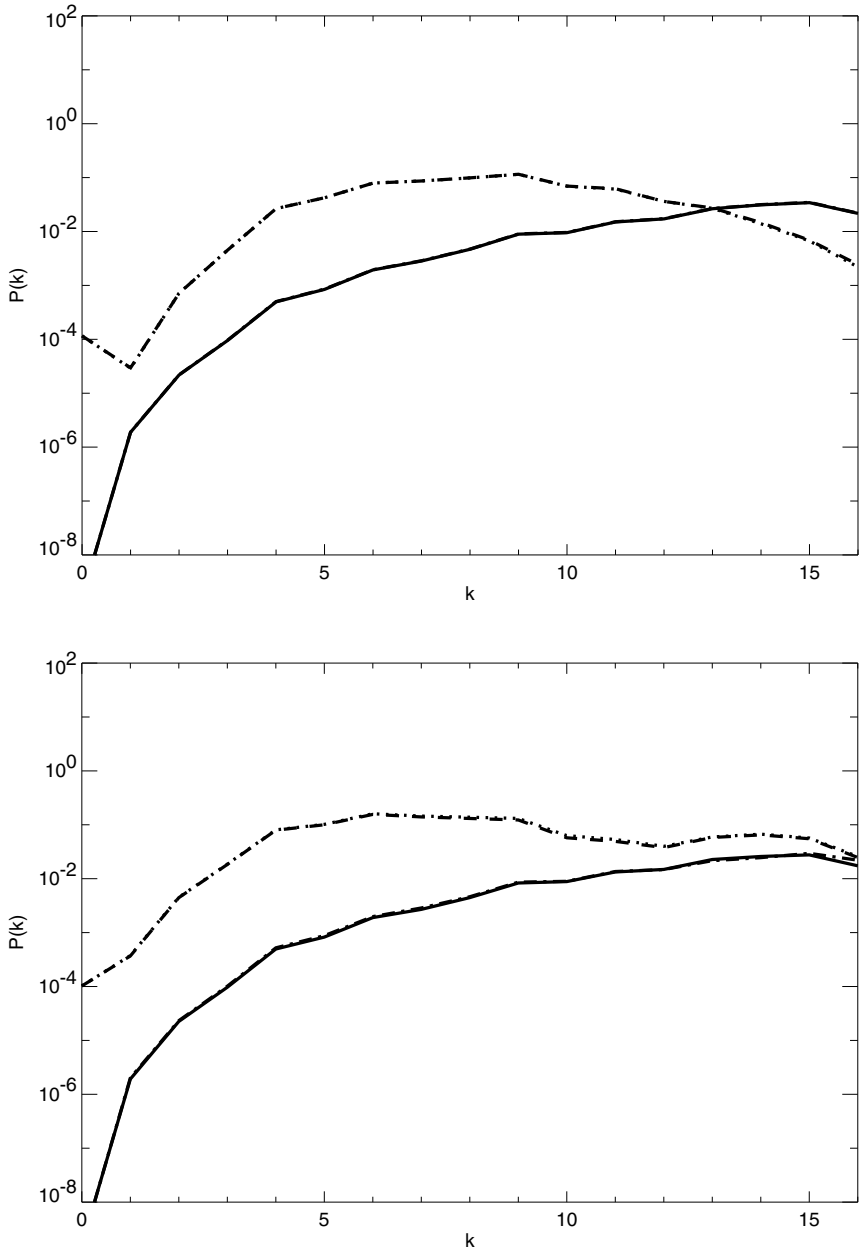

Figure 6.12: (top) The initial mean and transient palinstrophy spectra. (bottom) The mean and transient palinstrophy spectra at $t = 5.0$. Component field diagrams: mean field; DNS (dashed lines), CUQDIA (dotted lines), :transient field; DNS (solid lines), CUQDIA (dot dashed lines). As for Fig. 6.11 the respective DNS and CUQDIA mean and transient fields are almost indistinguishable.

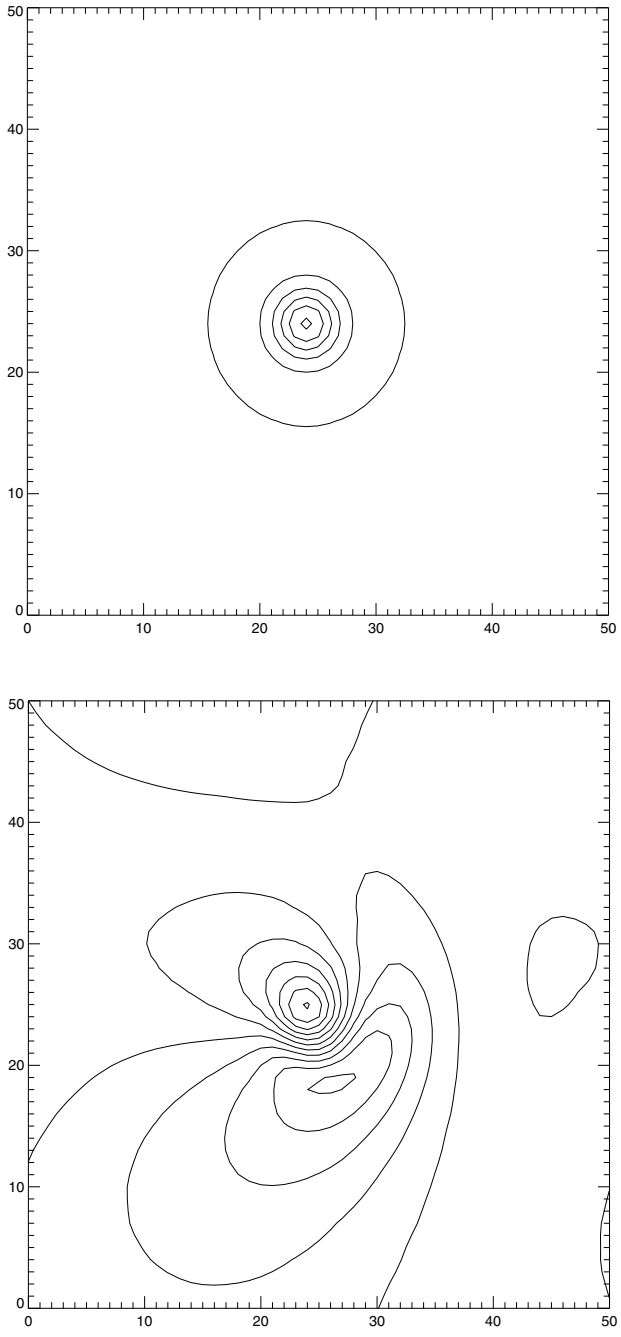

Figure 6.13: (top) The initial mean streamfunction and (bottom) the evolved mean streamfunction, excluding the Uy term, at $t = 5.0$. In the viscid forced case clear clockwise rotation occurs in the vicinity of the mountain with a downstream wave appearing.

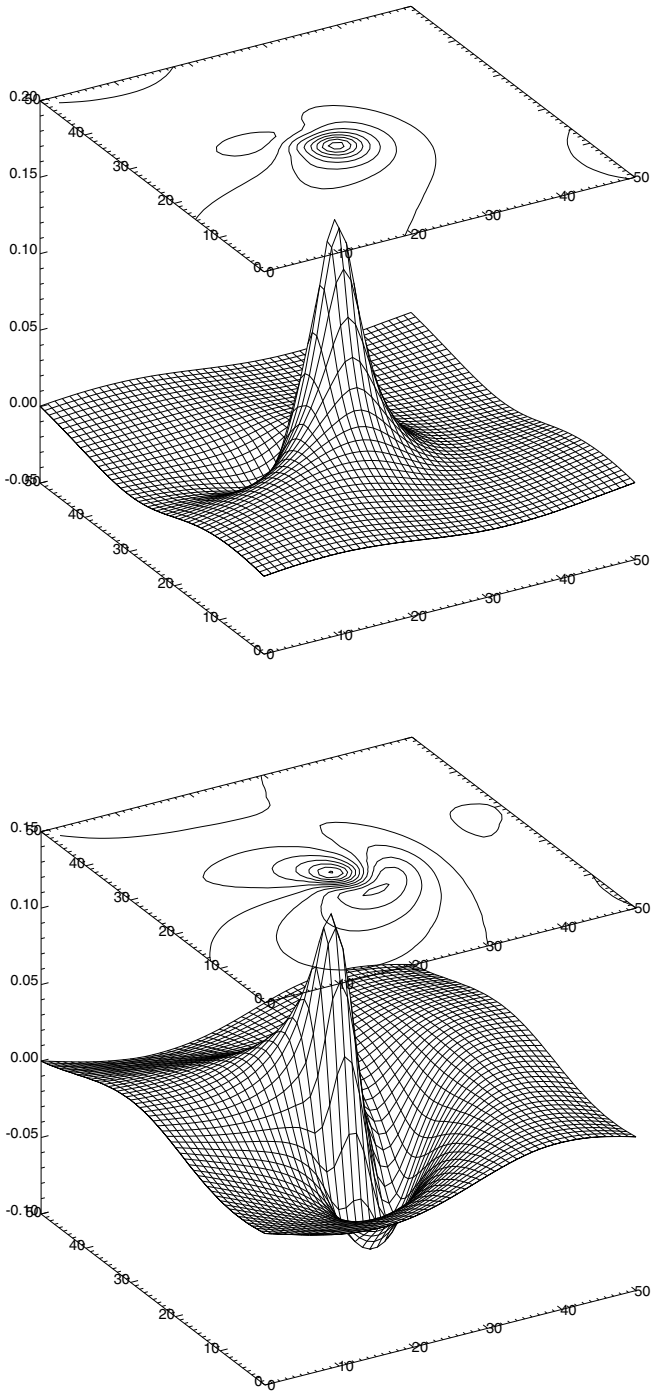

Figure 6.14: Comparison of the evolved mean streamfunctions for (top) initially westward large-scale flow and (bottom) initially eastward flow as for Fig. 6.13. The case for westward flow exhibits some small counter-clockwise rotation near the mountain with no evidence of downstream waves developing.

In Fig. 6.14 (bottom) we can also begin to see the emergence of a downstream wave crest as is to be expected. In Fig. 6.14 (top) we have the same case but with the initial flow in the retrograde direction (westward). As in the C3 calculation (Fig. 6.3) there are no downstream waves evident; however some anticlockwise rotational effects have emerged which are more typical of large-scale f-plane flow. These effects are however small in amplitude with the primary negative vorticity core directly over the main topographic structure. This feature has been demonstrated previously in Fig. 13a of Verron and Le Provost [114].

6.7 Summary

In this chapter a logical extension of the QDIA and CUQDIA closure from an f-plane to a generalized β-plane is developed and shown to be in close agreement with DNS calculations for resolutions up to C16. The closure theory is found to produce behavior in broad agreement with that expected for flow over a Gaussian mountain on a β-plane and also for flow over single realization random topographies (not shown). The C3 inviscid unforced case shows the expected wavetrain response to isolated topography for eastward initial flow whereas for initially westward flow only local mean response was found with large transient Rossby waves evident. In the C16 case for forced dissipative flow with an initially eastward direction, there is a very strong response evident in the vicinity of the topographic structure, however the wavetrain response is weak due to the combined effect of viscosity and strong nonlinearity. Strong nonlinearity results in a pronounced clockwise rotation of the dipolar structure in the region of the topographic feature with the effective viscosity suppressing the downstream wavetrain. For the case of initially westward large-scale flow there is no evidence of a downstream wavetrain but some anti-clockwise rotation of the negative vorticity structure arises, again, due to nonlinear effects.

Chapter 7

Conclusion

In this thesis the quasi-diagonal direct interaction approximation (QDIA) for flow over mean topography has been implemented. As well, a variant has been developed in which the potentially long time-history integrals are periodically collapsed and the information they contain, namely the non-Gaussian cumulants are represented as non-Gaussian initial conditions at the subsequent timestep. This variant, termed the cumulant update quasi-diagonal direct interaction approximation (CUQDIA), is found to produce a close approximation to the QDIA while dramatically reducing the computational task. Low resolution studies (triad, C3) of the dynamics of both the QDIA and CUQDIA, as compared to DNS are found to be favorable as have higher resolution C16 studies of the total kinetic energy and total potential enstrophy.

The CUQDIA mean and transient fields are found to be in extremely close agreement with DNS for very low Reynolds number studies of the kinetic energy, enstrophy, potential enstrophy and palinstrophy for two topographies of significantly differing spectral slope. Resolutions up to C64 have been considered with only very slight discrepancies apparent in the very smallest scales of the closure transient fields. Low and moderate Reynolds number studies have shown that the CUQDIA gives very accurate estimates of the mean and transient fields in the case where the topography squared is of the form $|h_{\mathbf{k}}|^2 = \frac{4k}{(1+k^3)}$ and with a strong mean field at the small-scales comparative to the evolved transient field. More sensitive comparisons of the closure skewness factor and large-scale Reynolds number have also been shown to be in good agreement with DNS. However, in the case

with a very weak amplitude small-scale topography, it has been shown that the evolved DNS small-scale transient field dominates the evolved small-scale mean field. For this particular case the CUQDIA significantly under-estimated the evolved transients in much the same way as the non-topographic DIA theory. The closure mean fields on the other hand are well represented in comparison to DNS in both cases studied.

The obvious conclusion to be drawn is that the presence of a large amplitude small-scale topography and consequently a large amplitude small-scale mean field reduces the tendency of the CUQDIA to generate spurious convection effects that manifest themselves as an under-estimation of the small-scale transient fields. These spurious convection effects arise from the treatment by the direct interaction approximation of the three-point cumulant term. The inhomogeneous terms of the closure, namely those terms that incorporate the topography and mean field, are found to be remarkably accurate including for large amplitude small-scale topography and mean-field. This finding is a remarkable example of the power of renormalized perturbation theory given that the theory is developed assuming a small amplitude topographic component.

Finally, the CUQDIA has been extended from the f-plane to a generalized β-plane in which the standard β-plane dispersion relation has the vorticity of the large-scale flow in addition to the planetary vorticity. This additional term is incorporated in order that the standard β-plane be in a one-to-one correspondence with the spherical geometry. The generalized β-plane formulation also allows a symmetric formulation of the QDIA and CUQDIA closures thus rendering numerical implementation relatively straight forward. Respective studies of eastward and westward flow over a Gaussian mountain at C3 and C16 resolution display close agreement to DNS for a variety of initial conditions, as well as demonstrating behavior comparable to earlier DNS studies of quasi-geostrophic barotropic flows. However, no attempt was made to examine the model at higher resolutions or for increased Reynolds number, although for atmospheric flows the behavior of the mean flow in the large-scale is of most significance.

It is somewhat obvious that the CUQDIA closure model, as presented in this thesis, would benefit from the heuristic vertex renormalization known as regularization in the manner developed by Frederiksen and Davies [28] for the DIA. Regularization requires the

incorporation of a cut-off parameter in order that the triad interactions be made more local thus restricting the generation of spurious convection effects inherent in the DIA. As there are no clear impediments to the regularization of the CUQDIA closure model this approach to mitigating the problem of spurious convection effects could be carried out in a straight forward manner.

Appendix

I Eulerian renormalized perturbation theory

In this appendix a heuristic derivation of the direct interaction approximation (DIA) is presented for stationary, homogeneous and isotropic turbulence. This appendix is included in the interests of completeness. The main assumptions of the DIA such as weak dependence and quasi-normal distribution are detailed as is the renormalization procedure, after which the required interaction coefficients are also derived. Many similar derivations of the DIA appear in the literature and are too numerous to list; however, the books by Leslie [20], McComb [43] and Lesieur [79] contain comprehensive discussions of most aspects of the DIA.

I.1 Isotropic turbulence in an incompressible fluid

In order to begin our examination of the Eulerian renormalized perturbation theory we first define the covariance between two velocity fields v_i ,v_j as

$$U_{ij}(\mathbf{x},t;\acute{\mathbf{x}},\acute{t}) = \left\langle v_i(\mathbf{x},t); v_j(\acute{\mathbf{x}},\acute{t})\right\rangle . \tag{A.1}$$

In the case of stationary, homogeneous and isotropic turbulence we may express the covariance function U_{ij} as a scalar

$$U_{ij}\left(\mathbf{x},t;\acute{\mathbf{x}},\acute{t}\right) = \mathbf{Curl}U\left(\left|\mathbf{x}-\acute{\mathbf{x}}\right|,\left|t-\acute{t}\right|\right)\epsilon_{ijl}\left(x_l-\acute{x}_l\right). \tag{A.2}$$

We may write the Navier-Stokes (N-S) equation in the form

$$\frac{\partial v_i}{\partial t} + \frac{\partial\left(v_i v_j\right)}{\partial x_j} = \nu \bigtriangledown^2 v_i - \frac{\partial \overline{\omega}}{\partial x_i} + f_i \tag{A.3}$$

where $\overline{\omega} = \frac{p}{\rho}$ is the pressure-density ratio. Incompressibility implies $\frac{\partial v_i}{\partial x_i} = 0$, while for divergence free forcing we have that $\frac{\partial f_i}{\partial x_i} = 0$. We now work in spectral space via the Fourier Transform procedure outlined below

$$v_i(\mathbf{x},t) = (VT)^{-\frac{1}{2}} \sum_{k,\omega} v_i(\mathbf{k},\omega) \exp i(\mathbf{k}\cdot\mathbf{x} - \omega\mathbf{t}) \tag{A.4}$$

$$f_i(\mathbf{x},t) = (VT)^{-\frac{1}{2}} \sum_{k,\omega} f_i(\mathbf{k},\omega) \exp i(\mathbf{k}\cdot\mathbf{x} - \omega\mathbf{t}) \tag{A.5}$$

$$\overline{\omega}_i(\mathbf{x},t) = (VT)^{-\frac{1}{2}} \sum_{k,\omega} \overline{\omega}_i(\mathbf{k},\omega) \exp i(\mathbf{k}\cdot\mathbf{x} - \omega\mathbf{t}) \tag{A.6}$$

where

$$\lim_{T\to\infty} \frac{1}{VT} \sum_{k,\omega} \to \frac{1}{(2\pi)^4} \int d^3\mathbf{k} \int \mathbf{d}\omega \tag{A.7}$$

with $k = (k_1, k_2, k_3, -\omega) = (\mathbf{k}, -\omega)$, $x = (x_1, x_2, x_3, t) = (\mathbf{x}, t)$ and $\Omega = VT$. Here V represents the volume of a large four dimensional box and temporal extent T [29]. Thus we may write

$$v_i(x) = \Omega^{-\frac{1}{2}} \sum_k v_i(k) \exp i(k\cdot x), \tag{A.8}$$

$$\frac{1}{\Omega} \sum_k \to \frac{1}{(2\pi)^4} \int d^4k. \tag{A.9}$$

Substituting Eqs. A.4, A.5, and A.6 into the N-S Eq. A.3 and integrating over x we find

$$\begin{aligned} -i\omega v_i(k) + \Omega^{-\frac{1}{2}} i \sum_{\acute{k}+\grave{k}=k} \left[\acute{k}_j v_i\left(\acute{k}\right) v_j\left(\grave{k}\right)\right] \\ = -\nu\mathbf{k}^2 v_i(k) - ik_i\overline{\omega}(k) + f_i(k). \end{aligned} \tag{A.10}$$

We derive the $\overline{\omega}$ term by multiplying Eq. A.10 by $k_i k^{-2}$ and employing the divergence condition, which requires $k_i v_i = k_i f_i = 0$; thus,

$$\overline{\omega} = -\frac{1}{\Omega^{\frac{1}{2}}\mathbf{k}^2} \sum_{\acute{k}+\grave{k}=k} k_i \acute{k}_j v_i\left(\acute{k}\right) v_j\left(\grave{k}\right). \tag{A.11}$$

Then substituting Eq. A.11 back into the N-S equation gives

$$\begin{aligned} -i\omega v_i(k) + \nu\mathbf{k}^2 v_i(k) = f_i(k) \\ + \frac{i}{\Omega^{\frac{1}{2}}} \{k_j \sum_{\acute{k}+\grave{k}=k} v_i\left(\acute{k}\right) v_j\left(\grave{k}\right) \\ - \frac{k_i k_j k_m}{\mathbf{k}^2} \sum_{\acute{k}+\grave{k}=k} v_m\left(\acute{k}\right) v_j\left(\grave{k}\right)\}. \end{aligned} \tag{A.12}$$

Now we make use of the following identities (see Appendix I.4 for derivation)

$$P_{ij}(\mathbf{k}) = \delta_{ij} - \frac{k_i k_j}{\mathbf{k}^2} \tag{A.13}$$

$$P_{ijm}(\mathbf{k}) = k_j P_{im}(\mathbf{k}) + k_m P_{ij}(\mathbf{k}). \tag{A.14}$$

Finally Eq. A.12 becomes

$$\left(-i\omega + \nu\mathbf{k}^2\right) v_i(k) = f_i(k) - i\frac{P_{ijm}(\mathbf{k})}{2\Omega^{\frac{1}{2}}} \sum_{\acute{k}+\grave{k}=k} v_m\left(\acute{k}\right) v_j\left(\grave{k}\right). \tag{A.15}$$

I.2 The impulse response function

Let us write Eq. A.15 in a more compact form

$$\left(\frac{\partial}{\partial t} + \nu\mathbf{k}^2\right) v_i(\mathbf{k},t) - N_{ijm}(k) \sum_{\acute{\mathbf{k}}} v_j\left(\acute{\mathbf{k}},t\right) v_m\left(\mathbf{k}-\acute{\mathbf{k}},t\right) = f_i(\mathbf{k}) \tag{A.16}$$

where $N_{ijm}(k) = -\frac{i}{2\Omega^{\frac{1}{2}}} P_{ijm}(\mathbf{k})$. We may now consider the response r_i to an infinitesimal linear forcing function given by $f_i = \delta f_n \delta_{in} \delta\left(t-\hat{t}\right)$. Thus

$$\left(\frac{\partial}{\partial t} + \nu\mathbf{k}^2\right) r_i - \sum_{jm} N_{ijm} r_j r_m = \delta f_n \delta_{in} \delta\left(t-\hat{t}\right). \tag{A.17}$$

$$\delta_{in} = \begin{cases} 1 & \text{if } i{=}n; \\ 0 & \text{otherwise.} \end{cases} \tag{A.18}$$

The difference $r_i - v_i = \delta v_i$ is obtained to give

$$\left(\frac{\partial}{\partial t} + \nu\mathbf{k}^2\right) \delta v_i - \sum_{jm} N_{ijm}\left(r_j r_m - v_j v_m\right) = \delta f_n \delta_{in} \delta\left(t-\hat{t}\right). \tag{A.19}$$

Thus substituting $r_i = \delta v_i + v_i$ into Eq. A.19 and neglecting $O(\delta v)^2$ terms we find the impulse response function satisfies the equation

$$\left(\frac{\partial}{\partial t} + \nu\mathbf{k}^2\right) G_{in}\left(t-\hat{t}\right) - 2\sum_{jm} N_{ijm} v_j(t)\, G_{mn}\left(t-\hat{t}\right) = \delta_{in}\left(t-\hat{t}\right) \tag{A.20}$$

where $G_{in}\left(t-\hat{t}\right) = \frac{\delta v_i}{\delta f_n(\hat{t})}$ and we have used the symmetry property $N_{ijm} = N_{imj}$.

I.3 The direct interaction approximation

We next implement the direct interaction approximation of Kraichnan[19] beginning with the spectral form of the Navier-Stokes equations,

$$\left(\frac{\partial}{\partial t}+\nu\mathbf{k}^2\right)v_i-\sum_{jm}N_{ijm}v_jv_m=0, \tag{A.21}$$

and Eq. A.20. We define a perturbation parameter λ and expand v_i and G_{in} in powers of λ i.e.

$$v_i=v_i^0+\lambda v_i^1+\lambda^2v_i^2+O\left(\lambda^3\right) \tag{A.22}$$

$$G_{in}=G_{in}^0+\lambda G_{in}^1+\lambda^2G_{in}^2+O\left(\lambda^3\right). \tag{A.23}$$

Substituting Eqs. A.22 and A.23 into Eqs. A.20 and A.21 and equating in powers of λ up to 2^{nd} order gives

$$\frac{d}{dt}v_i^0+\nu\mathbf{k}^2v_i^0=0 \tag{A.24}$$

$$\frac{d}{dt}v_i^1+\nu\mathbf{k}^2v_i^1=\sum_{jm}N_{ijm}v_j^0v_m^0 \tag{A.25}$$

$$\left(\frac{d}{dt}+\nu\mathbf{k}^2\right)G_{in}^0=\delta_{in}\delta\left(t-\acute{t}\right) \tag{A.26}$$

$$\left(\frac{d}{dt}+\nu\mathbf{k}^2\right)G_{in}^1=2\sum_{jm}N_{ijm}v_j^0G_{mn}^0. \tag{A.27}$$

In order to calculate the two-point cumulant we multiply Eq. A.21 by $v_i\left(\acute{t}\right)$and take the ensemble average denoted by $\langle\,\rangle$. Thus we find that

$$\left(\frac{\partial}{\partial t}+\nu\mathbf{k}^2\right)U_i\left(t-\acute{t}\right)=\sum_{jm}N_{ijm}\left\langle v_j\left(t\right)v_m\left(t\right)v_i\left(\acute{t}\right)\right\rangle \tag{A.28}$$

where $U_i\left(t-\acute{t}\right)=\left\langle v_i\left(t\right)v_i\left(\acute{t}\right)\right\rangle$.

To proceed further we require an equation for v_i^1. This is obtained by solving Eq. A.25:

$$\begin{aligned}v_i^1\left(t\right)&=\sum_{jm}N_{ijm}\int_0^t e^{-\nu k^2\left(t-\acute{t}\right)}v_j^0\left(\acute{t}\right)v_m^0\left(\acute{t}\right)\,d\acute{t}\\&=\sum_{jmp}\int_0^t N_{pjm}G_{ip}^0\left(t-\acute{t}\right)v_j^0\left(\acute{t}\right)v_m^0\left(\acute{t}\right)\,d\acute{t}\end{aligned} \tag{A.29}$$

where

$$G_{in}^{0}\left(t-\acute{t}\right)=\begin{cases}\delta_{ij}\,e^{-\nu k^{2}\left(t-\acute{t}\right)} & \text{if } t>\acute{t}\\ 0 & \text{if } t<\acute{t}\end{cases} \tag{A.30}$$

Eq. A.30 is easily deduced from Eq. A.26 with the appropriate causality condition for $t<\acute{t}$. We may now consider the three-point correlation

$$\left\langle v_{i}^{1}\left(\acute{t}\right)v_{j}^{0}\left(t\right)v_{m}^{0}\left(t\right)\right\rangle =2\sum_{prs}\int_{0}^{t}$$
$$\left\langle G_{ip}^{0}\left(t-\acute{t}\right)\right\rangle N_{prs}\left\langle v_{j}^{0}\left(t\right)v_{m}^{0}\left(t\right)v_{r}^{0}\left(\grave{t}\right)v_{s}^{0}\left(\grave{t}\right)\right\rangle \,d\grave{t} \tag{A.31}$$

where we have assumed Kraichnan's weak dependence principle[19], ie.,

$$\left\langle G^{0}v^{0}v^{0}v^{0}v^{0}\right\rangle =G^{0}\left\langle v^{0}v^{0}v^{0}v^{0}\right\rangle . \tag{A.32}$$

A further application of "weak dependence" allows us to write

$$\left\langle v_{i}^{1}\left(\acute{t}\right)v_{j}^{0}\left(t\right)v_{m}^{0}\left(t\right)\right\rangle =2\sum_{p}\int_{0}^{t}$$
$$\left\langle G_{ip}^{0}\left(\acute{t}-\grave{t}\right)\right\rangle N_{pjm}U_{j}^{0}\left(t-\grave{t}\right)U_{m}^{0}\left(t-\grave{t}\right)\,d\grave{t}. \tag{A.33}$$

We next consider $\left\langle v_{i}\left(\acute{t}\right)v_{j}\left(t\right)v_{m}\left(t\right)\right\rangle$ up to 2^{nd} order in terms of the expansion parameter λ and apply the normal distribution condition. Note that we have assumed the initial velocity field to have Gaussian distribution such that $\left\langle v_{i}^{0}\right\rangle =0\rightarrow\left\langle v_{i}^{0}v_{j}^{0}v_{m}^{0}\right\rangle =0$. Thus upon substitution of Eq. A.33 in Eq. A.31 we find that

$$\left\langle v_{i}\left(\acute{t}\right)v_{j}\left(t\right)v_{m}\left(t\right)\right\rangle =2\lambda\sum_{p}\int_{0}^{t}($$
$$\left\langle G_{ip}^{0}\left(\acute{t}-\grave{t}\right)\right\rangle N_{pjm}U_{j}^{0}\left(t-\grave{t}\right)U_{m}^{0}\left(t-\grave{t}\right)\,d\grave{t}$$
$$+\left\langle G_{jp}^{0}\left(t-\grave{t}\right)\right\rangle N_{ipm}U_{p}^{0}\left(t-\grave{t}\right)U_{m}^{0}\left(\acute{t}-\grave{t}\right)\,d\grave{t}$$
$$+\left\langle G_{mp}^{0}\left(t-\grave{t}\right)\right\rangle N_{ijp}U_{j}^{0}\left(\acute{t}-\grave{t}\right)U_{p}^{0}\left(t-\grave{t}\right)\,d\grave{t})$$
$$+O\left(\lambda^{2}\right). \tag{A.34}$$

Upon substitution of Eq. A.34 into Eq. A.28, and, with the bare two-point covariance and propagator terms, U^{0} and G^{0} replaced by the generalized terms U and G (renormalized),

we find that

$$\left(\frac{\partial}{\partial t}+\nu\mathbf{k}^2\right)U_i\left(t-\acute{t}\right)=2\sum_{jmp}N_{ijm}\int_{-\infty}^{t}($$
$$\left\langle G_{ip}\left(\acute{t}-\grave{t}\right)\right\rangle N_{pjm}U_j\left(t-\grave{t}\right)U_m\left(t-\grave{t}\right)\,d\grave{t}$$
$$+\left\langle G_{jp}\left(t-\grave{t}\right)\right\rangle N_{ipm}U_i\left(t-\grave{t}\right)U_m\left(\acute{t}-\grave{t}\right)\,d\grave{t}$$
$$+\left\langle G_{mp}\left(t-\grave{t}\right)\right\rangle N_{ijp}U_i\left(t-\grave{t}\right)U_j\left(\acute{t}-\grave{t}\right)\,d\grave{t})$$
$$=2\sum_{jmp}N_{ijm}\int_{-\infty}^{t}($$
$$\left\langle G_{ip}\left(\acute{t}-\grave{t}\right)\right\rangle N_{pjm}U_j\left(t-\grave{t}\right)U_m\left(t-\grave{t}\right)\,d\grave{t}$$
$$+2\left\langle G_{jp}\left(t-\grave{t}\right)\right\rangle N_{ipm}U_i\left(t-\grave{t}\right)U_m\left(\acute{t}-\grave{t}\right)\,d\grave{t}\,). \tag{A.35}$$

Note in Eq. A.35 we have used symmetry ($N_{ijk}=N_{ikj}$) to combine the $\left\langle v_i^0v_j^0v_m^1\right\rangle$ and $\left\langle v_i^0v_j^1v_m^0\right\rangle$ terms. Finally in order to close the system we must express $\left\langle G_{ij}\left(t-\acute{t}\right)\right\rangle$ in terms of $U_i\left(t-\acute{t}\right)$. Taking the expectation of Eq. A.20 we have

$$\left(\frac{\partial}{\partial t}+\nu\mathbf{k}^2\right)\left\langle G_{in}\left(t-\acute{t}\right)\right\rangle$$
$$-2\sum_{jm}N_{ijm}\left\langle v_j\left(t\right)G_{mn}\left(t-\acute{t}\right)\right\rangle$$
$$=\delta_{in}\delta\left(t-\acute{t}\right). \tag{A.36}$$

In similar fashion to the two-point cumulant we expand $\left\langle v_j\left(t\right)G_{mn}\left(t-\acute{t}\right)\right\rangle$ in powers of λ using Eqs. A.22 and A.23. Thus

$$\left\langle v_j\left(t\right)G_{mn}\left(t-\acute{t}\right)\right\rangle$$
$$=\left\langle v_j^0\left(t\right)G_{mn}^0\left(t-\acute{t}\right)+v_j^0\left(t\right)\lambda G_{mn}^1\left(t-\acute{t}\right)\right.$$
$$\left.+\,\lambda v_j^1\left(t\right)G_{mn}^0\left(t-\acute{t}\right)\right\rangle+O\left(\lambda^2\right). \tag{A.37}$$

Applying "weak dependence" and averaging to Eq. A.29, with a change in indicies, $i\rightarrow j$, $j\rightarrow m$, $m\rightarrow n$ for clarity, we find

$$\left\langle v_j^1\left(t\right)\right\rangle=\sum_{mnp}\int_0^t N_{pmn}\left\langle G_{jp}^0\left(t-\grave{t}\right)\right\rangle\left\langle v_m^0\left(\grave{t}\right)v_n^0\left(\grave{t}\right)\right\rangle\,d\grave{t} \tag{A.38}$$

where $\left\langle v_m^0\left(\grave{t}\right)v_n^0\left(\grave{t}\right)\right\rangle=0$ for $m\neq n$ (that is, the distribution is multivariate normal). Thus for $m=n$

$$\left\langle v_j^1\left(t\right)\right\rangle=\sum_{mmp}\int_0^t N_{pmm}\left\langle G_{jp}^0\left(t-\grave{t}\right)\right\rangle U_m^0\left(\grave{t}\right)\,d\grave{t}. \tag{A.39}$$

However $N_{pmm} = 0$ by definition and Eq. A.39 along with the 2^{nd} term in Eq. A.37 vanishes. Similarly the 1^{st} term in Eq. A.37 is also identically zero as $\left\langle v^0 G^0 \right\rangle = \left\langle v^0 \right\rangle G^0 = 0$. Thus it remains to evaluate $G^1_{mn}\left(t - \hat{t}\right)$. We proceed by integrating Eq. A.27

$$G^1_{mn}\left(t - \hat{t}\right) = 2 \sum_{pqn} \int_0^t G^0_{mp}\left(t - \grave{t}\right) N_{pqn} v^0_p\left(t - \grave{t}\right) G^0_{mn}\left(\grave{t} - \hat{t}\right) d\grave{t}. \tag{A.40}$$

Substituting

$$\left\langle v_j\left(t\right) G_{mn}\left(t - \hat{t}\right)\right\rangle = \lambda \left\langle v^0_j\left(t\right) G^1_{mn}\left(t - \hat{t}\right)\right\rangle \tag{A.41}$$

into Eq. A.36 with G^1 given by Eq. A.40 and $\lambda = 1$ we find that

$$\left(\frac{\partial}{\partial t} + \nu \mathbf{k}^2\right) \left\langle G_{in}\left(t - \hat{t}\right)\right\rangle - 4 \sum_{jmpr} N_{ijm} \int_0^t \left\langle G_{mp}\left(t - \hat{t}\right)\right\rangle N_{pjr} U_j\left(t - \grave{t}\right) \left\langle G_{in}\left(\grave{t} - \hat{t}\right)\right\rangle d\grave{t} = \delta_{in} \delta(t - \hat{t}). \tag{A.42}$$

Here, we have again replaced the U^0 and G^0 terms with U and G. Thus, Eqs. A.35 and A.42 close the system at second order and the closure outlined constitutes the direct interaction approximation. Note: Eqs. A.35 and A.42 correspond to Eqs. 6.28 and 6.31 of McComb[43].

I.4 The P_{ijm} and P_{ij} terms

The P_{ijm} and P_{ij} terms are important as they represent the coupling terms for the interactions and hence define, in a sense, the nonlinearity. In other words the symmetric operator P_{ijm} represents the bare vertex terms or anharmonicity. In order to derive the P_{ijm} and P_{ij} terms we again begin with the Navier Stokes equation

$$\frac{\partial v_i\left(\mathbf{x}, \mathbf{t}\right)}{\partial t} + v_m\left(\mathbf{x}, \mathbf{t}\right) \frac{\partial v_i\left(\mathbf{x}, \mathbf{t}\right)}{\partial x_m} - \nu \bigtriangledown^2 v_i\left(\mathbf{x}, \mathbf{t}\right) = -\frac{\partial \overline{\omega}}{\partial x_i} \tag{A.43}$$

where $\overline{\omega} = \frac{p}{\rho}$ with ρ the density. In order to eliminate the pressure we take the divergence of Eq. A.43. We now make use of the continuity condition i.e. $\frac{\partial v_j(\mathbf{x},t)}{\partial x_j} = 0$ and the fact that $\frac{\partial}{\partial x_i}\frac{\partial}{\partial t}$ can replace $\frac{\partial}{\partial t}\frac{\partial}{\partial x_i}$ to find the pressure condition

$$-\bigtriangledown^2 \overline{\omega} = \frac{\partial v_m}{\partial x_i} \frac{\partial v_i}{\partial x_m}. \tag{A.44}$$

However, the continuity condition allows us to write

$$
\begin{aligned}
-\bigtriangledown^2\overline{\omega} &= \frac{\partial v_j}{\partial x_i}\frac{\partial v_i}{\partial x_j} + v_j\frac{\partial}{\partial x_j}\left(\frac{\partial v_i}{\partial x_i}\right) \\
&= \frac{\partial}{\partial x_j}\left[v_i\frac{\partial v_j}{\partial x_j} + u_j\frac{\partial v_i}{\partial x_j}\right] \\
= \frac{\partial}{\partial x_i}\frac{\partial}{\partial x_j}\left(v_i v_j\right) &= \frac{\partial}{\partial x_j}\frac{\partial}{\partial x_m}\left(v_j v_m\right). \qquad \text{(A.45)}
\end{aligned}
$$

Thus

$$
\overline{\omega} = -\frac{1}{\bigtriangledown^2}\frac{\partial}{\partial x_j}\frac{\partial}{\partial x_m}\left(v_j v_m\right). \qquad \text{(A.46)}
$$

Substituting Eq. A.46 into Eq. A.43 we find

$$
\begin{aligned}
&\frac{\partial v_i}{\partial t} - \nu\bigtriangledown^2 v_i + \Bigg[v_m\frac{\partial v_i}{\partial x_m} \\
&-\frac{\partial}{\partial x_i}\left(\frac{1}{\bigtriangledown^2}\frac{\partial}{\partial x_j}\frac{\partial}{\partial x_m}\left(v_j v_m\right)\right)\Bigg] = 0. \qquad \text{(A.47)}
\end{aligned}
$$

After some manipulation the term in square brackets may be written as

$$
\begin{aligned}
[\,] = &\frac{1}{2}\left(\frac{\partial}{\partial x_m}\left(\delta_{ij}\left(v_j v_m\right) - \frac{1}{\bigtriangledown^2}\frac{\partial^2}{\partial x_i x_j}\left(v_j v_m\right)\right)\right) \\
&+\frac{1}{2}\left(\frac{\partial}{\partial x_j}\left(\delta_{im}\left(v_j v_m\right) - \frac{1}{\bigtriangledown^2}\frac{\partial^2}{\partial x_i x_m}\left(v_j v_m\right)\right)\right) \qquad \text{(A.48)}
\end{aligned}
$$

where we have used $v_m\frac{\partial v_i}{\partial x_m} = \frac{\partial}{\partial x_m}\left(v_i v_m\right)$ and $\frac{\partial}{\partial x_m}\left(v_i v_m\right) = \delta_{ij}\frac{\partial}{\partial x_m}\left(v_j v_m\right)$. We now identify the following terms

$$
P_{ij} = \delta_{ij} - \frac{1}{\bigtriangledown^2}\frac{\partial^2}{\partial x_i x_j} \qquad \text{(A.49)}
$$

and

$$
P_{ijm} = \frac{\partial}{\partial x_m}P_{ij} + \frac{\partial}{\partial x_j}P_{im}. \qquad \text{(A.50)}
$$

Finally, we take the Fourier Transform of Eq. A.50 i.e.

$$
\begin{aligned}
&F.T.\left[\frac{\partial}{\partial x_m}P_{ij} + \frac{\partial}{\partial x_j}P_{im}\right] \\
&= ik_m\left(\delta_{ij} - \frac{k_i k_j}{k^2}\right) + ik_j\left(\delta_{im} - \frac{k_i k_m}{k^2}\right) \qquad \text{(A.51)}
\end{aligned}
$$

as required.

II Barotropic vorticity interaction coefficients

In this appendix the interaction coefficients $K(\mathbf{k},\mathbf{p},\mathbf{q})$ and $A(\mathbf{k},\mathbf{p},\mathbf{q})$ as defined in Eqs. 3.7 and 3.8 are derived. We first consider the Jacobian

$$J(\psi,\zeta+h)=\frac{\partial\psi}{\partial x}\frac{\partial(\zeta+h)}{\partial y}-\frac{\partial\psi}{\partial y}\frac{\partial(\zeta+h)}{\partial x} \tag{A.52}$$

where

$$\sum_{\mathbf{k}}\psi_{\mathbf{k}}(t)\exp(i\mathbf{k}\cdot\mathbf{x})=-\sum_{\mathbf{k}}\frac{1}{k^2}\zeta_{\mathbf{k}}(t)\exp(i\mathbf{k}\cdot\mathbf{x}). \tag{A.53}$$

Thus

$$\begin{aligned}J(\psi,\zeta+h)=\sum_{\mathbf{p}}\sum_{\mathbf{q}}\frac{p_xq_y-p_yq_x}{p^2}\\ \times\zeta_{\mathbf{p}}(t)[\zeta_{\mathbf{q}}(t)+h_{\mathbf{q}}]\exp(i\mathbf{p}\cdot\mathbf{x}+i\mathbf{q}\cdot\mathbf{x}).\end{aligned} \tag{A.54}$$

Now take

$$\frac{1}{(2\pi)^2}\int\int_0^{2\pi}d\mathbf{x}\ \ \exp(-i\mathbf{k}\cdot\mathbf{x})=\langle\phi(\mathbf{x})| \tag{A.55}$$

thus

$$\langle\phi(\mathbf{x})|\psi(\mathbf{x})\rangle=$$

$$\frac{1}{(2\pi)^2}\int\int_0^{2\pi}d\mathbf{x}\ \ \exp(-i\mathbf{k}\cdot\mathbf{x})\sum_{\acute{k}_x}\sum_{\acute{k}_y}\psi_{\acute{k}_x\acute{k}_y}\exp(-i\acute{\mathbf{k}}\cdot\mathbf{x}) \tag{A.56}$$

$$=\psi_{\mathbf{k}} \tag{A.57}$$

subsequently

$$\langle\phi(\mathbf{x})|J(\psi,\zeta+h)\rangle=$$

$$\sum_{\mathbf{p}}\sum_{\mathbf{q}}\delta(\mathbf{k},-\mathbf{p},-\mathbf{q})\frac{(p_xq_y-p_yq_x)}{p^2}\zeta_{\mathbf{p}}(t)[\zeta_{\mathbf{q}}(t)+h_{\mathbf{q}}]. \tag{A.58}$$

So that ultimately we find

$$\langle\phi(\mathbf{x})|-J(\psi,\zeta)\rangle=$$

$$\sum_{\mathbf{p}}\sum_{\mathbf{q}}\delta(\mathbf{k},\mathbf{p},\mathbf{q})K(\mathbf{k},\mathbf{p},\mathbf{q})\zeta_{-\mathbf{p}}(t)\zeta_{-\mathbf{q}}(t) \tag{A.59}$$

$$\langle \phi(\mathbf{x})| - J(\psi,h)\rangle = \sum_{\mathbf{p}}\sum_{\mathbf{q}} \delta(\mathbf{k},\mathbf{p},\mathbf{q}) A(\mathbf{k},\mathbf{p},\mathbf{q}) \zeta_{-\mathbf{p}}(t) h_{-\mathbf{q}} \tag{A.60}$$

where the coefficients for the $\zeta_{-\mathbf{p}}(t)\zeta_{-\mathbf{q}}(t)$ terms can be symmetrized to give

$$K(\mathbf{k},\mathbf{p},\mathbf{q}) = \frac{1}{2}\frac{(p_x q_y - p_y q_x)(p^2 - q^2)}{p^2 q^2} \tag{A.61}$$

and the coefficients for the $\zeta_{-\mathbf{p}}(t)h_{-\mathbf{q}}$ terms remain unchanged as the topographic terms are non-dynamic variables ie

$$A(\mathbf{k},\mathbf{p},\mathbf{q}) = -\frac{(p_x q_y - p_y q_x)}{p^2}. \tag{A.62}$$

III Two-point restart via fluctuation-dissipation theorem

In this appendix an alternate derivation of the two-point restart terms (derived in section 3.4.2 using perturbation theory) is developed. The following approach makes use of the fluctuation dissipation theorem. Consider the equation for the off-diagonal two-time cumulant

$$\begin{aligned} C_{\mathbf{k}-\mathbf{l}}(t,\acute{t}) = \int_{t_0}^{t} & ds R_{\mathbf{k}}(t,s) C_{-\mathbf{l}}(\acute{t},s)[A(\mathbf{k},-\mathbf{l},\mathbf{l}-\mathbf{k}) h_{\mathbf{k}-\mathbf{l}} \\ & + 2K(\mathbf{k},-\mathbf{l},\mathbf{l}-\mathbf{k})\langle \zeta_{\mathbf{k}-\mathbf{l}}(s)\rangle] \\ + \int_{t_0}^{\acute{t}} & ds C_{\mathbf{k}}(t,s) R_{-\mathbf{l}}(\acute{t},s)[A(-\mathbf{l},\mathbf{k},\mathbf{l}-\mathbf{k}) h_{\mathbf{k}-\mathbf{l}} \\ & + 2K(-\mathbf{l},\mathbf{k},\mathbf{l}-\mathbf{k})\langle \zeta_{\mathbf{k}-\mathbf{l}}(s)\rangle]. \end{aligned} \tag{A.63}$$

We now suppose that the propagator can be written in the form

$$R_{\mathbf{k}}(t,s) = R_{\mathbf{k}}(t,T) R_{\mathbf{k}}(T,s) \tag{A.64}$$

and that the fluctuation-dissipation theorem for the $O(1)$ diagonal propagator holds, ie.,

$$C_{\mathbf{k}}(t,s)\theta(t-s) = R_{\mathbf{k}}(t,s) C_{\mathbf{k}}(s,s). \tag{A.65}$$

Thus for $t \geq \acute{t} \geq T$

$$\begin{aligned} C_{\mathbf{k}-\mathbf{l}}(t,\acute{t}) = \int_T^t \; & dsR_{\mathbf{k}}(t,s)C_{-\mathbf{l}}(\acute{t},s)[A(\mathbf{k},-\mathbf{l},\mathbf{l}-\mathbf{k})h_{\mathbf{k}-\mathbf{l}} \\ & +2K(\mathbf{k},-\mathbf{l},\mathbf{l}-\mathbf{k})\langle\zeta_{\mathbf{k}-\mathbf{l}}(s)\rangle] \\ + \int_T^{\acute{t}} \; & dsC_{\mathbf{k}}(t,s)R_{-\mathbf{l}}(\acute{t},s)[A(-\mathbf{l},\mathbf{k},\mathbf{l}-\mathbf{k})h_{\mathbf{k}-\mathbf{l}} \\ & +2K(-\mathbf{l},\mathbf{k},\mathbf{l}-\mathbf{k})\langle\zeta_{\mathbf{k}-\mathbf{l}}(s)\rangle] \\ +R_{\mathbf{k}}(t,T)R_{-\mathbf{l}}(\acute{t},T)\int_{t_0}^T \; & dsR_{\mathbf{k}}(T,s)C_{-\mathbf{l}}(T,s)[A(\mathbf{k},-\mathbf{l},\mathbf{l}-\mathbf{k})h_{\mathbf{k}-\mathbf{l}} \\ & +2K(\mathbf{k},-\mathbf{l},\mathbf{l}-\mathbf{k})\langle\zeta_{\mathbf{k}-\mathbf{l}}(s)\rangle] \\ +R_{\mathbf{k}}(t,T)R_{-\mathbf{l}}(\acute{t},T)\int_{t_0}^T \; & dsC_{\mathbf{k}}(T,s)R_{-\mathbf{l}}(T,s)[A(-\mathbf{l},\mathbf{k},\mathbf{l}-\mathbf{k})h_{\mathbf{k}-\mathbf{l}} \\ & +2K(-\mathbf{l},\mathbf{k},\mathbf{l}-\mathbf{k})\langle\zeta_{\mathbf{k}-\mathbf{l}}(s)\rangle]. \end{aligned} \tag{A.66}$$

Now writing Eq. A.66 in compact form as

$$\begin{aligned} C_{\mathbf{k}-\mathbf{l}}(t,\acute{t}) = \int_T^t \; & dsR_{\mathbf{k}}(t,s)C_{-\mathbf{l}}(\acute{t},s)[A(\mathbf{k},-\mathbf{l},\mathbf{l}-\mathbf{k})h_{\mathbf{k}-\mathbf{l}} \\ & +2K(\mathbf{k},-\mathbf{l},\mathbf{l}-\mathbf{k})\langle\zeta_{\mathbf{k}-\mathbf{l}}(s)\rangle] \\ + \int_T^{\acute{t}} \; & dsC_{\mathbf{k}}(t,s)R_{-\mathbf{l}}(\acute{t},s)[A(-\mathbf{l},\mathbf{k},\mathbf{l}-\mathbf{k})h_{\mathbf{k}-\mathbf{l}} \\ & +2K(-\mathbf{l},\mathbf{k},\mathbf{l}-\mathbf{k})\langle\zeta_{\mathbf{k}-\mathbf{l}}(s)\rangle] \\ & +R_{\mathbf{k}}(t,T)R_{-\mathbf{l}}(\acute{t},T)C_{\mathbf{k}-\mathbf{l}}(T,T). \end{aligned} \tag{A.67}$$

We note that we only need $C_{\mathbf{k}-\mathbf{l}}(t,\acute{t})$ in the closure equations and not $R_{\mathbf{k}-\mathbf{l}}(t,\acute{t})$ as we are assuming white noise.

Bibliography

[1] J.C. McWilliams. The emergence of isolated coherent vortices in turbulent flow. *J. Fluid Mech.*, 146:21, 1984.

[2] A.N. Kolmogorov. The local structure of turbulence in incompressible viscous fluid for very large Reynolds number. *Dokl. Akad. Nauk SSSR*, 30:301, 1941.

[3] R. Fj∅rtoft. On the changes in the spectral distribution of kinetic energy for two-dimensional non-divergent flow. *Tellus*, 5:225, 1953.

[4] R.H. Kraichnan. Inertial ranges in two-dimensional turbulence. *Phys. Fluids*, 10:1417, 1967.

[5] C.E. Leith. Diffusion approximation for two-dimensional turbulence. *Phys. Fluids*, 11:671, 1968.

[6] G.K. Batchelor. Computation of the energy spectrum in homogeneous two-dimensional turbulence. *Phys. Fluids*, 12:233, 1969.

[7] G. Holloway and M.C. Hendershott. Stochastic closure for nonlinear Rossby waves. *J. Fluid Mech.*, 82:747, 1974.

[8] R. Salmon, G. Holloway and M.C. Hendershott. The equilibrium statistical mechanics of simple quasi-geostrophic models. *J. Fluid Mech.*, 75:691, 1976.

[9] F.P. Bretherton and D.B. Haidvogel. Two-dimensional turbulence above topography. *J. Fluid Mech.*, 78:129, 1976.

[10] J.S. Frederiksen and B.L. Sawford. Topographic waves in nonlinear and linear spherical barotropic models. *J. Atmos. Sci.*, 38:69, 1981.

[11] J.S. Frederiksen. Eastward and westward flows over topography in nonlinear and linear barotropic models. *J. Atmos. Sci.*, 39:2477, 1982.

[12] B.L. Sawford and J.S. Frederiksen. Mountain torque and angular momentum in barotropic planetary flows: Equilibrium solutions. *Q. J. R. Meteorol. Soc.*, 109:309, 1983.

[13] G.F. Carnevale and J.S. Frederiksen. Nonlinear stability and statistical mechanics of flow over topography. *J. Fluid Mech.*, 175:157, 1987.

[14] G. Holloway. Systematic forcing of large-scale geophysical flows by eddy-topographic interaction. *J. Phys. Oceanogr.*, 184:463, 1987.

[15] A.M. Treguier. Topographically generated steady currents in barotropic turbulence. *Geophys. Astrophys. Fluid Dyn.*, 47:43, 1989.

[16] W.J. Merryfield and G. Holloway. Topographic stress parameterizations in a quasi-geostrophic barotropic model. *J. Fluid Mech.*, 341:1, 1997.

[17] G. Holloway. Representing topographic stress for large-scale ocean models. *J. Phys. Oceanogr.*, 22:1033, 1992.

[18] R.H. Kraichnan. Dynamics of nonlinear stochastic systems. *J. Math. Phys.*, 2:124, 1961.

[19] R.H. Kraichnan. The structure of isotropic turbulence at very high reynolds number. *J. Fluid. Mech.*, 5:497, 1959.

[20] D.C. Leslie. *Developments in the Theory of Turbulence*. Clarendon Press, Oxford, 1973.

[21] J.S. Schwinger. On the green's functions of quantized fields. I and II. *Proc. Natl. Acad. Sci*, 37:452, 1951.

[22] J.S. Schwinger. Quantum electrodynamics. III. The electromagnetic properties of the electron - radiative corrections to scattering. *Phys. Rev.*, 76:790, 1949.

[23] F.J. Dyson. The radiation theories of Tomonaga, Schwinger, and Feynman. *Phys. Rev.*, 75:486, 1949.

[24] R.P. Feynman and A.R. Hibbs. *Quantum Mechanics and Path Integrals.* McGraw-Hill, New York, 1965.

[25] R.P. Feynman. An operator calculus having applications in quantum electrodynamics. *Phys. Rev.*, 84:108, 1951.

[26] J.R. Herring and R.H. Kraichnan. *Statistical Models of Turbulence.* Springer, 1972.

[27] R.H. Kraichnan. Isotropic turbulence and inertial range structure. *Phys. Fluids*, 9:1728, 1966.

[28] J.S. Frederiksen and A.G. Davies. The regularized dia closure for two-dimensional turbulence. *Geophys. Astrophys. Fluid Dyn.*, Feb 2002. submitted.

[29] H.W. Wyld. Jr. Formulation of the theory of turbulence in an incompressible fluid. *Annal. Phys.*, 14:143–165, 1961.

[30] L.L. Lee. A formulation of the theory of isotropic hydromagnetic turbulence in an incompressible fluid. *Annal. Phys.*, 32:292–321, 1965.

[31] P.C. Martin, E.D. Siggia and H.A. Rose. Statistical dynamics of classical systems. *Phys. Rev. A*, 8:423, 1973.

[32] R.V. Jensen. Functional integral approach to classical statistical dynamics. *J. Stat. Phys.*, 25:183–210, 1981.

[33] V. L'Vov and I. Procaccia. Exact resummations in the theory of hydrodynamic turbulence. Technical report, Les Houches Summer School, 1994.

[34] R.H. Kraichnan. Irreversible statistical mechanics of incompressible hydrodynamic turbulence. *Phys. Rev.*, 109:1407, 1958.

[35] W. Heisenberg. Zur statistischen Theorie der turbulenz. *Z. Phys.*, 124:628, 1948.

[36] W. Heisenberg. On the theory of statistical and isotropic turbulence. *Proc. Roy. Soc. A*, 195:402, 1948.

[37] S. Chandrasekar. A theory of turbulence. *Proc. Roy. Soc. A*, 229:1, 1955.

[38] R.H. Kraichnan. Kolmogorov's hypothesis and Eulerian turbulence theory. *Phys. Fluids*, 7:1723, 1964.

[39] R.H. Kraichnan. Relation between Lagrangian and Eulerian correlation times of a turbulent velocity field. *Phys. Fluids*, 7:142, 1964.

[40] R.H. Kraichnan. Lagrangian History closure approximation for turbulence. *Phys. Fluids*, 8:575, 1965.

[41] R.H. Kraichnan. Eulerian and Lagrangian renormalization in turbulence theory. *J. Fluid Mech.*, 83:349, 1977.

[42] J.R. Herring and R.H. Kraichnan. A numerical comparison of velocity-based and strain based Lagrangian-history turbulence approximations. *J. Fluid Mech.*, 91:581, 1979.

[43] W.D. McComb. *The Physics of Fluid Turbulence.* Oxford engineering science series 25. Clarendon Press, Oxford, 1990.

[44] G.I. Taylor. Diffusion by continuous movements. *Proc. Lond. Math. Soc., Series 2*, 20:196, 1922.

[45] R.H. Kraichnan and J.R. Herring. A strain-based Lagrangian-History turbulence. *J. Fluid Mech.*, 88:355, 1978.

[46] J.R. Herring and R.H. Kraichnan. A numerical comparison of velocity based and strain-based Lagrangian-History turbulence approximations. *J. Fluid Mech.*, 91:581, 1979.

[47] Y. Ogura. A consequence of the zero fourth cumulant approximation in the decay of isotropic turbulence. *J. Fluid Mech.*, 16:33, 1963.

[48] S.A. Orszag. Statistical theory of turbulence. In R. Balian and J.-L. Peube, editors, *Fluid Dynamics 1973*, Les Houches Summer School of Theoretical Physics, page 237. Gordan and Breech, London, 3rd edition, 1977.

[49] J.C. Bowman, J.A. Krommes and M. Ottaviani. The realizable Markovian closure I. General theory, with applications to 3-wave dynamics. *Phys. Fluids*, 5:3558, 1993.

[50] B.K. Shivamoggi, M.D. Taylor and S. Kida. On some mathematical aspects of the direct-interaction approximation in turbulence theory. *J. Math. Anal. and Appl.*, 229:639, 1999.

[51] P.C. Martin and C. DeDominicis. Stationary entropy principle and renormalization in normal and superfluid systems . 1 algebraic formulation. *J. Math. Phys.*, 5:14, 1964.

[52] R.P. Feynman. A spacetime approach to quantum electrodynamics. *Phys. Rev.*, 76:769, 1949.

[53] K. Hasselmann. Feynman diagrams and interaction rules for wave-wave scattering processes. *Reviews of Geophysics*, 4:1, 1966.

[54] R. Phythian. Self consistent perturbation series for stationary homogeneous turbulence. *J. Phys. A*, 2:181, 1969.

[55] R. Phythian. The functional formalism of classical statistical dynamics. *J. Phys. A*, 10:777–789, 1977.

[56] J.A. Krommes, R.G. Kleva and C. Oberman. Plasma transport in stochastic magnetic fields. Part 3. Kinetics of test particle diffusion. *J. Plasma Physics*, 30, 1982.

[57] R.H. Kraichnan. Classical fluctuation-relaxation theorem. *Phys. Rev.*, 113:1181, 1959.

[58] C.E. Leith. Climate response and fluctuation dissipation. *J. Atmos. Sci.*, 32:2022, 1975.

[59] T.L. Bell. Climate sensitivity from fluctuation dissipation: Some simple model tests. *J. Atmos. Sci.*, 37:1700, 1980.

[60] U. Deker and F. Haake. Fluctuation-dissipation theorems for classical processes. *Phys. Rev. A*, 6:2043–2056, 1975.

[61] G.F. Carnevale, M. Falcioni, S. Isola, R. Purini and A. Vulpiani. Fluctuation-response relations in systems with chaotic behavior. *Phys. Fluids A*, 1991.

[62] J.R. Herring. Self-consistent-field approach to turbulence theory. *Phys. Fluids*, 8:2219, 1965.

[63] W.D. McComb, M.J. Filipiak and V. Shanmugasundaram. Rederivation and further assessment of the LET theory of isotropic turbulence, as applied to passive scalar convection. *J. Fluid Mech.*, 245:279, 1992.

[64] S.F. Edwards. The statistical dynamics of homogeneous turbulence. *J.Fluid Mech.*, 18:239, 1964.

[65] G.F. Carnevale and J.S. Frederiksen. Viscosity renormalization based on direct-interaction closure. *J. Fluid Mech.*, 131(289), 1983.

[66] R.H. Kraichnan. Approximations for steady-state isotropic turbulence. *Phys. Fluids*, 7:1163, 1964.

[67] R.P. Feynman. Mathematical formulation of the quantum theory of electromagnetic interaction. *Phys. Rev.*, 80:440, 1950.

[68] H.K. Janssen. On a Lagrangean for classical field dynamics and renormalization group calculations of dynamical critical properties. *Z. Phys. B*, 23:377, 1976.

[69] C. DeDominicis. Techniques de renormalisation de la théorie des champs et dynamique des phénoménes critiques. *J. Phys. (Paris) Colloq.*, 1:247, 1976.

[70] C. DeDominicis and L. Peliti. Field-theory renormalization and critical dynamics above t_c: Helium, antiferromagnets, and liquid-gas systems. *Phys. Rev. B*, 18:353, 1978.

[71] B. Jouvet and R. Phythian. Quantum aspects of classical and statistical fields. *Phys. Rev. A*, 19:1350, 1979.

[72] E.A. Novikov. Functionals and the random force-method in turbulence. *Sov. Phys. JETP*, 20:1290, 1965.

[73] J.A. Krommes and R.G. Kleva. Aspects of a renormalized weak plasma turbulence theory. *Phys. Fluids*, 22:2168, 1979.

[74] M. Millionshtchiktov. On the theory of homogeneous isotropic turbulence. *Dokl. Acad. Nauk. SSSR*, 32:615, 1941.

[75] P.Y. Chou. On an extension of Reynold's method of finding apparent stress and the nature of turbulence. *Chin. J. Phys.*, 4:1, 1940.

[76] I. Proudman and W.H. Reid. On the decay of a normally distributed and homogeneous turbulent velocity field. *Phil. Trans. Roy. Soc.*, Vol A 247:163, 1954.

[77] T. Tatsumi. The theory of decay process of incompressible isotropic turbulence. *Proc. Rot. Soc. London*, Ser. A 239:16, 1957.

[78] S.A. Orszag. Analytical theories of turbulence. *J. Fluid Mech.*, 41:363, 1970.

[79] M. Lesieur. *Turbulence in Fluids*. Fluid mechanics and its applications. Kluwer academic publishers, 3rd edition edition, 1997.

[80] H. Rose and P.L. Sulem. Fully developed turbulence and statistical mechanics. *Journal de Physique (Paris)*, 39:441, 1978.

[81] C.E. Leith. Atmospheric predictability and two-dimensional turbulence. *J. Atmos. Sci.*, 28:145, 1971.

[82] R.H. Kraichnan. Inertial-range transfer in two and three dimensional turbulence. *J. Fluid Mech.*, 47:525, 1971.

[83] R.H. Kraichnan. An almost Markovian Galilean invariant turbulence model. *J. Fluid Mech.*, 47:513, 1971.

[84] C.E. Leith and R.H. Kraichnan. Predictability of turbulent flows. *J. Atmos. Sci.*, 29:1041, 1972.

[85] R.H. Kraichnan. Test-field model for inhomogeneous turbulence. *J. Fluid Mech.*, 56:287, 1972.

[86] J.R. Herring, D. Schertzer, M. Lesieur, G.R. Newman, J.P.Chollet and M. Larchevêque. A comparative assessment of spectral closures as applied to passive scalar diffusion. *J. Fluid Mech.*, 124:411, 1982.

[87] J.C. Bowman and J.A. Krommes. The realizable Markovian closure and realizable test-field model II: Application to anisotropic drift-wave dynamics. *Phys. Plasmas*, 4:3895, 1997.

[88] M. Eby and G. Holloway. Sensitivity of a large-scale ocean model to a parameterization of topographic stress. *J. Phys. Oceanogr.*, 24:2577, 1994.

[89] G. Holloway, T. Sou and M. Eby. Dynamics of circulation of the Japan Sea. *J. Mar. Res.*, 53:539, 1995.

[90] J. Fyfe and G. Marinone. On the role of unresolved eddies in a model of the residual currents in the central straits of Georgia. *Atmos.-Ocean*, 33:613, 1995.

[91] J.S. Frederiksen. Subgrid-scale parameterizations of eddy-topographic force, eddy viscosity, and stochastic backscatter for flow over topography. *J. Atmos. Sci.*, 56:1481, 1999.

[92] R.H. Kraichnan. Diagonalizing approximation for inhomogeneous turbulence. *Phys. Fluids*, 7:1169, 1964.

[93] J.R. Herring. On the statistical theory of two-dimensional topographic turbulence. *J. Atmos. Sci.*, 34:1731, 1977.

[94] J.S. Frederiksen and G.F. Carnevale. Stability properties of exact nonzonal solutions for flow over topography. *Geophys. Astrophys. Fluid Dyn.*, 35:173, 1986.

[95] J.S. Frederiksen and B.L. Sawford. Statistical dynamics of two-dimensional inviscid flow on a sphere. *J. Atmos Sci.*, 37:717, 1980.

[96] A.M. Treguier and J.C. McWilliams. Topographic influences on wind-driven, stratified flow in a beta-plane channel: An idealized model for the Antarctic circumpolar current. *J. Phys. Oceanogr.*, 20:321, 1990.

[97] A. Griffa and R. Salmon. Wind-driven ocean circulation and equilibrium statistical mechanics. *J. Mar. Res.*, 47:457, 1989.

[98] P.F. Cummins. Inertial gyres in decaying and forced geostrophic turbulence. *J. Mar. Res.*, 50:545, 1992.

[99] J. Wang and G. Vallis. Emergence of Fofonoff states in inviscid and viscous ocean circulation models. *J. Mar. Res.*, 52:83, 1994.

[100] J. Zou and G. Holloway. Entropy maximization tendency in topographic turbulence. *J. Fluid Mech.*, 263:361, 1994.

[101] G. Holloway. A spectral theory of nonlinear barotropic motion above irregular topography. *J. Phys. Oceanogr.*, 8:414, 1978.

[102] T.J. O'Kane and J.S. Frederiksen. Integro-differential closure equations for inhomogeneous turbulence. *ANZIAM J.*, 2002. in press.

[103] H.A. Rose. An efficient non-Markovian theory of non-equilibrium dynamics. *Physica D*, 14:216, 1985.

[104] J.S. Frederiksen, A.G. Davies and R.C. Bell. Closure equations with non-Gaussian restarts for truncated two-dimensional turbulence. *Phys. Fluids*, 6:3153, 1994.

[105] P.D. Thompson. The integral invariants of two-dimensional inviscid flow and their role in the theory of two-dimensional turbulence. *J. Atmos. Sci.*, 31:1453, 1974.

[106] V.I. Arnold. On conditions for nonlinear stability of plane stationary curvilinear flows of an ideal fluid. *Sov. Math. Dokl.*, 6:773, 1965.

[107] J.S. Frederiksen and A.G. Davies. Performance of integro-differential closure equations for two-dimensional turbulence. In R.L. May and A.K. Easton, editors, *Computational techniques and applications: CTAC95*, page 319. World Scientific Publishing Co, 1996.

[108] J.S. Frederiksen and A.G. Davies. Dynamics and spectra of cumulant update closures for two-dimensional turbulence. *Geophys. Astrophys. Fluid Dynamics*, 92:197, 2000.

[109] R.H. Kraichnan. Decay of isotropic turbulence in the direct-interaction approximation. *Phys. Fluids*, 7:1030, 1964.

[110] J.R. Herring and J.C. McWilliams. Comparison of direct numerical simulation of two-dimensional turbulence with two-point closure: the effect of intermittency. *J. Fluid Mech.*, 153:229, 1985.

[111] L.C. Kells and S.A. Orszag. Randomness of low-order models of two-dimensional inviscid dynamics. *Phys. Fluids*, 21:162, 1978.

[112] J.R. Herring, S.A. Orszag, R.H. Kraichnan and D.G. Fox. Decay of two-dimensional homogeneous turbulence. *J. Fluid Mech.*, 66:417, 1974.

[113] P.B. Rhines. Waves and turbulence on a β-plane. *J. Fluid Mech.*, 69:417, 1975.

[114] J. Verron and C. Le Provost. A numerical study of quasi-geostrophic flow over isolated topography. *J. Fluid Mech.*, 154:231, 1985.

[115] C.S. Frederiksen and J.S. Frederiksen. Flow over topography and instability on beta-planes: The effects of different expansion representations. *J. Atmos. Sci.*, 46:1664, 1989.

[116] J.R. Holton. *An Introduction to Dynamic Meteorology.* International Geophysics Series. Academic Press Inc, 111 Fifth Avenue, New York, second edition, 1979.

[117] I. Silberman. Planetary waves in the atmosphere. *Journal of Meteorology*, 11:27, 1954.

[118] A. Katz. *Principles of Statistical Mechanics*. Freeman, 1967.

[119] P.R. Bannon. Rotating barotropic flow over finite isolated topography. *J. Fluid Mech.*, 101:281, 1980.

[120] G.J. Boer and T.G. Shepherd. Large-scale two-dimensional turbulence in the atmosphere. *J. Atmos. Sci.*, 40:164, 1983.